PolyPublie
Polytechnique Montréal

POLYTECHNIQUE MONTRÉAL
UNIVERSITÉ D'INGÉNIERIE

Titre: Title:	Plasma Actuation for Boundary Layer Separation Control in Engine Ducts
Auteur: Author:	Xiaofei Xu
Date:	2011
Type:	Mémoire ou thèse / Dissertation or Thesis
Référence: Citation:	Xu, X. (2011). Plasma Actuation for Boundary Layer Separation Control in Engine Ducts [Thèse de doctorat, École Polytechnique de Montréal]. PolyPublie. https://publications.polymtl.ca/743/

Document en libre accès dans PolyPublie
Open Access document in PolyPublie

URL de PolyPublie: PolyPublie URL:	https://publications.polymtl.ca/743/
Directeurs de recherche: Advisors:	Huu Duc Vo, Xuefeng Zhang, & Njuki W. Mureithi
Programme: Program:	Génie mécanique

Ce fichier a été téléchargé à partir de PolyPublie, le dépôt institutionnel de Polytechnique Montréal
This file has been downloaded from PolyPublie, the institutional repository of Polytechnique Montréal

https://publications.polymtl.ca

UNIVERSITÉ DE MONTRÉAL

PLASMA ACTUATION FOR BOUNDARY LAYER SEPARATION CONTROL IN ENGINE DUCTS

XIAOFEI XU
DÉPARTEMENT DE GÉNIE MÉCANIQUE
ÉCOLE POLYTECHNIQUE DE MONTRÉAL

THÈSE PRÉSENTÉE EN VUE DE L'OBTENTION
DU DIPLÔME DE PHILOSOPHIÆ DOCTOR (Ph.D.)
(GÉNIE MÉCANIQUE)
DÉCEMBRE 2011

© Xiaofei Xu, 2011.

UNIVERSITÉ DE MONTRÉAL

ÉCOLE POLYTECHNIQUE DE MONTRÉAL

Cette thèse intitulée:

PLASMA ACTUATION FOR BOUNDARY LAYER SEPARATION CONTROL IN ENGINE DUCTS

présentée par: XU, Xiaofei

en vue de l'obtention du diplôme de: Philosophiæ Doctor

a été dûment acceptée par le jury d'examen constitué de:

M. VÉTEL, Jérôme, Ph.D., président

M. VO, Huu Duc, Ph.D., membre et directeur de recherche

M. MUREITHI, Njuki, Ph.D., membre et codirecteur de recherche

M. ZHANG, Xuefeng, Ph.D., membre et codirecteur de recherche

M. TRÉPANIER, Jean-Yves, Ph.D., membre

Mme. TSIFOURDARIS, Panagiota, Ph.D., membre externe

Dedication

To my lovely wife Minxuan Wang

Acknowledgements

The work reported in this thesis was performed in collaboration with the National Research Council Gas Turbine Laboratory (NRC GTL) in Ottawa, as a part of the research project "Application of Plasma Actuation-Based Flow Control Technology Strategies for Gas Turbines". Their generous financial support is highly appreciated.

During the course of my doctoral study, I have received continuous guidance and support from my supervisors Professor Huu Duc Vo, Professor Njuki Mureithi and Dr. George Zhang. I have also received considerable help from the members of the Wind Tunnel Laboratory at École Polytechnique de Montréal and the NRC Gas Turbine Laboratory.

I am very pleased to acknowledge the assistance with the computational resources from Mr. Omar Toukal, and the help from Mr. Sebastien Lemire for providing the body force field and mapping it onto the CFD mesh. I am also particularly grateful to Mr. Philippe Versailles for providing the test data for plasma actuation in quiescent air. The assistance from Mr. Shinya Ueno and Mr. Kenny Huynh with the preliminary experimental setup at École Polytechnique de Montréal is gratefully acknowledged.

The work at NRC GTL would have been impossible without the outstanding work of Dr. Ali Mahallati and Mr. Paul Hunt on the 2-D experimental setup, and Mr. Bob McLaughlin for building the new plasma actuation system. The great help of Dr. Shuzhen Hu and Dr. Yanfeng Zhang in the work on inter-turbine ducts (ITDs) is also highly appreciated.

I reserve my deepest gratitude to my wife Minxuan Wang. Without her continuous support and love this work would not have been successfully completed.

Résumé

Le décollement de la couche limite turbulente est un problème important pour une multitude d'applications, notamment pour les conduits en forme de S comme des entrées d'air non axiales de moteurs d'avion et les conduits de transition entre les turbines (ITD) de ces moteurs. Le décollement de la couche limite turbulente dans les entrées d'air non axiales provoque une distorsion de l'écoulement entrant dans le moteur d'avion, ce qui détériore la performance du moteur et diminue la durée de vie de ses composantes. D'autre part, la conception du ITD est susceptible de devenir plus agressive (ITD plus court) pour répondre à des exigences de poids, de consommation de carburant et environnementales pour les nouveaux moteurs d'avion. Un design plus agressif peut mener au décollement de la couche limite turbulente causant des pertes de pression. Pour empêcher une réduction conséquente de la performance du moteur, ce design nécessiterait l'application de techniques de contrôle de l'écoulement. Diverses techniques ont été étudiées pour le contrôle du décollement de la couche limite, dont les générateurs de vortex, des jets générateurs de vortex, et des jets synthétiques. L'avènement récent des actionneurs plasma, aussi connus sous le nom de *Dielectric Barrier Discharge* (DBD) peut potentiellement fournir une méthode alternative plus efficace et robuste. Les actionneurs plasma convertissent l'électricité directement en quantité de mouvement du fluide. Comparés à d'autres techniques de contrôle de l'écoulement, ces actionneurs électriques dépourvus de pièces mobiles ont un temps de réponse rapide et sont simples, potentiellement robustes et faciles à intégrer et ne perturbent pas l'écoulement lorsque non utilisés (presque ou sans intrusion dans l'écoulement), ce qui les rend idéaux pour les applications aérodynamiques.

Le présent travail évalue l'efficacité du concept d'actionnement plasma pour supprimer le décollement de la couche limite turbulente dans des conduits en forme de S. Premièrement, des études numériques et expérimentales sur le contrôle du décollement de la couche limite turbulente par actionnement plasma sont effectuées sur des diffuseurs génériques 2-D, représentant des modèles simplifiés de conduits 3-D en forme de S. Les trouvailles des travaux

numériques et expérimentales sont similaires. Les résultats montrent que l'actionnement plasma peut réduire ou même supprimer le décollement de la couche limite turbulente dans les deux modes d'opération, soient en mode continu et en mode pulsé. L'efficacité du contrôle (en termes de rendement en pression) augmentent avec la force d'actionnement. L'emplacement optimal de l'actionneur est généralement proche et en amont du point de séparation de la couche limite. En mode pulsé, la fréquence optimale de pulsation correspond à une fréquence adimensionnelle (basée sur la vitesse de l'écoulement principal et la longueur de décollement de la couche limité) de l'ordre de 1 et est égale (en dedans de la résolution de mesure) à la fréquence dominante de l'écoulement dans la couche limite turbulente non actionnée. Ce résultat signifie que l'actionnement pulsé fonctionne par la résonance des structures turbulentes dominantes augmentant ainsi le taux de mélange et par conséquent le transfert de quantité de mouvement entre l'écoulement à haute vitesse plus loin de la surface et l'écoulement à basse vitesse près de la surface. La réduction du décollement de la couche limite turbulente augmente avec le facteur de cycle (pourcentage du cycle pulsé où l'actionneur est allumé). Cependant, pour un rendement optimal en termes d'efficacité versus puissance consommée, le facteur de cycle doit être choisi entre 10% et 50%. En outre, l'actionnement en mode pulsé à la fréquence de pulsation optimale est plus efficace qu'en mode continu pour une puissance consommée similaire.

Guidé par les résultats des études sur les diffuseurs génériques 2-D, des études numériques et expérimentales sont effectuées sur une conduite ITD pour démonter l'efficacité des actionneurs plasma pour contrôler le décollement de la couche limite turbulente dans une conduite 3-D en forme de S, du moins en mode continu. Les tendances en termes de l'influence de la position de l'actionneur et de la force d'actionnement sur l'efficacité (mesurée par la réduction de la perte de pression associée au décollement de la couche limite turbulente) sont consistantes avec celles des études de diffuseurs 2-D. De plus, des règles de design préliminaires empiriques pour actionnement plasma en mode continu obtenues avec les données de simulations numériques de diffuseurs génériques 2-D ont réussi à donner une prédiction approximative et

conservative de la force d'actionnement requise pour la suppression du décollement de la couche limite dans le ITD.

Abstract

Turbulent boundary layer separation is an important problem for a variety of applications, including S-shaped aircraft engine intakes and inter-turbine ducts (ITDs). Turbulent boundary layer separation in the engine intakes causes inlet flow distortion, resulting in deteriorated engine performance and reduced engine component life. The design of ITDs is likely to become more aggressive in response to requirements for lighter, more efficient and environment-friendly aircraft engines. Such aggressive ITDs would likely suffer large pressure losses due to turbulent boundary layer separation leading to reduced engine performance, and therefore require the application of flow control techniques. Various flow control techniques have been studied to control turbulent boundary layer separation, such as vortex generators, vortex generator jets and synthetic jets. The recent advent of dielectric barrier discharge (DBD) plasma actuators can potentially provide a more effective and robust alternative. Plasma actuators convert electricity directly into flow momentum near the surface through partial ionization of air. Compared to other flow control techniques, these electrical solid-state actuators have fast response time and are simple, potentially robust and easy to integrate and non-intrusive (low to zero protrusion), which make them ideal for aerodynamic applications.

The present work studies the effectiveness of DBD plasma actuators in the suppression of turbulent boundary layer separation in S-shaped engine ducts. First, numerical and experimental studies on the control of turbulent boundary layer separation by plasma actuation are carried out in 2-D generic diffusers, as simplified models of 3-D S-shaped engine ducts. The findings from both CFD simulations and experiments are similar. Results show that plasma actuation can reduce and even suppress turbulent boundary layer separation in both continuous and pulsed modes. The effectiveness of the actuation (in terms of pressure recovery) increases with the actuator strength. The optimal actuator location is generally close to and upstream of the boundary layer separation point. In the pulsed mode, the optimal pulsing frequency corresponds to a dimensionless frequency (based on freestream velocity and separation length) on the order of

1 and is equal to (within measurement resolution) the dominant frequency in the non-actuated turbulent boundary layer. This implies that the pulsed actuation works through resonance of dominant turbulence flow structures and improves flow mixing and momentum transfer from outer high-momentum flow to near-surface low-momentum flow. The actuation effectiveness increases with duty cycle. However, for optimal efficiency in terms of effectiveness versus power consumption in pulsed actuation, the duty cycle should be chosen between 10% and 50%. In addition, pulsed actuation at the optimal frequency is more effective than continuous actuation for similar power consumption.

With the results from 2-D diffusers as a general guide, numerical and experimental studies are conducted on an annular inter-turbine duct (ITD) to demonstrate the effectiveness of plasma actuation in controlling turbulent boundary layer separation in 3-D S-ducts in continuous actuation mode. The trends in terms of the influence of actuator location and strength on effectiveness (reduction of total pressure loss from boundary layer separation) are consistent with those from the 2-D diffusers studies. Moreover, empirical design rules for continuous plasma actuation, obtained from data collapse of computational simulations in 2-D generic diffusers, successfully provide a conservative prediction of the required actuator strength for reduction of turbulent boundary layer separation in the ITD.

Contents

Dedication ..... **iii**

Acknowledgements ..... **iv**

Résumé ..... **v**

Abstract ..... **viii**

Contents ..... **x**

List of Figures ..... **xii**

List of Tables ..... **xx**

List of Appendices ..... **xxi**

Chapter 1 Introduction **1**

Chapter 2 Literature Review **8**

2.1 Flow Distortion in Serpentine Ducts 8

2.2 Flow Control 12

2.3 Plasma Actuation 20

Chapter 3 Methodology **30**

3.1 Numerical/Analytical Study 30

3.1.1 Computational Tool Setup and Integration of Actuation Model 30

3.1.2 Conceptual Study on Generic Diffusers 33

3.1.3 Establishment of Design Rules 36

3.2 Experimental Study 39

3.2.1 Experimental Apparatus 39

3.2.2 DBD Plasma Actuators 48

3.2.3 Experiments 49

3.2.4 Data Reduction and Presentation 49

3.3 Application to Real Design 51

Chapter 4 Numerical Study on Separation Control in 2-D Diffusers **56**

4.1 Validation of Computational Tool 56
4.2 Numerical Assessment of Boundary Layer Separation Control Concept 64
4.2.1 Effect of Actuator Location 65
4.2.2 Effect of Actuator Strength 68
4.2.3 Effect of Duty Cycle 70
4.2.4 Effect of Pulsed Actuation Frequency 72
4.2.5 Effect of Power Consumption 74
4.3 Determination of Design Rules 78
4.4 Summary 88
Chapter 5 Experimental Study on Separation Control in 2-D Diffusers 89
5.1 Dielectric Barrier Discharge Plasma Actuators 89
5.1.1 DBD Plasma Actuator Design 89
5.1.2 Characteristics of Plasma Actuators Selected for Flow Control 94
5.2 Boundary Layer Separation in Non-Actuated Diffuser 100
5.3 Flow Control with Plasma Actuators 102
5.3.1 Effect of Actuator Strength 102
5.3.2 Effect of Pulsed Actuation Frequency 110
5.3.3 Effect of Duty Cycle 118
5.4 POD Analysis 121
5.5 Summary 127
Chapter 6 Separation Control in S-shaped Ducts 128
6.1 Boundary Layer Development in ITD Ducts 128
6.2 Flow Control with Plasma Actuators in ITD Ducts 135
Chapter 7 Conclusions and Recommendations 142
References 145
Appendices 153

List of Figures

Figure 1.1: S-shaped intake and the total-pressure distortion at the engine face..... 2
Figure 1.2: A schematic of diffusing serpentine duct 3
Figure 1.3: Vortex development in a serpentine duct (Sullivan *et al.*, 1982)..... 3
Figure 1.4: Typical ITD region in a turbofan engine (Hu *et al.*, 2011)..... 4
Figure 1.5: A schematic representation of plasma actuator 5
Figure 2.1: Total-pressure contours along the center-plane of an inlet (Brear *et al*., 2004) 10
Figure 2.2: Classifications of different flow control strategies..... 13
Figure 2.3: Configurations of fences and vortex generators (Sullerey *et al.*, 2002)..... 15
Figure 2.4: An illustration of vortex generator jet (VGJ) and definition of VGJ angles (Pradeep and Sullerey, 2006) 16
Figure 2.5: Schematic of (a) ZNMF jet actuator and (b) induced flow by ZNMF jets (Smith and Glezer, 1998)..... 17
Figure 2.6: Instantaneous streamwise velocity (white line: zero) for periodic forcing (a) and without forcing (b) (Herbst and Henningson, 2006)..... 19
Figure 2.7: Induced flow in quiescent air by DBD (Enloe *et al.*, 2004)..... 20
Figure 2.8: Time evolution of voltage, current, induced axial and normal velocity above the actuator (Forte *et al.*, 2007)..... 21
Figure 2.9: An illustration of pulsed actuation..... 23
Figure 2.10: Subdivision of the domain over the covered electrode into *N* volume (Lemire and Vo, 2011) 25
Figure 2.11: Different plasma actuator configurations (Rizzetta *et al.*, 2008) 27
Figure 2.12: Schematic of the test section side view (Hultgren and Ashpis, 2003) 28
Figure 2.13: Streamlines above a hump model, showing effects of plasma actuator on suppressing turbulent separation (He, 2007) 29

Figure 3.1: Time-averaged force distribution of plasma actuator for implementation into CFX . 32
Figure 3.2: Simulated diffuser with moderate adverse pressure gradient 34
Figure 3.3: Simulated diffuser with high adverse pressure gradient 34
Figure 3.4: Configuration of plasma actuation in different modes 35
Figure 3.5: A generic 2-D S-duct 37
Figure 3.6: Generic geometry for CFX simulations to determine actuation requirements 37
Figure 3.7: Experimental setup at NRC GTL 40
Figure 3.8: Configuration of low speed wind tunnel at NRC GTL 41
Figure 3.9: Configuration of plasma actuator implementation 43
Figure 3.10: Experimental setup of plasma actuator implementation 43
Figure 3.11: Experimental setup of Pitot tube 44
Figure 3.12: Setup for PIV measurement 47
Figure 3.13: An illustration of phase-locked measurement 47
Figure 3.14: Annular test rig with changeable ITD test section (Hu *et al.*, 2011) 54
Figure 3.15: Measurement locations and actuator locations in experiments 54
Figure 3.16: Plasma actuators on ITD casing (viewed from ITD exit) 55
Figure 3.17: ITD with an upstream vane in CFD simulations 55
Figure 4.1: Geometry and mesh of a planar diffuser (10 deg, length of diffuser = 21*H*) 57
Figure 4.2: Axial velocity profiles at *x/H*=24 for CFX and FLUENT simulations vs. experiment (DalBello *et al.*, 2005) 58
Figure 4.3: Separation streamlines for CFX and FLUNET simulations vs. DalBello *et al.*'s simulation (SST turbulence model) 58
Figure 4.4: Geometry and mesh of a diffuser with transition 59
Figure 4.5: Mesh for simulating mixing layer instability 61
Figure 4.6: Instantaneous fields showing geometrically-similar large structure: (a) instantaneous vorticity field in the present work, (b) colour-schlieren image (Slessor *et al.*, 1998) 61
Figure 4.7: Instantaneous vorticity fields for plasma actuator in quiescent air (a) PIV measurement,

(b) CFD simulation 62
Figure 4.8: Instantaneous velocity fields with pulsed plasma actuation at 108 mN/m, 40 Hz, duty cycle of 40% for several selected phases 63
Figure 4.9: Contour of time-averaged axial velocity and axial wall shear stress along the plate without actuation with indicated monitor points 66
Figure 4.10: Effect of actuator location 67
Figure 4.11: Effect of actuator strength 69
Figure 4.12: Contours of time-averaged axial velocity with continuous actuation at 180 mm: (a) 90 mN/m, (b) 240 mN/m, (c) 390 mN/m 70
Figure 4.13: Effect of duty cycle in pulsed mode at 180 mm, 50 Hz 71
Figure 4.14: Time evolution of axial velocities with actuation for different duty cycles (x = 180 mm, 300 mN/m, 50 Hz) at monitor point 1 72
Figure 4.15: Effect of actuation frequency in pulsed mode at 160 mm, 300 mN/m, 30% duty cycle 73
Figure 4.16: Time-averaged turbulent kinetic energy distribution in the plane of monitor point 1 for different actuation frequencies (x = 160 mm, 300 mN/m, 30% duty cycle) 74
Figure 4.17: Effect of power consumption 75
Figure 4.18: Effect of duty cycle in pulsed mode at 180 mm, 50 Hz 76
Figure 4.19: Time evolution of axial velocities at monitor point 1 with actuation at 180 mm, 50 Hz. 77
Figure 4.20: Boundary layers with and without actuation 80
Figure 4.21: Prediction of term Ⅰa in Equation (4.7) 83
Figure 4.22: Prediction of term Ⅰb in Equation (4.7) 84
Figure 4.23: Prediction of term Ⅲ in Equation (4.7) 84
Figure 4.24: Prediction of term Ⅳ in Equation (4.7) 85
Figure 4.25: Prediction of final equation (left hand side versus right hand side of Equation (4.7)) 86

Figure 4.26: 2-D planar diffuser 87

Figure 4.27: Comparison of pressure distributions in different ways (left- pressure distribution; right- pressure difference between inviscid simulation and 1-D calculation) 87

Figure 5.1: Chosen plasma actuator configuration 92

Figure 5.2: Plasma actuator operated in filamentary mode 93

Figure 5.3: Teflon damage due to arc formation 93

Figure 5.4: Measured thrust versus peak-to-peak voltage for final plasma actuator configuration 95

Figure 5.5: Contour of axial velocity for different modulation frequencies at 52.7 kV_{pp}, 40%: (a) 15.63 Hz, (b) 40 Hz, (c) 100 Hz, (d) 250 Hz 96

Figure 5.6: Contour of axial velocity for different duty cycles at 52.7 kV_{pp}, 40 Hz: (a) 20%, (b) 40%, (c) 60% 97

Figure 5.7: Modulation frequency effect on thrust and power (Teflon plate, 47.2 kV_{pp}, 2 kHz, duty cycle 50%) 98

Figure 5.8: Duty cycle effect on thrust and power (Teflon plate, 47.2 kV_{pp}, 100 Hz/2 kHz) 99

Figure 5.9: Flow effect on power consumption (Plexiglas plate, HV covered connection, 2.5 kHz, 100%) 100

Figure 5.10: An illustration of windows for PIV measurement 102

Figure 5.11: Contours of time-averaged axial velocity without actuation (refer to the highlighted window in Figure 5.10) 103

Figure 5.12: Time-averaged static pressure distribution along the flat plate without and with continuous actuation 103

Figure 5.13: Spectral analysis of axial velocities without actuation from hot-wire measurement at three points: (a) shear layer region near separation (point 1), (b) edge of shear layer (point 2), (c) core flow (point 3) 104

Figure 5.14: Pressure recovery with different actuator strengths 106

Figure 5.15: Time-averaged flow field with different actuator strengths: (a) 39.7 kV_{pp}, (b) 47.1

kV_{pp}, (c) 52.7 kV_{pp} 107

Figure 5.16: Time-averaged boundary layer shape factor *H* for the cases with continuous actuation 108

Figure 5.17: Comparison of power consumption for continuous and pulsed actuation 109

Figure 5.18: Time-averaged flow field with Teflon plasma actuator at 68.4 kV_{pp}, 100% 109

Figure 5.19: Pressure recovery with different actuator frequencies at 40% duty cycle.....112

Figure 5.20: Instantaneous flow fields with pulsed actuation at 40 Hz, 47.1 kV_{pp}, 40% 114

Figure 5.21: Instantaneous flow fields with pulsed actuation at 15.63 Hz, 47.1 kV_{pp}, 40% 115

Figure 5.22: Instantaneous flow fields with pulsed actuation at 200 Hz, 47.1 kV_{pp}, 40% 116

Figure 5.23: *x*-*t* diagram of phase-locked unsteady boundary layer shape factor *H* for the case with actuation at 40 Hz, 40% 117

Figure 5.24: *x*-*t* diagram of phase-locked unsteady boundary layer shape factor *H* for the case with actuation at 15 Hz, 40% 117

Figure 5.25: *x*-*t* diagram of phase-locked unsteady boundary layer shape factor *H* for the case with actuation at 200 Hz, 40% 118

Figure 5.26: Pressure recovery versus different duty cycles for pulsed actuation at 40 Hz 119

Figure 5.27: *x*-*t* diagram of phase-locked unsteady boundary layer shape factor *H* for the case with actuation at 20%, 52.7 kV_{pp} 120

Figure 5.28: *x*-*t* diagram of phase-locked unsteady boundary layer shape factor *H* for the case with actuation at 60%, 52.7 kV_{pp} 120

Figure 5.29: Topos of velocity for the case without actuation (contours of axial velocity and streamlines) 123

Figure 5.30: Chronos of velocity for the case without actuation 124

Figure 5.31: Topos of velocity for cases with continuous actuation at 47.1 kV_{pp} 125

Figure 5.32: Topos of velocity for cases with pulsed actuation at 47.1 kV_{pp}, 40%, 40 Hz 126

Figure 5.33: Energy distribution for different cases 127

Figure 6.1: Pitchwise mass-averaged static pressure coefficients without actuation 131

Figure 6.2: Flow visualization and simulated wall shear stress on ITD casing without actuation 132
Figure 6.3: Development of measured total pressure coefficients along the duct without actuation 133
Figure 6.4: Development of simulated total pressure coefficients along the duct without actuation 134
Figure 6.5: Flow visualization and simulated wall shear stress on ITD casing with actuation .. 138
Figure 6.6: Effect of plasma actuator location (as normalized axial location) on ITD total pressure loss 139
Figure 6.7: Effect of actuator strength on ITD total pressure loss for plasma actuator at optimal location in Figure 6.6 139
Figure 6.8: Contour of simulated wall shear stress on ITD casing with actuation 140
Figure 6.9: Simulated total pressure coefficients at ITD outlet with actuation 141
Figure A.1: Contour of TKE for laminar separation case without actuation 154
Figure A.2: Contours of time-averaged TKE for different cases in laminar separation control (vertical extent expanded by a factor of two) 155
Figure A.3: Time-averaged axial wall shear for different cases in laminar separation control .. 156
Figure A.4: Contour of time-averaged axial velocity without actuation with indicated monitor points 158
Figure A.5: Time-averaged axial wall shear stress along the plate in Figure A.4 without actuation 159
Figure A.6: Time evolution of normal velocities at monitor points: (a) point 1 (separated shear layer region), (b) point 3 (turbulent separation region) 159
Figure A.7: Spectral analysis of normal velocities without actuation at two monitor points: (a) separated shear layer region (point 1), (b) turbulent separation region (point 3) 161
Figure A.8: Contours of time-averaged axial velocity with actuation: (a) LSP, co-flow, continuous (case L1), (b) LSP, co-flow, 100 Hz (case L2), (c) LSP, co-flow, 400 Hz (case L4), (d) TRP,

co-flow, continuous (case T1) 162
Figure A.9: Contours of instantaneous axial velocity with actuation: (a) LSP, co-flow, 100 Hz (case L2), (b) LSP, co-flow, 400 Hz (case L4), (c) TRP, co-flow, 100 Hz (case T3), (d) LSP, counter-flow, 100 Hz (case L6) 163
Figure A.10: Time-averaged axial wall shear stress for cases with actuation: (a) at the LSP, (b) at the TRP 165
Figure A.11: Time evolution of axial velocities with actuation at two monitor points: (a) separated shear layer region (point 1), (b) turbulent separation region (point 3) 167
Figure A.12: Spectral analysis of axial velocities with actuation: (a) LSP, co-flow, 100 Hz, (case L2), (b) LSP, co-flow, 400 Hz (case L4), (c) TRP, co-flow, 100 Hz (case T3), (d) TRP, co-flow, 400 Hz (case T5) 168
Figure C.1: A schematic representation of plasma generation system 183
Figure C.2: Plasma generation system 184
Figure C.3: LabView interface for signal generation 184
Figure C.4: Power amplifier connection 185
Figure C.5: Resistor module 186
Figure C.6: Transformers 187
Figure C.7: Main components of plasma generation system 188
Figure C.8: LabView interface for data acquisition 190
Figure C.9: Force/thrust measurement 190
Figure D.1: Different waveform shapes 193
Figure D.2: Exposed electrodes with different shapes 193
Figure D.3: Foil-type exposed electrode with different insulation 194
Figure D.4: Bi-electrode versus tri-electrode configurations 194
Figure D.5: Effect of dielectric material 195
Figure D.6: Contour of axial velocity with Teflon sheet and HV exposed electrode for different voltages 197

Figure D.7: Profile of axial velocity with Teflon sheet and HV exposed electrode for different location 198
Figure D.8: Maximum induced axial velocity with Teflon sheet and HV exposed electrode for different voltages (x = 15 mm, y = 1 mm) 199
Figure D.9: Thrust versus power for various waveforms 200
Figure D.10: Electrical measurement for various waveforms at 2.5 kHz 201
Figure D.11: Thrust versus power for various AC frequencies 203
Figure D.12: Thrust versus peak-to-peak voltage for various AC frequencies 203
Figure D.13: Voltage measurement for various frequencies with square waveform 204
Figure D.14: Thrust versus RMS voltage for the effect of insulated exposed electrode 205
Figure D.15: Thrust versus power for the effect of insulated exposed electrode 205
Figure D.16: Plasma for the serrated and straight exposed electrodes (negative sawtooth) 208
Figure D.17: Thrust versus power for the effect of exposed electrode shape 209
Figure D.18: Thrust versus RMS voltage for the effect of exposed electrode shape 209
Figure D.19: Thrust versus RMS voltage for wire-type exposed electrode 211
Figure D.20: Thrust versus power for wire-type exposed electrode 211
Figure D.21: Electrical measurement for the actuators with wire-type electrode at 2 kHz 212
Figure D.22: Plasma for wire-type exposed electrode with a diameter of 0.025 mm 213
Figure D.23: Thrust versus RMS voltage (negative sawtooth) for tri-electrode configuration 215
Figure D.24: Thrust versus RMS voltage for tri-electrode configuration 216
Figure D.25: Thrust versus power for tri-electrode configuration 216
Figure D.26: AC power versus RMS voltage for tri-electrode configuration 217
Figure D.27: DC power versus RMS voltage for tri-electrode configuration 217

List of Tables

Table 1: Comparison of transition location 60

Table 2: Characteristics of various dielectric materials 90

Table 3: Simulation cases for laminar separation control 153

Table 4: Pressure recovery for different cases with laminar/turbulent separation 160

Table 5: Cables and Connectors 191

Table 6: Transformer Leads 191

Table 7: Parametric study test matrix 192

List of Appendices

Appendix A: Preliminary Numerical Results 153

Appendix B: Preliminary Experiment Tests and Results 170

Appendix C: Plasma Generation System 183

Appendix D: Parametric Study on DBD Plasma Actuators 192

Appendix E: Proper Orthogonal Decomposition (POD) 218

Chapter 1

Introduction

An air intake (engine inlet) on an aircraft is a passage or duct for the ambient air entering the aircraft engine. For an ideal intake, the flow properties, *e.g.*, total pressure, should be uniformly distributed at the engine entrance face, or aerodynamic interface plane (AIP). However, this situation never happens in a real engine intake. The variation of total pressure across the engine face is named total pressure distortion. This is the most significant among inlet distortions (engine face flow distortions). The reduced velocity in the distorted region of the engine face is detrimental to engine performance and causes undesirable fluctuating forces on the turbomachinery blades as they pass in and out of this region, which may lead to fatigue and shortened engine component life. Moreover, the inlet distortion reduces the stall margin of the fan and compressor and can result in engine surge, a flow instability characterized by flow oscillation across the engine. This results in thrust drop and may cause damage to the engine. There are numerous sources of inlet distortion, among which are (Seddon and Goldsmith, 1999; Anderson *et al.*, 1994): 1) flow separation at the cowl lip at high flow ratio (ratio of velocity at lip plane to freestream velocity $V_l / V_\infty > 1$), 2) shock-induced boundary layer separation on the compression surfaces, 3) ingestion of vortices either from upstream disturbances or due to cross-wind flow separation from intake side-plates, 4) secondary flow and possibly flow separation within the inlet duct itself, either from the curvature of inside wall bends or from high diffusion rates.

Aircraft design considerations, such as in the case of turboprops and helicopters, can force the use of non-axial S-shaped engine inlets. The benefits of S-shaped inlets include: 1) conveying the air to engine buried in the fuselage, where axial air suction is not feasible, 2) reducing the overall engine length, thus the weight of engine and aircraft, as a result of ultra-compact, highly offset duct, with a specific area ratio D_2/D_1 (in Figure 1.2), 3) concealing the compressor face

and providing a multiple bounce cavity for reducing radar signature (Wellborn *et al.*, 1994).

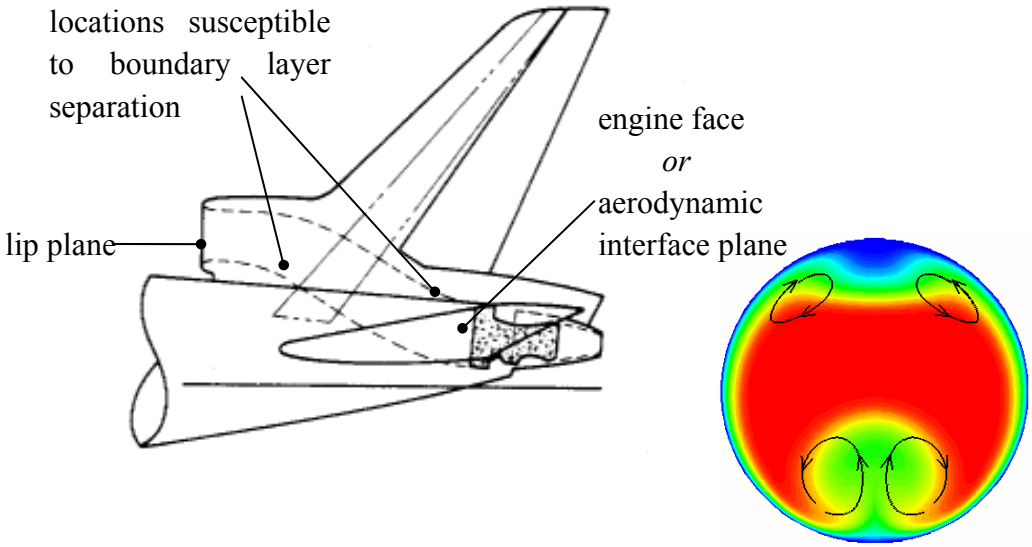

Figure 1.1: S-shaped intake and the total-pressure distortion at the engine face

A typical diffusing serpentine duct, as shown in Figure 1.2, has a curved centerline, two bends and a cross-sectional area increase ($D_2>D_1$). The curvature of the bends and the cross-sectional area change lead to streamline curvature. The cross-stream pressure gradient, resulting from the streamline curvature, leads to cross-stream flow. The cross-stream flow develops along the duct, and eventually a pair of counter-rotating vortices arises, as shown in Figure 1.3. A similar situation happens for the second bend, with a smaller counter-rotating vortex pair. These two sets of counter-rotating vortex pairs at the engine face, originating, respectively, near the insides of the two bends, are shown in Figure 1.1. In addition, adverse streamwise pressure gradient, as a result of the increased cross-sectional area (diffusing duct), can induce flow separation. This can accelerate the formation of vortex pairs, because the secondary flow is relatively stronger in the separation region. The formation of counter-rotating vortex pairs with streamwise flow separation in a diffusing S-duct was demonstrated in the experiment of Wellborn *et al.* (1994). The secondary flow and possibly flow separation within the diffusing S-shaped inlet duct, is the primary source of flow distortion.

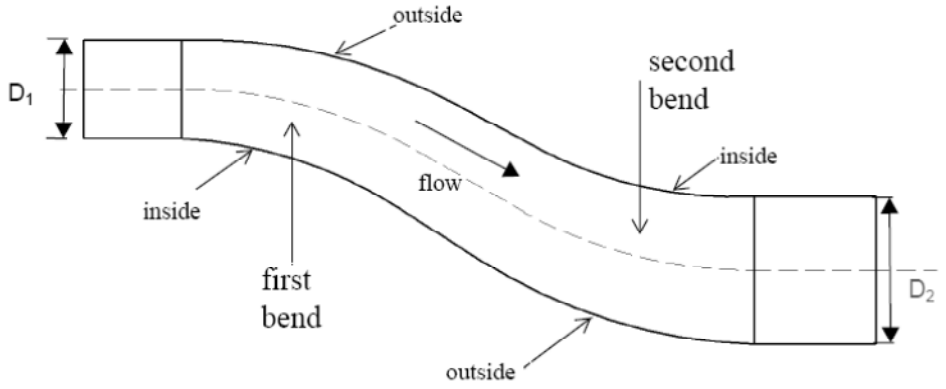

Figure 1.2: A schematic of diffusing serpentine duct

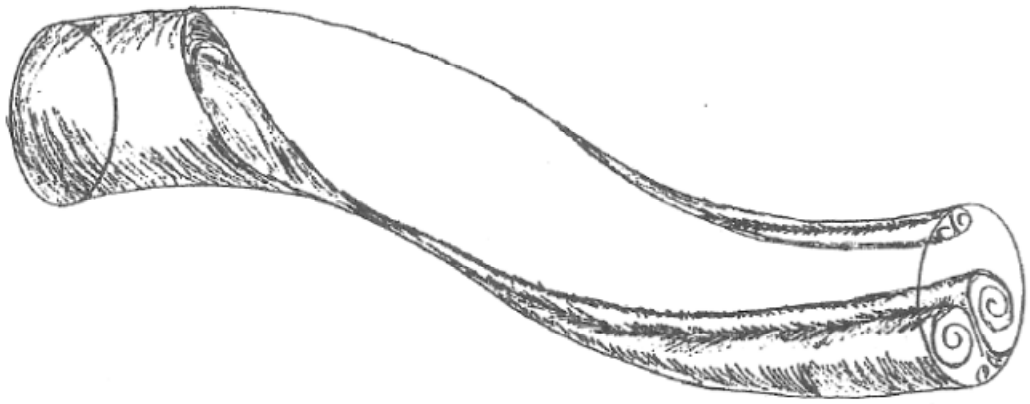

Figure 1.3: Vortex development in a serpentine duct (Sullivan *et al.*, 1982)

Another S-shaped duct generally used in aircraft engines is the inter-turbine duct (ITD), which is located between the high-pressure turbine (HPT) and low-pressure turbine (LPT), as shown in Figure 1.4. The ITD is a key gas turbine component for keeping the overall engine weight and fuel consumption low. The design of ITDs is likely to become more aggressive with the demands for lighter, more efficient and environment-friendly aircraft engines. Such aggressive inter-turbine ducts (AITD) could have shorter axial length and/or larger HP-to-LP radial offset, which will reduce the hot-end cost, size and weight. Compared to S-shaped intake

ducts, the ITDs are annular diffusers. These aggressive ITDs may suffer large pressure losses due to turbulent boundary layer separation leading to reduced engine performance, and therefore require the application of flow control techniques.

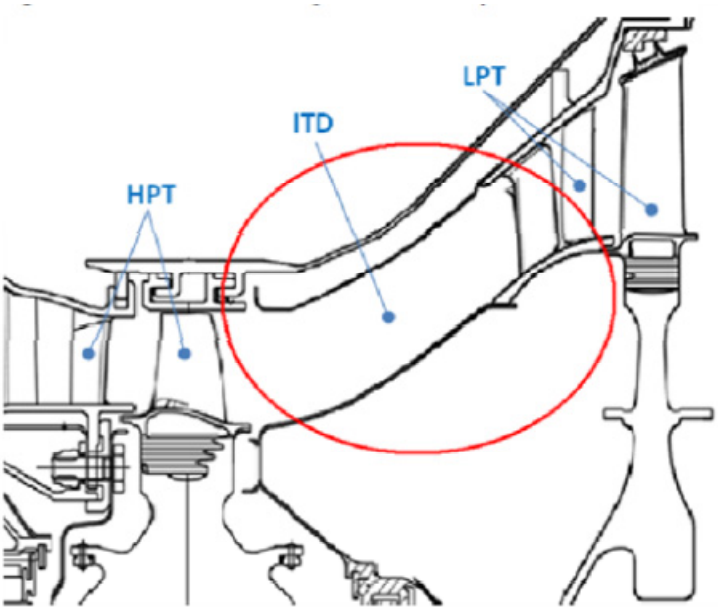

Figure 1.4: Typical ITD region in a turbofan engine (Hu *et al.*, 2011)

Various flow control techniques have been applied on the S-shaped ducts for performance improvement, such as vortex generator jets (VGJs) and zero-net-mass-flow (ZNMF) jets. VGJs require an air supply system, likely taken from engine bleed, and associated pipes and valves, which imply penalty in engine performance and in weight. ZNMF jets require a system with oscillating mechanical parts that may limit the robustness of the actuator under operational conditions. Moreover, there is a risk of clogging of the orifices, especially if small actuators are used to minimize actuation power and response time.

Compared to these relatively complex actuators, the recent advent of dielectric barrier discharge (DBD) plasma actuators can potentially provide a non-intrusive and robust method for suppressing inlet distortion in engine intakes and flow separation in ITDs. A plasma actuator consists of two electrodes, as shown in Figure 1.5, one exposed to the air and the other hidden

beneath a layer of dielectric material. When the electrodes are subjected to a sufficiently high amplitude AC voltage, the air above the hidden electrode partially ionizes. In the presence of the electric field, this results in a flow acceleration (momentum addition to the flow) near the surface. More information on plasma actuators can be found in Enloe *et al.* (2004), Forte *et al.* (2007) and Roth *et al.* (2006).

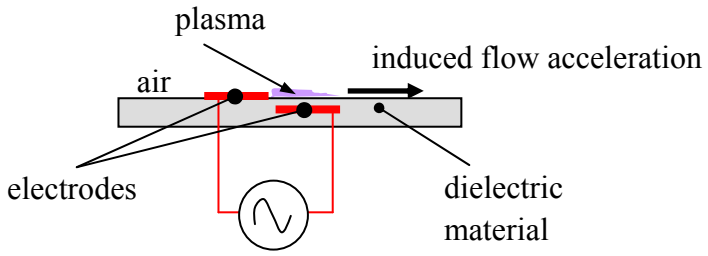

Figure 1.5: A schematic representation of plasma actuator

The relative low-power consumption, simplicity, non-intrusion and potential robustness of these new actuators make them ideal for aerodynamics applications. Several applications have been proposed in recent years in external flow, such as increasing lift on airfoils (Orlov *et al.*, 2007; Patel *et al.*, 2008) and vortex control on delta wings (Visbal and Gaitonde, 2006). However, applications of plasma actuation in more challenging internal aerodynamics are just beginning. The new concept proposed in this project is among the first such application and consists of using plasma actuators to increase flow momentum at strategic locations to suppress boundary layer separation in engine ducts. The actuator can be used in continuous or pulsed mode. In the latter mode, the pulsing frequency can be chosen to amplify turbulent flow structures in the boundary layer to improve momentum transfer from the outer high-velocity fluid and thus suppress separation with minimal power input. This project is done in collaboration with the National Research Council Gas Turbine Laboratory (NRC GTL) in Ottawa.

Research Question

How can one achieve optimal suppression of separation in engine ducts by the use of plasma actuation? In other words, how to choose actuator parameters, *e.g.*, actuator position, strength and mode (continuous or pulsed), such that the separation in a given engine duct can be suppressed by plasma actuators with minimal power input?

Objectives

1) Assess and demonstrate boundary layer control technology using plasma actuators to significantly reduce flow distortion from turbulent boundary layer separation in engine ducts

2) Develop and validate design rules for implementing plasma actuators in engine ducts

Chapter 2 presents a review of the previous literature, which focuses on three topics. The first is the flow distortion within S-shaped engine ducts. The second discusses various flow control techniques and associated examples for boundary layer separation suppression and flow control in S-shaped ducts. The last section deals with the mechanism and the application of plasma actuation.

Chapter 3 presents the chosen methodology which consists of three phases: 1) conceptual study on separation control in 2-D generic diffusers by numerical simulations, 2) experimental study on separation control in 2-D generic diffusers, and 3) the application of plasma actuators in a 3-D S-shaped duct. The detailed research procedures are also included.

Numerical study on separation control in 2-D diffusers is presented in Chapter 4. First, a computational tool with integration of a plasma actuator model is validated. Second, the effects of plasma actuation, in different modes, on the control of boundary layer separations in 2-D diffusers are demonstrated. Third, a preliminary design rule for the continuous plasma actuation

on turbulent boundary layer separation control is developed and discussed.

Following the numerical study, the corresponding experimental study on the boundary layer separation control in 2-D diffusers is carried out and the results are presented in Chapter 5. Prior to this, a parametric study on DBD plasma actuators is conducted in order to optimize them for flow control.

In Chapter 6, plasma actuators are applied to a realistic S-shaped ITD duct in order to suppress the boundary layer separation within it and thus improve duct performance.

Finally, the conclusions of the current study and suggestions for the future work are presented in Chapter 7.

Chapter 2

Literature Review

2.1 Flow Distortion in Serpentine Ducts

Inlet distortion (*e.g.*, total pressure distortion) always happens in a realistic engine intake as introduced in Chapter 1. The main cause of inlet distortion in a serpentine (S-shaped) duct, a commonly used intake geometry, is the secondary flow and possibly flow separation within the inlet duct itself, either from the curvature of inside wall bends or from high diffusion rates.

Singh *et al.* (2008) investigated numerically the influence of the entry shape on the performance of diffusing S-ducts. With the same circular S-duct exit, various entry shapes, including square, rectangle, oval, ellipse and semi-circle, were investigated. The entry area for different shapes was the same, and an area ratio of exit area to entry area was always AR = 2. The chosen turbulence model was the RNG $k-\varepsilon$, which had been validated by experiments. Cross-flow distribution at the duct exit showed the presence of two pairs of counter-rotating vortices, one being smaller. As for the shape effect, oval and elliptical entry section gave better performance whereas square entry section had relatively worse performance, based on the comparison of distortion coefficient and swirl coefficient.

Berrier and Allan (2004) conducted experimental and computational evaluations of flush-mounted, boundary layer ingesting (BLI) S-duct inlets. In this evaluation, a large range of Mach numbers (0.25-0.83) and Reynolds numbers (up to realistic operating conditions) were considered. Increased free-stream Mach number was generally detrimental to BLI S-duct inlet performance (pressure recovery and inlet distortion), with the losses at high subsonic speeds dominated by duct curvature. However, increased Reynolds number had a negligible effect on inlet distortion but increased inlet pressure recovery. As for the numerical prediction, CFD, with $k-\omega$ shear stress transport (SST) turbulence model, was able to capture the pressure recovery

and distortion trends with increasing Mach number and inlet mass flow, while the CFD results generally predicted larger losses than experimental measurements.

Brear *et al.* (2004) examined the flow separation effect within the engine inlet of an UCAV (Unmanned Combat Air Vehicle). The performance of the inlet strongly depended on the flow separation within the inlet, as shown in Figure 2.1. The time-averaged structure and unsteadiness of this separation were also studied. The separation accompanied by unsteady structures, caused both a reduction in inlet pressure recovery and an increase in inlet unsteadiness (*e.g.*, total pressure fluctuation). Finally, separation flow control should be applied in S-shaped ducts, because inlet size reduction and Mach number increase led to stronger adverse pressure gradient and thus stronger separation, which eventually led to poorer inlet performance.

The above review is on flow development in S-shaped engine intake ducts. Flow development in annular ITDs is discussed next. Compared to intake ducts, the flow in ITDs on normal operation has rotational-periodic structures and influence from complex upstream flow conditions such as blade wakes and swirl. Some fundamental work has been conducted to investigate the influence of non-rotating wakes (Dominy and Kirkham, 1996) and swirl (Dominy and Kirkham, 1995) on the performance of inter-turbine diffusers through flow measurements within an annular cascade test rig. Dominy *et al.* (1998) discussed data from experiments with and without upstream swirl vanes and compared them with computational results. Although the blade wakes and swirl did not result in large changes in overall loss, the experimental data showed that the secondary flow structures and the distribution of losses within the duct were significantly modified by the wakes and swirl. Subsequently, Norris and Dominy (1997) experimentally and numerically compared the diffusion of two ITD geometries with the same exit-to-entry area ratio of 1.5 but different lengths. The wake intensity was found to have little effect on the freestream flow. However, for the 30% shorter duct, both numerical and experimental results showed a 10% decrease in static pressure recovery.

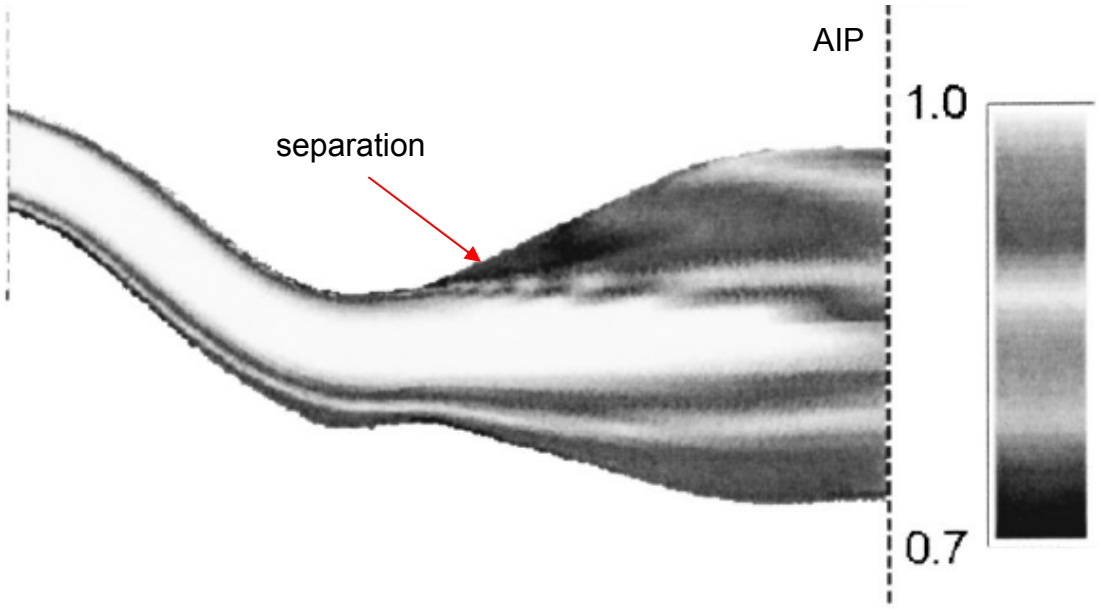

Figure 2.1: Total-pressure contours along the center-plane of an inlet (Brear *et al*., 2004)

To generate more realistic turbine inlet conditions, a large scale low-speed facility with an HPT stage upstream of the ITD was examined by Arroyo *et al*. (2006). Using this facility, Axelsson *et al*. (2007) and Axelsson and Johansson (2008) experimentally investigated the flow features in the ITD, with the installation of an LPT vane downstream of the ITD to simulate real exit boundary conditions. The time-averaged results demonstrated the development of vortex structures along the ITD. Two co-rotating vortices were formed near the casing and started to pair together upon reaching the LPT vanes.

Marn *et al.* (2007) and Göttlich *et al.* (2007) experimentally investigated the influence of the upstream rotor tip gap size on the performance of an aggressive ITD in a transonic turbine test facility. An unsteady numerical investigation of the above AITD was then performed by Sanz *et al.* (2009). It was observed that CFD simulations could capture the influence of changes in tip clearance on flow field behavior. From both experimental and numerical investigations, no separation was detected in this duct. The results also showed that the tip leakage flow had a significant beneficial effect on the static pressure recovery. Although the tip leakage flow only

affected the outer 20% of the duct span, it brought a very different flow field to the downstream section of the duct. Marn *et al*. (2009) later experimentally and numerically investigated the effect of tip clearance size on the flow development in a highly-aggressive ITD, which was 20% shorter than the one presented in Marn *et al.* (2007). Oil flow visualizations showed massive separation along the casing.

Shorter, more compact, more offset S-shaped inlets and ITDs result in larger flow separation, higher flow unsteadiness, and thus decreased duct pressure recovery and higher flow distortion, which cause a deterioration in the performance of the propulsion system. Therefore, to utilize the aggressive geometry of S-shaped engine ducts with an acceptable performance, flow control techniques are needed. Flow control is discussed in the next section.

2.2 Flow Control

Flow control involves employing passive or active devices to change the characteristics of a naturally developed flow field, *e.g.*, wall-bounded and free-shear flows, to a new desired state (Gad-el-Hak, 2000). The goals of flow control include laminar-turbulent transition delay or advancement, suppression of boundary layer separation, lift increase, drag reduction, noise reduction, flow-induced vibration damping, *etc*.

The classifications based on different criteria are many. Two obvious categories are passive and active flow controls as shown in Figure 2.2. Passive flow control involves a fixed modification to the flow field, requiring no auxiliary power, such as the shaping of the bodies, addition of riblets and vortex generators. In contrast, active flow control requires energy input to modify the flow, such as blowing, suction, acoustic actuation, magneto-hydrodynamic and electro-hydrodynamic actuations. Active flow control can further be divided into predetermined and reactive flow controls. Predetermined flow control is the application of control devices regardless of the specific flow state, while reactive control, *i.e.*, feedforward or feedback looped, strongly depends on the current flow field information, obtained by various sensors.

Predetermined active flow control can be divided into steady and unsteady regimes. In the steady regime, energy is added to the flowfield to obtain a beneficial result, such as separation suppression and laminar-turbulent transition advancement. The amount of energy input is strongly dependent on the energy or momentum deficit in the flow. For example, the suppression of larger and stronger turbulent boundary layer separation would require higher external energy input.

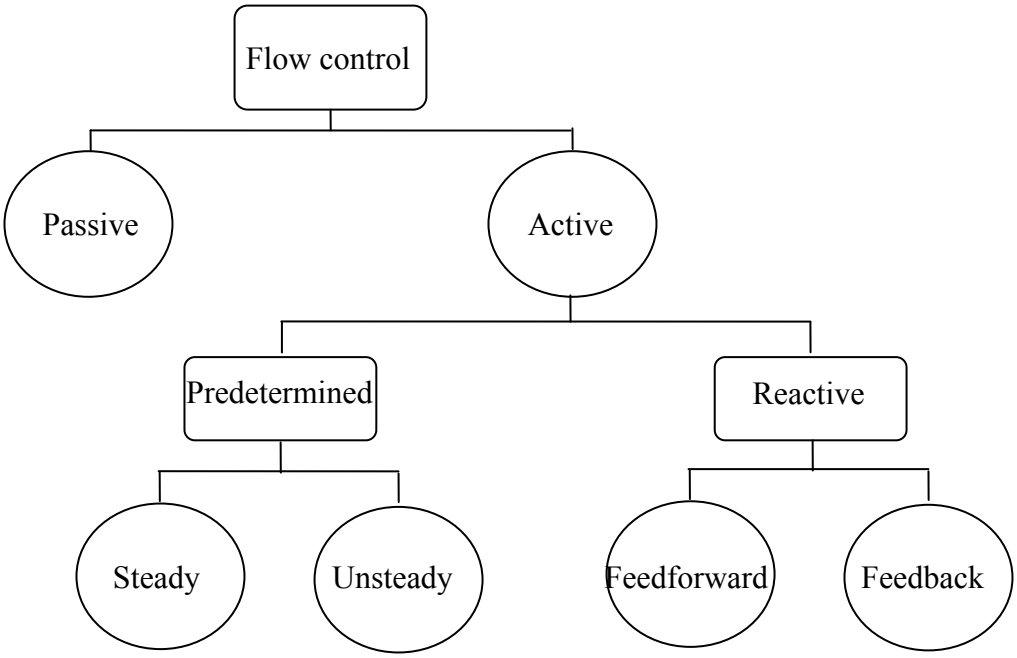

Figure 2.2: Classifications of different flow control strategies

In contrast, unsteady flow control, widely researched since the 1990s, is primarily based on suppressing or amplifying the instabilities present in the flow, such as Tollmien-Schlichting waves in laminar-turbulent transition and instabilities in mixing layers. As for the suppression of turbulent boundary layer separation, unsteady control mode with an actuation frequency related to a natural frequency in the flow can be used to enhance mixing between the higher momentum fluid in the outer region and the lower momentum fluid near the wall. The energy consumption for unsteady flow control is relatively small compared to that for steady flow control. Efficient unsteady flow control relies on the identification and understanding of the instabilities in the flow. These instabilities can be classified as convective or absolute based on the linear response of the system to an initial localized impulse (Huerre and Monkewitz, 1990). A flow is convectively unstable, if its response to an initial impulse at any fixed location decays in time, or if all growing disturbances convect downstream from their source. Suppression of convective instabilities is especially effective when applied near the source point. On the other hand, the flow is absolutely unstable, if the local response to an initial impulse grows in time. Absolute

instabilities are generally more dangerous and more difficult to control. However, absolute instabilities are more easily amplified as needed in some flow control cases.

In the control of turbulent flow, such as wall-bounded or free-shear layers, coherent structures naturally present in this flow should be understood and utilized. However, there are no universal coherent structures. For example, organized motions in wakes are different from those in boundary layers (Gad-el-Hak, 2000). The coherent structures in free-shear flows are generally easier to detect and identify than those in the wall-bounded flow. This difference can also be shown by the characteristic length scales in these flows: one in the free-shear flow versus at least two (*e.g.*, in outer and inner layers) in the wall-bounded flow. Issues about the origin of the different structures in the shear layer, the inner-outer layer interaction, regeneration mechanism and Reynolds number effects remain unresolved to date.

While a large amount of literature exists on flow control techniques and applications, only a few will be discussed, mainly pertaining to boundary layer separation control and flow control in the S-shaped ducts.

Sullerey *et al.* (2002) studied the effect of various fences and vortex generator configurations (Figure 2.3) in reducing distortion and improving total pressure recovery in 2D diffusing S-ducts. To obtain the best performance, the fence height was chosen as 120 percent of the boundary layer thickness without flow control, while the height of vortex generator was 50 percent. The vortex generators were fixed in such a way that the vortices shed by the vortex generators opposed the naturally occurring secondary flows and thus aiding in control of secondary flow losses. It was observed that the performance of these two techniques depended on the centerline curvature or radius ratio (ratio of centerline radius of curvature to half duct height). The fences performed better when used in diffusing ducts of greater radius ratio while tapered-fin vortex generators performed better in diffusing ducts of smaller radius ratio.

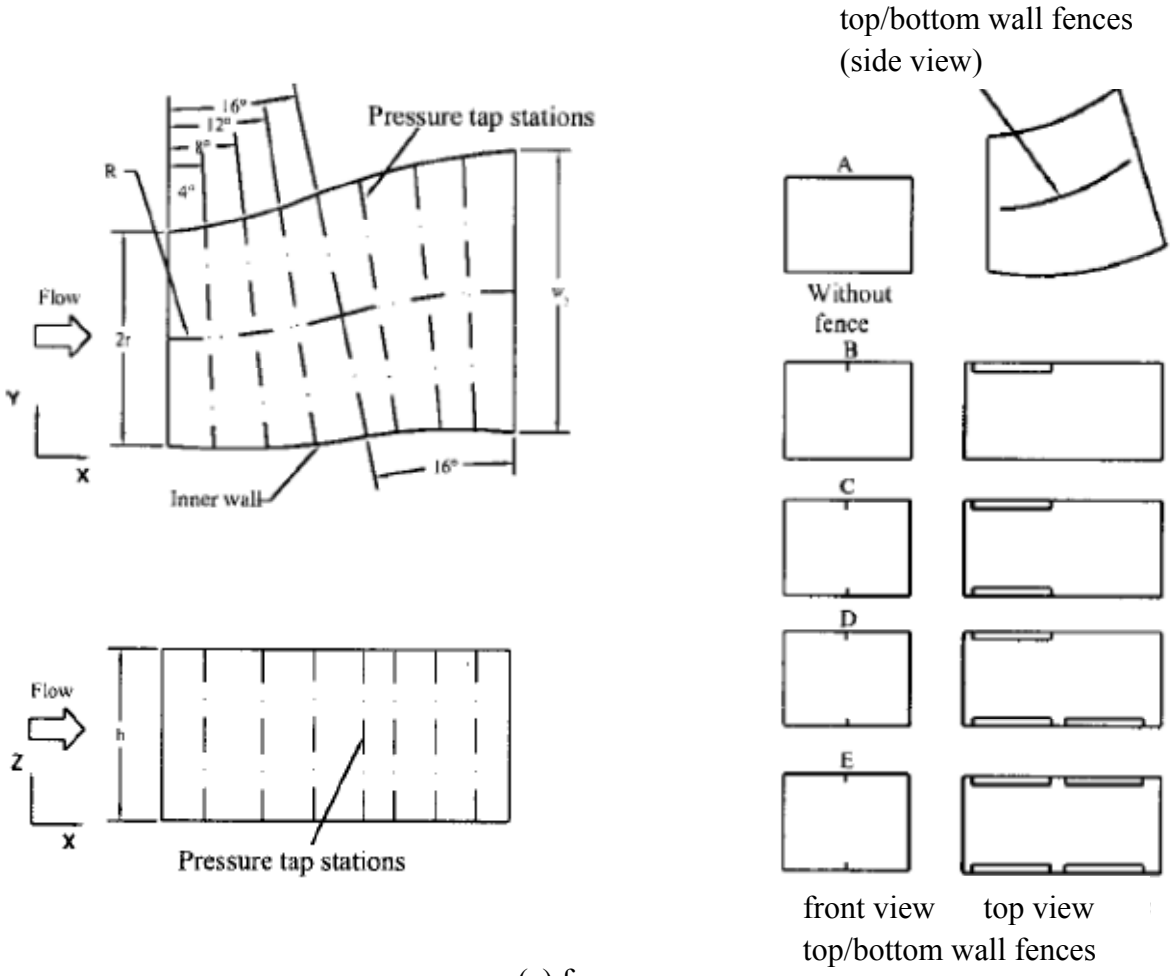

(a) fences

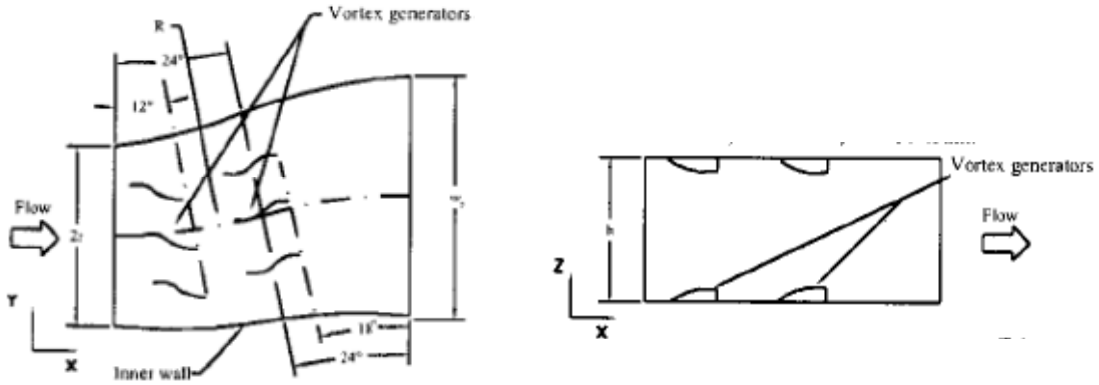

(b) vortex generator

Figure 2.3: Configurations of fences and vortex generators (Sullerey *et al.*, 2002)

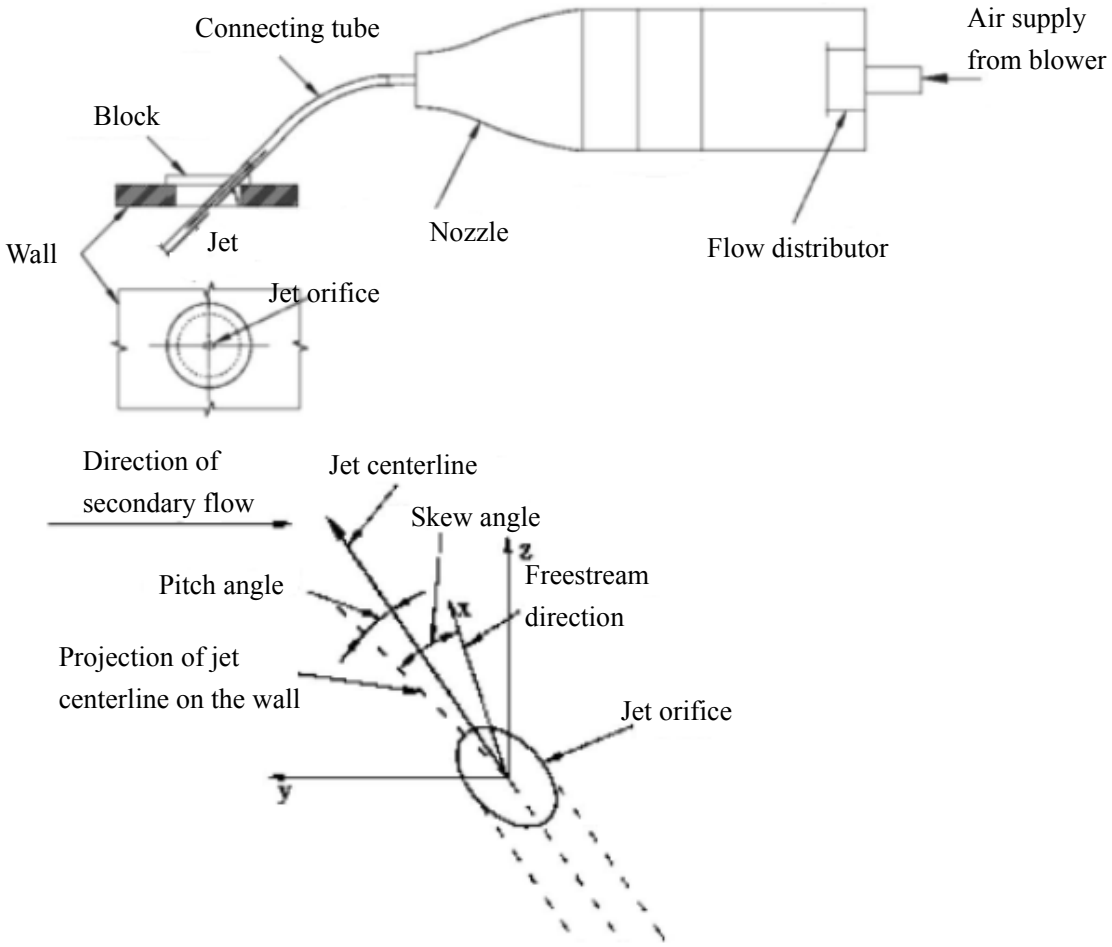

Figure 2.4: An illustration of vortex generator jet (VGJ) and definition of VGJ angles (Pradeep and Sullerey, 2006)

Pradeep and Sullerey (2006) later investigated the performance enhancement of 3D diffusing S-ducts (circular and rectangular-to-circular transitioning) by secondary flow and separation control using vortex generator jets (VGJs), as shown in Figure 2.4. In the active separation control, both steady VGJs and VGJs with feedback control were tried, with feedback control further improving the effectiveness of VGJs. Besides, the active control type was shown to be significantly more effective than tapered fin vortex generators in Figure 2.3(b) (passive flow control). Moreover, an attempt was made to explain the physical mechanism of VGJs in secondary flow and separation control. The larger the size of the vortex, the better would be the

control and thus more mixing of the low momentum boundary layer fluid with the high momentum freestream fluid. It was observed that the vortices generated when the VGJs were oriented at 135 deg skew angle have sizes greater than those at other orientations.

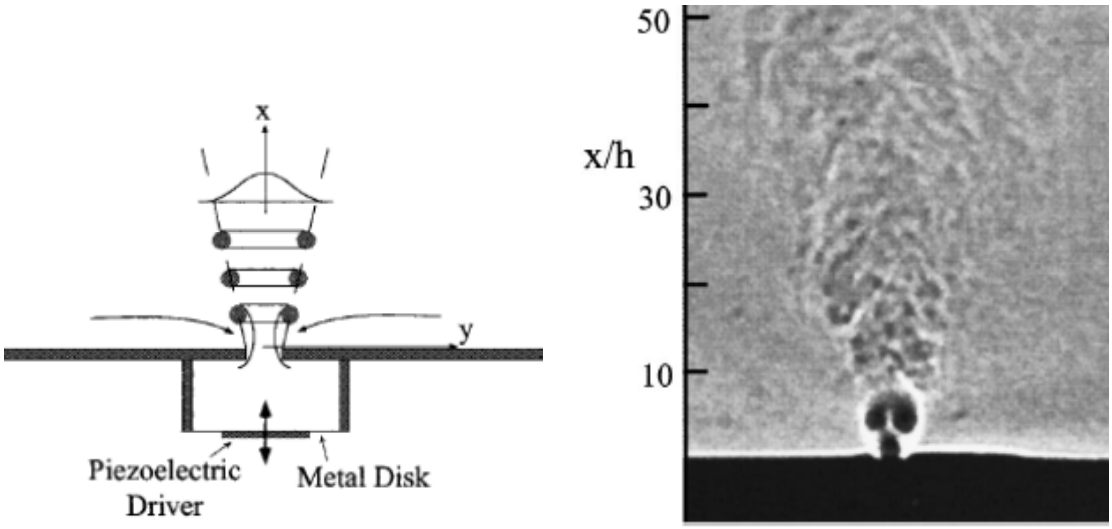

Figure 2.5: Schematic of (a) ZNMF jet actuator and (b) induced flow by ZNMF jets (Smith and Glezer, 1998)

Separation control using zero-net-mass-flow (ZNMF) jets in diffusing S-ducts was studied by Mathis *et al.* (2008). To generate ZNMF jets, the devices should contain three elements: a cavity, a slot and a pressure fluctuation generator, as shown in Figure 2.5(a). The cavity pressure fluctuations are generated by an oscillating piezoelectric element, which is driven by an electric AC signal. Consequently, velocity oscillations and vortices (see Figure 2.5(b)) are formed at the exit slot. With the ZNMF jets, the momentum is transferred from the actuator to the fluid without net mass injection, which is similar to plasma actuator (the main difference is actuation direction, *i.e.*, non-tangential to wall for ZNMF jets versus tangential to wall for plasma actuators). One important parameter is actuation frequency or strouhal number $St = fD/U_{j,rms}$, where $U_{j,rms}$ is the rms velocity and D is the diameter of the ZNMF jet. A stability analysis of the wall normal base flow at the location of the applied control was presented and the most effective actuation frequency was estimated, corresponding to the most spatially unstable mode in the original flow.

With this actuation frequency and the jet located close to the time-averaged separation point, only a very low energy input was necessary to suppress the separation in the duct with high degree of curvature.

Cierpka *et al.* (2007) investigated the electromagnetic control of separated flows above a stalled plate using periodic excitation with different frequencies, amplitudes and wave forms. In the electromagnetic control, the fluid is electrically conducting and the momentum addition can be achieved by electromagnetic (Lorentz) force. The Lorentz force appears as a body force on the flow. This situation is similar to the mechanism of DBD plasma actuators, where the electric force imposes the mass fluxes (no mass injection). The optimal frequency was found to correspond to the dimensionless frequency $F^+ = O(1)$, a widely recognized value for the stalled airfoil control, based on chord length and freestream speed. As for the effect of wave form, the rectangular wave form generated the smallest separation bubble compared to sinusoidal and triangular wave forms.

The influence of periodic excitation on a turbulent separation bubble was studied by Herbst and Henningson (2006), using direct numerical simulations (DNS). The excitation was generated by an oscillating body force perpendicular to the surface, similar to ZNMF jets above. In this work, the influence of forcing position, forcing amplitude and forcing frequency was considered. To effectively control the turbulent separation, the excitation position should be near the separation point, as the critical point, and the dimensionless frequency, based on free-stream velocity and mean reattachment length without forcing, should be $F^+ \approx O(1)$. Relatively high amplitudes (above a threshold) were necessary in order to prevent separation. Figure 2.6 shows the instantaneous streamwise velocity for periodic forcing with optimal parameters. To understand why low frequencies were necessary to eliminate separation by time periodic forcing, a linear stability analysis was performed. From the analysis, only low frequency modes were unstable, corresponding to wavelength of the order of the bubble length, and also indicating a possibility of a global instability of the turbulent separation bubble.

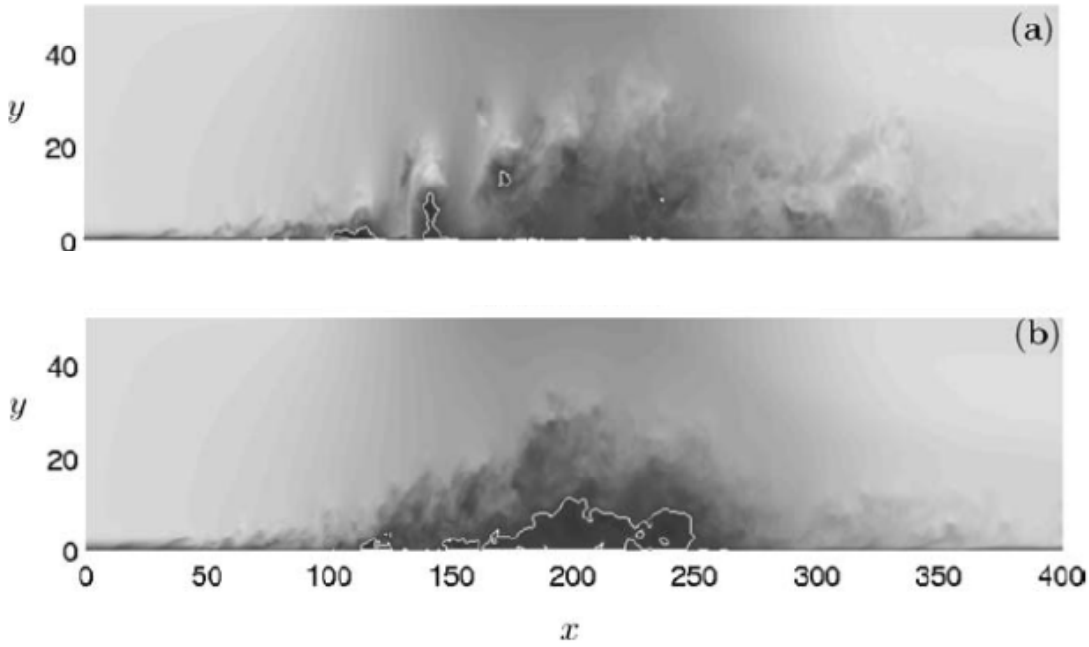

Figure 2.6: Instantaneous streamwise velocity (white line: zero) for periodic forcing (a) and without forcing (b) (Herbst and Henningson, 2006)

Various flow control regimes and techniques have been introduced in the above review. Effective suppression of boundary layer separation by unsteady/pulsed actuation requires that the actuation location be near the separation point and actuation frequency be related to some natural frequency of the uncontrolled flow. To suppress the secondary flow in S-shaped ducts, the vortex generated by actuators should oppose the natural secondary flow.

2.3 Plasma Actuation

Applications of weakly ionized plasmas in propulsion and aerodynamics are a group of emerging technologies. In weakly ionized plasmas, the ionization fraction of gas molecules ranges from 10^{-8} to 10^{-2} (Macheret, 2008). Plasma-based actuation is generally based on the following mechanisms (Shin *et al.*, 2007): 1) thermal effect, which is rapid gas heating resulting from the Joule dissipation, such as through direct-current (DC) filamentary discharges, 2) non-thermal effect, which comes as magneto-hydrodynamic (MHD) or electro-hydrodynamic (EHD) forcing to accelerate or decelerate the gas in the flow, such as through DC glow discharges and single dielectric barrier discharge (DBD), as shown in Figure 2.7.

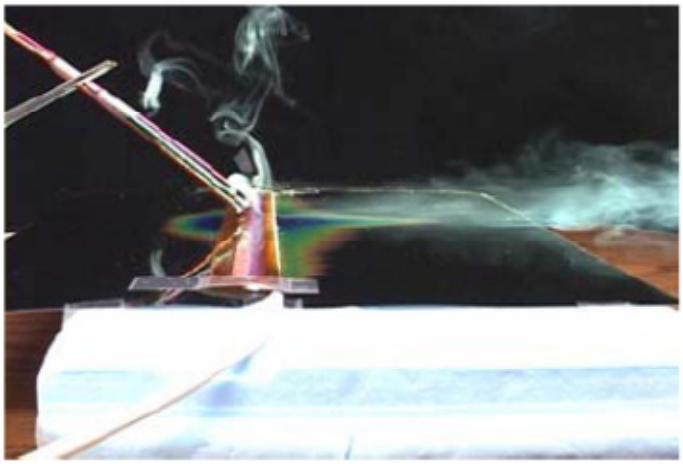

Figure 2.7: Induced flow in quiescent air by DBD (Enloe *et al.*, 2004)

The DBD plasma actuator is a pretty simple and potentially robust device without moving parts that can effectively induce laminar-turbulent transition, suppress and/or delay boundary layer separation. A typical DBD plasma actuator, as illustrated in Figure 1.5, consists of two electrodes arranged asymmetrically, one exposed to the air and the other hidden beneath a layer of dielectric material. When the electrodes are subjected to a sufficiently high amplitude AC voltage (~1-10 kV_{pp}) at high frequency (~1-10 kHz), the air above the hidden electrode partially ionizes. In the presence of the electric field, this results in a flow acceleration (momentum

addition to the flow) near the surface. The time evolution of AC voltage, current, induced axial and normal velocity above the actuator (Forte *et al.*, 2007) is shown in Figure 2.8. One can notice that the discharge does not behave similarly during the positive and negative half-cycles. The negative half-cycle induces more velocity than the positive one. The time-averaged velocity induced by the plasma actuator has positive axial and negative normal components. This effect can be represented by a volumetric force distribution, with the direction from the exposed electrode to the hidden electrode.

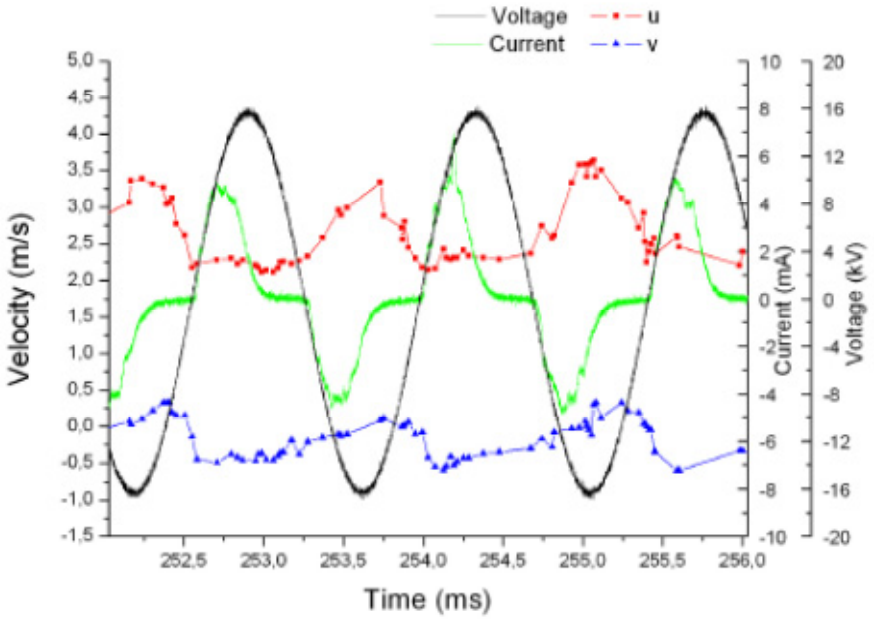

Figure 2.8: Time evolution of voltage, current, induced axial and normal velocity above the actuator (Forte *et al.*, 2007)

Though the generation mechanism of plasma actuator is beyond the scope of the current work, some basic knowledge need be introduced here because it will be used to explain the trends in the parametric study to optimize plasma actuators for experiments. When the applied voltage is positive and increases (positive-going), the plasma is ignited. This is termed the *backward discharge* because the electrons accelerate backward and toward the upstream exposed electrode. When the applied voltage is positive and decreases, the plasma is quenched. When the applied voltage is negative and decreases (negative-going), the plasma is ignited again. This is

termed the *forward discharge* because the electrons accelerate forward and away from the exposed electrode. When the applied voltage is negative and increases, the plasma is quenched.

The forward discharge performs most of the momentum transfer to the neutral fluid (force generation)(Boeuf *et al.*, 2009; Enloe *et al.*, 2008). A few high current pulses (corresponding to streamers) are observed during the backward discharge, while the forward discharge is composed of a much larger number of current pulses of smaller amplitudes. The streamers can perturb the development of the force such that the force is zero during the streamer formation and restarts from zero after each streamer.

Enloe *et al.* (2004) investigated the working mechanism of single DBD by taking optical, electrical, and thrust measurements. The temporal and macro-scale structure of the plasma actuator was revealed. Their work also indicated that an interaction of the plasma with the applied electric field in the discharge was responsible for the momentum transfer to the neutral fluid through plasma-neutral collisions (collisions between drifting ions and neutral particle). Boeuf *et al.* (2005) however focused on the calculation of electro-hydrodynamic force produced by the plasma actuator, based on a 2-D fluid model of the surface discharge. They showed that the nature of the force was same as that of the electric wind in a corona discharge, and the force magnitudes in two cases were also comparable.

The DBD plasma actuator can be used in continuous mode or pulsed mode. For the latter mode, the significant parameters, as shown in Figure 2.9, include actuation/modulation frequency ($1/T_c$), duty cycle and strength. The continuous mode can be regarded as a duty cycle of 100%. In the pulsed mode, the pulsing frequency can be chosen to excite resonant turbulent flow structures in the boundary layer to improve momentum transfer from the outer high-velocity fluid and thus suppress separation with minimal power input.

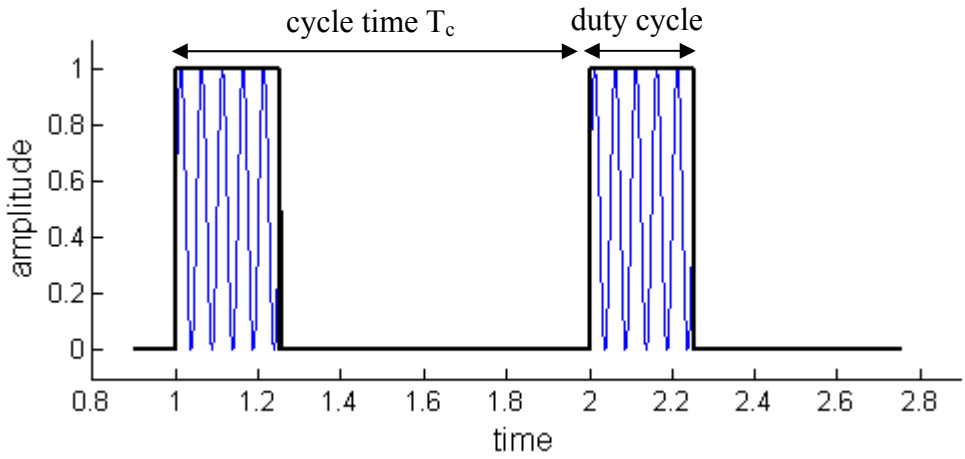

Figure 2.9: An illustration of pulsed actuation

Optimization of the plasma actuator to obtain increased body force and velocity of plasma wind was studied by Forte *et al.* (2007), Roth *et al.* (2006) and Thomas *et al.* (2009). The investigated parameters include dielectric material and thickness, applied voltage amplitude and frequency, voltage waveform, exposed electrode geometry, covered electrode width and multiple actuator arrays (Thomas *et al.*, 2009). From the above parametric study, actuators with thick dielectric material of low dielectric constant produce a body force that is an order of magnitude larger than those with Kapton dielectric material used in many previous plasma flow control studies.

In order to investigate the physics and the flow control applications of DBD plasma actuators, significant effort has been made in modeling the actuator for numerical simulations. Generally, Lemire and Vo (2011) classified these models into two main categories: 1) the sophisticated "scientific" models that aim to simulate the physics and working of plasma actuators on a microscopic scale, and 2) the "engineering" or "phenomenological" models that aim to reproduce the global effects of the actuators on the flow with minimal computational cost.

The "scientific" models include those by Roy and Gaitonde (2006) and Jayaraman *et al.* (2006). These models solve the transport equations of discharge species to obtain the force generated by the actuator. Although these models use only three species (*i.e.*, ions, electrons and

neutrals), they are computationally expensive and their direct implementation into CFD simulations in macroscopic aerodynamic applications is not yet practical.

Among the simplified "engineering" models are those by Shyy *et al.* (2002), Suzen *et al.* (2005) and Orlov *et al.* (2007). The model proposed by Shyy *et al.* (2002) adopted an empirically-guided approach to produce a linear time-averaged (over an AC input cycle) force distribution to study the momentum coupling with the neutral fluid. Suzen *et al.* proposed a more sophisticated model to obtain a more realistic non-linear spatial body force distribution, by solving for the spatial distribution of electric potential and charge density taking into account the actuator geometry and dielectric/air material properties. Orlov *et al.* employed a lumped-element circuit model, which incorporated more of the plasma physics, to solve the spatial and temporal variation of the body force (variation of the electric potential and discharge). Moreover, a "hybrid" model, which combines the features of the models of Suzen *et al.* and Orlov *et al.*, is found to predict a spatial body force distribution that most resembles that obtained with a sophisticated scientific model (Lemire and Vo, 2011).

The hybrid actuator model basically consists of solving two equations, at each time step in the AC input cycle, for the spatial distributions of electric potential (ϕ) and charge density (ρ_c), as given by Suzen *et al.* (2005):

$$\nabla(\varepsilon\nabla\phi) = 0 \tag{2.1}$$

$$\nabla(\varepsilon\nabla\rho_c) = \frac{\rho_c}{\lambda_d^2} \tag{2.2}$$

where ε is the local relative permittivity (compared to air) and λ_d is the Debye length (a plasma characteristic).

Orlov *et al.* (2007) basically divides the domain over the dielectric surface into N volumes (Figure 2.10) to which a network of N parallel electric circuits is associated. The electric potential $V_n(t)$ and the current $I_{pn}(t)$ for each circuit at every time step of the AC period can then

be obtained from the input voltage properties (amplitude, frequency) and from the properties associated to the spatial position of the circuit. The charge density on the dielectric surface over the covered electrode $\rho_{cn}(t)$ is computed as a function of the current through the plasma resistance $I_{pn}(t)$ and the volume associated to the electric circuit (Figure 2.10) as follows:

$$\rho_{cn}(t) = \frac{I_{pn}(t) \cdot \Delta t}{Volume_n} \qquad n = 1, 2, ..., N \tag{2.3}$$

where Δt corresponds to the time step increment used in the computation of $V_n(t)$ and $I_{pn}(t)$ over one AC input period.

Once the spatial distributions of electric potential and charge density in the plasma are solved from Equations (2.1) and (2.2) at each time step, the corresponding body force distribution (per unit actuator length into the paper) can be computed with Equation (2.4):

$$\vec{F} = \rho_c \vec{E} A = \rho_c (-\nabla \phi) A \quad [N/m] \tag{2.4}$$

where A is the area of the mesh.

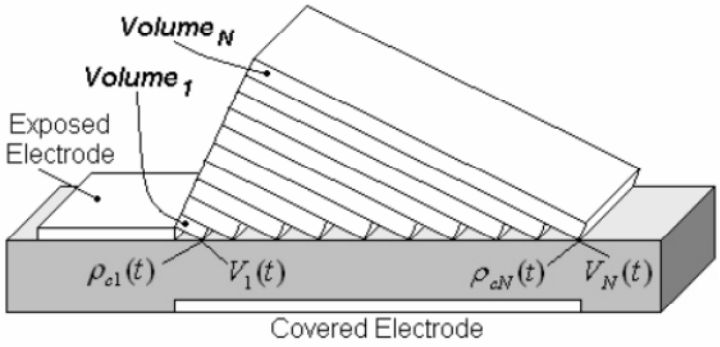

Figure 2.10: Subdivision of the domain over the covered electrode into N volume (Lemire and Vo, 2011)

The effect of a single DBD plasma actuator on flow control, at least for low Mach number/incompressible flow regimes, can be modeled as a time-averaged spatial body force distribution, which is the usual approach taken for simulating flow control concepts with plasma actuators. This is justified by the fact that the time scales associated with the ionization and with

the AC input cycle of the actuator are, respectively, several and at least one order of magnitude faster than the response of the flow (Jayaraman and Shyy, 2008). The plasma formation process is thus quasi-steady from the point of view of the flow. Numerical investigation of DBD plasma actuators in flow control with the integrated engineering plasma actuator model includes laminar separation control on airfoils (Orlov *et al.*, 2007) and on turbine blades (Rizzetta and Visbal, 2008) and turbulent separation control (He *et al.*, 2007). More information on the modeling of DBD plasma actuators can be found in the review by Jayaraman and Shyy (2008).

In the following review, only a few applications of plasma actuators on flow control are discussed, from which some useful ideas for the current work such as related to actuation mode (continuous versus pulsed), actuation frequency and actuation direction can be obtained.

Many researchers have studied the application of plasma actuators on airfoils and gas turbines. Orlov *et al.* (2007) numerically and experimentally studied the effects of DBD actuator to control the leading edge separation and thus increase airfoil lift at different angles of attack. It was found that steady actuation delayed stall by approximately 2 degrees of angle of attack, while unsteady actuation was shown to produce even better results, with the stall angle delayed by 5 degrees.

Due to the limited velocity induced by existing DBD plasma actuators, experimental tests of plasma actuator in real flight conditions are presently impossible. Thus Patel *et al.* (2008) investigated the scaling effects of an aerodynamic plasma actuator for leading edge separation control on airfoils between laboratory and real flight conditions. An optimum pulsed actuation frequency for minimizing the actuator voltage to reattach the flow was $F^+ = fc/U_\infty = O(1)$, where c is the chord length and U_∞ freestream velocity. At this optimum frequency, the required minimum voltage was weakly dependent on chord Reynolds number and strongly dependent on the poststall angle of attack and leading edge radius.

Rizzetta *et al.* (2008) studied plasma-based flow control for transitional highly loaded

low-pressure turbines, for which the separation was effectively controlled by laminar-turbulent transition induced by plasma actuators. In this work, the strategies of plasma-based control included chordwise location of actuation (Figure 2.11(a) versus (b)), spanwise periodic arrays of actuators (Figure 2.11(d) and (e)), multiple actuation in the streamwise direction (Figure 2.11(c)), and spanwise actuation (Figure 2.11(e) and (f)). As for the working modes of DBD plasma actuator, comprehensive tests and comparisons of continuous co-flow, pulsed co-flow and pulsed counter-flow actuation were done by Visbal and Gaitonde (2006). These working modes were used for triggering laminar-turbulent transition to delay stall of an airfoil at high attack angles, and also for changing the vortex breakdown location on the vertical flow above a swept delta wing.

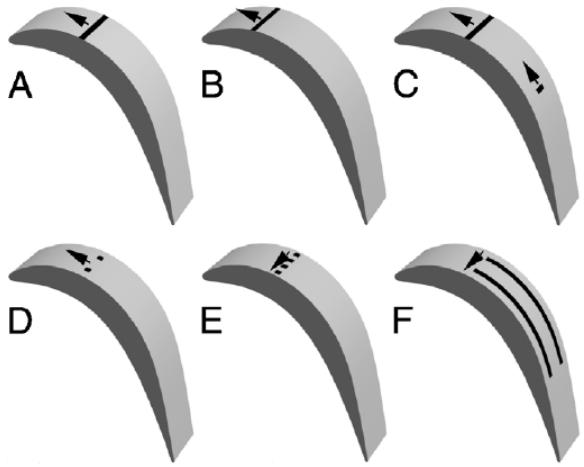

Figure 2.11: Different plasma actuator configurations (Rizzetta *et al.*, 2008)

Hultgren and Ashpis (2003) experimentally studied the effect of plasma actuator on suppression of laminar boundary layer separation. The test section in this work is shown in Figure 2.12, which is similar to our test section in this project (in contrast, the turbulent boundary layer separation control is the main goal in this project). The separation was generated near the test wall by the suction on top wall. The plasma actuator was placed upstream of the separation point, and worked by triggering early laminar-turbulent transition in the shear layer above the

separation bubble thus leading to rapid reattachment. Suppression of laminar boundary layer separation by plasma actuation was also studied by Boxx *et al.* (2006). The test section is similar to that in Figure 2.12.

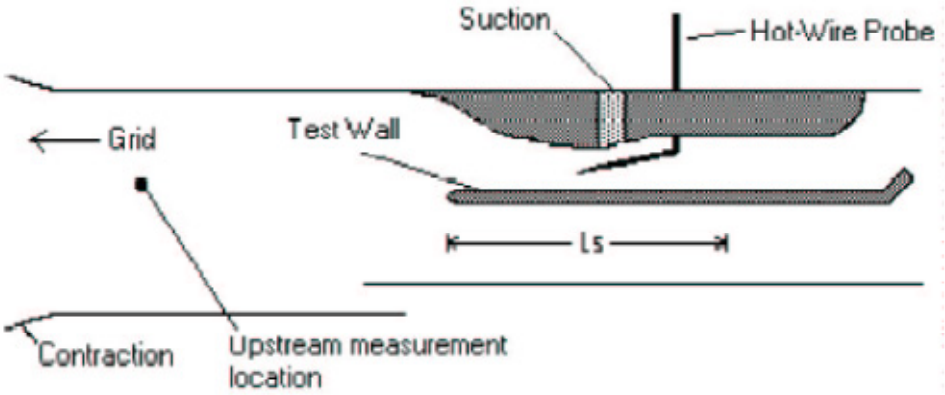

Figure 2.12: Schematic of the test section side view (Hultgren and Ashpis, 2003)

The research and results of plasma actuation, however, mainly focus on the suppression of laminar separation and laminar-turbulent transition, which are very receptive to imposed small-amplitude disturbance (Schlichting, 1979). Research on the more challenging control of turbulent boundary layer separation by plasma actuation is just beginning. In order to achieve sufficient control authority for turbulent boundary layers, the actuator amplitude must be above a certain threshold level (Visbal *et al.*, 2006).

He (2007) investigated numerically and experimentally turbulent flow separation and its control by plasma actuators. The turbulent boundary layer separation was generated over a wall-mounted hump model, as shown in Figure 2.13. Both streamwise and spanwise (refer to Figure 2.11(f)) plasma actuations were used and shown to work well for the turbulent separation control, even though the streamwise plasma actuation was better than spanwise plasma actuation.

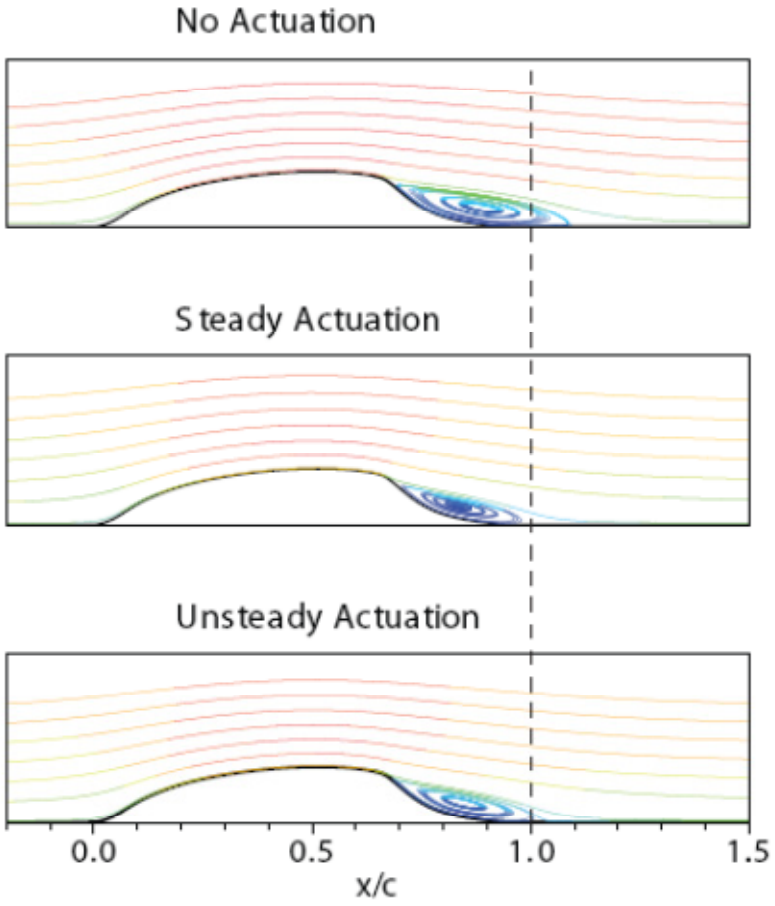

Figure 2.13: Streamlines above a hump model, showing effects of plasma actuator on suppressing turbulent separation (He, 2007)

The above works by Visbal *et al.* (2006) and He (2007) are the only known works in open literature that use plasma actuators to suppress turbulent boundary layer separation. However, the freestream velocity over the hump model in the above works is only 10 m/s. No work has addressed the issue of turbulent boundary layer separation suppression with higher velocity by using plasma actuators. Moreover, no work can be found in the literature which established a design tool to estimate the required strength and location of plasma actuators in terms of operating parameters, such as boundary layer shape and pressure gradient, to suppress turbulent boundary layer separation. In addition, few work is found to apply plasma actuation on suppression of flow distortion in engine ducts.

Chapter 3

Methodology

The methodology chosen consists of three phases. Phase 1 aims to numerically (through the use of a validated computational tool) develop the turbulent boundary layer separation control concepts on a generic 2-D planar diffuser. In this generic model of an engine duct, the boundary layer shape and pressure gradient can be easily controlled to establish the design rules. The effects of plasma actuation on turbulent boundary layer separation control are then experimentally investigated on a generic 2-D diffuser in Phase 2. Finally, those rules for plasma-based flow control achieved in Phases 1 and 2 are applied and demonstrated on a real 3-D S-shaped inter-turbine duct (ITD) in Phase 3.

3.1 Numerical/Analytical Study

3.1.1 Computational Tool Setup and Integration of Actuation Model

This task consists of developing a computational fluid dynamics (CFD) simulation tool through careful selection of a CFD code and integration of a plasma actuator model. In this project, the boundary layer separation and the effect of plasma actuation on separation suppression will be simulated. The physical features needed to be captured as accurately as possible are:

1) Boundary layer separation

2) Boundary layer transition

3) Flow instabilities/unsteadiness in shear layer/boundary layer

4) Effect of plasma actuation on the flow.

The boundary layer separation is the main flow feature to be controlled in this project by plasma actuators. In the first stage, the simulation of boundary layer separation need be as

accurate as possible. The candidate computational tools to simulate this feature are two commercial CFD codes, CFX and FLUENT. The selection of the better code is done through a comparative study with computational and experimental data in a diffuser with boundary layer separation in DalBello *et al.* (2005). The simulations are run in steady mode.

The boundary layer separation to be considered in this project can be laminar or turbulent. For the laminar boundary layer separation, the separation-induced transition is very important, because the flow control will focus on the delay/triggering of the laminar-turbulent transition. The assessment of accuracy of the candidate CFD code for simulating boundary layer transition is carried out through a comparative study with the work of Feng *et al.* (1999), which presents a study of laminar-turbulent transition flow on a flat plate in a low-speed wind tunnel at different Reynolds numbers. The simulations are also run in steady mode.

In the pulsed mode of plasma actuation, attention should be paid not only to the time-averaged flow field but also to the instantaneous flow field. From the instantaneous flow field, the interaction/mixing level between outer flow with higher momentum and that near the surface with lower momentum can be assessed at least qualitatively for different actuation cases. The assessment of the selected CFD code capacity to simulate flow unsteadiness/instabilities is carried out on a mixing layer (free shear layer) simulation. Please note that the simulations in this and following validations are carried out in unsteady mode.

As discussed previously, the effect of a single DBD plasma actuator can be modeled as a time-averaged spatial body force distribution for CFD simulations (Orlov *et al.*, 2007; Visbal and Gaitonde, 2006; Rizzetta *et al.*, 2008). The body force distribution in this project is predicted with the model of Lemire and Vo (2011), which is found to predict a spatial body force distribution that most resembles that obtained with a sophisticated scientific model. The model is implemented on a very fine actuator mesh to resolve the length scales associated with a plasma actuator. The body force distribution for the CFD mesh is subsequently obtained through mapping the fine actuator mesh onto the coarse CFD mesh as described in Lemire and Vo (2011).

Subsequently the body force distribution is implemented into CFD simulations, by the User Fortran option in CFX and the User Defined Functions (UDF) option in FLUENT. The force distribution representing the effect of plasma actuators is shown in Figure 3.1. In this figure, the location with x = 0 mm is defined as the location of plasma actuator (corresponding to the trailing edge of the exposed electrode in Figure 1.5). The actuator strength (total force) is thus the integral of the force distribution. In the simulations, the desired actuator strength is obtained by scaling this force distribution, assuming that the relative spatial body force distribution remains unchanged with the actuator strength. This approach has been used by several other researchers such as Gaitonde *et al.* (2006). The qualitative validation of the selected CFD code with integrated plasma actuator model includes two parts: 1) comparison of instantaneous flow fields induced by a plasma actuator on a flat plate working in pulsed mode in quiescent air, 2) comparison of separation reduction in a 2-D diffuser by plasma actuation working in pulsed mode. The experimental data for both comparisons is obtained from experiments carried out at Ecole Polytechnique de Montreal and NRC, respectively.

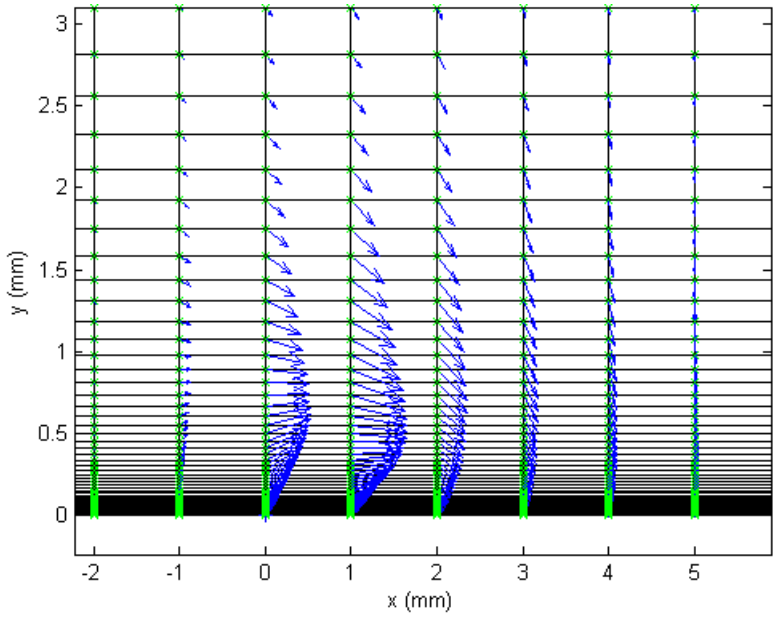

Figure 3.1: Time-averaged force distribution of plasma actuator for implementation into CFX

3.1.2 Conceptual Study on Generic Diffusers

This task aims to determine through numerical simulations the requirements for plasma actuation to suppress boundary layer separation in generic 2-D planar diffusers. Different actuation modes, *e.g.*, continuous vs. pulsed, and co-flow vs. counter-flow, are simulated and their effectiveness in terms of boundary layer separation control is assessed.

The preliminary simulations on laminar and laminar/turbulent separations are first carried out (as shown in Appendix A), from which some knowledge is learnt for the flow control on turbulent boundary layer separation.

The laminar separation is generated in a diffuser of moderate adverse pressure gradient (Figure 3.2). The diffuser exit is 88 mm high, and the throat-to-exit area ratio is 0.72. The laminar/turbulent separation is generated in a diffuser of high adverse pressure gradient (Figure 3.3). The boundary layer with laminar/turbulent separation experiences a laminar separation, separation-induced transition and a turbulent separation. The diffuser exit is 88 mm high, and the throat-to-exit area ratio is 0.41. In the current study, a 2-D structured mesh with the node number of 1437×124 (axial×normal directions) is used after a mesh dependency study. The grid has a y^+ of less than one near the wall. With a large adverse pressure gradient (such as obtained from the diffuser in Figure 3.3), there is no turbulent reattachment downstream of separation-induced transition for the laminar/turbulent separation. The SST transitional model is applied over the entire viscous surface for both cases with laminar and laminar/turbulent separations. All the simulations in this conceptual study on generic diffusers are carried out in unsteady mode.

Figures 3.2 and 3.3 also show the boundary conditions in the simulations. The inlet boundaries have constant total gauge pressure P_{trel} = 440 Pa for laminar separation cases and P_{trel} = 217 Pa for laminar/turbulent separation cases. The outlet boundary is at constant static gauge pressure P_{srel} = 0 Pa. It should be noted that the gauge pressure is relative to 1 atm. With the inlet total and exit static pressure being constant, the change in pressure recovery by reduction or suppression boundary layer separation alters the mass flow rate. The condition at the upper wall

is inviscid or free slip, thus the flow separation only occurs at the bottom plate. Implementation of this boundary condition simplifies the diffuser model (no suction slits at the upper wall), and thus reduces the mesh size near the upper wall as well as the computational time. The boundary layer starts from the leading edge of the plate, as a result of the no slip wall condition on the plate and the symmetry condition along the boundary upstream of the plate leading edge.

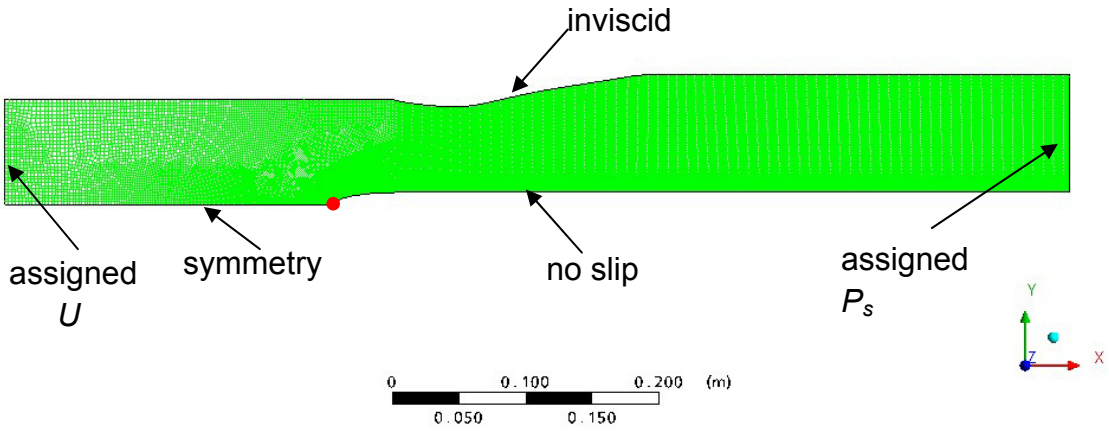

Figure 3.2: Simulated diffuser with moderate adverse pressure gradient

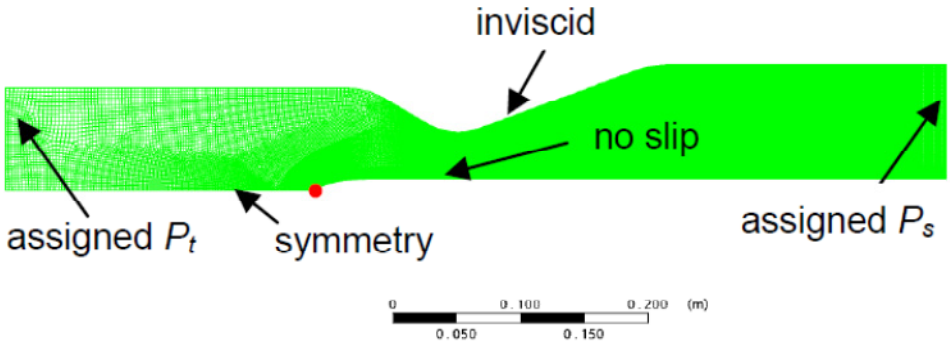

Figure 3.3: Simulated diffuser with high adverse pressure gradient

To determine the effectiveness of plasma actuation in suppressing boundary layer separation, various parameters of plasma actuation (*e.g.*, continuous vs. pulsed modes, actuator strength, location, frequency, direction and number of actuators) are considered. In pulsed mode, an actuation frequency is chosen to excite resonance of turbulent flow structures in the boundary

layer in order to improve momentum transfer between the outer high-velocity and inner low-velocity flows and thus suppress separation with minimal power input. This frequency can be chosen from resonant frequencies of the no-control flow, achieved by spectral analysis of unsteady signals acquired at several points of interest in the flow.

Two actuator locations are chosen: 1) laminar separation point (LSP), 2) a location in the turbulent boundary layer region (TRP) for the laminar/turbulent separation cases.

As for the actuation direction, both co-flow and counter-flow are considered, as illustrated in Figure 3.4. The counter-flow actuation is chosen because counter-flow actuation even with low strength can induce perturbations in the flow and trigger laminar-turbulent transition to prevent the laminar separation (Visbal *et al.*, 2006) and may also be effective in resonating turbulent structures.

In addition, an array of actuators is considered, as shown in Figure 3.4(c). The separation distance between actuators is chosen based on the new separation point. For example, the second actuator is put near the new separation point by the use of only the first actuator.

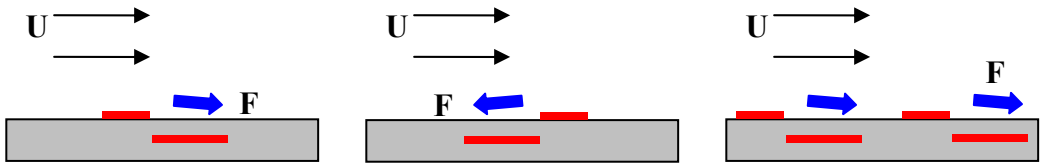

(a) co-flow (b) counter-flow (c) multi-actuator

Figure 3.4: Configuration of plasma actuation in different modes

The above preliminary study has demonstrated the effects of some plasma actuator parameters on the control of boundary layer separation. However, for each parameter, only several cases are tested, which are chosen based on literature review. This is because 1) the above work can be regarded as a preliminary study to demonstrate the effectiveness of plasma actuators and to decide the parameters for further detailed investigation; 2) the CFD simulations of boundary layer separation with transition is time-consuming and thus to simulate a series of

cases for each parameter is not an effective option.

In the subsequent final simulations, the boundary layer separation is only turbulent, through the use of the SST turbulence model, instead of SST transitional model. The boundary layer in a realistic S-shaped engine duct is usually turbulent, as a result of high Reynolds number and high adverse pressure gradient. The SST turbulence model takes transport effects into the formulation of the eddy-viscosity and thus gives a highly accurate prediction of the onset and the amount of flow separation under adverse pressure gradients. An automatic near-wall treatment is applied for the SST model in CFX. The other parameters about the simulation setting are the same as those for the above study on laminar/turbulent boundary layer separation (see Figure 3.3). The influence of actuator location, actuator strength, pulsed actuation frequency and duty cycle on the suppression of turbulent boundary layer separation is further investigated.

3.1.3 Establishment of Design Rules

This part of the research aims to provide a design tool to estimate the required strength and location of plasma actuators in terms of operating parameters, *e.g.*, boundary layer shape and pressure gradient, to suppress turbulent boundary layer separation.

In other words, for an arbitrary 2-D S-duct with two locations susceptible to flow separation, as shown in Figure 3.5, the aim is to establish a relationship between actuation strength F to delay separation by distance L_{gain} and operating parameters, as follows:

$$F = f(U, \rho, \mu, \nabla P, L_{gain} or\ \Delta P, \theta, H, I) \tag{3.1}$$

where $\Delta P = (P_{sep} - P_{act})_{inviscid}$ is the pressure rise in the inviscid case between the actuation and new separation points, and $L_{gain} = X_{sep} - X_{act}$ is the distance along the surface between the actuation and new separation points. Note that the actuation location is taken near the original (no actuation) separation point. $H = \delta^* / \theta$ is the shape factor at the actuation location and I is the freestream turbulence intensity above the actuation location.

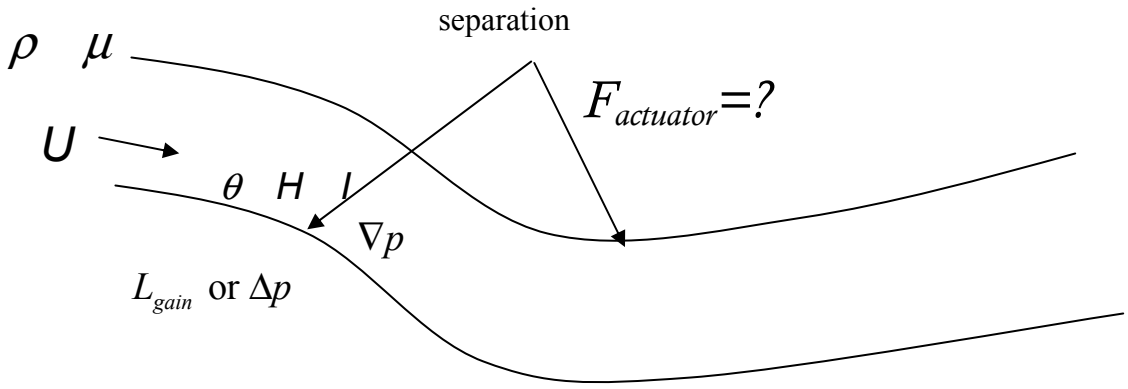

Figure 3.5: A generic 2-D S-duct

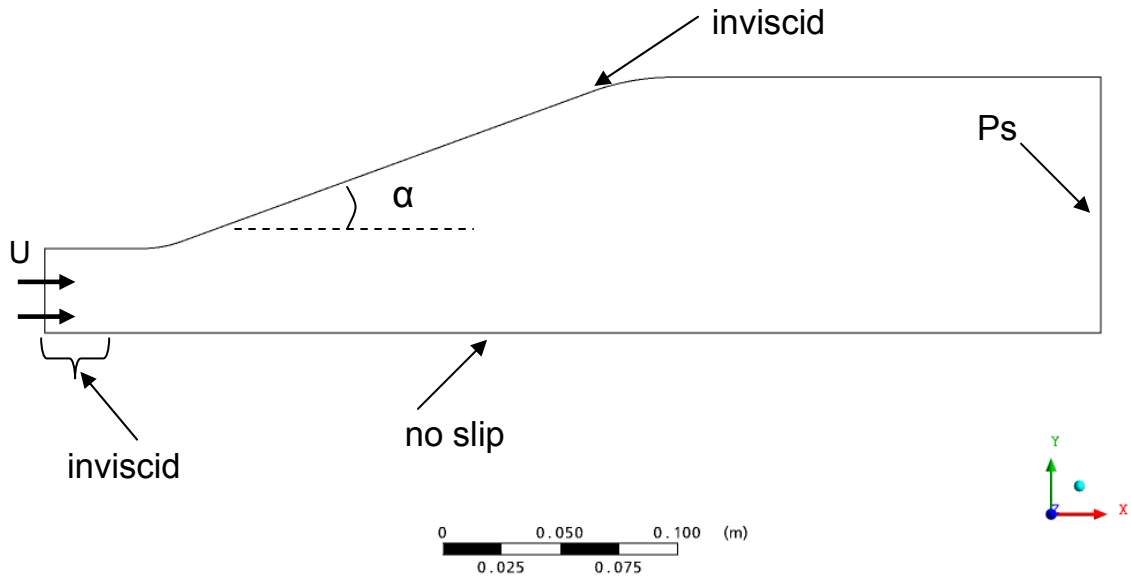

Figure 3.6: Generic geometry for CFX simulations to determine actuation requirements

The main hypotheses in the establishment of design rules are:

1) 2-D flow

2) Incompressible flow (Mach number < 0.3)

3) Turbulent boundary layer separation control

4) Continuous actuation

The 2-D assumption allows the secondary flow in the diffuser to be neglected so as to focus on the boundary layer separation control. The incompressible flow hypothesis is based on the fact that the flow in most engine intakes is low subsonic (usually Ma ~ 0.4) at the engine face and the achievable plasma actuator strength as of now is not strong enough for higher flow velocities. Moreover, the flow control target is only turbulent boundary layer separation, since the boundary layer in a realistic engine intake is usually turbulent, as a result of high Reynolds number and high adverse pressure gradient, resulting in boundary layer transition near the intake lip. Finally, the study on the continuous actuation is relatively easier than that on the pulsed actuation and the establishment of corresponding design rules is more feasible, since for the pulsed mode, more parameters (such as actuation frequency and duty cycle) and more information about the uncontrolled flow (such as instability) are needed.

To determine the design rules for plasma actuation requirements on the suppression of turbulent boundary layer separation, the database is provided by a series of numerical simulations in CFX. A computational approach is chosen over experiments because of the ease of setting up different cases and of obtaining detailed information on the flow field. The data is reduced using relevant non-dimensional parameters determined through an integral boundary layer approach, with the goal of collapsing the data for various simulations and configurations into a single set of curves to serve as design rules.

The generic geometry for the numerical experiments is shown in Figure 3.6. The boundary conditions imposed are the inlet velocity (constant freestream velocity), inviscid upper wall, no-slip bottom plate and specified exit static pressure. The SST turbulence model is used, because the detailed information on the boundary layer should be as accurately as possible captured. With this type of geometry, the diffuser divergence angle α can be varied to generate different adverse pressure gradients, and the diffusing length can be modified to induce different separation bubbles in terms of length and location. In addition, by specifying no-slip length upstream of the diffuser entrance (the start of the diffusing section), different boundary layer

shape factors at the diffuser entrance and thus different boundary layer separation features (*e.g.*, separation-reattachment length) in the diffuser can also be obtained.

3.2 Experimental Study

This phase consists of conducting experiments on 2-D generic diffusers intended to demonstrate the effect of plasma actuation on suppression of boundary layer separation, and to investigate the flow control mechanism of different actuation modes, especially pulsed actuation. The experiment is carried out at the NRC Gas Turbine Laboratory.

Before the actual experimental study, a preliminary experiment is set up and conducted in a low-speed test section at Ecole Polytechnique de Montreal in order to 1) demonstrate the performance of plasma actuation on suppressing boundary layer separation, and 2) test experimental/measurement techniques (*e.g.*, PIV and hot-wire anemometry) on a simpler-to-modify-and-operate rig in preparation for the final tests at NRC. The detailed setup and results can be found in Appendix B (Xu *et al.*, 2010).

Compared to the preliminary experiment, the main differences of the second test section are: 1) smaller diffusing rate by the change of upper wall contour, which corresponds to a smaller separation; 2) modified plasma actuator implementation, which allows higher AC voltage and has higher plasma force generation (actuator strength); 3) a series of pressure taps along the plate, and a streamwise slit along the upper wall, for hot-wire measurement along streamwise locations; 4) boundary layer trips placed upstream of the throat to trigger early transition, such that only turbulent boundary layer separation arises at the plate; 5) higher throat velocities.

3.2.1 Experimental Apparatus

The experimental apparatus located at the NRC GTL is shown in Figure 3.7. The setup mainly consists of a wind tunnel, a plasma generation system, a Particle Image Velocimetry (PIV) system and a hot-wire measurement system.

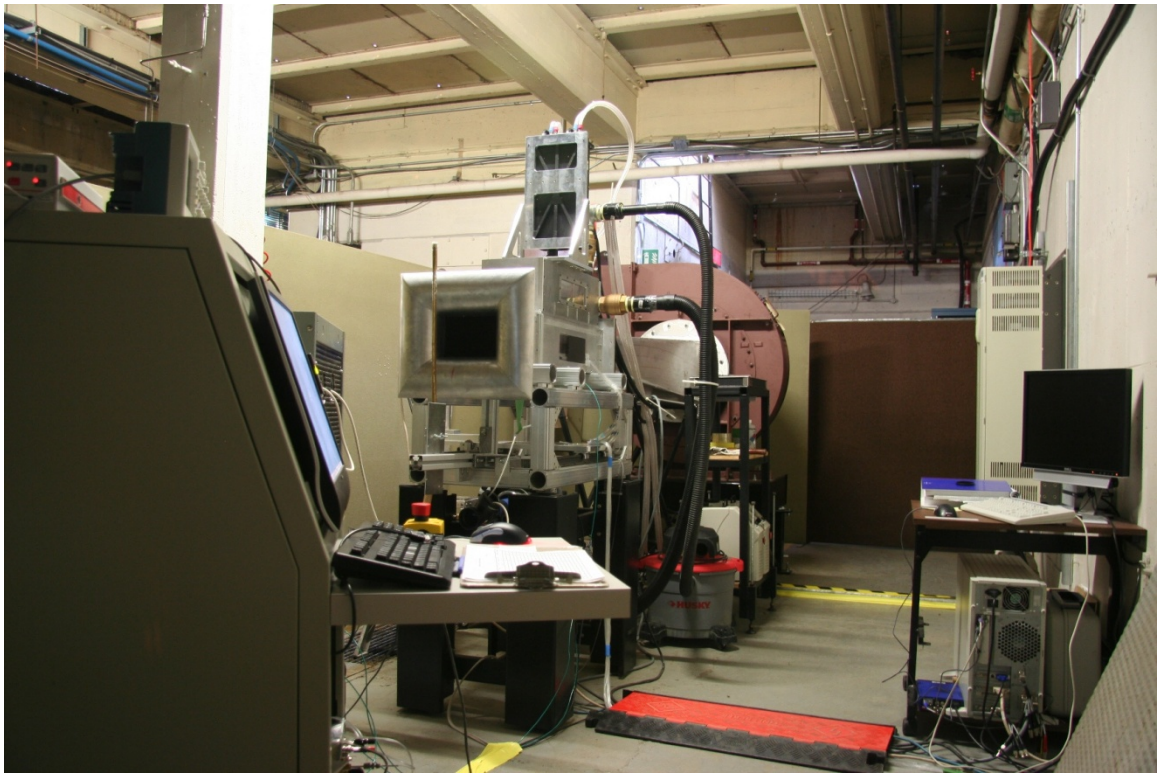

Figure 3.7: Experimental setup at NRC GTL

Wind Tunnel

A small-scale open-loop suction-type wind tunnel has been designed and constructed at the NRC GTL. The wind tunnel, as illustrated in Figure 3.8, has a bell-mouth, a straight inlet channel, a convergent-divergent test section and an exit channel. Two honeycomb pieces are put in the inlet channel and exit channel, respectively, to minimize the corner vortex induced by the four corners of the rectangular bell-mouth. For example, the measured flow angle relative to the freestream at the end of the straight inlet channel is reduced to 0±0.5 degrees with the inlet honeycomb compared to that of 2±0.5 degrees without the inlet honeycomb. A fine grid between the inlet honeycomb and test section generates freestream turbulence intensity (FSTI) of 1.6%. The test section has a cross-section at the diffuser exit of 203.2 mm width and 88 mm height.

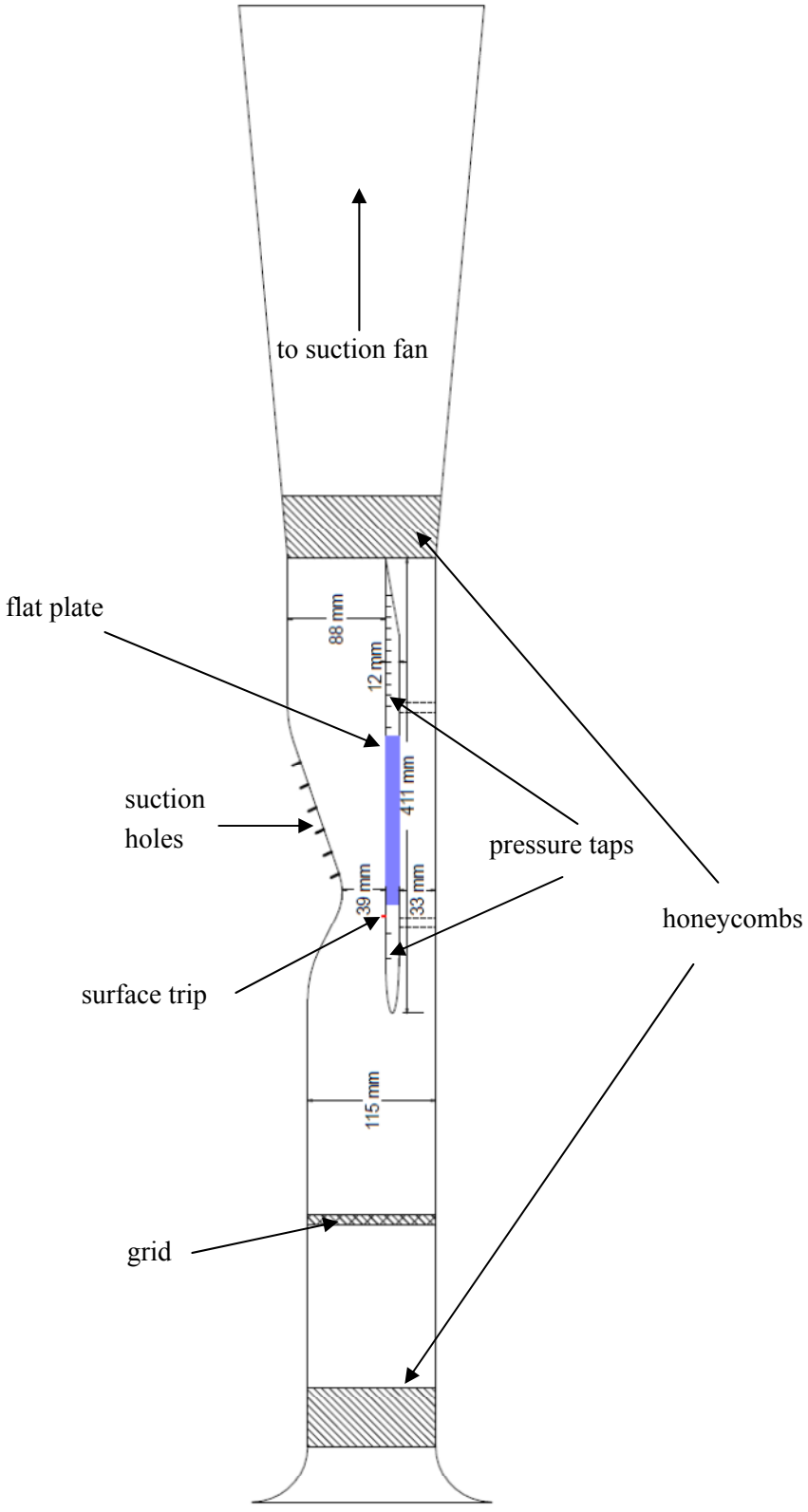

Figure 3.8: Configuration of low speed wind tunnel at NRC GTL

A flat plate is inserted in the test section to generate a diffuser with a throat-to-exit area ratio of 0.41. The main flow is generated by a centrifugal suction fan connected to the exit channel. The contoured upper wall imposes a desired pressure distribution on the flat plate in the test section. To avoid the flow separation on the upper wall, six series of suction holes, each spanning the width of the test section, are placed along the diverging section of the upper wall, and are connected to two shop vacuums, to remove the upper wall boundary layer. A Plexiglas window on one of the two side-walls provides the optical access for PIV measurement.

The centrifugal fan is driven by a 150 HP AC motor. The flow velocity can be controlled by adjusting the power input through the VFD (variable frequency drive) controller. The area-averaged throat flow velocity in the experiment is kept as around 30 m/s. The Reynolds number, based on the throat height and the area-averaged throat flow velocity, is 72,000.

The flat plate is composed of three parts: leading edge, plasma actuator part and trailing edge. The leading edge and trailing edge is made of aluminum, while the plasma actuator part is made of a dielectric material (Plexiglas or Teflon in this study). A strip of 2.5 mm wide and 3 mm high is put on the leading edge part (x = 85 mm) to trip the boundary layer as turbulent downstream of the throat.

The leading edge and trailing edge are instrumented with 2 and 12 surface static pressure taps (0.8 mm in diameter) in the plate centerline, respectively. The plasma actuator used in this experiment is illustrated in Figures 3.9 and 3.10, based on the parametric study on DBD plasma actuators. The two electrodes made of copper foil (0.04 mm thick) are separated by a Plexiglas/Teflon sheet of 12.7 mm thick and 203.2 mm wide. The electrodes span only 160 mm to avoid the discharge between the two electrodes. The lower electrode connected to an AC signal is insulated from the air by the rubber electrical tape (3M Scotch) and glue (Loctite 1750 Urethane), while the upper electrode connected to the aluminum test section is grounded. To avoid a discharge or power loss, the high voltage cable for connecting the lower electrode is suspended in the air and away from any metal part of the test section. The highly flexible cable

has a maximum working voltage of 42 kVDC. The entire plasma actuator is fixed between the leading and trailing edge parts. The position of the actuator (origin of the coordinate) is referred to the right corner of the upper electrode.

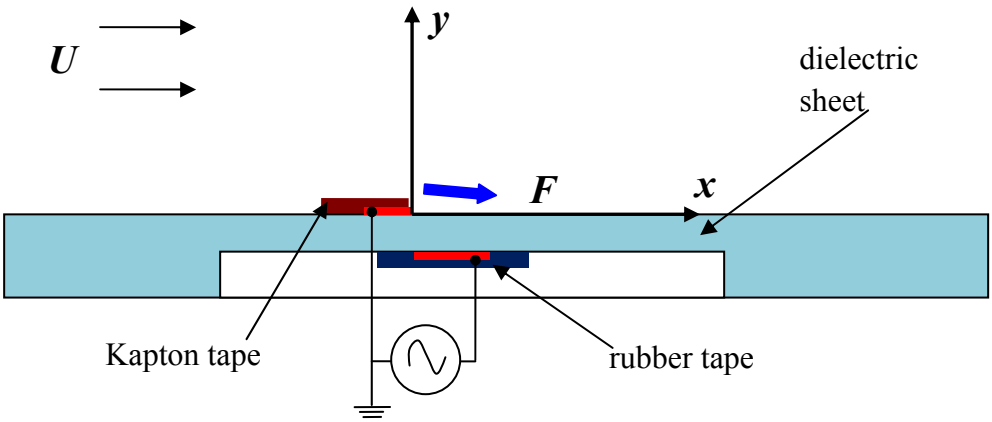

Figure 3.9: Configuration of plasma actuator implementation

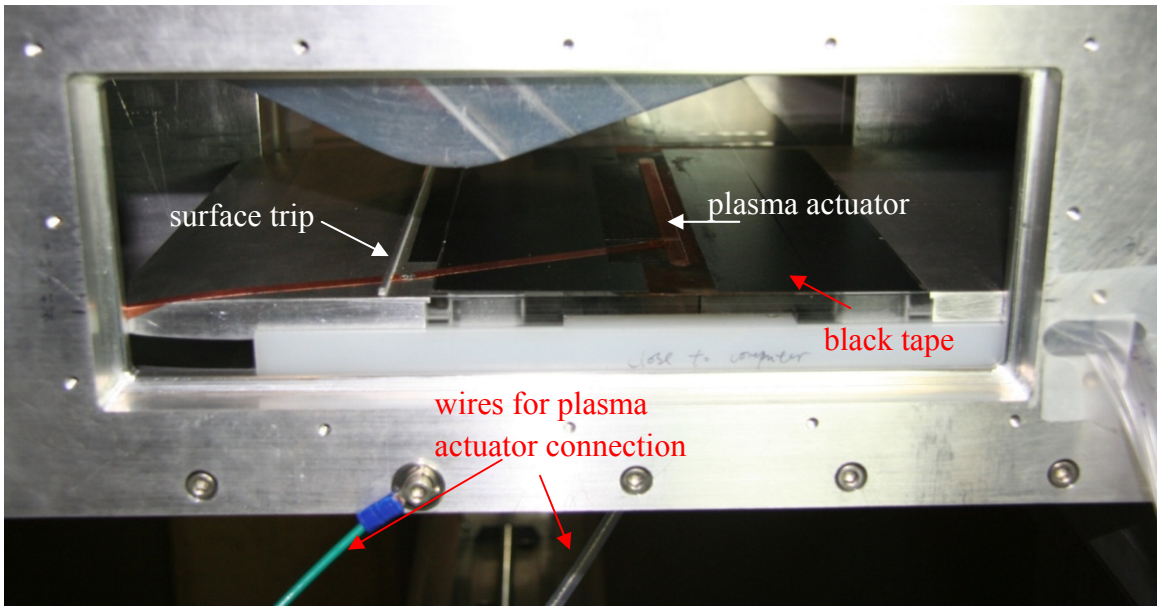

Figure 3.10: Experimental setup of plasma actuator implementation

Pressure Measurement

The time-averaged surface static pressure distributions on the flat plate and plasma-induced

flow velocity were measured by using a Scanivalve DSA 3217 pressure scanner. The scanner has sixteen temperature compensated differential pressure transducers with a measurement range of ± 1250 Pa. The uncertainty in the measured pressure is estimated to be about 1.0 Pa. The pressure is averaged over 2000 samples acquired at 100 Hz along the plate centerline.

To measure the plasma-induced flow velocity, a Pitot tube is hand-made through the bonding of two ceramic tubes (see Figure 3.11). The smaller tube has an outer diameter of 0.8 mm while that the larger tube is 6.35 mm. The Pitot tube is mounted on a 2-D traverse system, with a range of 28 mm in the vertical direction.

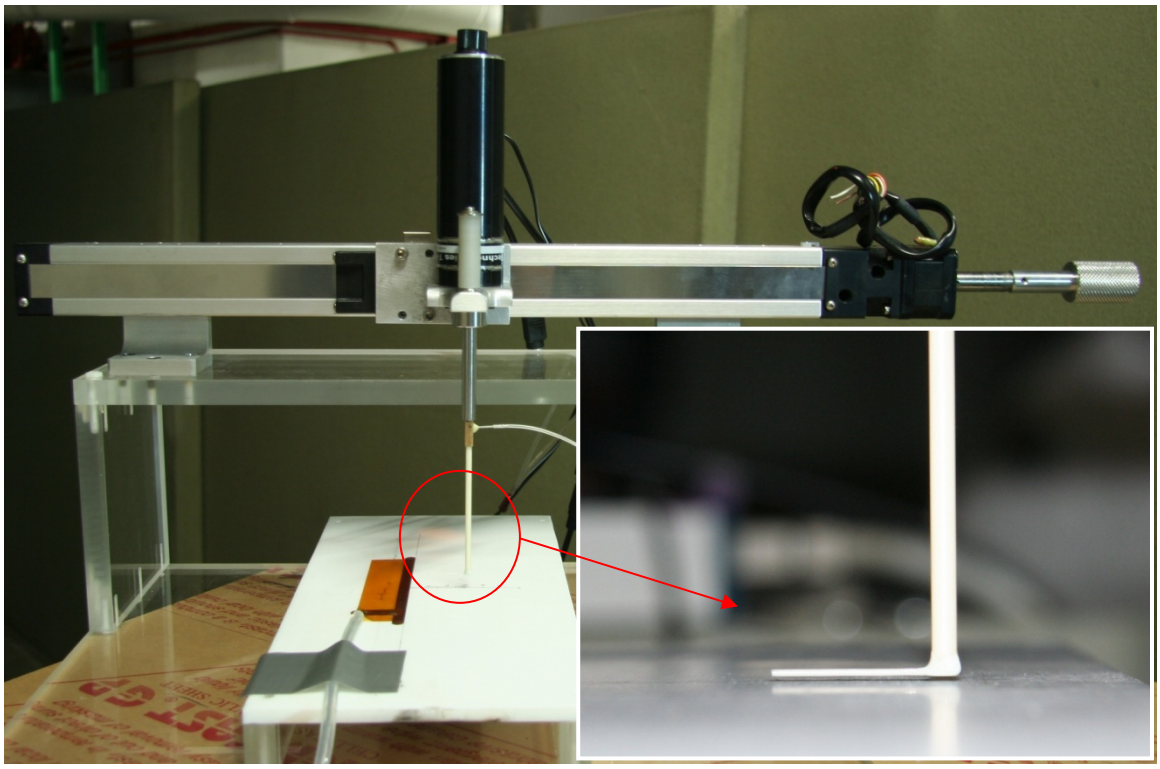

Figure 3.11: Experimental setup of Pitot tube

Particle Image Velocimetry (PIV)

Particle Image Velocimetry (PIV) is a full-field, non-intrusive and instantaneous flow measurement technique. The flow is seeded with neutrally buoyant particles. A double-pulsed laser produces two successive pulses of light beams in a rapid succession with the associated

images recorded by a camera. The time difference (*dt*) between the firings of the two lasers is adjusted to produce a detectable displacement of the particles in the two successive images. The drawn displacement vectors divided by *dt* gives the instantaneous distribution of velocity vectors in the flow field. Normally the displacement should be greater than one pixel and less than a quarter of the size of the interrogation window (the local sample of a PIV image from which a velocity vector is derived). A LaVison 2-D PIV system is used in the current study (see Figure 3.12). It consists of a double-pulsed Nd:YAG laser and a high-resolution CCD camera. A time delay between two laser pulses of 10 μs is used.

High-quality of PIV images are usually associated with a uniform concentration of seeding particles. Since PIV is a technique that derives the flow velocity from the measured velocity of the seeding particles, it is very important that the seeding particles should be small enough to follow the flow and big enough to produce enough scattering for images to be recorded. In the current study, the flow was seeded by using a TSI Six-Jet Atomizer. A large quantity of oil particles are introduced through the notched tube put upstream of the bell-mouth to ensure the uniformity of the seeding particles in the test section of interest.

An optic lens system adjusts the laser beams into thin and intense light sheets in order to illuminate the seeded flow field of interest. The laser light sheet is directed into the test section (with the sheet plane near the centerline) through a streamwise slot on the upper wall of test section. To avoid the suction of ambient air into the test section, a clear Plexiglas piece is inserted into the slot. Generally, the light sheet in the area of interest should be chosen thick enough to capture a sufficient number of particles while thin enough to observe the distinct particle displacement. In the current study, the light sheet thickness and the power level of the laser are adjusted so as to minimize the reflection from the flat plate surface. Please note that a layer of black tape is put on the flat plate surface of interest to further reduce reflection (see Figure 3.10).

The two successive images of the illuminated flow field are recorded by a double-frame

12-bit digital CCD camera with 1600×1200 pixels through a 50 mm lens. The camera is placed perpendicular to the laser sheet. To increase the spatial resolution, the camera is focused to get an image size of 80 mm×60 mm. A band-pass filter is used to avoid the laser light from going directly into the camera, which would result in a permanent damage to the CCD chip inside the camera.

The current PIV system only provides a maximum data transfer rate of 10 Hz for pairs of images. In the unsteady study, it is not possible to capture a sequence of images with enough temporal resolution within one pulsed actuation period. An initial delay is thus applied to a trigger signal generated by plasma actuator control panel thereby allowing the PIV images to be acquired at selected phases relative to rising edge of modulation signal (see Figure 3.13). In the current unsteady measurements, 320 images at each of 32 phases are recorded during one pulsed actuation period. The images from different actuation input cycles are then assembled into one cycle to get the flow field variation during one actuation input cycle.

The software DaVis is used for handling the measurements and for computing the velocity vector fields from the captured image pairs. The velocity components are computed using a cross-correlation algorithm with adaptive multipass, interrogation windows of 16×16 pixels and an overlap of 50 %. The spatial resolution of the PIV measurement is 0.4 mm (8 pixels). The error of velocity measurement is about 0.5 m/s. The near-wall flow (y < 0.8 mm) cannot be captured because of wall reflection.

Hot-Wire Measurement

A Dantec Dynamics constant temperature anemometry system (CTA) is used for hot-wire measurements. An overheat ratio of 0.8 was used for the hot-wire measurements. The signals are sampled at a frequency of 10 kHz with low-pass filtering of 10 kHz. In the measurements 40 ensembles of data were taken. Each ensemble consists of 4096 samples. A Dantec single-wire (of 5 μm in diameter and 1.2 mm in length) boundary layer probe mounted on the 2-D traverse system in Figure 3.11 was used to make the boundary layer traverses. The hot-wire was

calibrated in a blowing calibration facility in accordance with a 4th order polynomial curve fitting

$$U = C_0 + C_1 E + C_2 E^2 + C_3 E^3 + C_4 E^4 \tag{3.2}$$

where C_0, C_1, C_2, C_3,and C_4 are calibration constants.

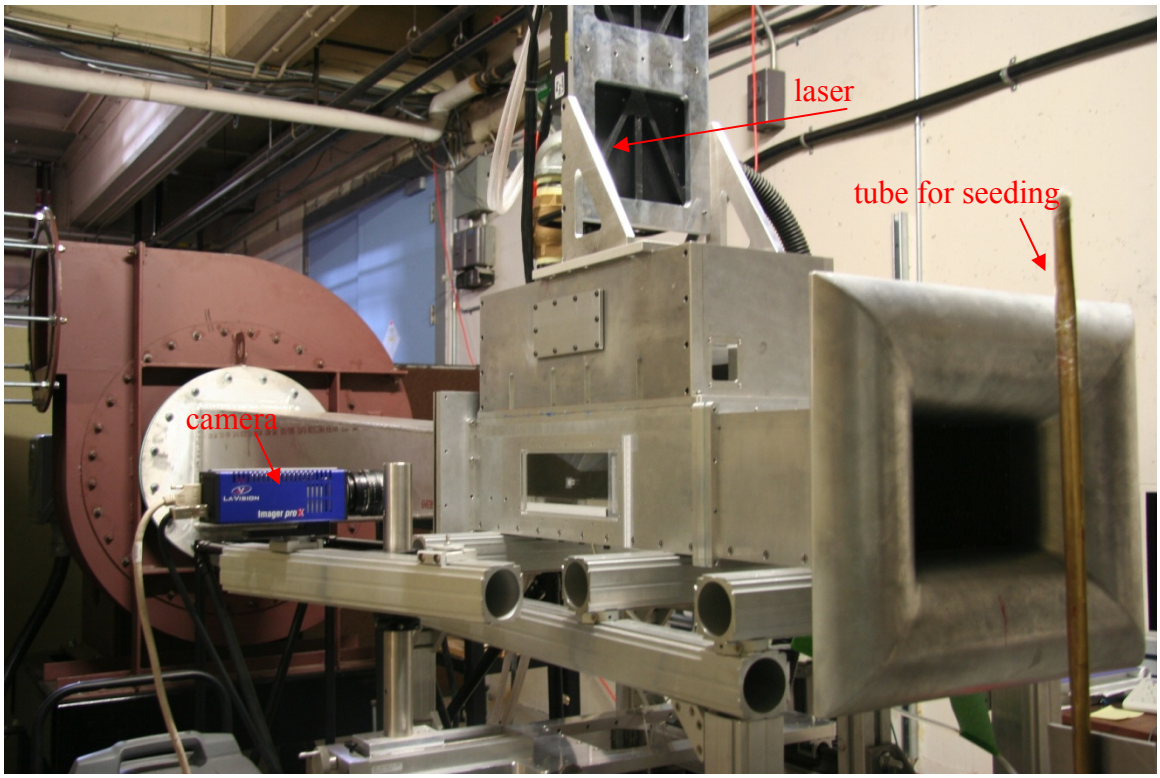

Figure 3.12: Setup for PIV measurement

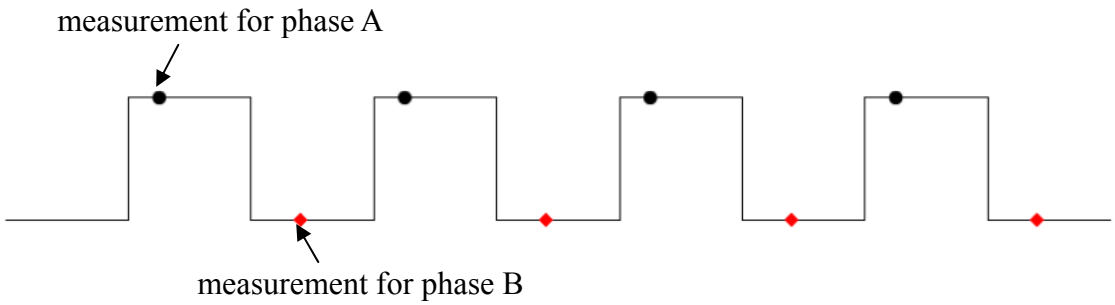

Figure 3.13: An illustration of phase-locked measurement

3.2.2 DBD Plasma Actuators

The present task studies the effects of different operation parameters and configurations of DBD plasma actuators in order to optimize them for flow control in S-shaped engine ducts. The optimization goal is either to increase the maximum obtainable plasma-induced force or to improve the force efficiency (force versus power), *i.e.*, minimize the power input for a certain force. Firstly, a new plasma generation system is built, through a selection of important components, *i.e.*, power amplifiers, a resistor module and transformers. Subsequently, this system is used to study the influence of different operation parameters and configurations on plasma-induced force and force efficiency.

The previous high-voltage generator Minipuls6 for plasma actuators is made by Electrofluidsystems®. The Minipuls6 generator is designed to generate high frequency and high voltages AC signal in a range from 5 to 30 kHz with amplitudes up to 68 kV_{pp} (peak-to-peak voltage). The device consists of one integrated low-voltage-control-circuit board and a high voltage transformer cascade. Power is supplied from a DC power supply (Voltcraft PS 3620).

At a specific frequency, plasma force (strength) increases with the applied AC voltage. However, this trend is limited at higher applied voltages, when the increase of applied voltage does not result in a significant increase in plasma force but does significantly increase the dissipated power, because the plasma actuator no longer generates purely uniform plasma but rather filamentary structures (streamers) which generates heat. The maximum obtainable force at a specific frequency is referred as the actuator's saturation force. The saturation force decreases with the increasing applied frequency. Therefore to obtain a higher saturation force, the plasma actuator and the plasma generation system should be operated at lower frequencies. Because the working frequency of the previous plasma generation system is higher than 5 kHz, a new system with the operation frequency lower than 5 kHz needs to be built. The detailed description of the new plasma actuator system is included in Appendix C.

Using the newly-built plasma actuator system, the effects of different operation parameters

and configurations of DBD plasma actuators are studied in order to optimize them for flow control. The investigated operation parameters of plasma actuators include dielectric material, applied waveform and frequency, and different shapes of exposed electrode, while the investigated configurations include bi-electrode and tri-electrode configurations.

3.2.3 Experiments

The flow without actuation is first investigated. The measurement techniques consists of PIV, CTA hot-wire measurement and static pressure measurement along the plate. The hot-wire measurement is used for capturing velocity fluctuations at several chosen locations in the test section which is then used for spectral analysis.

The effects of actuator strength, pulsed actuation frequency and duty cycle on flow control are subsequently investigated. The continuous and pulsed actuations at several specific frequencies are tested with variable applied AC voltages to demonstrate the effect of actuator strength. The pulsed actuation at several specific actuator strengths is tested to demonstrate the effect of pulsed actuation frequency. As for the effect of duty cycle, the actuation at several actuator strengths is tested with variable duty cycle from 0% to 100%. In each run with pulsed actuation, the phase-locked PIV measurement is adopted. In the phase-locked measurement, one cycle of pulsed actuation is divided into many specific phases, and for each phase, large amounts of data can be acquired and time-averaged to produce the instantaneous flow field at that phase. In addition, the static pressure distribution along the plate for different cases can be measured with pressure taps. The static pressure distribution along the plate is a global variable to demonstrate the effects of different plasma actuations.

3.2.4 Data Reduction and Presentation

Boundary Layer Integral Parameters

The boundary layer integral parameters are calculated from the PIV measurement at each axial location. The displacement thickness δ^*, is defined as

$$\delta^* = \int_{y=0}^{\infty} (1 - \frac{u}{U}) dy \tag{3.3}$$

where U is the freestream velocity.

The momentum thickness θ, is defined as

$$\theta = \int_{y=0}^{\infty} \frac{u}{U} (1 - \frac{u}{U}) dy \tag{3.4}$$

The boundary layer shape factor H, is defined as

$$H = \delta^* / \theta \tag{3.5}$$

Ensemble Average

Ensemble averaging or phase-locked averaging is a well-established method to process the periodic measurement data. It is used for PIV measurement to obtain the flow field variation during one actuation input cycle. The ensemble average of a periodic quantity is obtained by taking an average of the signal at a specific phase over a large number of periods. The phase in the measurement is determined by the time, t, with respect to a specific trigger signal.

The ensemble average of a quantity x at a specific phase or time t is defined as

$$\bar{x}(t) = \frac{1}{N} \sum_{1}^{N} x(t + (N-1)T) \tag{3.6}$$

where N is the total number of the ensembles and T is the period of the periodic data.

Proper Orthogonal Decomposition (POD)

Proper orthogonal decomposition (POD) is a method to extract a reduced number of typical modes in a signal associated with their time evolution (Hemon and Santi, 2003). These signals can be pressure or velocity, obtained by experimental measurements or numerical simulations. The detailed equations and definitions can be found in Appendix E. The POD offers representation of time-evolving vector field by using energetic spatial and temporal modes called *topos* and *chronos*, respectively. The energy contained in different modes decreases with

increasing mode number (order). Moreover, the entropy *H*, a normalized factor, can be used to compare the disorder levels of different signals. If all the energy is concentrated in the first mode, *H* is zero. In contrast, if the energy is uniformly distributed among all the modes, *H* attains its maximum value 1. Aubry *et al.* (1991) suggested the entropy *H* as an effective way to detect the laminar-to-turbulent transition.

The POD has been used to extract the coherent structures in the separated shear layer around a wing by Hoarau *et al.* (2006), and in the turbulent separation bubble by Mathis *et al.* (2009). In this current work, POD is also proposed to extract the coherent structures in the flow with turbulent boundary layer separation, and to quantify the effects of different plasma actuation regimes on boundary layer separation control.

3.3 Application to Real Design

This phase aims to experimentally and numerically demonstrate the effects of plasma actuation on the duct performance in S-shaped ITD geometry. The preliminary design rule established in Phase 1 is also used to predict the required actuator strength. The ITDs are chosen instead of engine intake ducts, because they have more complex flow structures as a result of upstream wakes and swirls.

The experimental investigation is conducted in a large scale, low-speed, axial turbine facility at the NRC Gas Turbine Laboratory. A large centrifugal blower draws the air into a settling chamber through a wide-angle diffuser. After the settling chamber, a contraction and an ellipsoidal nose cone guide the flow into an annular section, as shown in Figure 3.14. A grid made of round-bar mesh is placed after the contraction to produce a freestream turbulence intensity of 2.3% with an integral length scale of 7 mm at the ITD inlet. A ring of 48 swirl vanes is installed 25 mm upstream of the ITD to provide wakes and swirl to the test section. The ITD test section is an annular test rig with changeable casing and hub sections. The ITD casing can be rotated to provide circumferential traverse for measurements.

In the current study, the vane has a uniform swirl angle of 20 degrees from hub to casing. This ITD geometry, namely Build D, is representative of an aggressive ITD with boundary layer separation. It has a duct outlet-to-inlet area ratio of 1.53. The inlet annulus height is 76.2 mm. The non-dimensional duct length (ITD axial length/inlet annulus height) is 3.35.

An L-shaped seven-hole pressure probe with a tip diameter of 1.6 mm and a tip cone angle of 30° is used for detailed 2-D mapping measurement. The measurement grid in each plane consists of at least 31 points radially and 31 points circumferentially to cover one upstream swirl vane passage (7.5°). The first measurement point is placed as close as 0.5 mm to both hub and casing surfaces with the distance between positions increasing exponentially as the probe is retracted from the surfaces. The measurement locations in the ITD test section are shown in Figure 3.15. A linear traverse system is mounted on the rotatable ITD casing to provide full area traversing at five different planes (D1 to D5). Location D1 is at the ITD inlet plane and Location D5 is at the ITD outlet plane. Three more traverse planes (D2, D3 and D4) are placed inside the duct and roughly perpendicular to both hub and casing surfaces.

One row of 40 static pressure taps are distributed along the ITD rotatable casing. Two rows of 40 static pressure taps with half pitch spacing are distributed along the stationary ITD hub. Surface oil flow visualization is also used to examine the flow behavior on both hub and casing surfaces. A mixture of alkali refined linseed oil and titanium dioxide powder is applied in an extremely thin layer over the surfaces. After letting the tunnels run at condition for roughly 30 minutes, the parts are removed and photographed.

To reduce the boundary layer separation on the ITD casing, two plasma actuators similar to those in the previous flat plate experiment are used, with the locations shown in Figure 3.15. The induced body force is directed downstream. The two actuators together can provide a relatively high body force for a long time (about 8 minutes), because each actuator is operated at lower AC voltage. The actuator locations are chosen as upstream as possible, however this is limited by the location of plastic window for actuator implementation. Both actuators circumferentially span

about 300 mm to cover about 7 upstream swirl vane passages.

The numerical simulation is carried out by using CFX in steady mode in order to reduce computational time compared to unsteady mode while the main flow features can be captured. The computational domain used in CFD simulations is shown in Figure 3.17. The structured mesh consists of approximated 7.14 million nodes, determined from a grid independence study. The grid has a y^+ of less than two near the wall. To simulate the turbulence in the flow, the SST turbulence model is applied after a comparison of different turbulence models by Zhang *et al.* (2010). The inlet boundary condition for the simulations is established with measured velocity profiles, turbulence intensity profiles and turbulence length scale profiles. The freestream velocity is about 30 m/s and turbulence intensity is 2.3% with an integral length scale of 7 mm. The Reynolds number, based on the height of the ITD inlet and the freestream velocity, is 150,000. The outlet boundary condition is set as uniform atmospheric pressure. No slip and adiabatic conditions are imposed at all solid wall boundaries.

The simulated results without and with actuation are first compared with the measured results, in order to assess the capability of CFD to simulate the flow and the effects of plasma actuation within the ITD. Subsequently, more cases with continuous actuation at higher actuator strengths (than the experimentally obtainable strengths) are simulated to demonstrate the effects of actuator strength and location on duct performance improvement.

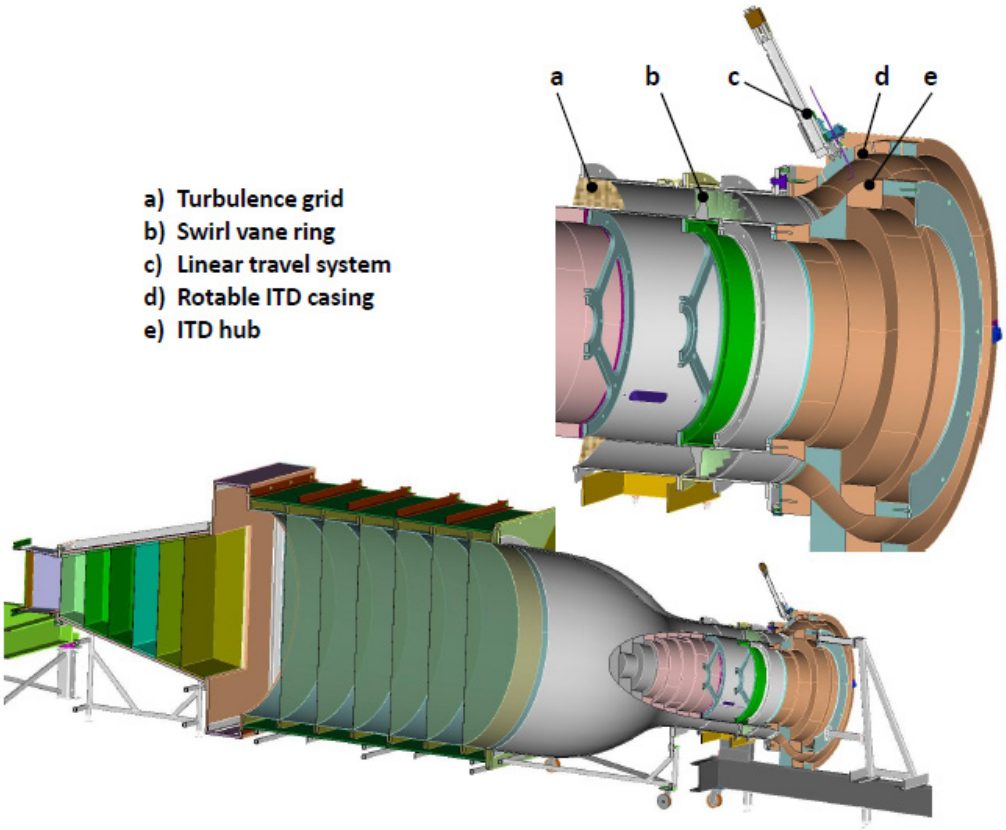

Figure 3.14: Annular test rig with changeable ITD test section (Hu *et al.*, 2011)

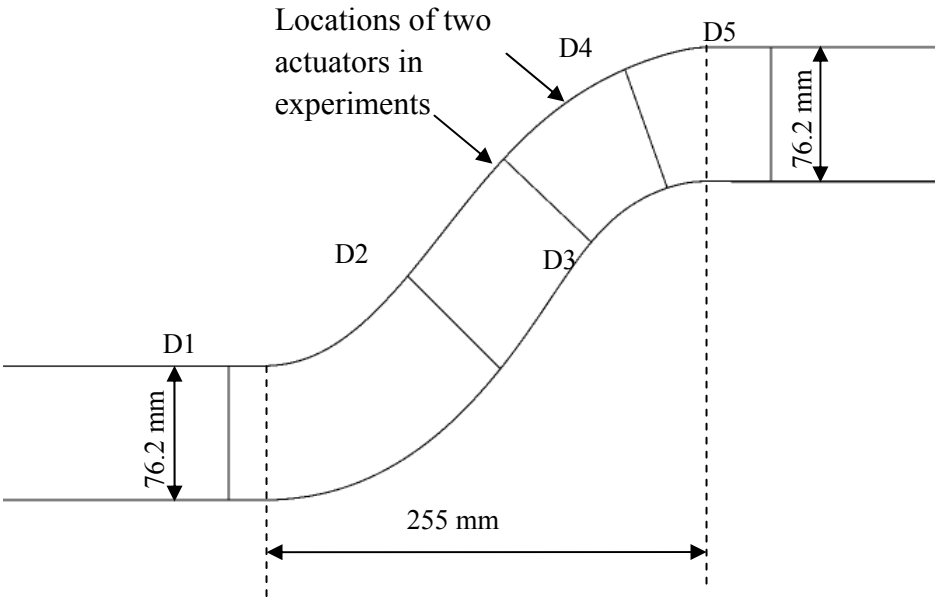

Figure 3.15: Measurement locations and actuator locations in experiments

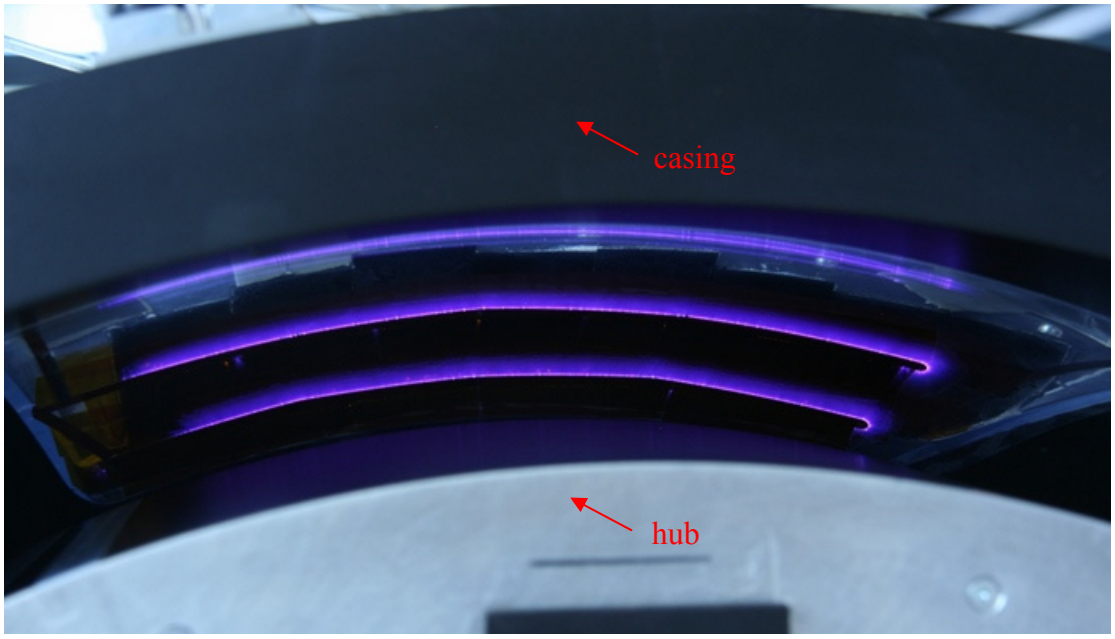

Figure 3.16: Plasma actuators on ITD casing (viewed from ITD exit)

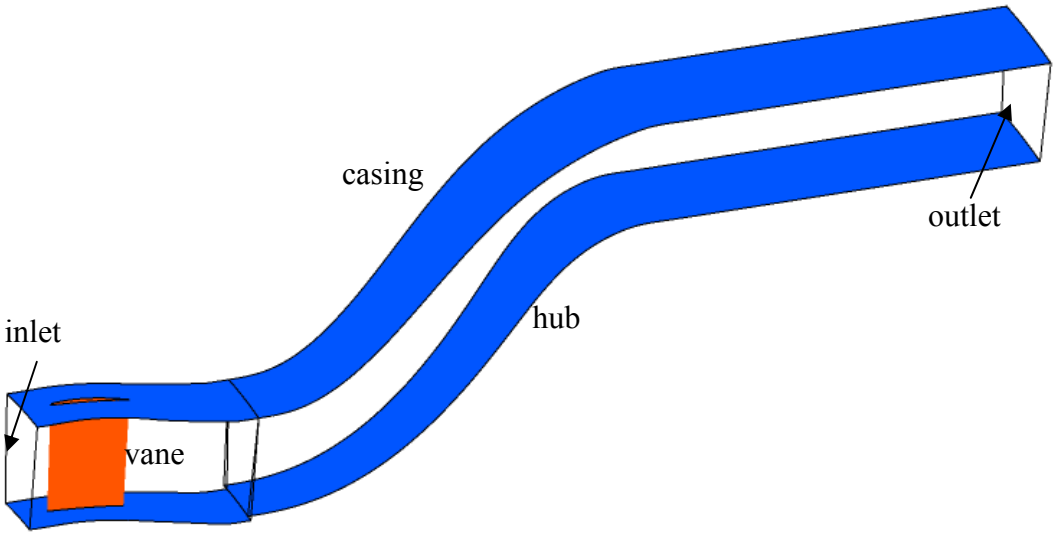

Figure 3.17: ITD with an upstream vane in CFD simulations

Chapter 4

Numerical Study on Separation Control in 2-D Diffusers

This chapter covers the results from the numerical study. First, the validation results of computational tool and integration of plasma actuator model are presented. Second, the effects of plasma actuation, in different modes, on the control of boundary layer separations in 2-D diffusers are demonstrated. Third, a preliminary design rule for the continuous plasma actuation on turbulent boundary layer separation control is developed and discussed.

4.1 Validation of Computational Tool

This part presents the validation results of the computational tool in terms of capturing four physical flow features in the flow, *i.e.*, 1) boundary layer separation, 2) boundary layer transition, 3) flow instabilities in shear layer/boundary layer, and 4) effects of plasma actuation on the flow, respectively.

First, to assess the ability of CFX and Fluent to accurately simulate boundary layer separation, the comparison of their predictions is referred to the computational and experimental study by DalBello *et al.* (2005) of the separated flow through a 2-D asymmetric subsonic diffuser.

Figure 4.1 shows the geometry and mesh of the planar diffuser. The mesh in the present work is identical to that of DalBello *et al.*, with a mesh size of 341×81 (axial×normal directions). The mesh was adopted based on a mesh dependency study. In the results presented, H and U_b represent the inlet duct height and the average inlet velocity, respectively. The axial location x starts from the diffuser inlet.

Figure 4.2 plots the mean axial velocity profiles at x/H = 24 from simulations with CFX, FLUENT versus the simulations and experiments by DalBello *et al*. In all three simulations, the

shear-stress-transport (SST) turbulence model is applied. One can observe that CFX can simulate a larger reversed flow region than FLUENT, and is closer to the experimental and simulation results by DalBello *et al*. It should be noted that in the turbulence model study by DalBello *et al.*, the SST turbulence model provided the best predictions (versus Spalart-Allmaras and $k-\varepsilon$ models) in comparison to experimental data in terms of velocity profiles.

Figure 4.3 compares the separation streamlines obtained using CFX, FLUENT versus those from the simulation by DalBello *et al.* (no available experimental result). The simulation result from Dalbello *et al.* can be used as reference because it has been validated for other parameters (*e.g.*, wall shear stress) with the experimental data. The separation streamline is a streamline starting from the separation point. From this figure, one can observe that CFX can simulate a larger and more accurate separation than FLUENT, compared to the simulation by DalBello *et al*.

The above results suggest that CFX with the SST turbulence model is the better CFD code in terms of simulating boundary layer separation in a diffuser, which is of central importance to this research. Thus, the rest of the assessment will be limited to CFX to confirm it as a tool for this project.

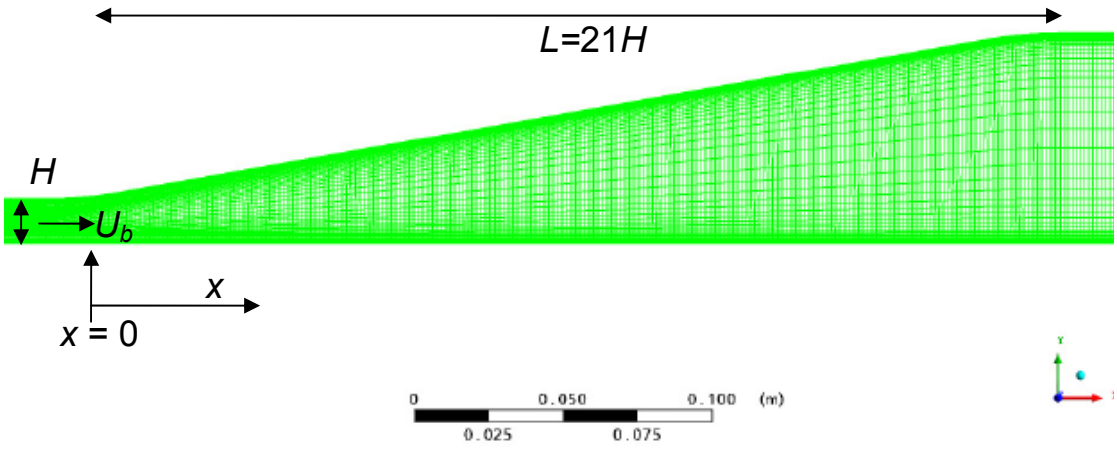

Figure 4.1: Geometry and mesh of a planar diffuser (10 deg, length of diffuser = 21*H*)

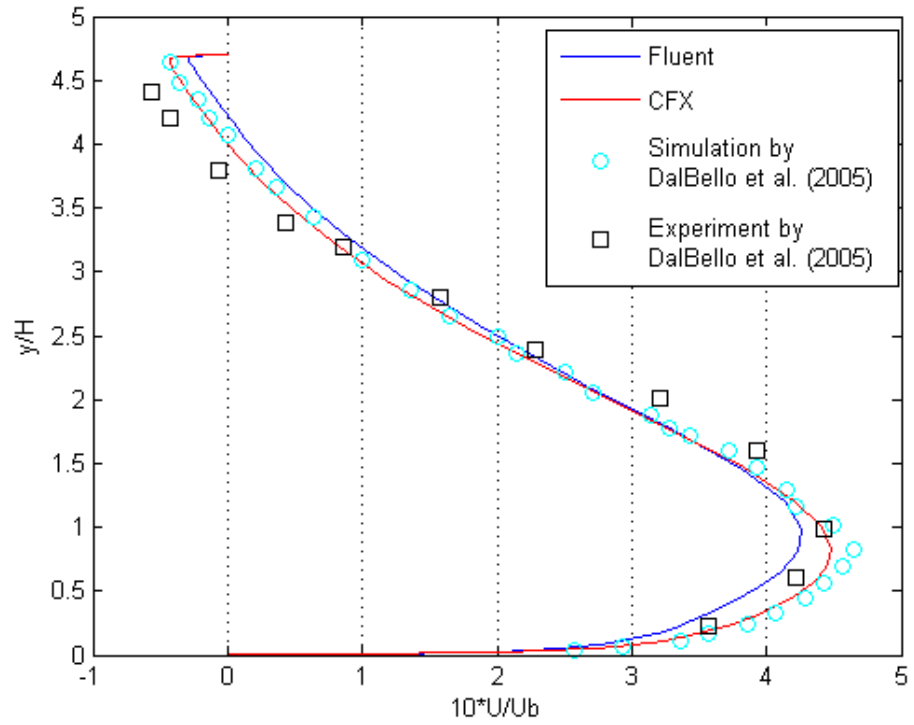

Figure 4.2: Axial velocity profiles at *x/H*=24 for CFX and FLUENT simulations vs. experiment (DalBello *et al.*, 2005)

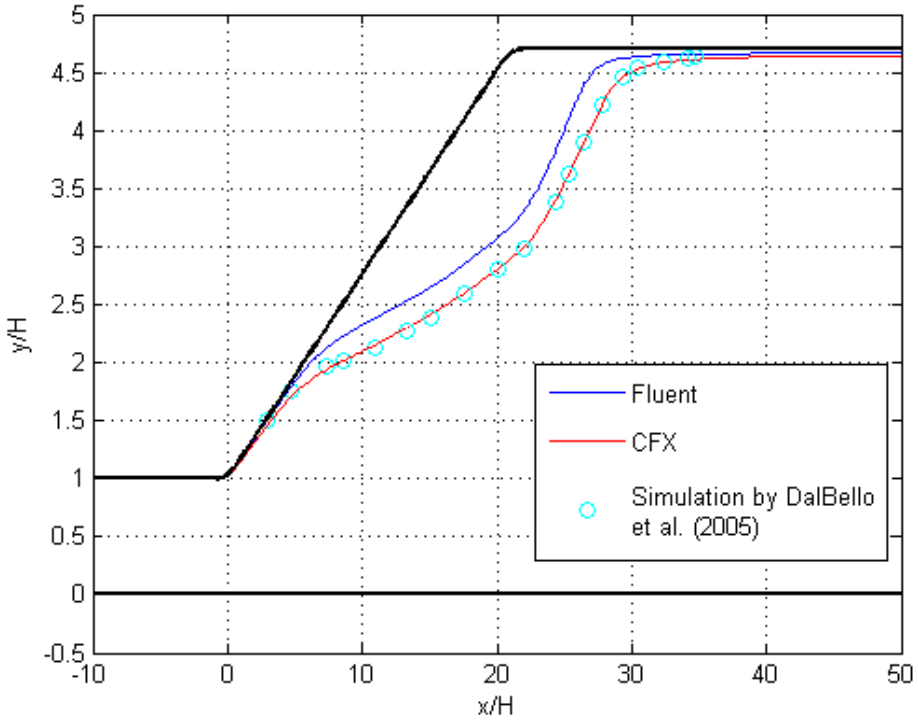

Figure 4.3: Separation streamlines for CFX and FLUNET simulations vs. DalBello *et al.*'s simulation (SST turbulence model)

Second, the assessment for boundary layer transition prediction is carried out through the comparison with the numerical and experimental studies by Feng *et al.* (1999) of laminar-turbulent transition in the flow on a flat plate in a low-speed wind tunnel at different Reynolds numbers. In the simulations, the transition locations were predicted using MISES, in which a modified Abu-Ghannam/Shaw (AGS) transition criterion with a combination of the e^n envelope criterion was implemented. MISES is suitable to model natural transition. However, CFX adopts the Langtry and Menter transitional model, a two-equation model, which can simulate both natural and bypass transitions.

Figure 4.4 shows the geometry and mesh of the planar diffuser for transition location comparison. In the present simulation, the length of the plate c is 1 m. The grid has a y^+ of less than one (the wall-normal mesh should be fine enough to correctly capture the laminar and transitional boundary layers), as suggested by the CFX user manual.

Table 1 lists the transition locations predicted by CFX in the present simulation versus those from the simulation and experiment (only two available cases) by Feng *et al.*. Since the transition locations for the first two cases from the simulation with MISES and experiment match well, the simulation results for the other cases are used for comparison with CFX results. One can see that CFX is able to accurately simulate laminar-turbulent transition in a diffuser.

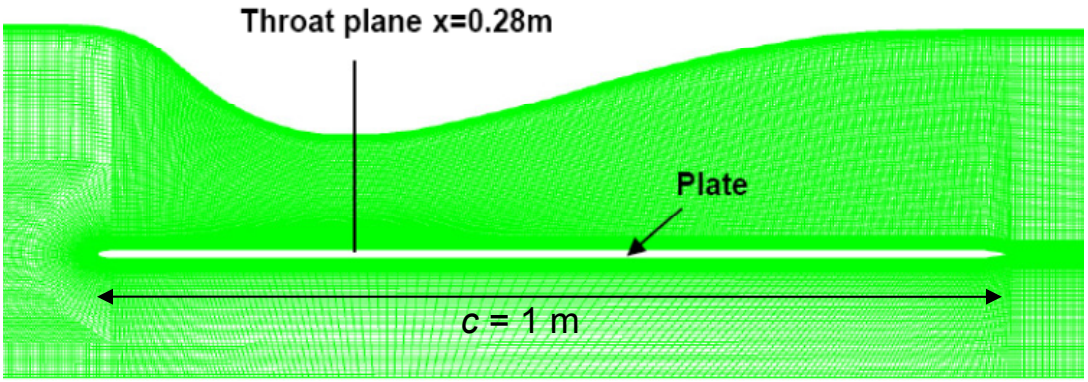

Figure 4.4: Geometry and mesh of a diffuser with transition

Table 1: Comparison of transition location

Incoming velocity (m/s)	3.5	9.5	15.0	20.5
Predicted transition location (x/c) (MISES)	0.479	0.433	0.407	0.390
Experimental result of transition location	0.475	0.445		
CFX result of transition location	0.470	0.430	0.408	0.398

Third, the capability of CFX to simulate flow instabilities is evaluated through the simulation of a mixing layer between two parallel flows at different velocities. Figure 4.5 shows the geometry and mesh for the mixing layer simulation. The mesh near the splitter plate and within the mixing layer is refined to capture shear layer instability.

In the simulation, the velocities of two air streams are 100 and 40 m/s, respectively. The inlet turbulence intensity is 1%. The SST turbulence model is adopted. The two stream velocities are chosen, referred to Slessor *et al.* (1998), which presents the results from a set of incompressible mixing-layer flow experiments, at high Reynolds number. In this reference, the two streams are made of mixed gases, and different compositions (reacting or non-reacting gases) are considered. However, in the present simulation, the two streams are made of non-reacting air, because CFX can not match the properties of the reacting gases.

Figure 4.6(a) and (b) show the instantaneous vorticity field from the present work and the colour-schlieren image by Slessor *et al.*, respectively, from which the geometrically-similar large structures are clearly shown and qualitatively match well. However, the goal of this assessment is to demonstrate the capability of CFX to simulate flow instabilities. Thus a qualitative comparison of the flow structures with the results from Slessor *et al.* is judged to be sufficient. Therefore, CFX can simulate instabilities in boundary and shear layers.

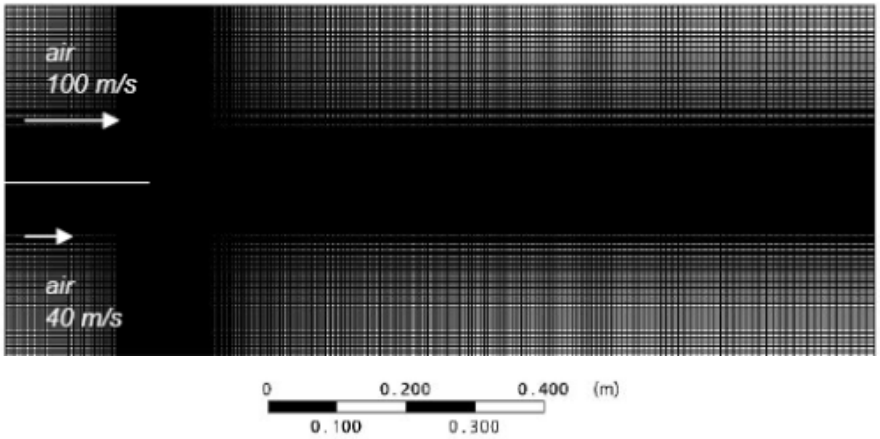

Figure 4.5: Mesh for simulating mixing layer instability

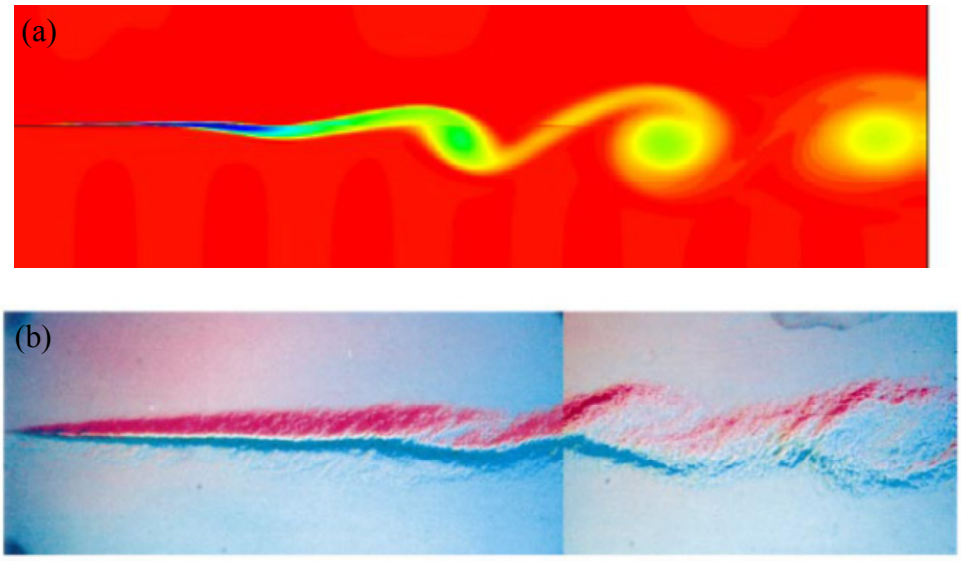

Figure 4.6: Instantaneous fields showing geometrically-similar large structure: (a) instantaneous vorticity field in the present work, (b) colour-schlieren image (Slessor *et al.*, 1998)

Finally, an assessment of CFX with the implemented plasma actuator model is carried out through comparison of its effect on quiescent air and on boundary layer separation with experimental data.

Figure 4.7 shows the experimental and simulated instantaneous vorticity fields for a plasma actuator on a plate with actuator strength F = 30 mN/m, actuation frequency of 5 Hz, and duty cycle of 50%. In the experiment at Ecole Polytechnique de Montreal, the plate with a plasma

actuator mounted is placed in the center of a wind tunnel, and thus the wall-effects from the wind tunnel on the induced flow by the plasma actuator can be negligible. PIV measurements are used to capture the instantaneous flow field.

From Figure 4.7, a wall jet starting from the actuator location and thereafter a pair of vortices can be observed. This structure is consistent with documented wall jet experiments and computations (Visbal and Gaitonde, 2006; Visbal *et al.*, 1998). The counter-clockwise vortex (positive vorticity) is from the shear layer induced by plasma actuation, while the clockwise vortex (negative vorticity) is from the induced boundary layer. Based on the comparison of the general structure and size of the counter-rotating vortex pair from experimental measurement and CFD simulation, CFX with the integrated plasma actuator model can simulate the effects of plasma actuation in pulsed mode in quiescent air.

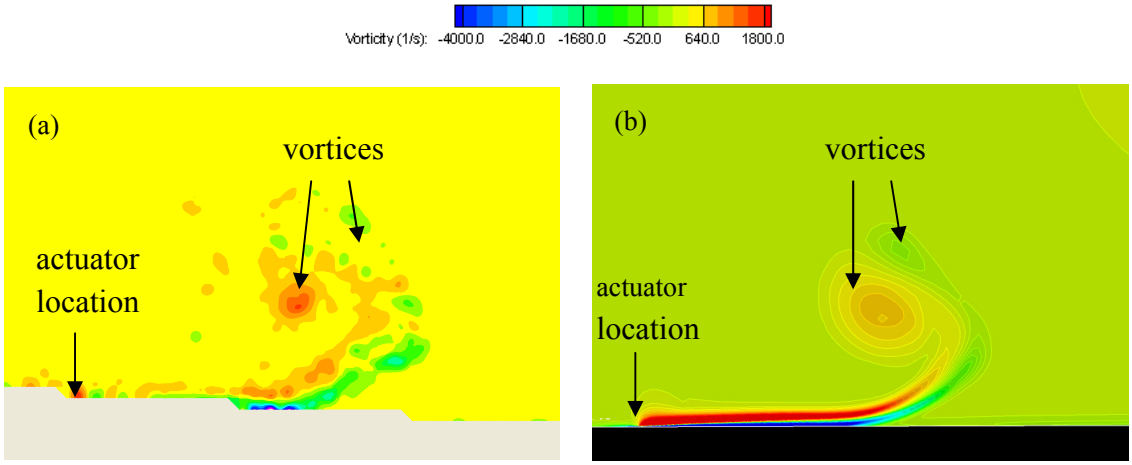

Figure 4.7: Instantaneous vorticity fields for plasma actuator in quiescent air (a) PIV measurement, (b) CFD simulation

The plasma actuator is then numerically implemented in pulsed mode to control boundary layer separation. The actuator has a strength F = 108 mN/m, actuation frequency of 40 Hz, and duty cycle of 40%. The simulated instantaneous velocity field for several selected phases is compared with the experimental data, as shown in Figure 4.8. The experimental data is obtained in the tests at NRC as described in Section 3.2. Please note that the actuator strength is measured

as a thrust in the experiment while it is a body force in the CFD simulations. The difference between the thrust and body force is the shear force on the wall, which can be calculated from the results of PIV measurement as used in Baughn *et al.* (2006). The actuator strength in the CFD simulations thus match that in the experiments

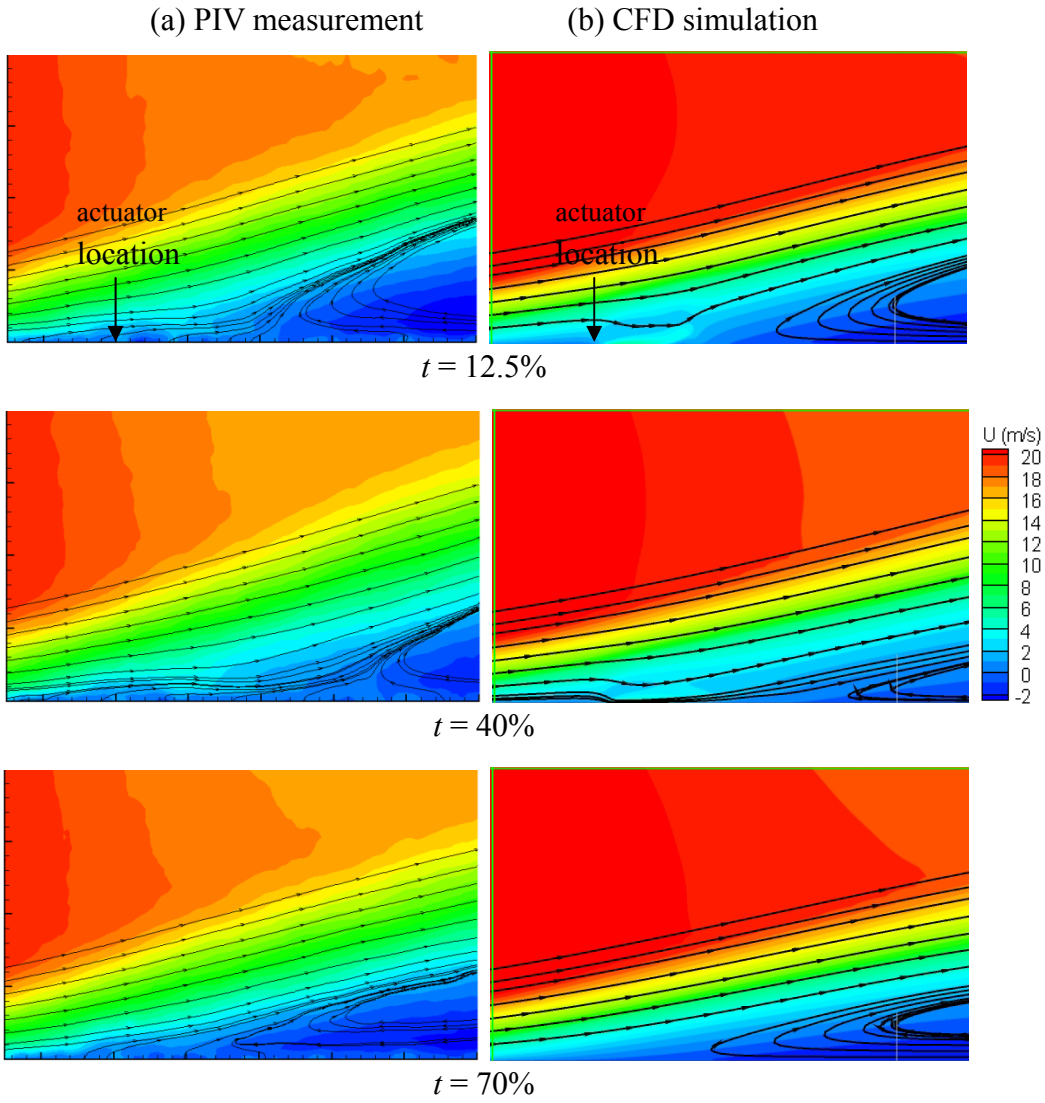

Figure 4.8: Instantaneous velocity fields with pulsed plasma actuation at 108 mN/m, 40 Hz, duty cycle of 40% for several selected phases

From phase 12.5% to 40%, the boundary layer separation is further reduced, as observed from the reduced separation size. In contrast, from phase 40% to 70%, the boundary layer size

increases, since the plasma actuation is turned off at phase 40% and the associated momentum addition process is also shut off. Generally, the CFD simulation can capture the variation of flow field induced by pulsed actuation discussed above. However, the CFD simulations predict a thinner separated shear layer than experimental investigation. This deviation is not important in the present study, because the suppression of boundary layer separation is the main consideration and the following parametric study is based on the same no-control case.

4.2 Numerical Assessment of Boundary Layer Separation Control Concept

The results in Section 4.1 show that CFX simulations with an integrated plasma actuator model can capture the effects of the plasma actuation in suppressing boundary layer separation. In this section, the results from a numerical assessment of boundary layer separation suppression in a generic diffuser by plasma actuation with different actuation modes, locations, directions and actuator numbers are presented. The boundary layer separation to be considered can be 1) laminar, 2) turbulent and 3) laminar/turbulent, as discussed in Section 3.1.2.

The results from the preliminary simulations on laminar and laminar/turbulent separations are shown in Appendix A, from which some knowledge is learnt for the flow control on turbulent boundary layer separation:

1) Co-flow actuation, both continuous and pulsed, can delay or suppress the laminar separation in a diffuser with a moderate adverse pressure gradient, while at the same time the boundary layer can be kept laminar for a longer distance. In contrast, the counter-flow continuous actuation can suppress the laminar separation by inducing early transition over a shorter distance and make the boundary layer turbulent over a longer extent.

2) Co-flow actuation, both continuous and pulsed, can suppress the turbulent boundary layer separation in a diffuser with a high adverse pressure gradient, while counter-flow actuation is

ineffective even though it can also induce flow mixing. The counter-flow actuation is thus not chosen in the following study.

3) The actuator location near the laminar boundary layer separation point is shown better than the location in the turbulent boundary layer separation.

The following part presents and discusses the results from subsequent final numerical simulations on the geometry of Figure 3.3 to assess the influence of actuator location, strength, pulsed frequency and duty cycle on the suppression of turbulent boundary layer separation. Figure 4.9 shows contours of the time-averaged axial velocity and the time-averaged axial wall shear stress without actuation in the diffuser of Figure 3.3. The origin of coordinates is referred to the leading edge of the bottom plate (see Figure 3.3). As such, the throat plane is at x = 110 mm, and the exit plane is at x = 280 mm. Constant total pressure at the inlet and constant static pressure at the outlet were assigned to provide the area-averaged throat velocity for the no-control case of U_{throat} = 38 m/s. The Reynolds number, based on the throat height and the area-averaged throat velocity, is 91,400. A boundary layer separation can be clearly observed in Figure 4.9, which is also corroborated by the time-averaged axial wall shear stress distribution, where the zero axial shear stress corresponds to the separation or reattachment points. In the current case, the separation point is at x = 160 mm. Two monitor points are chosen in the flow field to capture the unsteadiness, which will be used for demonstrating the control effects. These two monitor points, as indicated in Figure 4.9, correspond to the regions of turbulent boundary layer separation (point 1) and the edge of turbulent separation (point 2), respectively.

4.2.1 Effect of Actuator Location

The effect of actuator location on boundary layer separation control is shown in Figure 4.10. In this figure, the results from both continuous and pulsed actuation are included. The line at x = 160 mm indicates the separation point without actuation. The pressure recovery coefficient η_p is defined as

$$\eta_p = (P_{exit} - P_{entrance}) / (0.5\rho U^2)_\infty \tag{4.1}$$

where P_{exit} is the area-averaged static pressure across the exit plane (x = 280 mm), $P_{entrance}$ is the area-averaged static pressure across the entrance plane (x = 30 mm) of the convergent duct, and $(0.5\rho U^2)_\infty$ is the dynamic pressure far upstream (at the inlet of the simulation domain). It should be noted that the reference static pressure $P_{entrance}$ can also be chosen at other locations, *e.g.*, at throat plane. However, the different choice of reference pressure for η_p does not affect the comparison of the effect of different actuation modes, since the new η_p is only shifted by a constant value for all cases from the one computed with Equation (4.1), assuming the total-pressure loss in the convergent duct is negligible compared to that in the divergent part. Based on the definition in Equation (4.1), the negative pressure recovery at lower actuator strength corresponds to a lower static pressure across the exit plane. The η_p is 0.433 for the ideal-inviscid case and -0.261 for the no-control case.

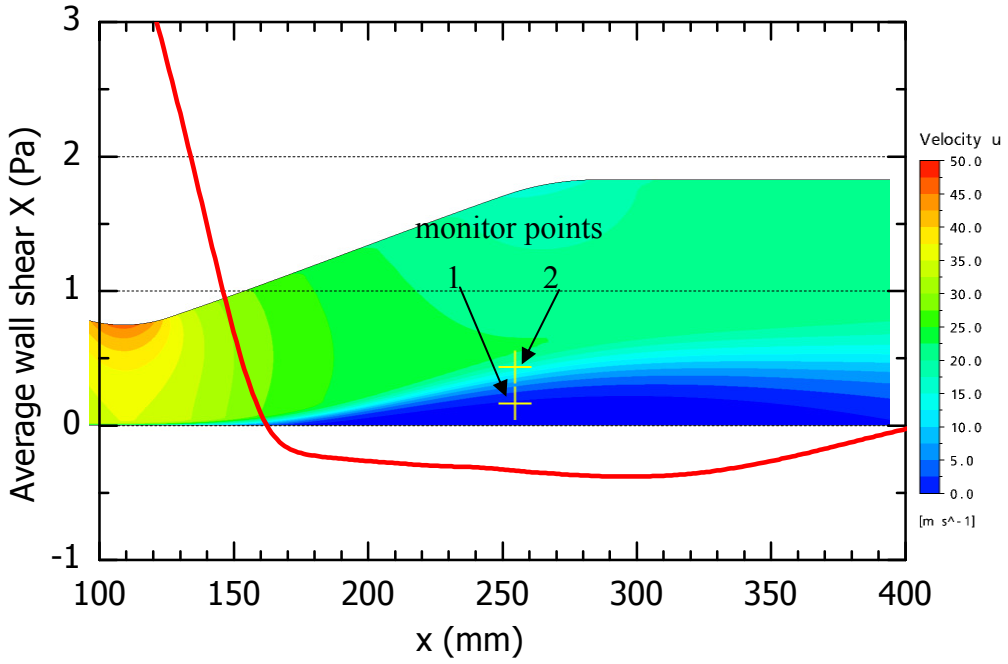

Figure 4.9: Contour of time-averaged axial velocity and axial wall shear stress along the plate without actuation with indicated monitor points

For continuous actuation, the optimal actuator location, which corresponds to the maximum pressure recovery, varies with actuation strength. When the strength is below 240 mN/m, the optimal location is just downstream of separation point (x = 160 mm). For these cases, boundary layer separation still exists. If the actuator location is far upstream of the separation point, where the boundary layer is relatively thin, the momentum from plasma actuation is added mainly to the outer high-momentum flow, instead of low-momentum boundary layer (refer to Figure 4.9), and thus the induced flow change is relatively smaller. However, if the actuator location is far downstream of the separation point, the boundary layer has already separated and the momentum is mainly added to the reverse flow inside the separation, therefore, its effect on separation control is limited. In contrast, when the strength is above 300 mN/m, the optimal location is located far upstream near the throat at x = 110 mm. Furthermore, the effect of actuator location for high strength cases is smaller than that for low strength, as observed from the difference of pressure recovery between different locations. This is because the boundary layer separation is suppressed and the associated pressure loss is already minimized.

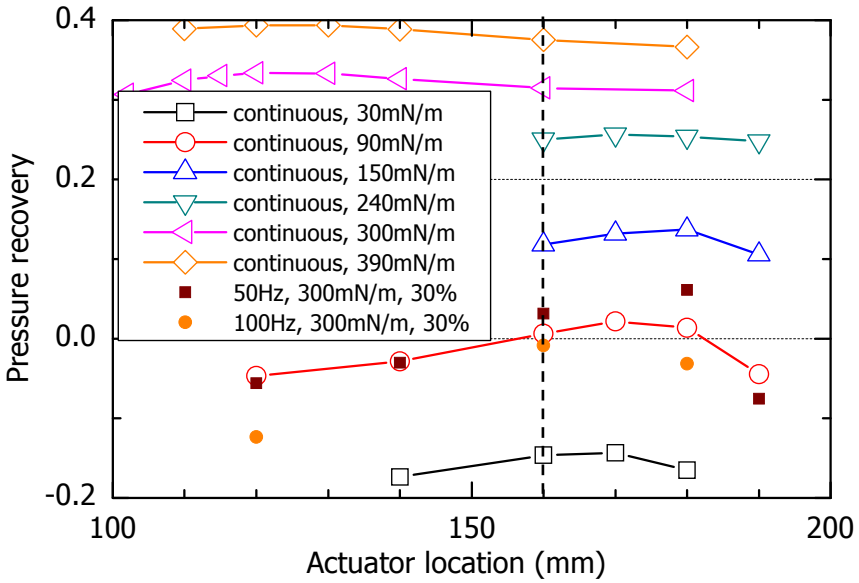

Figure 4.10: Effect of actuator location

As for the pulsed actuation, the effect of actuator location is illustrated for two series with different actuation frequencies (50 and 100 Hz), 300 mN/m, duty cycle of 30%. It is observed that 50 Hz is the optimal actuation frequency for pulsed actuation, which will be discussed later. From Figure 4.10, the optimal location for pulsed actuation is also near the separation point, which is similar to those for continuous actuation at low strength. As mentioned previously, the pulsed actuation works by exciting the resonant structures in the separated boundary layer separation to enhance the flow mixing between outer high-momentum and inner low-momentum flows. If the actuator is far upstream of the separation point, the resonant structures will not be sufficiently excited, while the flow mixing is only limited inside the separation region if the actuator is far downstream. At each investigated location the pulsed actuation with optimal frequency of 50 Hz is better than that with 100 Hz. To compare different actuation modes (*e.g.*, continuous vs. pulsed actuation) in the experiment, the power consumption is used. However, this parameter (integral of the product of instantaneous force and velocity) is difficult to achieve for CFD simulations in this study, because velocity is always varying in the flow with pulsed actuation. Instead the effective strength (for pulsed actuation the effective strength is the product of strength and duty cycle) as a representative of power consumption is adopted. Thus, the two pulsed actuation cases in Figure 4.10 have an effective strength of 90 mN/m. If one compares their effects on pressure recovery with that of the continuous actuation at the same effective strength of 90 mN/m, the pulsed actuation with 50 Hz is better than the continuous actuation, while the actuation with 100 Hz is worse. This demonstrates that the frequency of the pulsed actuation is very important. The detailed comparison will be presented later.

4.2.2 Effect of Actuator Strength

The effect of actuator strength is shown in Figure 4.11 for continuous actuation at x = 180 mm, which is in the region of optimal actuator locations determined from Figure 4.10. In this figure, the pressure recovery is shown to increase with actuator strength for continuous actuation. The reduced separation size by plasma actuation corresponds to the larger pressure recovery.

However, at higher strength the effect of plasma actuator strength on the recovery is smaller, since the separation is almost suppressed and the associated pressure loss is difficult to be minimized further. In other words, it is better to control the separation to a certain size, instead of fully suppressed.

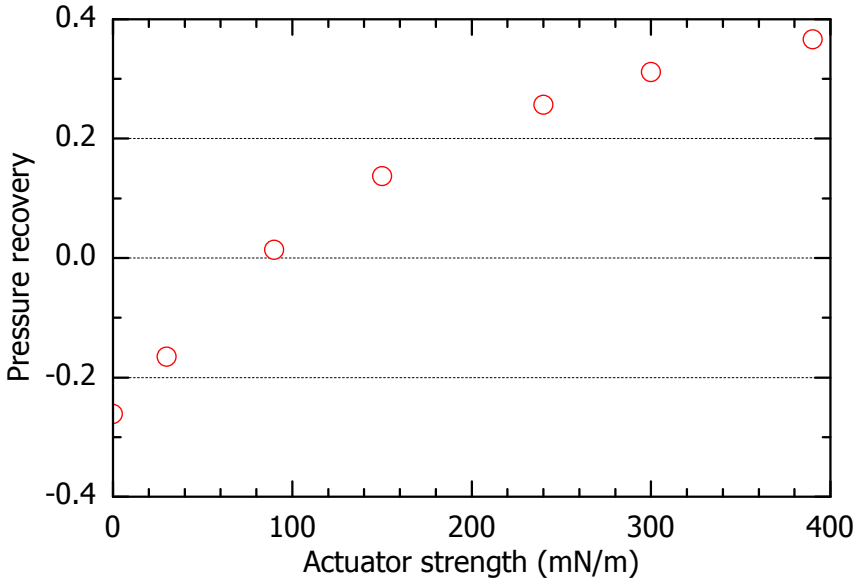

Figure 4.11: Effect of actuator strength

The contours of time-averaged axial velocity for cases of continuous actuation with different strengths are shown in Figure 4.12. The effect of actuator strength is also indicated by the separation bubble size as shown in the same figure. The separation bubble size is reduced with increased actuator strength. With continuous actuation at 390 mN/m, the boundary layer separation is completely suppressed. As observed from the 40 m/s axial velocity contour in Figure 4.12, the higher separation control effectiveness (larger separation reduction) leads to the higher axial velocity at the diffuser throat due to the assigned boundary conditions (refer to discussion in Section 3.1.2).

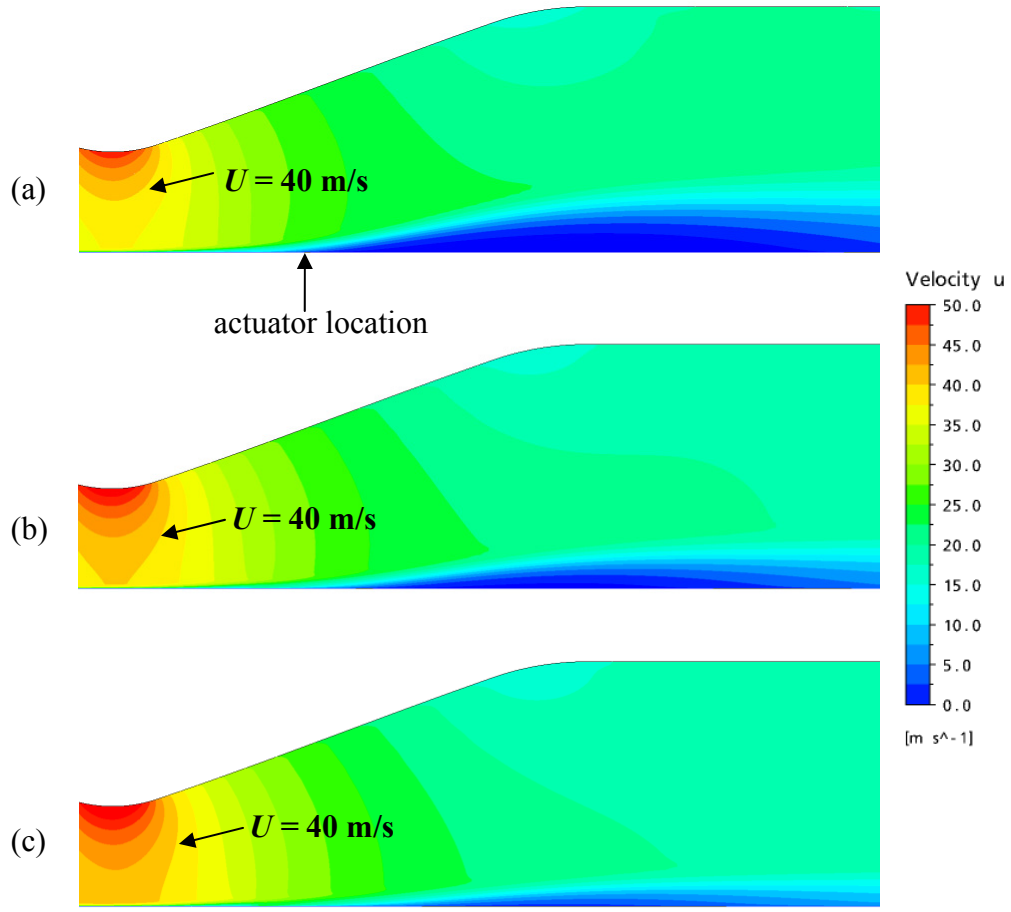

Figure 4.12: Contours of time-averaged axial velocity with continuous actuation at 180 mm: (a) 90 mN/m, (b) 240 mN/m, (c) 390 mN/m

4.2.3 Effect of Duty Cycle

The duty cycle for pulsed actuation at a specific actuator strength has an important effect on the suppression of boundary layer separation and the associated pressure recovery, as shown in Figure 4.13. Generally, the pressure recovery increases with duty cycle for both actuator strengths.

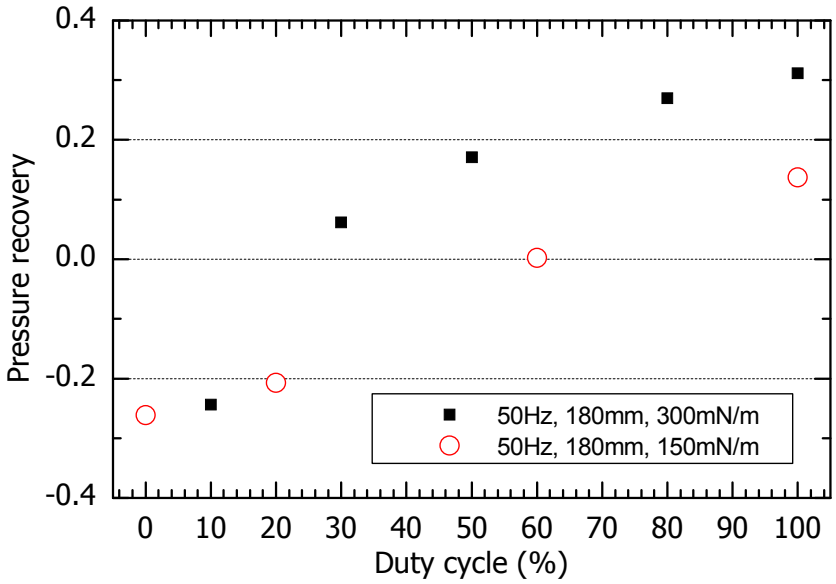

Figure 4.13: Effect of duty cycle in pulsed mode at 180 mm, 50 Hz

To better demonstrate the effect of duty cycle in pulsed mode, Figure 4.14 shows the time evolution of axial velocities with pulsed actuation at monitor point 1 for different duty cycles at 300 mN/m, 180 mm, 50 Hz. The *x*-axis variable "time" is referred to the percentage of pulsed actuation cycle. Time 0% and 100% thus are for the same phase. The flow with pulsed actuation is shown to periodically fluctuate with the applied actuation frequency. The periodic fluctuation implies that the flow with pulsed actuation is more organized or the large-scale structures with the frequency of 50 Hz within the boundary layer are amplified. The applied duty cycle, *i.e.*, the period when plasma actuator is on, corresponds to the interval between minimum and maximum axial velocity, as shown in Figure 4.14 for the pulsed actuation with a duty cycle of 80%. The axial velocity increases dramatically after the plasma is turned on (near the minimum axial velocity) and then it remains at a relatively constant level until the plasma is turned off (near the maximum axial velocity). Thereafter the axial velocity decreases to the minimum value to complete a cycle.

The axial velocity with larger duty cycle has a longer period of higher value, which corresponds to the better control effect as shown in Figure 4.14. However, for the case with 10%

duty cycle, the induced higher axial velocity is followed by a large reverse flow. This larger reverse flow corresponds to the worse performance of pulsed actuation at effective strength of 30 mN/m, as shown in Figure 4.14, which is even worse than no control.

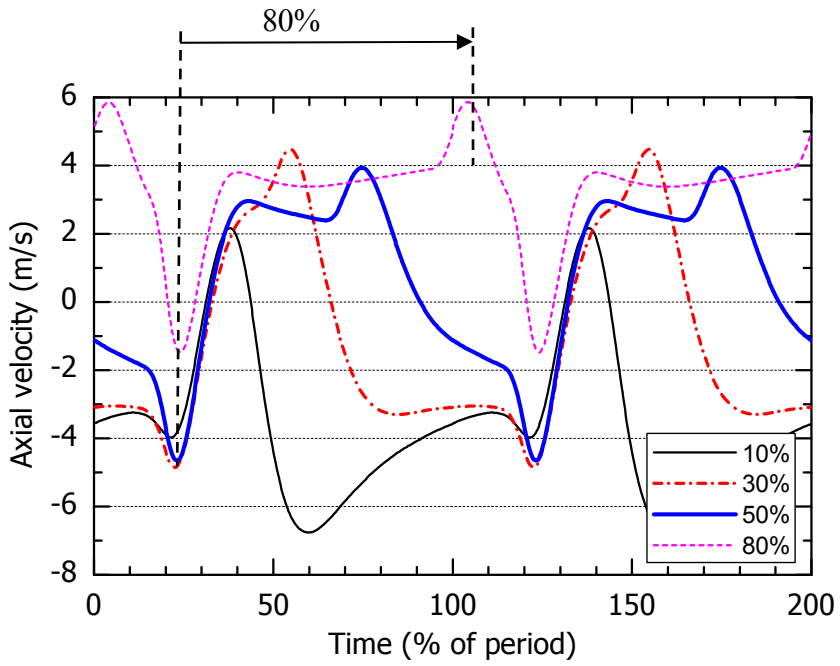

Figure 4.14: Time evolution of axial velocities with actuation for different duty cycles (x = 180 mm, 300 mN/m, 50 Hz) at monitor point 1

4.2.4 Effect of Pulsed Actuation Frequency

This section studies the effect of actuation frequency in pulsed mode for actuator location at x = 160 mm, strength of 300 mN/m and duty cycle of 30%. The pressure recovery factors at different actuation frequencies are plotted in Figure 4.15. From this figure, the optimal actuation frequency is observed around 50 Hz. The effect of pulsed actuation is dramatically reduced when the actuation frequency is higher than 100 Hz. This has been shown in Figure 4.15, where the pulsed actuation with 100 Hz is even worse than continuous actuation for the same effective actuator strength. However, there seems to be another locally effective frequency around 120 Hz. This frequency is about twice of the optimal frequency of 50 Hz, if we consider that the investigated frequencies are discrete.

The dimensionless frequency, $F^+ = fL_{se}/U_\infty$, corresponding to the most effective frequency of 50 Hz is 0.56 (based on a reattachment length – a distance between separation and reattachment points – L_{se} = 0.305 m and a freestream velocity at the separation point of U_∞= 27 m/s without actuation). The definition of the reference length scale and velocity is based on the work of Kiya *et al.* (1997). This frequency corresponds to the shedding-type instability in the flow (shedding of large-scale vortices from the separation bubble), which has a dimensionless frequency around 0.5 (Kiya *et al.*, 1997). This is because the mechanism which determines the most effective actuation frequency is the shedding-type instability. The most effective frequency of 50 Hz in the present study is consistent with the results of other researchers that show the optimal frequency for boundary layer separation control is $F^+ \sim O(1)$ (Cierpka *et al.*, 2007; Herbst and Henningson, 2006).

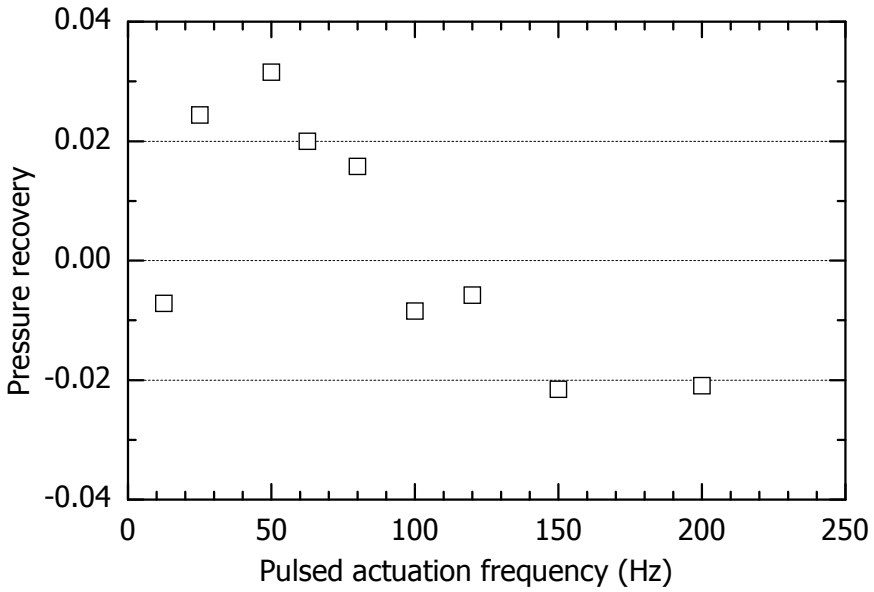

Figure 4.15: Effect of actuation frequency in pulsed mode at 160 mm, 300 mN/m, 30% duty cycle

To further investigate the effect of pulsed actuation frequency, time-averaged turbulent kinetic energy distribution in the plane of monitor point 1 with pulsed actuation at 160 mm, 300 mN/m, duty cycle of 30% is shown in Figure 4.16 for different actuation frequencies. Turbulent

kinetic energy can be used to quantify the mixing level in the flow and thus assess the effect of different actuation frequencies. From Figure 4.16, pulsed actuation at the optimal frequency of 50 Hz is associated with the maximum peak turbulent kinetic energy. In other words, the turbulent structures in the flow are most amplified for this optimal frequency, and the flow mixing between outer high-momentum and inner low-momentum fluids is most enhanced.

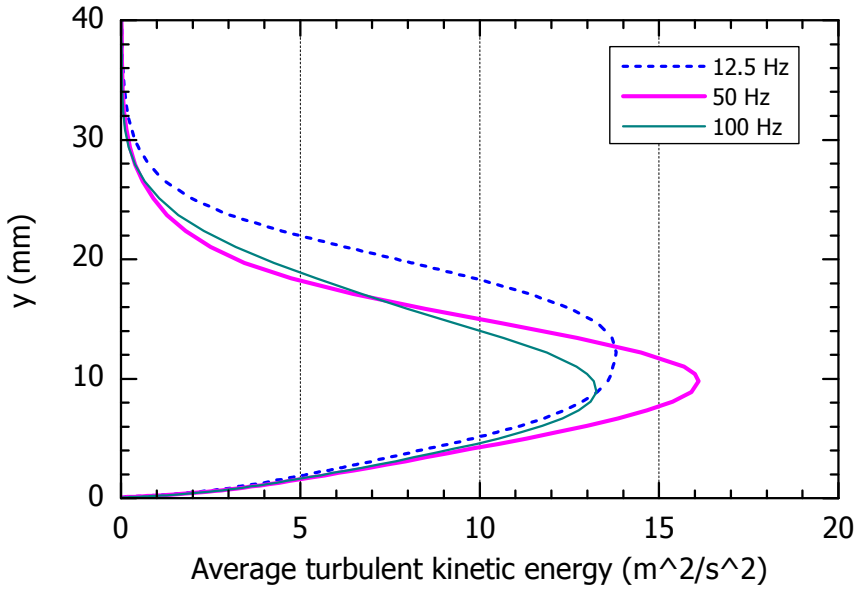

Figure 4.16: Time-averaged turbulent kinetic energy distribution in the plane of monitor point 1 for different actuation frequencies (x = 160 mm, 300 mN/m, 30% duty cycle)

4.2.5 Effect of Power Consumption

The effect of power consumption for continuous actuation can be regarded as the effect of actuator strength, as shown in Figure 4.11. However, for pulsed actuation it should be regarded as the effect of effective actuator strength, as introduced previously in Section 4.2.1. The associated results for both continuous and pulsed actuations are shown in Figure 4.17.

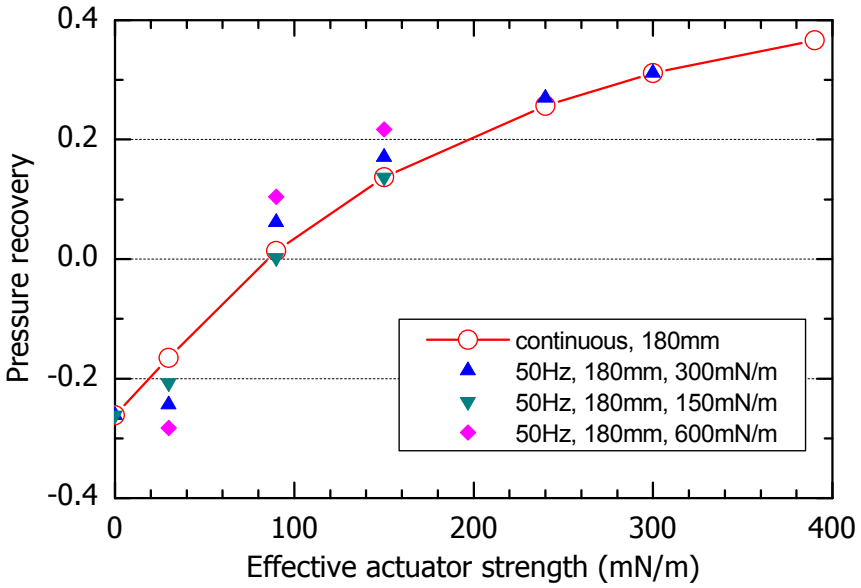

Figure 4.17: Effect of power consumption

In this figure, it is shown that the pressure recovery increases with effective actuator strength. For the same effective actuator strength, different actuator strengths or duty cycles have different pressure recoveries. The control effectiveness of pulsed actuation at higher effective actuator strength is better than that of the continuous actuation. However, the control effectiveness of pulsed actuation at low effective strength is worse than that of the continuous actuation. For example, the pressure recovery for all cases at effective strength of 30 mN/m is lower than that with continuous actuation. For the case with 600 mN/m, 180 mm, 50 Hz, duty cycle of 5%, the pressure recovery is even lower than that without actuation.

To further investigate the effect of actuator strength/duty cycle at the same effective strength, the pressure recovery versus duty cycle in pulsed mode at x = 180 mm, 50 Hz is used as shown in Figure 4.18. For each constant effective actuator strength, the duty cycle changes inversely with the actuator strength since the effective actuator strength is the product of actuator strength and duty cycle. The corresponding time evolution of axial velocities at monitor point 1 (see Figure 4.9) is shown in Figure 4.19.

As shown in Figure 4.18, for the effective strength of 30 mN/m, the pressure recovery

increases with duty cycle. In other words, the continuous actuation (duty cycle of 100%) at this effective strength is the best. It should be noted that the pressure recovery at this low effective actuator strength is almost constant when the duty cycle is more than 40%, as can be explained by the long period of relatively constant higher axial velocity shown in Figure 4.19(a) for duty cycle of 50% and 75%. The worse performance for low duty cycle (*e.g.,* 5%) can also be explained referring to Figure 4.19(a). The lower duty cycle corresponds to a higher actuator strength, which can induce higher axial velocity. However, the pulsed actuation with 5% duty cycle induces a larger reverse flow, caused by local high momentum addition over a very short period, even though it may induce large fluctuations. The actuation with low duty cycle resembles more a pulse-based flow control device, which is shown here not to be a good choice to control the turbulent boundary layer separation.

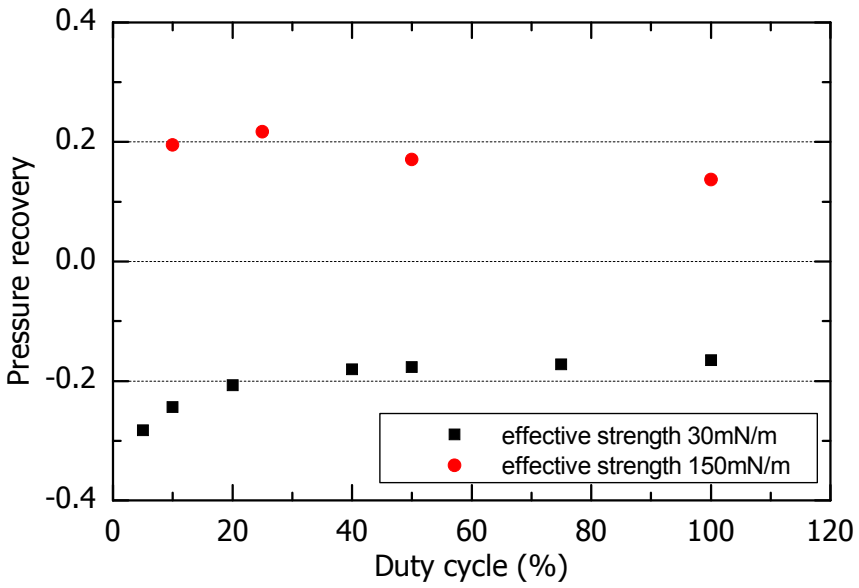

Figure 4.18: Effect of duty cycle in pulsed mode at 180 mm, 50 Hz

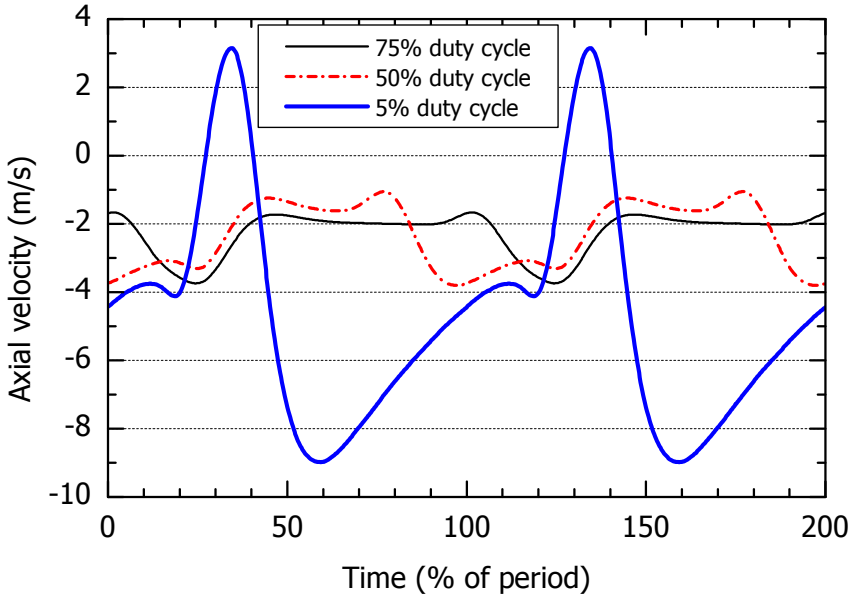

(a) Effective strength of 30 mN/m

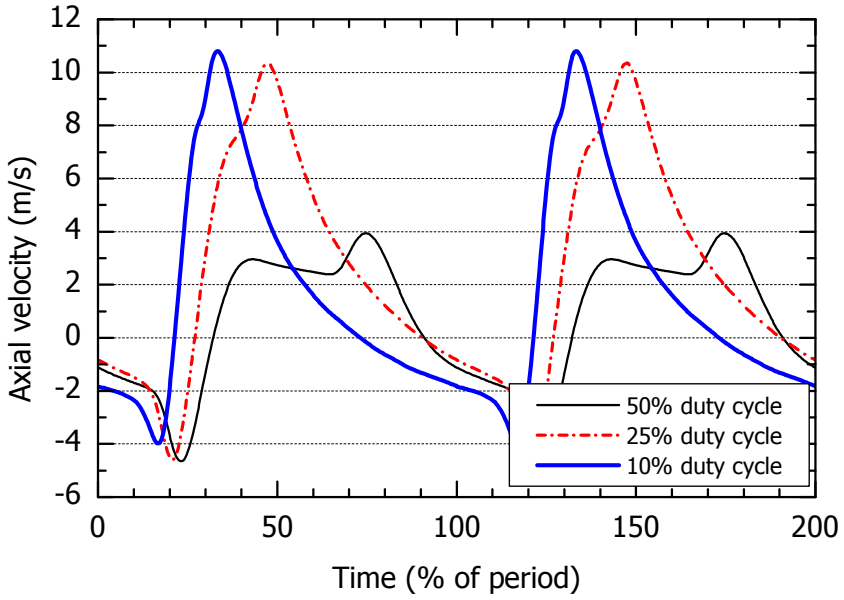

(b) Effective strength of 150 mN/m

Figure 4.19: Time evolution of axial velocities at monitor point 1 with actuation at 180 mm, 50 Hz.

In contrast, as shown in Figure 4.18, when the effective strength is increased to 150 mN/m, the pulsed actuation with any investigated duty cycle is better than the continuous actuation. The duty cycle of 25% is the best, which corresponds to the longest period of high axial velocity in

Figure 4.19(b). However, the control effectiveness of the pulsed actuation with a duty cycle of 50% is closer to that of the continuous actuation. The plot for this case in Figure 4.19(b) shows a longer period of relatively lower constant axial velocity, which deteriorates the effectiveness of pulsed actuation by reducing flow mixing.

The above discussion suggests that the optimal flow control in terms of power consumption corresponds to a combination of a high enough actuation strength and a proper duty cycle. Generally, as seen from Figure 4.18, for optimum efficiency in terms of effectiveness versus effective actuator strength (power consumption), the appropriate duty cycle for pulsed actuation should be chosen between 10% and 50%, which agrees with the observation of Visbal *et al.* (2006).

4.3 Determination of Design Rules

This part presents the results of the work on quantitative design rules based on the set of CFD simulations and proper parametric non-dimensionalization. These design rules can be used to estimate required actuator strength for suppressing turbulent boundary layer separation with continuous plasma actuation. The generic geometry for the numerical simulations is shown in Figure 3.6. With this type of geometry, the diffuser divergence angle α can be varied to generate different adverse pressure gradients, and the diffusing length can be modified to induce different separation bubbles in terms of length and location. In addition, by specifying a no-slip length upstream of the diffuser entrance (the start of the diffusing section), different boundary layer shape factors at the diffuser entrance and thus different boundary layer separation features (*e.g.*, separation-reattachment length) in the diffuser can also be obtained.

The first step involves obtaining the relevant dimensionless parameters with which to plot the data in search of the design rules, through an integral boundary layer approach. In other words, Equation (3.1) is split into a set of simpler equations, each of which depends on a single

dimensionless number.

The integral momentum equation for 2-D, incompressible boundary layer is

$$\frac{d(U^2\theta)}{dx} = \frac{\delta^*}{\rho}\frac{dP}{dx} + \frac{\tau_0}{\rho} \tag{4.2}$$

where displacement thickness δ^* , momentum thickness θ and shear stress at the wall τ_0 are defined as

$$\delta^* = \int_{y=0}^{\infty}(1-\frac{u}{U})dy$$

$$\theta = \int_{y=0}^{\infty}\frac{u}{U}(1-\frac{u}{U})dy \tag{4.3}$$

$$\tau_0 = \mu\left.\frac{\partial u}{\partial y}\right|_{y=0}$$

with U being the mainstream flow velocity just outside the boundary layer.

The integral momentum equation will be applied to establish the relationship between the boundary layers with and without actuation, as shown in Figure 4.20. In the "*no control*" case, the boundary layer naturally develops and finally a flow separation occurs due to the adverse pressure gradient. However, in the "*with actuation*" case, the boundary layer is changed as a result of the momentum input. The separation point is also delayed. In terms of nomenclature, the point labeled "*1*" represents a far upstream location, where the flow is assumed unchanged by actuation. The points labeled "*act*", "*cal*", and "*sep*" represent the actuation, calculation and separation points in the flow without control, respectively, while the "*act'* ", "*cal'* ", and "*sep'* " are the corresponding points in the flow with actuation, with the actuation and calculation points remaining at the same locations for the no-control and with-control cases. The calculation point is the downstream end of the body force region or the location with maximum induced velocity in quiescent air, which for the present simulations is located 1 cm downstream of the actuation

point (as shown in Figure 1.5, the actuation point or actuator location corresponding to the trailing edge of the exposed electrode).

For the no-control case, the Equation (4.2) is integrated from "*1*" to "*cal*".

$$U^2\theta\Big|_1^{cal} = \int_1^{cal} \left(\frac{\delta^*}{\rho}\frac{dP}{dx} + \frac{\tau_0}{\rho}\right)dx \tag{4.4}$$

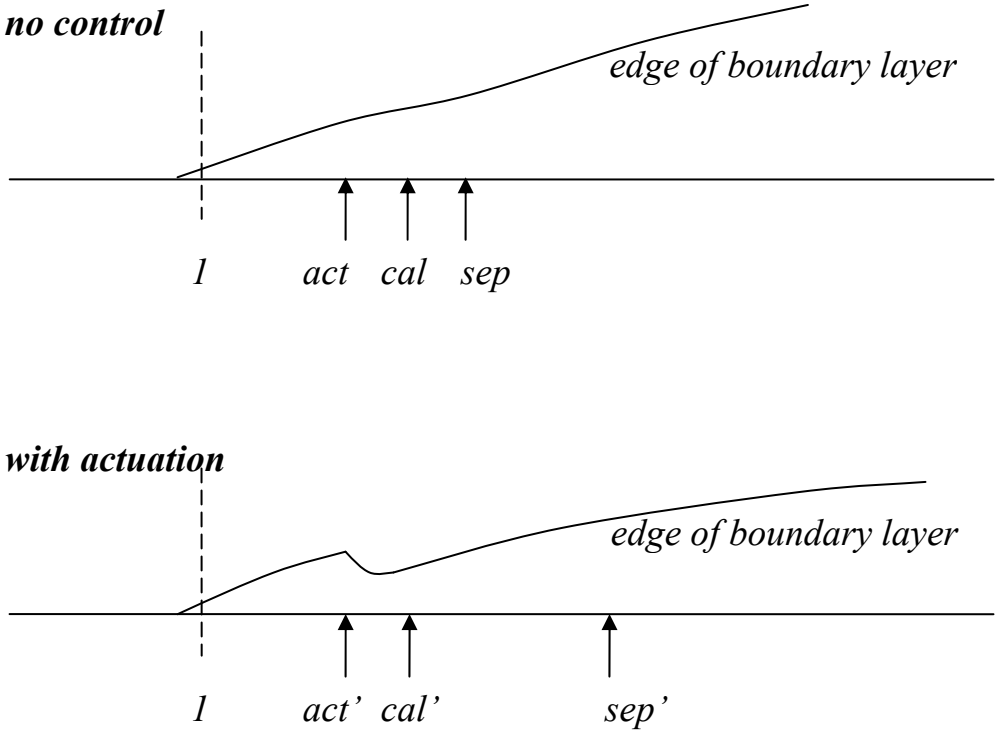

Figure 4.20: Boundary layers with and without actuation

For the case with actuation, Equation (4.2) is first integrated from "*1*" to "*cal'* " with the inclusion of an external force in the *x*-direction (F_x) representing the plasma actuator strength and subsequently from "*cal'* " to "*sep'* ".

$$U^2\theta\Big|_1^{cal'} = \int_1^{cal'} (\frac{\delta^*}{\rho}\frac{dP}{dx} + \frac{\tau_0}{\rho})dx - \frac{F_x}{\rho} \tag{4.5}$$

$$U^2\theta\Big|_{cal'}^{sep'} = \int_{cal'}^{sep'} (\frac{\delta^*}{\rho}\frac{dP}{dx} + \frac{\tau_0}{\rho})dx \tag{4.6}$$

Equation (4.6) can be rewritten as

$$U^2\theta\Big|_{sep'} - U^2\theta\Big|_{cal} + (U^2\theta\Big|_{cal} - U^2\theta\Big|_{cal'}) = \int_{cal'}^{sep'} (\frac{\delta^*}{\rho}\frac{dP}{dx} + \frac{\tau_0}{\rho})dx \tag{4.7}$$

Ⅰ － Ⅱ ＋ Ⅲ ＝ Ⅳ

In Equation (4.7), term Ⅱ is a known value from the no-control case. However, the other three terms related to actuation are unknown and need to be predicted based on the information obtained from no-control flow, which will be shown as follows.

First, the unknown terms Ⅰ, Ⅲ and Ⅳ in Equation (4.7) are obtained by dimensional analysis as:

$$\text{Ⅰ}a: \quad \frac{U_{sep'}}{U_{act}} = f(\frac{((KE_{act} - (P_{sep'} - P_{act'}))*2/\rho)^{0.5}}{U_{act}}) \tag{4.8a}$$

$$\text{Ⅰ}b: \quad \frac{\theta_{sep'}}{\theta_{act}} = f([\delta^*_{act}(P_{sep'} - P_{act'})/\rho]) \tag{4.8b}$$

$$\text{Ⅲ}: \quad [U^2\theta\Big|_{cal} - U^2\theta\Big|_{cal'}] = f([F_x/\rho]) \tag{4.8c}$$

$$\text{Ⅳ}: \quad [\int_{cal'}^{sep'} (\frac{\delta^*}{\rho}\frac{dP}{dx} + \frac{\tau_0}{\rho})dx] = f([U^2\theta\Big|_{sep'} - U^2\theta\Big|_{cal'}]) = f([\frac{\delta^*_{act}}{\rho}(P_{sep'} - P_{cal'})]) \tag{4.8d}$$

where [ ] means normalized by $(U^2\theta)_{act}$, and $KE_{act} = (0.5\rho U^2)_{act}$. It should be noted that Equation (4.8a) is based on the Bernoulli's equation $P + 0.5\rho U^2 = constant$ (constant total

pressure along the boundary layer edge/interface of core flow and boundary layer), while Equation (4.8c) is based on the equation obtained by the subtraction of Equation (4.4) and (4.5). Equation (4.7) normalized by $(U^2\theta)_{act}$ and Equations (4.8a)-(4.8d) are the simplified dimensionless equivalent of Equation (3.1).

The forms of the dimensionless independent variables on the right hand side of Equations (4.8a) to (4.8d) are obtained through trial and error so as to best collapse the data from simulations. The collapsed results are shown in Figures 4.21-4.24. In Figures 4.21, 4.23 and 4.24, the *y*-axis corresponds to the exact values from simulations with actuation, while the *x*-axis corresponds to the predicted value based on only the no-control simulation (in other words, the left hand sides versus the right hand sides of Equations (4.8a), (4.8c) and (4.8d)). Ideally, the relation is $y=x$. In Figure 4.22, an attempt is made to relate *y* and *x* with a simple linear function. In the establishment of design rules, the pressure is an important parameter, especially for the cases with actuation, as shown in Equation (4.8). However, the pressure with actuation is unknown and must be predicted from the no-control case (or the inviscid simulation). For the no-control case, the pressure downstream of the separation point is almost constant (reduced pressure recovery resulting from the separation) and thus differs greatly from that with actuation (increased pressure recovery due to suppression of boundary layer separation). On the other hand, the pressure from the inviscid simulation is close to that with actuation (assuming that the boundary layer upstream of separation are thin and its blockage to the core flow is small), which will be shown later, and is adopted in this part. Thus all the static pressure distribution in the current study is obtained from the inviscid simulation (without actuation), in which both top and bottom wall are set as free-slip, and $P_{act'} = P_{act}$, $P_{cal'} = P_{cal}$. In all the simulated cases, the actuation location corresponds to boundary layer shape factor $H \equiv \delta^*/\theta = 2.5$. This shape factor generally corresponds to a location near the separation point of turbulent boundary layers. The freestream turbulence intensity *I* is very low and its effect is negligible in this case.

The empirical relations obtained from curve fitting in Figures 4.21-4.24 are as follows:

$$\text{I}\,a: \quad \frac{U_{sep'}}{U_{act}} = 0.93\frac{((KE_{act} - (P_{sep'} - P_{act'})) * 2/\rho)^{0.5}}{U_{act}} + 0.07 \tag{4.9a}$$

$$\text{I}\,b: \quad \frac{\theta_{sep'}}{\theta_{act}} = 1.75[\delta^*_{act}(P_{sep'} - P_{act'})/\rho] + 1.0 \tag{4.9b}$$

$$\text{III}: \quad [U^2\theta\big|_{cal} - U^2\theta\big|_{cal'}] = [F_x/\rho] \tag{4.9c}$$

$$\text{IV}: \quad [\int_{cal'}^{sep'}(\frac{\delta^*}{\rho}\frac{dP}{dx} + \frac{\tau_0}{\rho})dx] = [U^2\theta\big|_{sep'} - U^2\theta\big|_{cal'}] = [\frac{\delta^*_{act}}{\rho}(P_{sep'} - P_{cal'})] \tag{4.9d}$$

These four predicted terms are then replaced into Equation (4.7), as plotted in Figure 4.25. From this figure, most of the points located near the ideal line $y=x$, except several points in cases with a 25 degree diffuser divergence angle. These points correspond to the separation points near the diffuser exit. This relatively large deviation of y at high values of x in Figure 4.25 mainly results from the deviation of $U_{sep'}/U_{act}$ in Figure 4.21 and $\theta_{sep'}/\theta_{act}$ in Figure 4.22, where the predicted value is lower than the exact value.

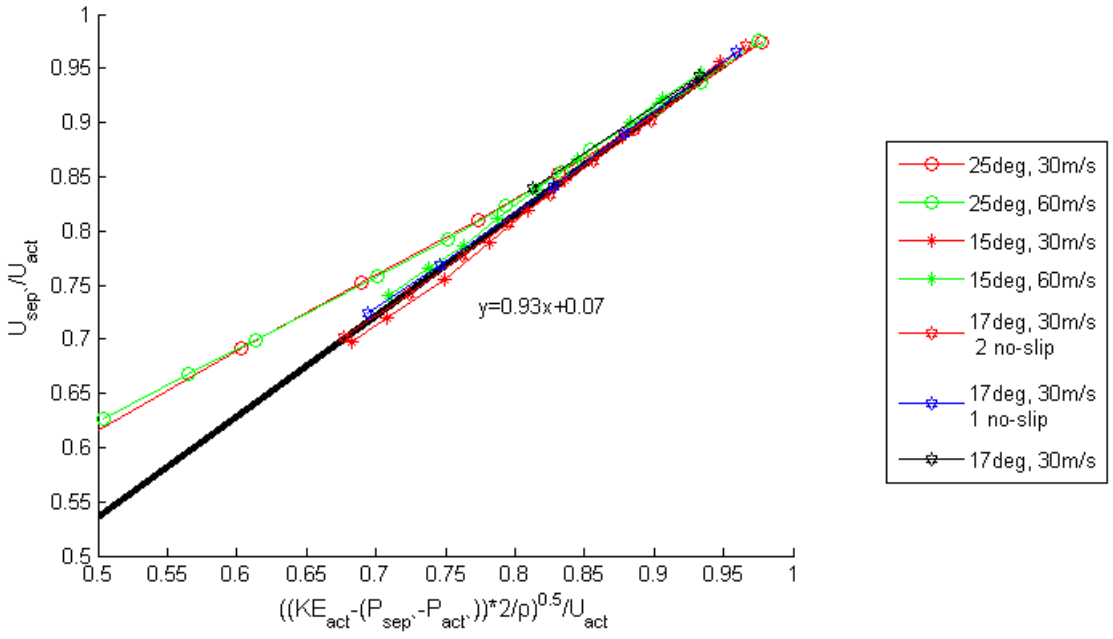

Figure 4.21: Prediction of term I a in Equation (4.7)

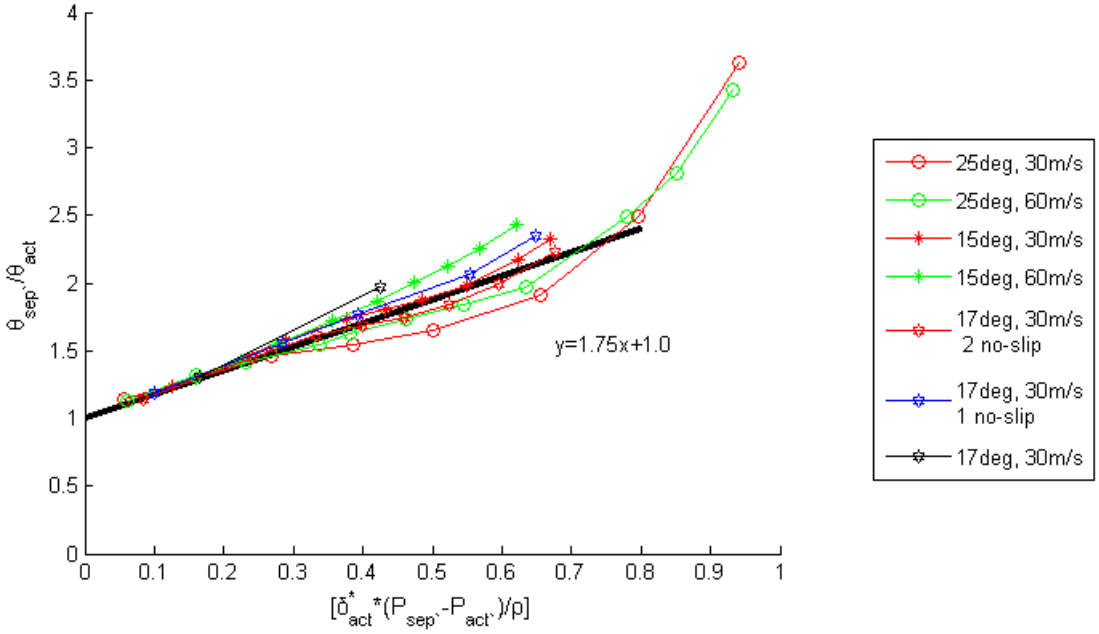

Figure 4.22: Prediction of term Ⅰb in Equation (4.7)

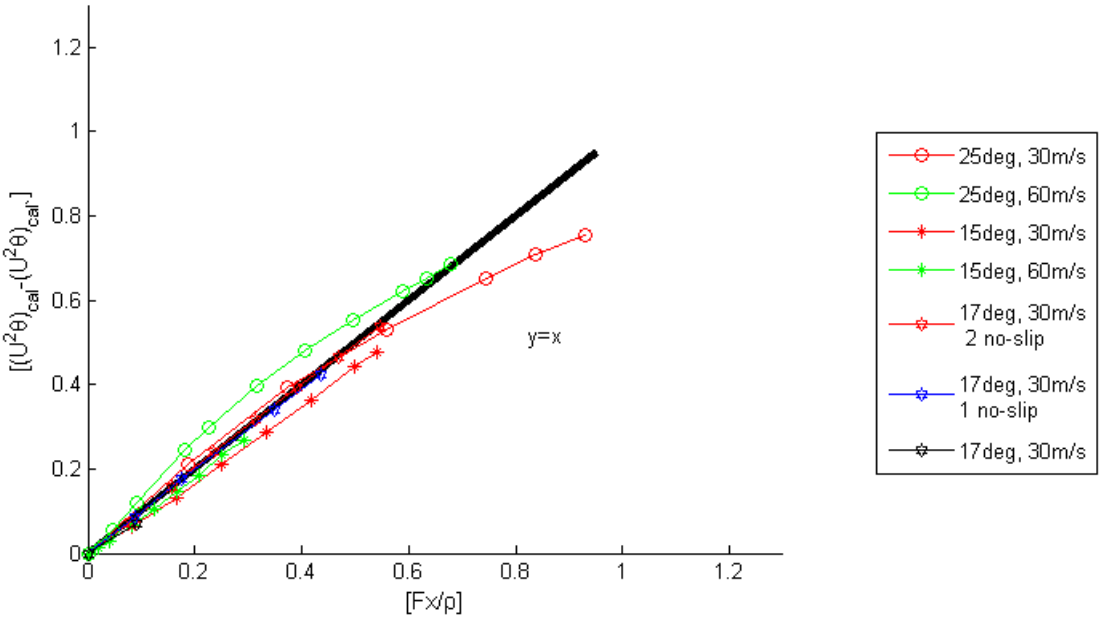

Figure 4.23: Prediction of term Ⅲ in Equation (4.7)

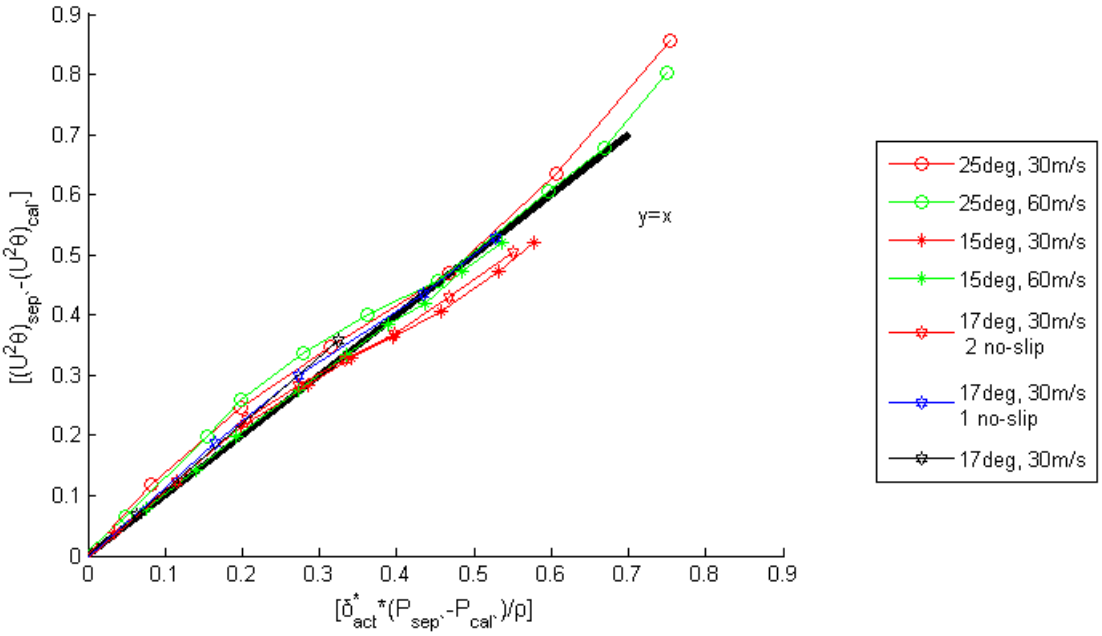

Figure 4.24: Prediction of term Ⅳ in Equation (4.7)

One possible reason for the deviation is that the pressure distribution used to evaluate the non-dimensional parameters is that along the bottom wall and assumed to be the same as in the rest of the diffuser (1-D assumption), whereas there are 2-D effects in the actual geometry. For a 2-D planar diffuser, as conceptually shown in Figure 4.26, the pressure at location 2 can be estimated from the information at location 1, based on a 1-D assumption, as:

$$p_2 - p_1 = \frac{1}{2}\rho U_1^2 \left[1 - \frac{1}{(1 + \frac{\tan\alpha}{A} x)^2} \right]$$

or (4.10)

$$y = a - \frac{b}{(1+cx)^{1/d}} \qquad \begin{aligned} a &= b = 1/2\rho U_1^2 \\ c &= \tan\alpha / A \\ d &= 0.5 \end{aligned}$$

Figure 4.27 shows the pressure distribution from the inviscid simulation and 1-D calculation

from the actuation point to the diffuser exit. Here, the pressure rise is relative to the actuator location. For the case with $15°$ and 30 m/s (freestream velocity at the diffuser entrance), the pressure distributions match well, except for a small region near the diffuser exit, due to 2-D effects caused by transition from divergence angle $15°$ to $0°$. For the case with $25°$ and 30 m/s, the simulated pressure rise (inviscid) is higher than 1-D calculation; however this trend is decreasing near the diffuser exit. The difference in pressure distribution due to 2-D effects, especially for the case in Figure 4.27(b), explains the deviation in $\theta_{sep'}$ from the linear curve fit seen in Figure 4.22. In Figure 4.27(b), the pressure distribution (from the actuation point to new separation point) for the viscous simulation with actuation is also plotted. One can observe that the viscous curve with actuation and inviscid curve match well over a large portion of the distance between the actuator and diffuser exit, thus suggesting that the pressure from the inviscid simulation can be used for the establishment of design rules.

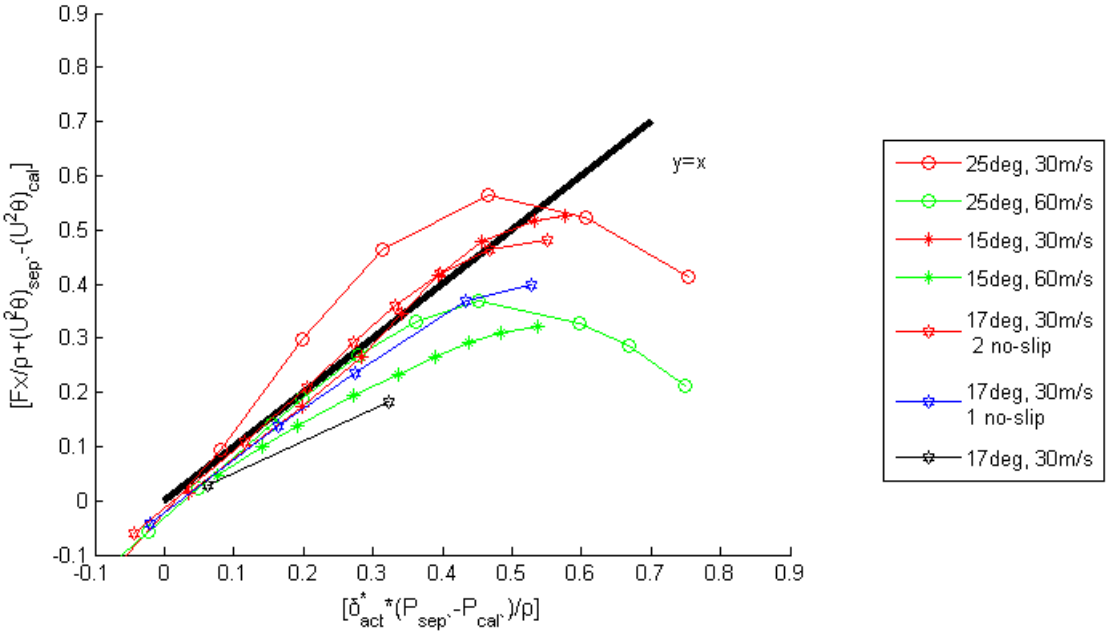

Figure 4.25: Prediction of final equation (left hand side versus right hand side of Equation (4.7))

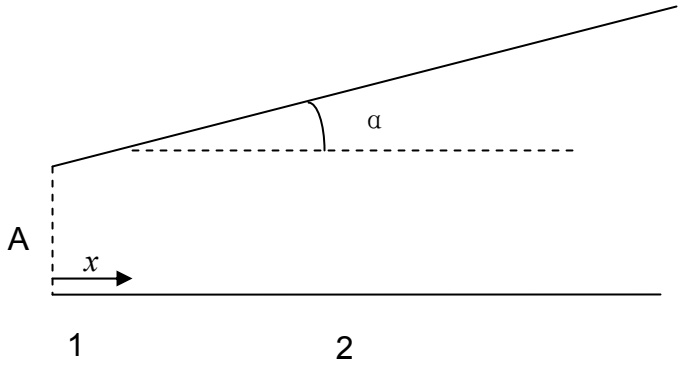

Figure 4.26: 2-D planar diffuser

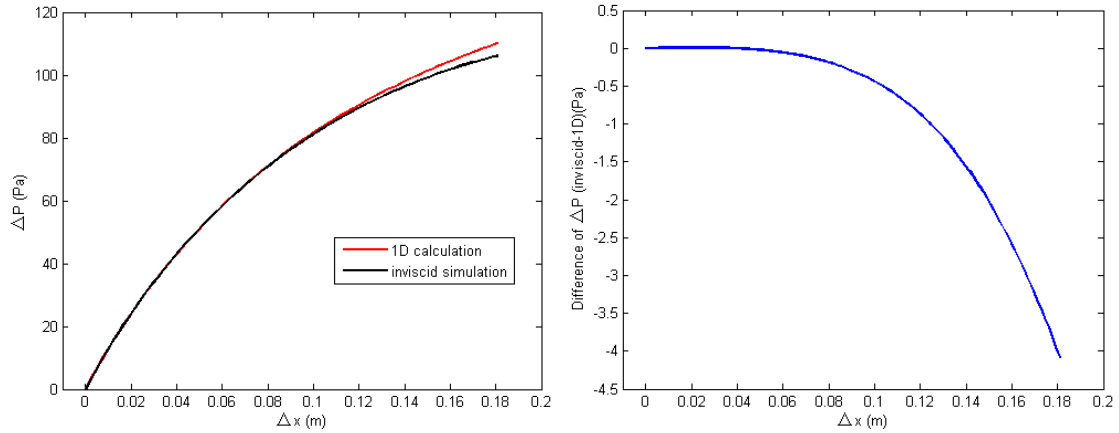

(a) 15 deg, 30 m/s

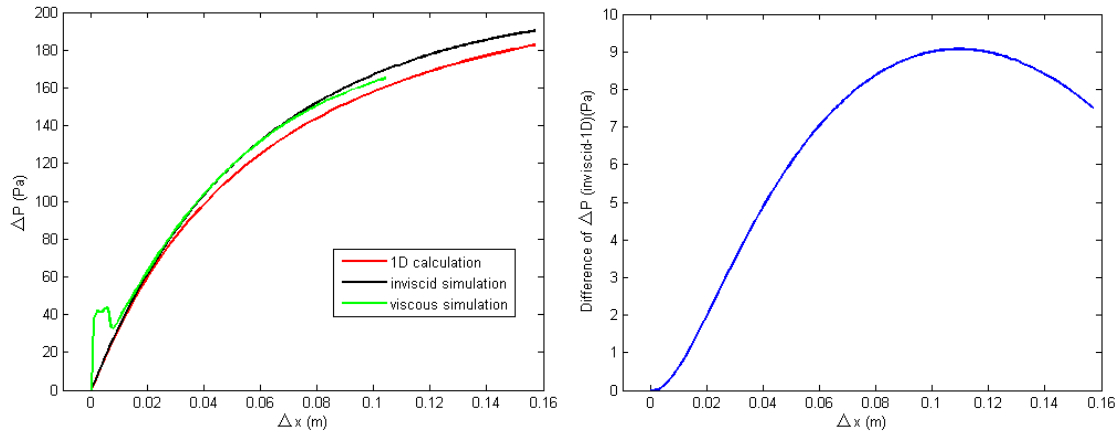

(b) 25 deg, 30 m/s

Figure 4.27: Comparison of pressure distributions in different ways (left- pressure distribution; right- pressure difference between inviscid simulation and 1-D calculation)

To use the design rule obtained above, the following steps are recommended:

1) Obtain KE_{act}, U_{act}, U_{cal}, ρ, δ^*_{act}, θ_{act}, θ_{cal} and term Ⅱ of Equation (4.7) from the uncontrolled flow,
2) Obtain $P_{act'}$, $P_{cal'}$, $P_{sep'}$ from the pressure distribution of an inviscid simulation,
3) Obtain the term Ⅰ of Equation (4.7) through computing $U_{sep'}$ and $\theta_{sep'}$ by Equations (4.9a) and (4.9b), respectively,
4) Compute the term Ⅳ of Equation (4.7) by Equation (4.9d),
5) Compute the required actuator strength F_x via Equation (4.9c).

4.4 Summary

In this numerical study on separation control in 2-D diffusers, the effects of plasma actuation have been investigated. Plasma actuation can reduce turbulent boundary layer separation in both continuous and pulsed modes. The optimal actuator location is generally close to the boundary layer separation point. In the pulsed mode, the actuation with an optimal actuation frequency, corresponding to a dimensionless frequency of the order of one, is found to most effectively suppress the turbulent separation. The effectiveness of turbulent boundary layer separation suppression increases with pulsed actuation duty cycle. However for optimum efficiency in terms of effectiveness versus power consumption, the duty cycle should be kept between 10% and 50%. Furthermore, pulsed actuation at the optimal actuator location and frequency is found to surpass the continuous actuation for the same effective actuation strength (power consumption). In addition, a preliminary design rule for the continuous plasma actuation on turbulent boundary layer separation control is developed.

The above observation on the effects of plasma actuation will be further investigated in the experimental study in Chapter 5, especially for pulsed actuation.

Chapter 5

Experimental Study on Separation Control in 2-D Diffusers

In this chapter, the results from a 2-D experimental study, following the CFD simulations in Chapter 4, are presented. The goal of the study is to experimentally demonstrate the effectiveness of plasma actuation on boundary layer separation control, especially in the case of pulsed actuation. With the plasma actuator configuration chosen, the results from the diffuser experiments follow. First, the main results of the parametric study to optimize the plasma actuators are presented. In addition, for integral performance assessment and flow visualization, the POD method is used to extract the coherent structures in the flow with boundary layer separation and quantify the effect of flow control by plasma actuation.

5.1 Dielectric Barrier Discharge Plasma Actuators

5.1.1 DBD Plasma Actuator Design

Kapton film has been widely chosen as the dielectric material for plasma actuators used for flow control on airfoils (Enloe *et al.*, 2004; Little, 2010). From Table 2, which summarizes the characteristics of some common dielectric materials, Kapton is shown to have a medium dielectric constant (ε_r = 3.4), while its dielectric strength (E = 303 kV/mm) is approximately an order of magnitude greater than other investigated dielectric materials. The dielectric constant is the ratio of the amount of electrical energy stored in a material by an applied voltage, relative to that stored in a vacuum. To obtain a plasma force of around 30 mN/m, only a layer of 0.15 mm thick Kapton film is required, which is very beneficial for application on airfoils. This is because limited space on airfoils can be used for the implementation of the plasma actuator.

Table 2: Characteristics of various dielectric materials

Material	Density (kg/m^3)	Dielectric constant ε_r	Dielectric strength E (kV/mm)	Max operation temperature (℃)	Price	Reference
Acrylic PMMA Plexiglas®	1180	4.0	15.7	65-93	$	Boedeker Plastics
Derlin®	1410	3.7	17.7	82	$$	DuPont
Kapton®	1420	3.4	303	400	$$$$$	DuPont
Macor® Ceramic	2520	6.03	39.4	1000	$$$$$	Boedeker Plastics
PVC	1260	5.5	25.6	70	$	MakeItFrom
Teflon®	2160	2.1	11.2	260	$$$	DuPont

However, flow control at higher Reynolds numbers and in more difficult situations (*e.g.*, turbulent boundary layer separation) requires plasma actuators with actuator strength much higher than 30 mN/m. For the above plasma actuator with thin Kapton film, continually increasing the applied voltage at constant frequency will drive the plasma actuator into the filamentary/streamer mode, an undesirable condition which limits the maximum achievable force. The choice of alternative materials and thicker dielectric barrier is an efficient way to obtain higher maximum achievable force. As shown in Table 2, Teflon has a lower dielectric constant (ε_r = 2.1) compared to other dielectric materials, and it can significantly increase the maximum achievable voltage (force) before the saturation (Thomas *et al.*, 2009). However, the dielectric thickness needs to be increased, because the dielectric strength E of Teflon (11.2 kV/mm) is much lower than Kapton (303 kV/mm).

In the current study, another material, Plexiglas, is also used, even though it only has a medium dielectric constant (ε_r = 4.0) and thus less maximum achievable force compared to that

of Teflon. The main reason is that Plexiglas is stable, cheap, and offers a high strength-to-weight ratio compared to Teflon. However, the factor of maximum operation temperature should be considered for Plexiglas, even though the DBD plasma actuator corresponds to non-thermal/cold plasma. The maximum operation temperature for Plexiglas is below 100 ℃. Following a period of continuous operation (about 10 minutes), multiple dots caused by the local heating of plasma can be observed near the exposed electrode on the Plexiglas sheet surface. To resolve this issue, a layer of Kapton film (maximum operation temperature of 400 ℃) of 0.1 mm thickness is thus placed between the electrodes and Plexiglas sheet surface (see Figure 5.1) to avoid the damage to the Plexiglas surface.

Using the newly-built plasma actuator system, the effects of different operation parameters and configurations of DBD plasma actuators are studied in order to optimize them for flow control. The associated results are shown in Appendix D.

Following the parametric study presented in Appendix D, the final plasma actuator configuration is chosen as shown in Figure 5.1. The dielectric plate has a size of 305 mm long by 152 mm wide by 6.35 mm thick. While some studies recommend the use of a slight axial gap of 1-5 mm (Roth and Dai, 2006) between the exposed electrode and hidden electrode, the no/zero gap design is chosen both in the parametric study and flow control, as used by Little (2010), because it is difficult to repeat the exact specific gap size for multiple builts.

The dielectric material used in the following flow control is chosen as either Plexiglas or Teflon with 6.35 mm thick. The hidden electrode of 25.4 mm wide is connected to an AC high voltage while the fully-covered exposed electrode (Figure D.3) of 6.35 mm wide is grounded. The plasma actuator is operated at 2.5 kHz, negative sawtooth waveform. In the following presentation, the Plexiglas actuator is the default one, unless otherwise specified.

The ends of electrodes are shaped as semi-circles, and copper electrodes are flattened on the dielectric material with a hard hand ruler. This process appears to reduce the sharp points and asperities at the electrode edges that would contribute to the growth of filaments and streamers

(Roth and Dai, 2006). The exposed electrode spans less than the hidden electrode such that the plasma uniformly occurs along the exposed electrode. The electrode ends should be at least 50 mm away from each other, otherwise air breakdown may occur between the two electrodes at high applied voltages (*e.g.*, 60 kV_{pp}). In addition, the plasma actuator should not be continuously operated in filamentary mode (see Figure 5.2) for a duration longer than 20 seconds, otherwise the dielectric material may break down (see Figure 5.3), due to local high heating and high electric field.

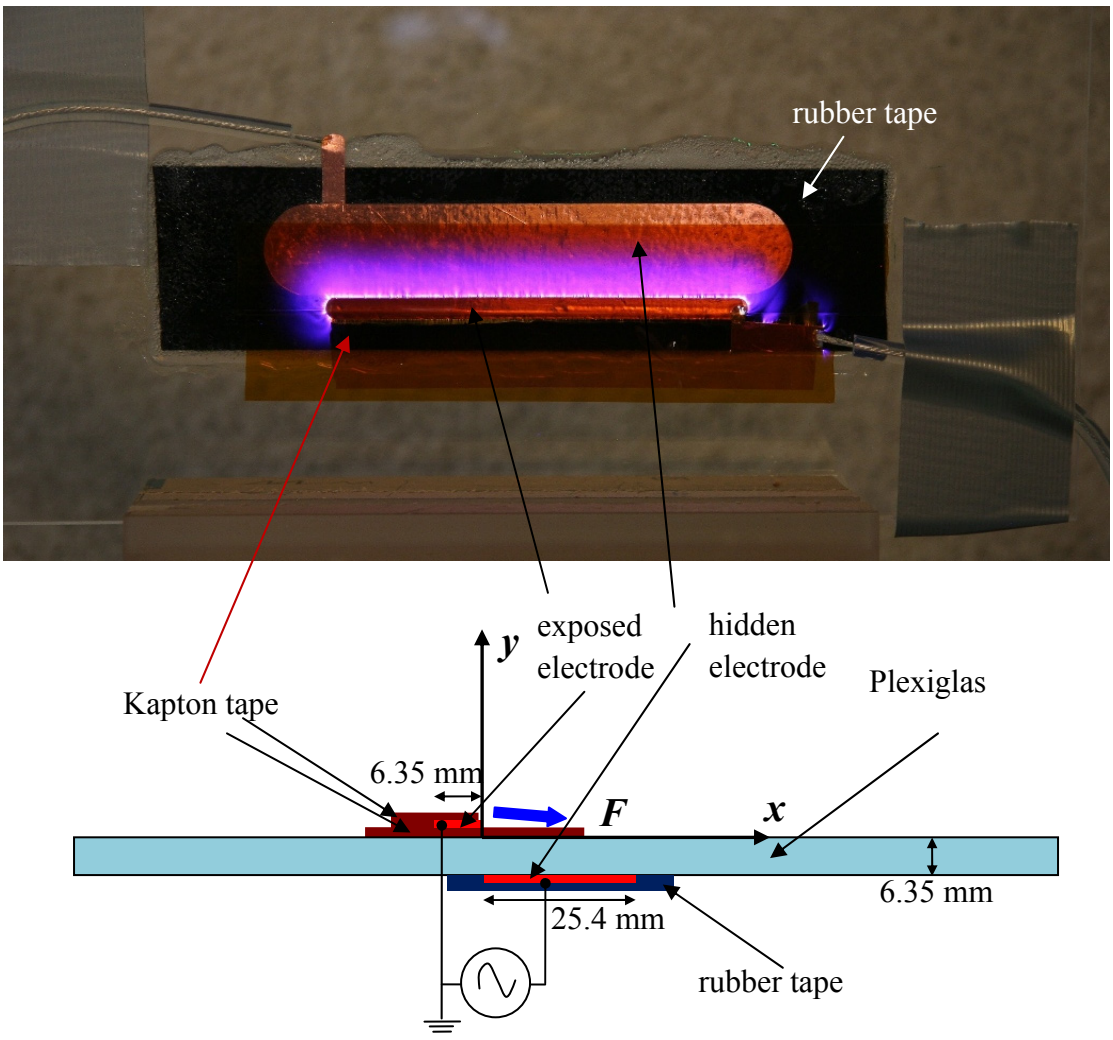

Figure 5.1: Chosen plasma actuator configuration

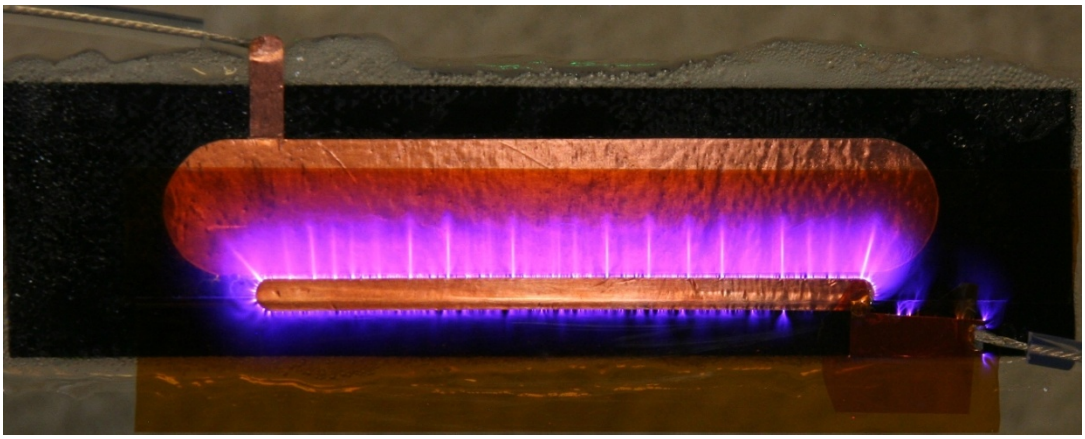

Figure 5.2: Plasma actuator operated in filamentary mode

Figure 5.3: Teflon damage due to arc formation

In addition, another configuration of DBD plasma actuator with multiple actuators should be mentioned. As discussed in the parametric study, higher actuator force normally corresponds to higher applied voltage and unstable operation (near filamentary mode), which limits the working time of plasma actuator. In contrast, the configuration of multiple actuators put in series can generate high total actuator strength while each actuator is still working at relatively low voltage. This concept will be experimentally applied on flow control in ITD ducts. More information about multiple actuators can be found in the paper by Thomas *et al.* (2009).

5.1.2 Characteristics of Plasma Actuators Selected for Flow Control

Figure 5.4 shows the relation between measured thrust and applied peak-to-peak voltage for the final plasma actuator configuration. The plasma actuator is operated continuously. From this figure, the measured thrust increases with applied AC voltage. At any specific applied voltage, Plexiglas has a higher measured thrust. Please note that the measured thrust is always smaller than the associated actuator strength (body force) as used in numerical study in Chapter 4. The difference comes from the shear stress in the opposite direction imposed by the dielectric surface where the exposed electrode is placed. Based on the work of Baughn *et al.* (2006), the shear stress covers about 15-25% of the actuator strength.

To characterize the final plasma actuator configuration in pulsed mode, its effect on a quiescent flow field is assessed with variation in modulation frequency and duty cycle. The time-averaged plasma-induced flow field from PIV measurement is shown in Figure 5.5 for different modulation frequencies, which represent those in the later application on flow control, chosen from spectral analysis without actuation. For the AC plasma cycle, the plasma actuator is operated at a frequency of 2.5 kHz, and amplitude of 52.7 kV_{pp} for negative sawtooth waveform. The duty cycle of 40 % is chosen for the modulation cycle. From Figure 5.5, a wall jet starting from the actuator (x = 0 mm) can be observed. The induced jet by pulsed plasma actuator is more diffuse for lower modulation frequency. This structure is consistent with documented wall jet experiments and simulations (Visbal and Gaitonde, 2006; Visbal *et al.*, 1998). The flow structure for higher modulation frequency is similar to continuous actuation (see Figure 5.5). The peak axial velocity in the jet increases with modulation frequency, even though the power consumption (integration of the instantaneous product of measured voltage and current) and measured thrust is almost the same (discussed later). This is because the induced flow is more concentrated at higher modulation frequency. Please note that the peak velocity is always observed between x = 10 and 20 mm for all tested DBD actuators.

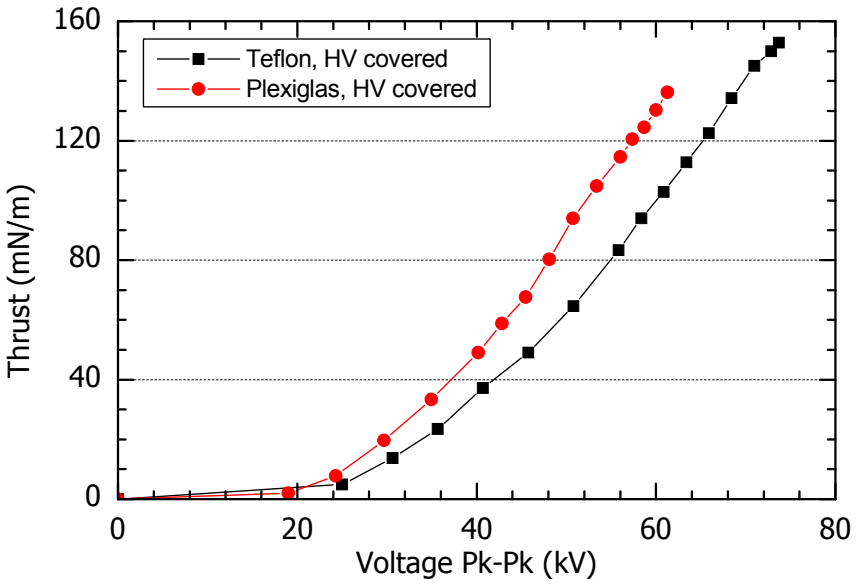

Figure 5.4: Measured thrust versus peak-to-peak voltage for final plasma actuator configuration

Another important parameter of pulsed actuation is duty cycle. The effect of duty cycle on the time-averaged induced flow field from PIV measurement is shown in Figure 5.6. The modulation frequency is chosen as 40 Hz, and other variables are chosen the same as in Figure 5.5. Generally, the flow structure (*e.g.*, peak velocity region, diffuse angle) is similar for different duty cycles. The peak velocity increases with duty cycle, and consumed power also increases. From Figure 5.6, the effect of duty cycle is similar to that of actuator strength as in Figure D.6.

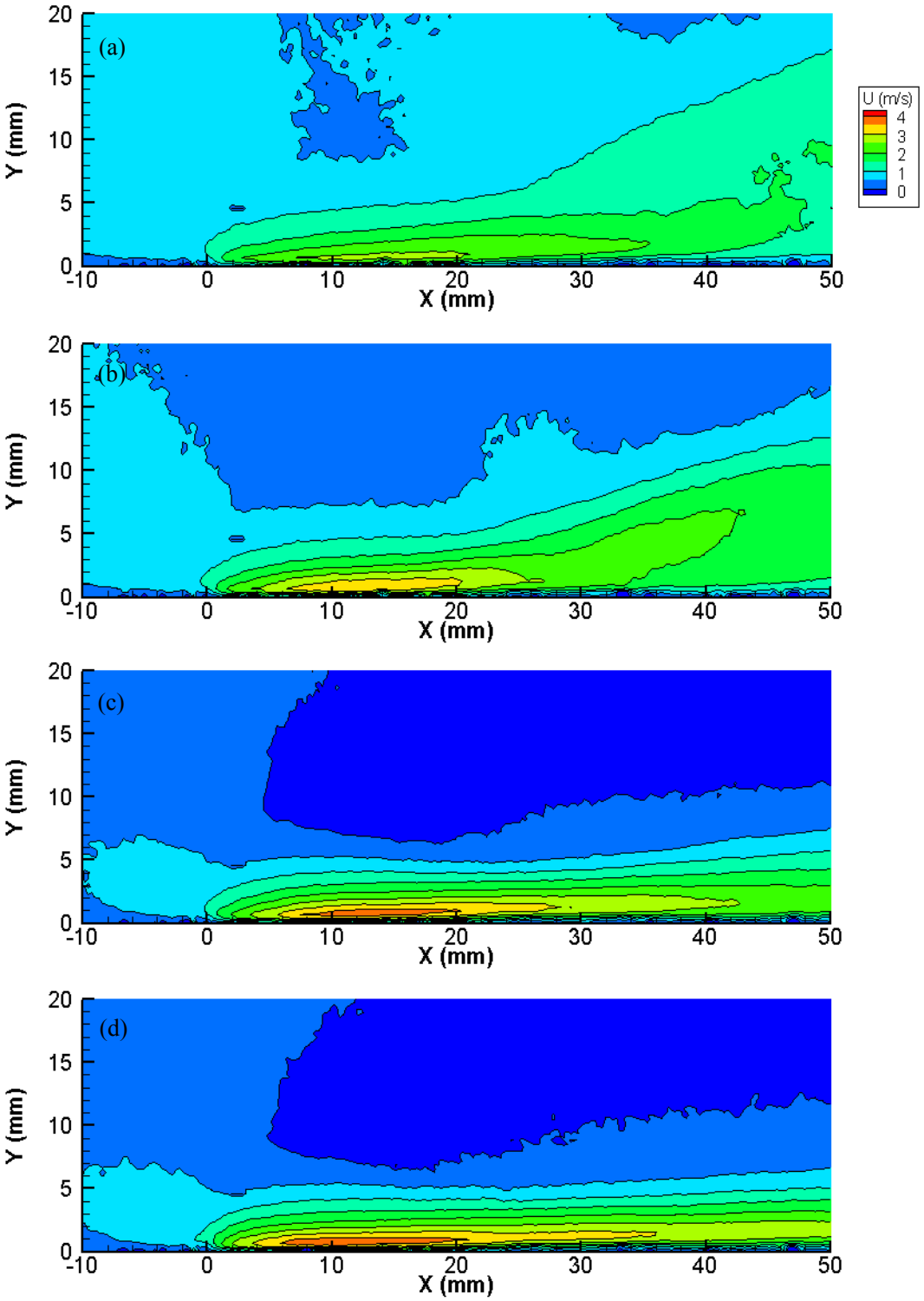

Figure 5.5: Contour of axial velocity for different modulation frequencies at 52.7 kV_{pp}, 40%: (a) 15.63 Hz, (b) 40 Hz, (c) 100 Hz, (d) 250 Hz

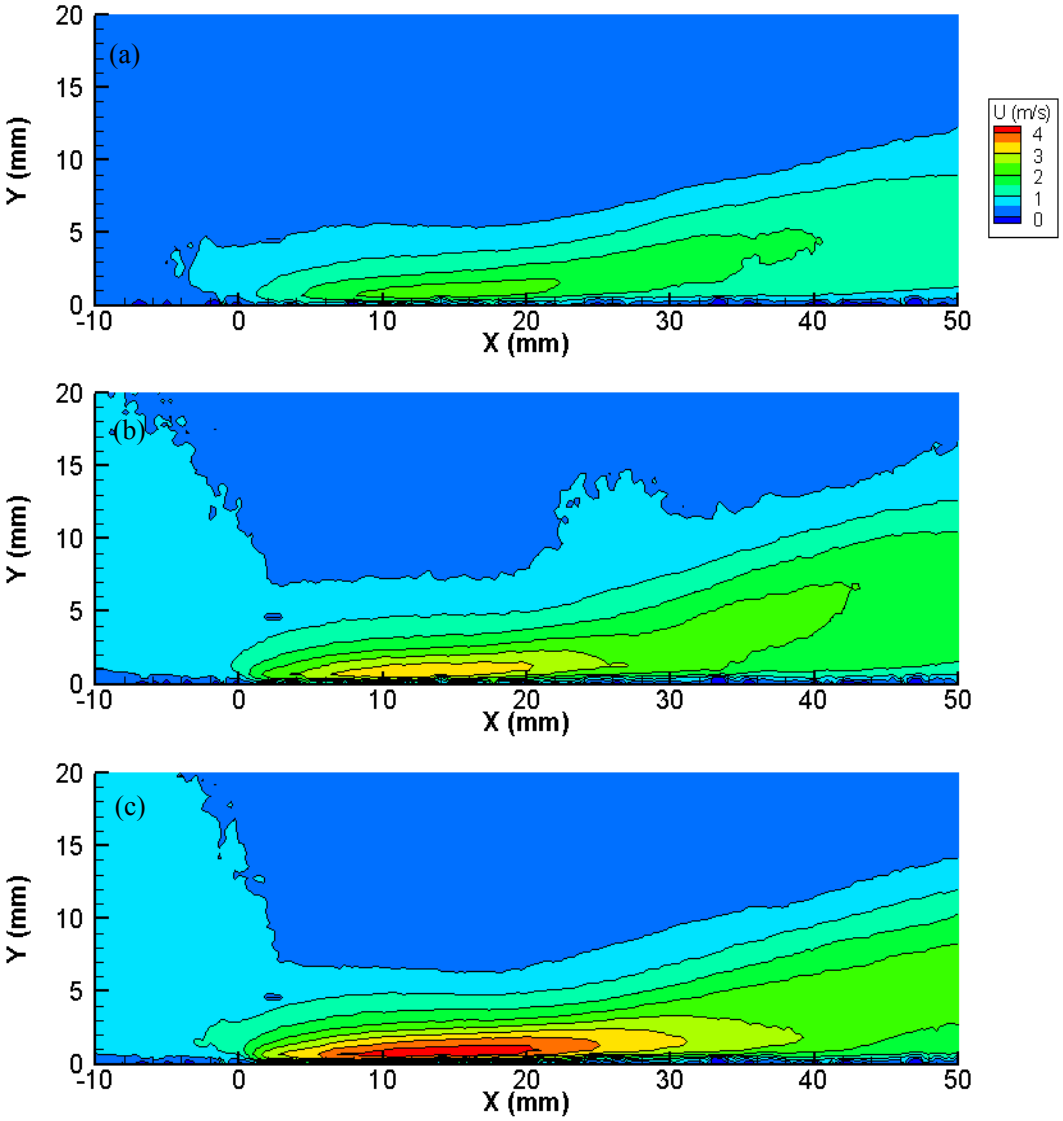

Figure 5.6: Contour of axial velocity for different duty cycles at 52.7 kV_{pp}, 40 Hz: (a) 20%, (b) 40%, (c) 60%

The above study has demonstrated the effect of pulsed actuation frequency and duty cycle on the quiescent flow field. Their effects on measured thrust and power consumption, which show a global effect, should also be considered as in Figures 5.7 and 5.8, respectively. Please note the results are obtained on a Teflon plate of 6.35 mm thick, with the electrodes connected to two high-voltage signals in opposite phases (refer to Figure C.1). With this connection, the imposed high voltage between electrodes is obtained while each transformer is operated at

relatively low voltage. For the AC cycle, the plasma actuator is operated at a frequency of 2 kHz, and amplitude of 47.2 kV_{pp} for negative sawtooth waveform. Even though the exact setting (e.g., dielectric material) in this study is different from that in the above study, the observed characteristics are the same. From Figure 5.7, the pulsed actuation frequency is shown to have no significant effect on the measured thrust and power consumption. It should be noted that the uncertainties for the measured thrust and power consumption are about 0.5 mN/m and 4%, respectively. To obtain similar results, one condition should be met which is that the number of active AC cycle (plasma is on) in each pulsed cycle should be either more than 5 or an integer (*e.g.*, 500 Hz/2 kHz, duty cycle of 50%). As for the effect of duty cycle, the variation of measured thrust and power consumption versus duty cycle are nearly linear as shown in Figure 5.8.

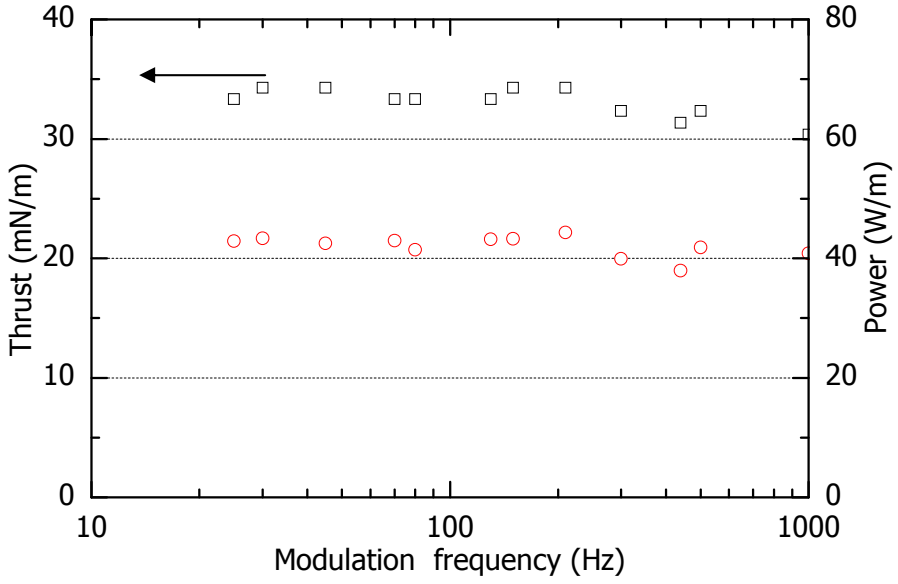

Figure 5.7: Modulation frequency effect on thrust and power (Teflon plate, 47.2 kV_{pp}, 2 kHz, duty cycle 50%)

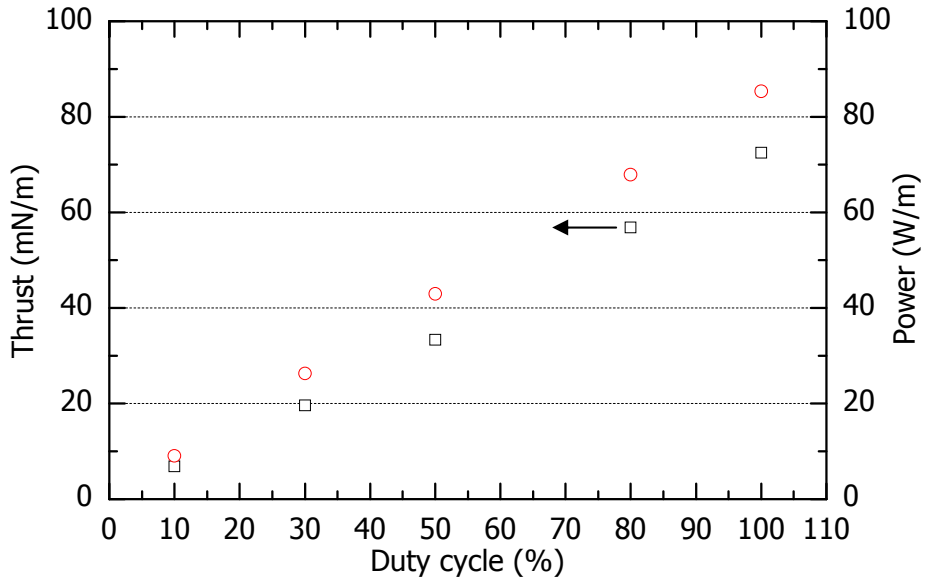

Figure 5.8: Duty cycle effect on thrust and power (Teflon plate, 47.2 kV_{pp}, 100 Hz/2 kHz)

In the above discussion, the plasma actuator is always operated in quiescent air (no background flow). For flow control, the background flow often exists and even changes with time. Therefore, the actuator performance with background flow should be tested and compared to that in quiescent air. The test is done in the wind tunnel at NRC GTL as shown in Figure 3.8. The power consumption versus applied voltage is shown in Figure 5.9 for both cases with and without background flow. The background flow velocity is chosen as 10 and 30 m/s, which represent the freestream velocity in the diffuser flow control experiment. From Figure 5.9, the background flow has no significant effect on the power consumption, at least for the investigated conditions. The general arguments in the above discussion can also apply to the plasma actuators in flow control.

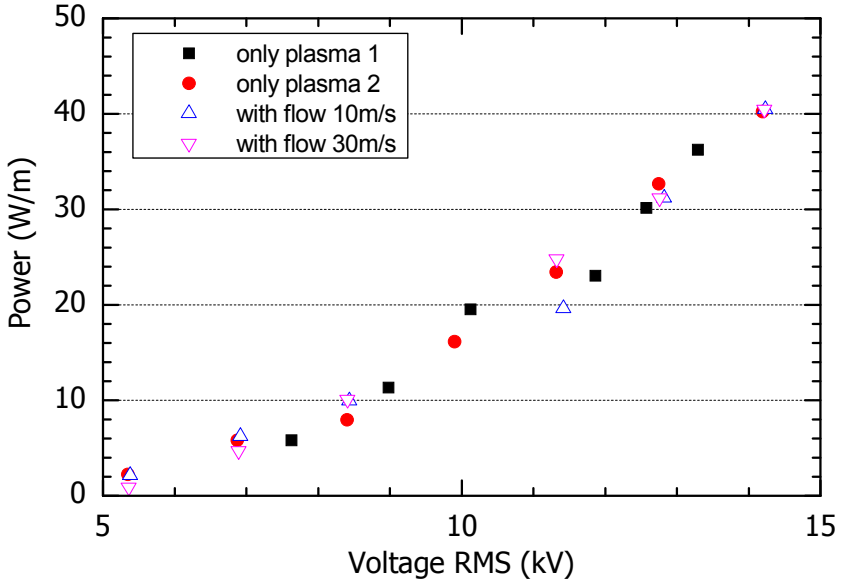

Figure 5.9: Flow effect on power consumption (Plexiglas plate, HV covered connection, 2.5 kHz, 100%)

5.2 Boundary Layer Separation in Non-Actuated Diffuser

The experimental study was conducted in a 2-D diffuser as shown in Figures 3.8 and 5.10. In Figure 5.10, the PIV measurement window of 65 mm long by 40 mm high is also highlighted. Figure 5.11 shows contours of the time-averaged axial velocity and streamlines from PIV measurements without actuation in the diffuser (refer to the highlighted window in Figure 5.10). From this figure, boundary layer separation can be clearly observed. This separation can be regarded as turbulent, caused by a tripping strip located upstream of the throat, as shown in Figure 3.8. The actuator location is chosen at x = 180 mm (from the leading edge of the flat plate in Figure 3.8), which is close to the separation point. Note that the exact separation point can not be determined from PIV measurement results because of the measurement error near the wall. This actuator location is determined based on the results showing the effect of actuator location in Figure 4.10. For the results presented in this chapter, the coordinate origin is located at the above actuator location (see Figure 5.11). As such the throat plane is at x = -70 mm. The time-averaged surface static pressure distribution obtained from a series of pressure taps along the flat plate is shown in Figure 5.12 for the no-control case and several cases with continuous

actuation. The time-averaged surface static pressure coefficient C_p is defined as

$$C_p = (P - P_{L2})/(P_{L1} - P_{L2}) \tag{5.1}$$

where P_{L1} and P_{L2} is the time-averaged static pressure at the first two pressure taps (x = -135 and -115 mm), and $(P_{L1} - P_{L2})$ is constant for the same mass flow rate as is the case in the current experiment.

Based on the above definition, the time-averaged surface static pressure coefficient C_p upstream of the throat is constant for different cases. In contrast, the cases with actuation have higher C_p than the no-control case at the locations downstream of actuator location (x = 0 mm), and higher C_p corresponds to better control effect. To compare the global effect of different actuation modes, the C_p at the last tap (x = 195 mm) is chosen as the surface pressure recovery value. Please note that the surface pressure recovery is different from that in Equation (4.1), which is based on the area-averaged static pressure on the diffuser cross section. However, the surface pressure recovery is enough for comparing the effects of plasma actuation in the present experiment.

In addition, three points in the plane of the actuator location (x = 0 mm), as shown in Figure 5.10, are chosen to capture the unsteadiness/instabilities in the flow field through hot-wire measurements. The hot-wire data is used to explain the optimal pulsed actuation frequencies shown later for separation control. The three points correspond to the shear layer near separation (y = 5 mm), edge of the shear layer near separation (y = 15 mm), and core flow (y = 25 mm), respectively.

The time evolutions of axial velocities are captured at the three points above for the no-control case. Spectral analysis is then carried out on the signals at these points, and the results are shown in Figure 5.13. At point 1 (in the shear layer near separation), a dominant frequency of 30 Hz can be clearly observed. This indicates that large-scale vortices are shed from the separation bubble at this frequency (Cherry *et al.*, 1984). At point 2 (edge of the shear layer near

separation), this dominant frequency is less distinct and several peaks near 30 Hz can be observed. Furthermore, at point 3 (core flow region), no dominant frequency can be observed, and the power spectrum energy decreases with frequency. This distribution is similar to that in the flow without boundary layer separation. It should be noted that the hot-wire measurement is also tried in the flow with actuation in order to demonstrate the effect of plasma actuation. However, the acquired signals from the hot-wire measurement indicate obvious electro-magnetic interference when the plasma actuator is on. The corresponding results are thus not included in this presentation.

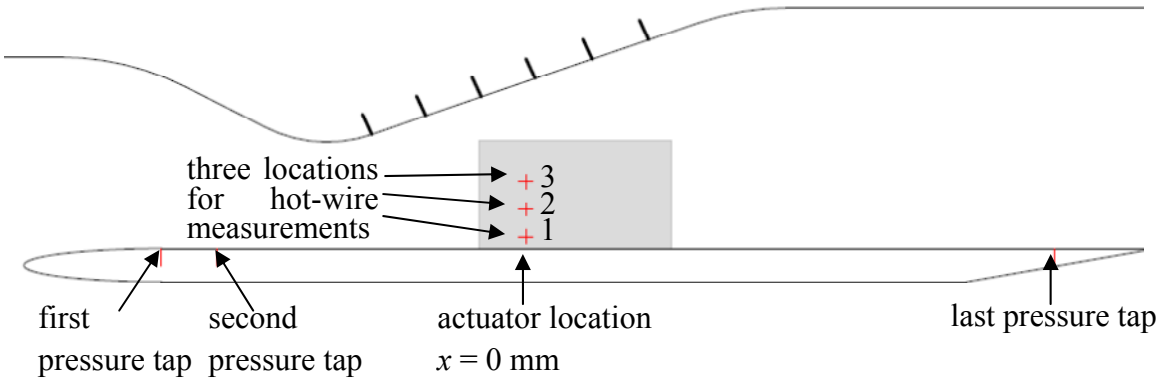

Figure 5.10: An illustration of windows for PIV measurement

5.3 Flow Control with Plasma Actuators

In the following experimental study, the effects of actuator strength, pulsed actuation frequency and duty cycle on the control of the above boundary layer separation are investigated.

5.3.1 Effect of Actuator Strength

The effect of actuator strength is shown in Figure 5.14, in terms of surface pressure recovery versus applied peak-to-peak voltage for both continuous and pulsed actuation. Figure 5.15 shows the contours of time-averaged axial velocity and streamlines for cases of continuous actuation with different strengths. The corresponding time-averaged boundary layer shape factor H along the axial direction is shown in Figure 5.16.

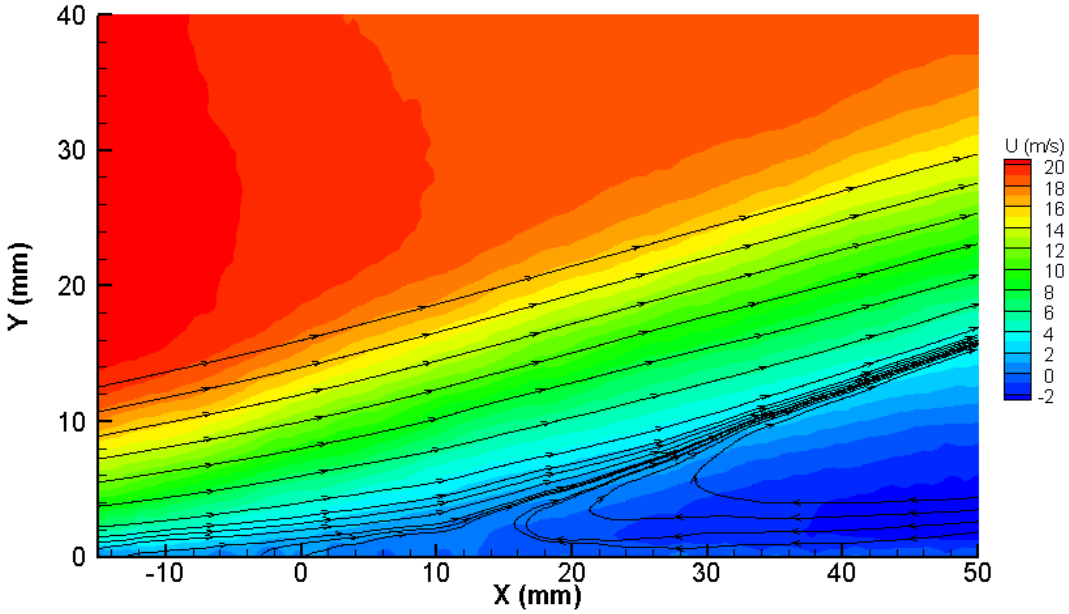

Figure 5.11: Contours of time-averaged axial velocity without actuation (refer to the highlighted window in Figure 5.10)

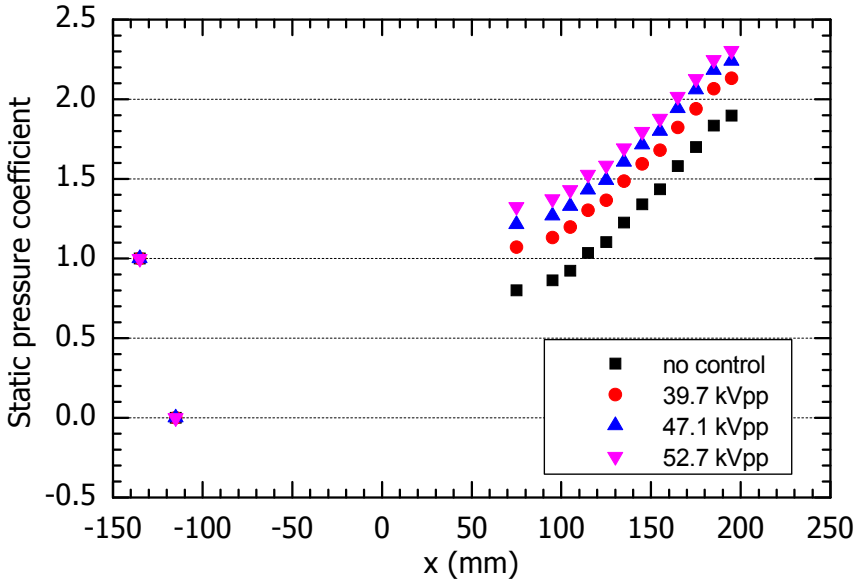

Figure 5.12: Time-averaged static pressure distribution along the flat plate without and with continuous actuation

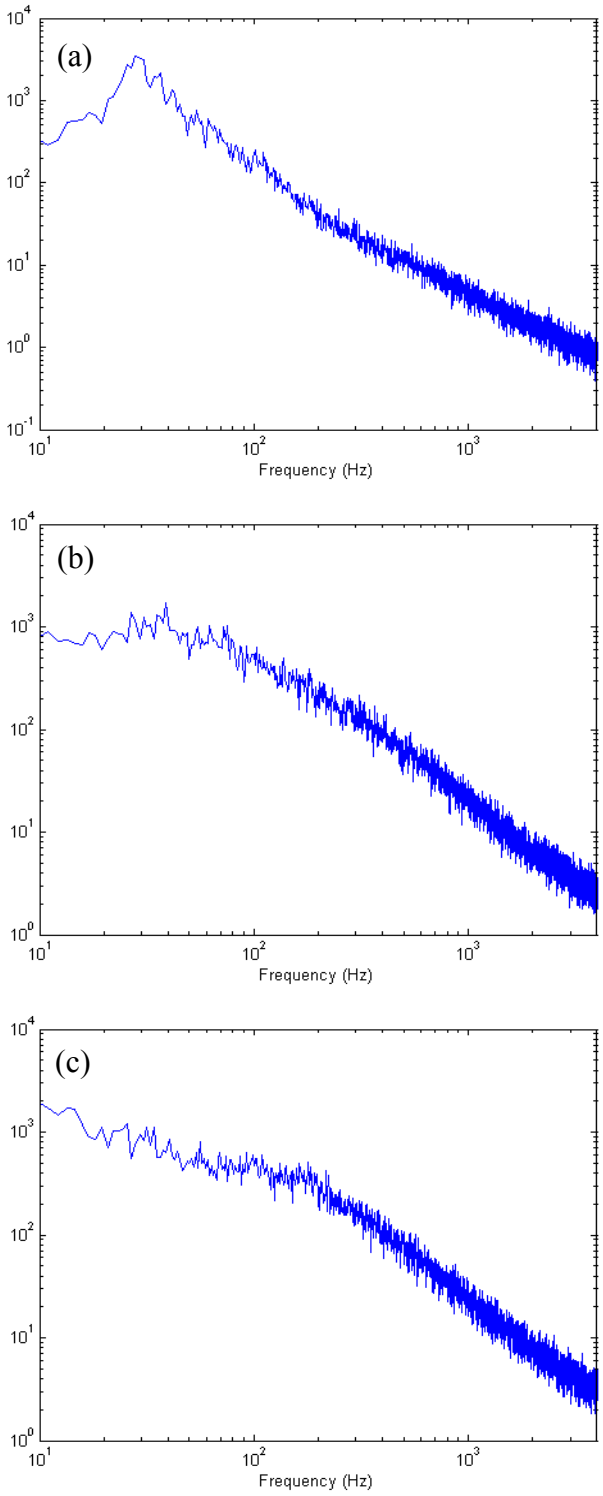

Figure 5.13: Spectral analysis of axial velocities without actuation from hot-wire measurement at three points: (a) shear layer region near separation (point 1), (b) edge of shear layer (point 2), (c) core flow (point 3)

From Figure 5.14, the pressure recovery is observed to increase with actuator strength for continuous actuation (with duty cycle of 100%). The reduced separation size by plasma actuation corresponds to the larger pressure recovery. For continuous actuation at 21 kV_{pp} (corresponding to a thrust of 5 mN/m in Figure 5.4), the pressure recovery is almost the same as the no-control case. This demonstrates that the applied high voltage should be above a certain level to have the sufficient plasma actuator strength and thus effective control. The effect of actuator strength is also indicated by the boundary layer separation location and bubble size as shown in Figure 5.15 for continuous actuation. The separation location is delayed and the separation bubble size is reduced with increased actuator strength. Note that the freestream velocity is kept almost constant by adjusting the suction fan speed.

The boundary layer shape factor H may be an easier way to quantify the change of the separation point induced by plasma actuation. From Figure 5.16, the shape factor increases along the axial direction, demonstrating the trend of the boundary layer separation in the diffuser. With plasma actuation, the shape factor is reduced along the axial direction. This indicates that the boundary layer is more stable and thus can endure a more adverse pressure gradient without separation. The boundary layer near separation normally has a shape factor between 2.5 and 3 (Castillo *et al.*, 2004). In the present study, since one only need compare the effects of different cases, a specific shape factor (*e.g.*, 3) can be chosen to correspond to the separation point. The separation location is thus delayed to x = 16 mm for 39.7 kV_{pp} and x = 32 mm for 52.7 kV_{pp}. Note that there seems to be a step/plateau near the actuator location (*i.e.*, x = 0 mm) for cases with actuation, which shows that the effect of plasma actuation is downstream. With the input of momentum by plasma actuation into the downstream boundary layer, it is more stable and the associated shape factor is reduced. While the upstream boundary layer is still less stable and boundary layer development is closer to that without actuation (higher shape factor).

The required actuator strength in continuous mode to delay the separation point to a new location can be also estimated by using the preliminary design rule established in Section 4.3.

The input information for this estimation includes the time-averaged velocity profile without actuation at the chosen actuator location from PIV measurements and the static pressure distribution along the bottom wall without actuation obtained from inviscid simulations. The required actuator strength is thus predicted by substituting the input information into Equations (4.7) and (4.9). In the following part, the case with continuous actuation at the applied voltage of 47.1 kV_{pp} (associated with a measured thrust of 80 mN/m and an approximate body force of 107 mN/m) is taken as an example, because the boundary layer separation is not completely suppressed (see Figure 5.15(b)). To have the new separation point as that of x = 30 mm for the above case with 47.1 kV_{pp} actuation, the required actuator strength is predicted as 162 mN/m (about 50% higher than the real strength of 107 mN/m). This shows that the design rule provides the estimation of the required actuator strength in a conservative way.

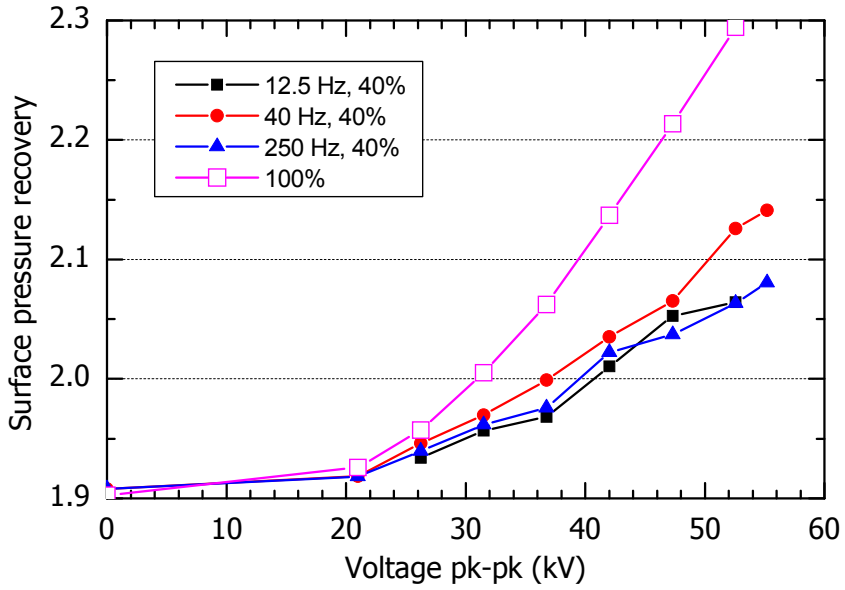

Figure 5.14: Pressure recovery with different actuator strengths

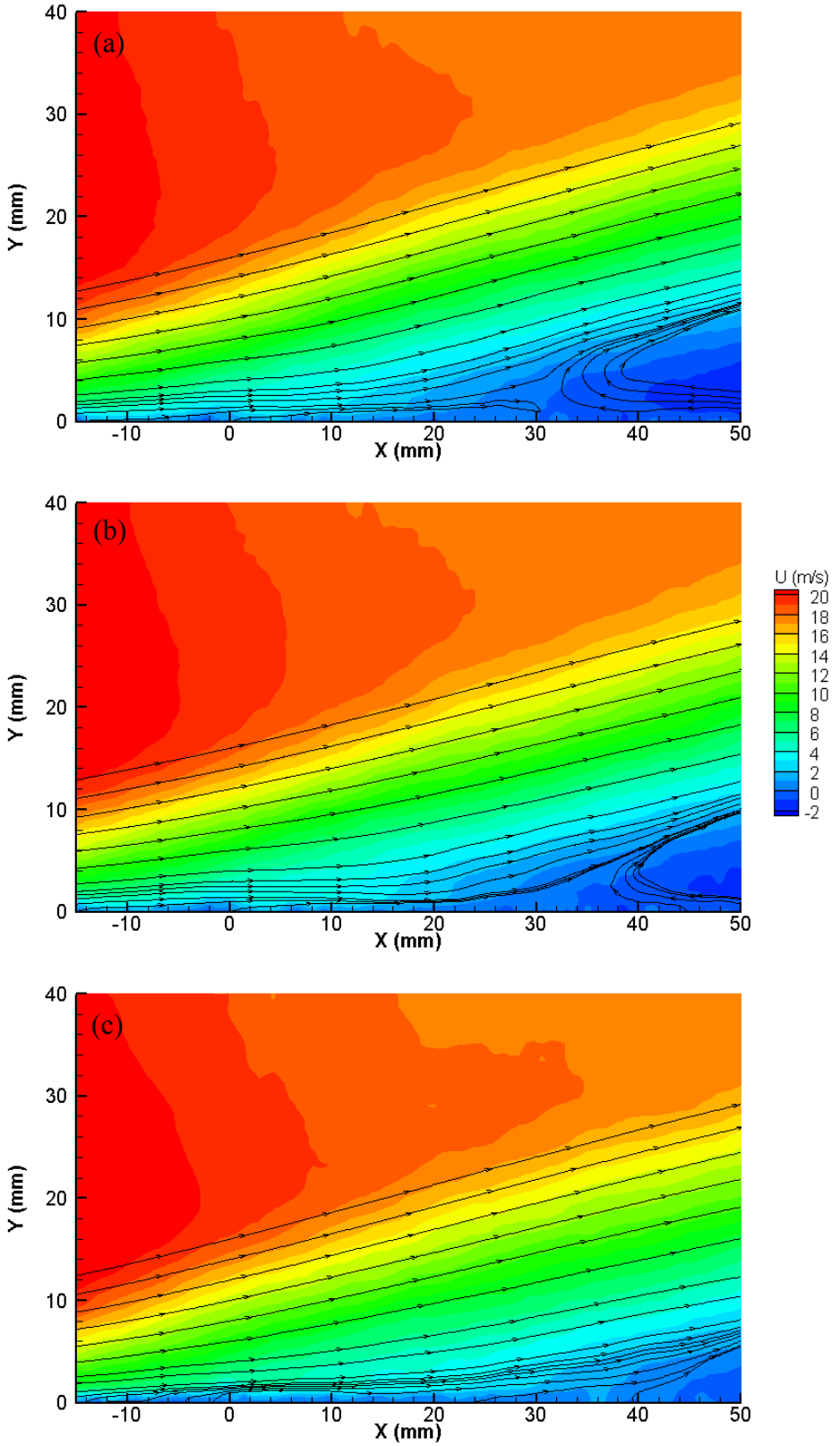

Figure 5.15: Time-averaged flow field with different actuator strengths: (a) 39.7 kV_{pp}, (b) 47.1 kV_{pp}, (c) 52.7 kV_{pp}

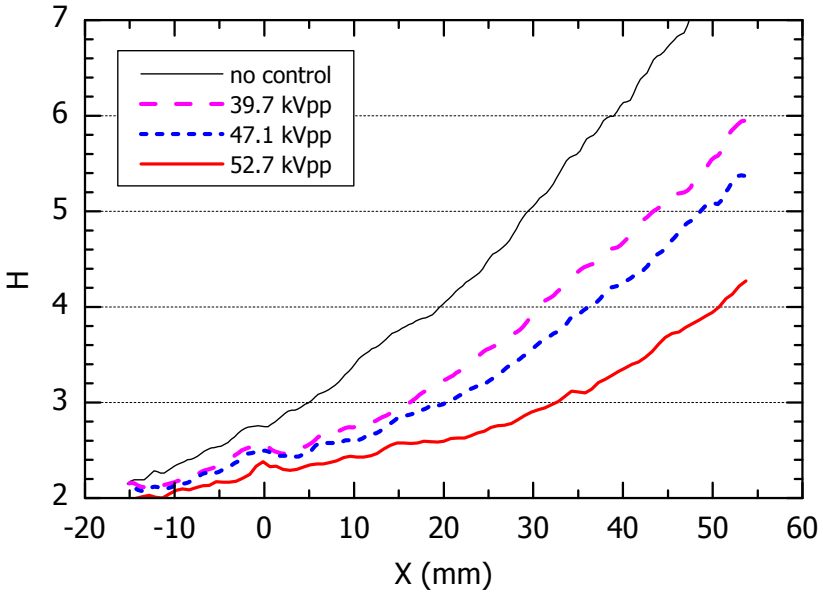

Figure 5.16: Time-averaged boundary layer shape factor *H* for the cases with continuous actuation

As for pulsed actuation, the effect of actuator strength is illustrated for three series with different actuation frequencies (12.5, 40 and 250 Hz), and a duty cycle of 40%. The duty cycle of 40% is chosen based on the parametric study of duty cycle in Section 4.2. From Figure 5.14, the pressure recovery for pulsed actuation is also seen to increase with actuator strength. At each applied voltage investigated, the pulsed actuation with 40 Hz has higher pressure recovery than those with 12.5 and 250 Hz. This shows that there exists an optimal actuation frequency for pulsed actuation, which will be discussed later.

For the same applied voltage, continuous actuation always provides the higher pressure recovery than pulsed actuation (see Figure 5.14). However, the power consumption for pulsed actuation is only a fraction (approximately equal to the duty cycle) of that of continuous actuation. To better compare continuous and pulsed actuation, the measured power consumption from voltage and current measurements is used (as opposed to the effective actuator strength in CFD simulations). Figure 5.17 shows pressure recovery versus power consumption for continuous and pulsed actuation at 40 Hz in Figure 5.14. To achieve the same pressure recovery, the required power consumption is less for pulsed actuation at the optimal frequency. This can be

explained by the fact that continuous actuation involves direct input of momentum into the flow to prevent boundary layer separation, while pulsed actuation enhances the momentum transfer between the outer and inner fluid by amplifying those large-scale turbulent structures within the boundary layer through resonance. In addition, the difference in power consumption between these two cases in Figure 5.17 increases with increased pressure recovery.

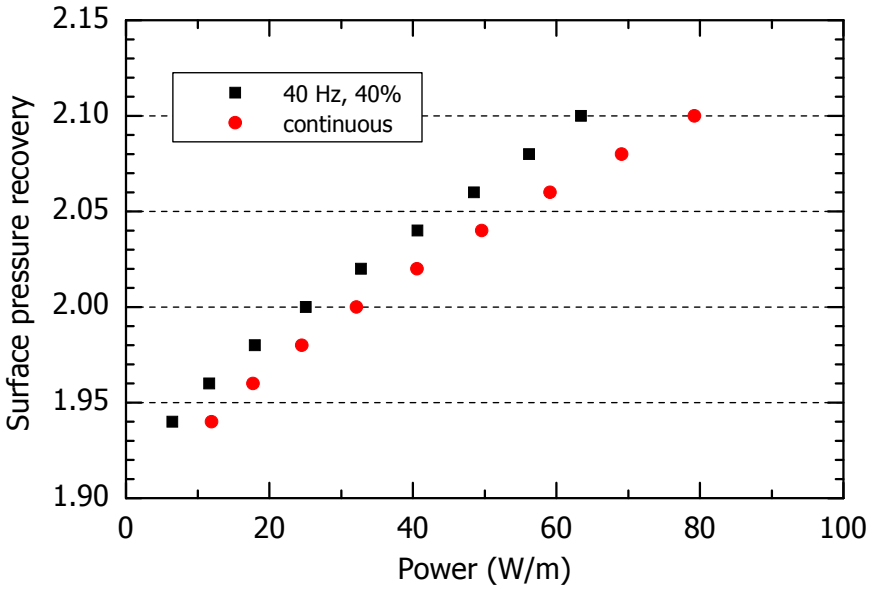

Figure 5.17: Comparison of power consumption for continuous and pulsed actuation

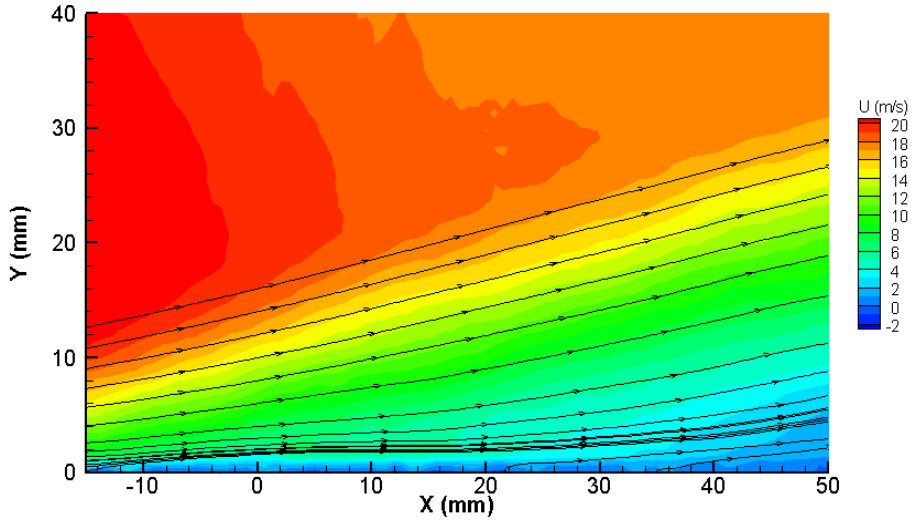

Figure 5.18: Time-averaged flow field with Teflon plasma actuator at 68.4 kV_{pp}, 100%

With continuous actuation using the Plexiglas dielectric actuator at 52.7 kV_{pp} (corresponding to a thrust of 107 mN/m), the boundary layer separation is not completely suppressed although it is significantly reduced (see Figure 5.15(c)). Instead the Teflon dielectric plasma actuator, which can generate higher body force, is used to demonstrate better control effect. The contours of the time-averaged axial velocity and streamlines with the Teflon actuator at 68.4 kV_{pp} (corresponding to a thrust of 137 mN/m) is shown in Figure 5.18. From this figure, it is evident that the boundary layer separation is fully suppressed, as observed from positive axial velocity near the wall.

5.3.2 Effect of Pulsed Actuation Frequency

This section studies the effect of actuation frequency in pulsed mode for a duty cycle of 40%. The surface pressure recovery at different actuation frequencies is plotted in Figure 5.19 for three tests with applied peak-to-peak voltages of 39.7, 47.1 and 52.7 kV, respectively. From this figure, the optimal actuation frequency is found to be between 20 and 40 Hz for all three tests. The effect of pulsed actuation is dramatically reduced when the actuation frequency is higher than 60 Hz. The pressure recovery is almost constant when the actuation frequency is higher than 100 Hz.

The optimal frequency observed above is consistent with the power spectrum without actuation in Figure 5.13(a), where 30 Hz is observed to be the dominant frequency (with the highest turbulence energy) at point 1. The turbulence energy at 100 Hz is one order of magnitude less than that at 30 Hz. In other words, the most energetic large-scale structures in the flow are most amplified when the actuation frequency is the same as the natural dominant frequency in the no-control flow, and thus the flow mixing of outer high-momentum and inner low-momentum flow is most enhanced. Please note that the hot-wire measurement is also proposed to be used in the flow with actuation in order to assess the effect of plasma actuation. However, the acquired signal from the hot-wire measurement indicates obvious influence of electrical interference when the plasma is on. The corresponding results are thus not included in

this presentation.

To better demonstrate the effect of the pulsed actuation frequency, Figures 5.20-5.22 shows the time evolution of flow fields in the highlighted window in 5.10 Figure from phased-locked PIV measurements (see Figure 3.13) with pulsed actuation at 47.1 kV_{pp}, duty cycle of 40% for actuation frequencies of 40, 15 and 200 Hz, respectively. In these figures, both phased-locked contours of axial velocity and streamlines are included for some specific phases. The corresponding time evolution of the phased-locked shape factor H is shown in Figures 5.23-5.25, respectively. For each specific time/phase, the above boundary layer integral parameter distribution along the axial direction is calculated from the corresponding flow field. The y-axis variable "time" in these figures corresponds to the percentage of the pulsed actuation cycle. Time 0% and 100% thus are for the same phase, with the plasma actuation just turned on.

Focusing first on Figures 5.20 and 5.23, one can follow the development of the flow field with pulsed actuation at 40 Hz, 40%. The plasma actuator is turned on at time t = 0% and kept on until the time t = 40% of the duty cycle. During this period, the momentum from plasma actuation is continuously added into the low-momentum boundary layer. The boundary layer separation point is at the same time delayed, as seen from 0% to 40% in Figure 5.20. This can also been seen in Figure 5.23, with the contour identified as A shifting downstream during the actuation time interval $0\% \le t \le 40\%$. Note that the other contours downstream of this contour demonstrate a similar trend, except for some phase delay, since it takes time for the effect of plasma actuation to propagate downstream.

At t = 40%, the plasma actuation is turned off and the associated momentum addition is shut down. Without the push of plasma actuation, the boundary layer stops the previous trend and retreats (e.g., separation point moves upstream) due to the work of the adverse pressure gradient in the diffuser. From Figure 5.23, the contour A moves upstream from the time t = 40% and reaches the relatively stable position at the time t = 60%. This can also be seen in Figure 5.20 from t = 40.63% to t = 62.50%, when the separated boundary layer becomes flatter compared to

the previous phases, as a result of the adverse pressure gradient. At the same time, the flow seems complex, as observed from the streamline and the saddle point. This indicates an instantaneous situation when adverse pressure gradient is just dominant while the flow still has the relatively high momentum opposed to the adverse pressure gradient as before due to the fluid inertia.

Thereafter the shape factor distribution seems to reach a stable level (see Figure 5.23 after t = 60%), at least in the region near the actuator location. In contrast, the corresponding flow fields in Figure 5.20 are not as simple as the shape factor distribution. A vortex initiating from the saddle point at t = 56.25% can be observed. This vortex should be beneficial for the pulsed actuation, because it could enhance flow mixing of high-momentum core flow and low-momentum boundary layer flow. The vortex disappears after t = 68.75%, because the adverse pressure gradient is dominant and the flow field is relatively stable. This situation is maintained until the plasma actuation is turned on again and a new cycle starts at t = 100%.

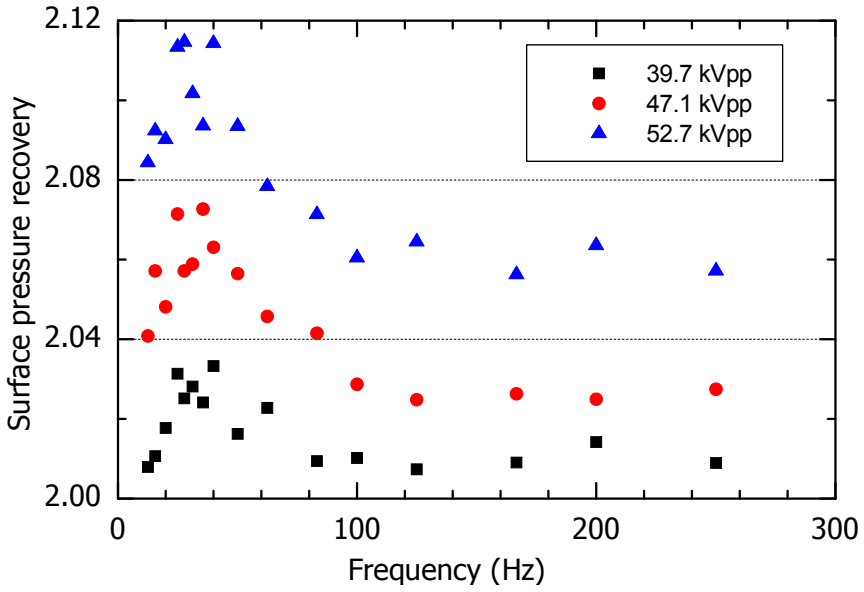

Figure 5.19: Pressure recovery with different actuator frequencies at 40% duty cycle

The development of the flow field with pulsed actuation frequencies of 15 and 200 Hz, is generally similar to that for 40 Hz actuation (see Figures 5.23-5.25). From these figures, the flow

with pulsed actuation is shown to periodically fluctuate with the applied actuation frequency, as observed from each specific contour. The periodic fluctuation implies that the flow with pulsed actuation is more organized or that large-scale structures with the actuation frequency within the boundary layer are amplified. The applied duty cycle of 40%, *i.e.*, the period when plasma actuator is on, corresponds to the time interval between upstream and downstream locations of each specific contour. Note that the fluctuation of shape factor distribution is obvious for the contour downstream of the actuator location, while it is not for those upstream. This indicates that the effect of plasma actuation is mainly downstream as desired.

Figure 5.19 showed that the optimal actuation frequency is between 20 and 40 Hz. This can be explained by comparison of the time evolution of the phased-locked flow field in Figures 5.20-5.22 and the corresponding time evolution of the phased-locked shape factor H in Figures 5.23-5.25. From Figure 5.25, the flow fluctuations induced by plasma actuation at 200 Hz are smaller than those at 40 Hz. The associated flow mixing is thus weaker and the control effectiveness is less. In some sense, the pulsed actuation at higher frequencies is closer to continuous actuation, where the direct momentum input is the mechanism to reduce the boundary layer separation. One may understand the working process of the pulsed actuation in another way. The pulsed actuation inputs some momentum into the flow when it is on in order to induce the strong fluctuation. This process is continuous in an actuation cycle. Since the flow needs some time to react to this momentum input due to fluid inertia, it does not achieve the necessary momentum for the pulsed actuation at higher frequency.

Pulsed actuation at 15 Hz can induce larger fluctuation as observed in Figure 5.24. However, the associated mixing level is not higher than that for the 40 Hz actuation, because the vortex at the time t = 65.63% for the 40 Hz actuation (Figure 5.20) can not be observed for the 15 Hz actuation (Figure 5.21). The development period of the vortex is observed to be between the plasma turned off (t = 40%) and the flow becoming relatively stable (t = 60%), while this period is very short for the 15 Hz actuation that the vortex can not arise.

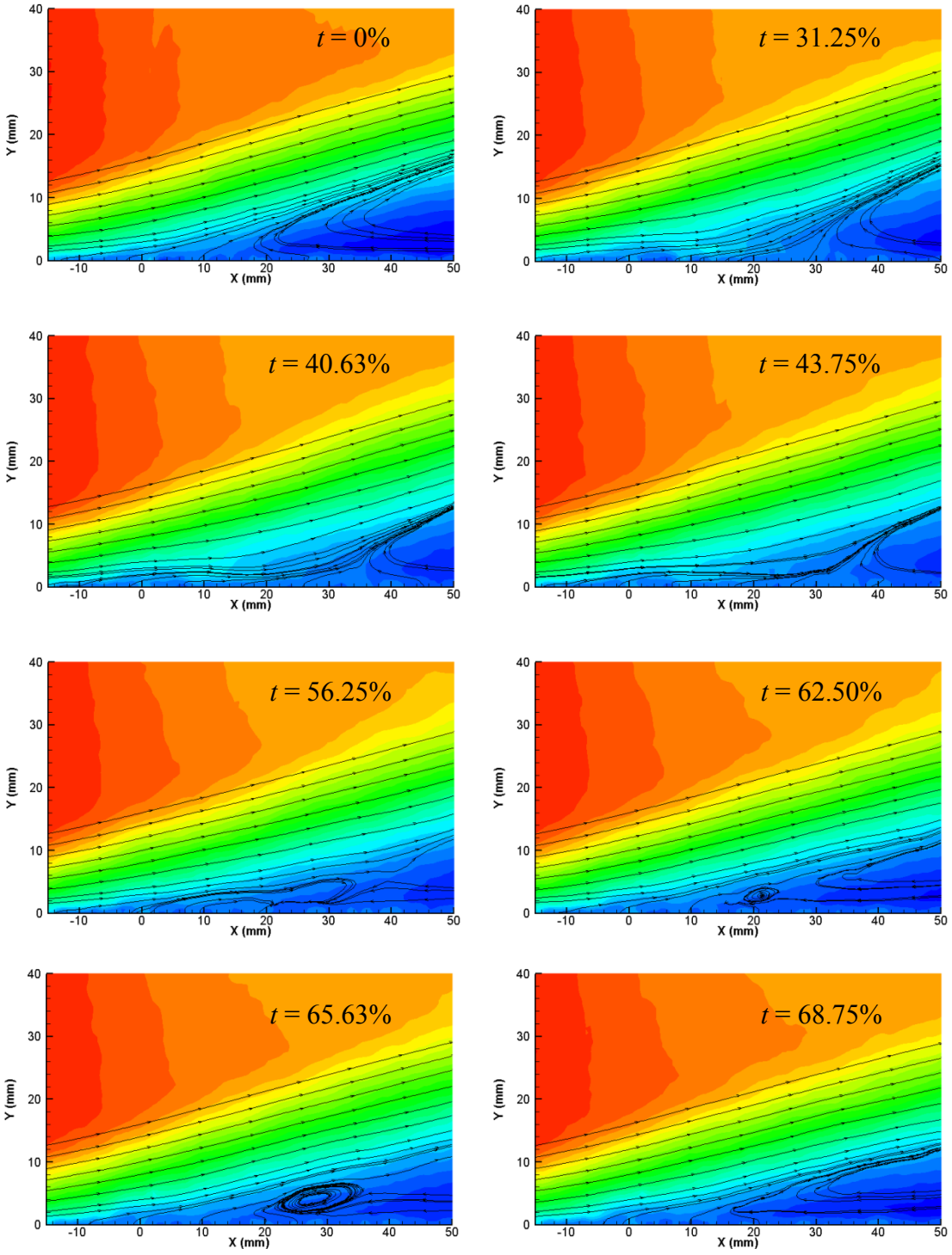

Figure 5.20: Instantaneous flow fields with pulsed actuation at 40 Hz, 47.1 kV_{pp}, 40%

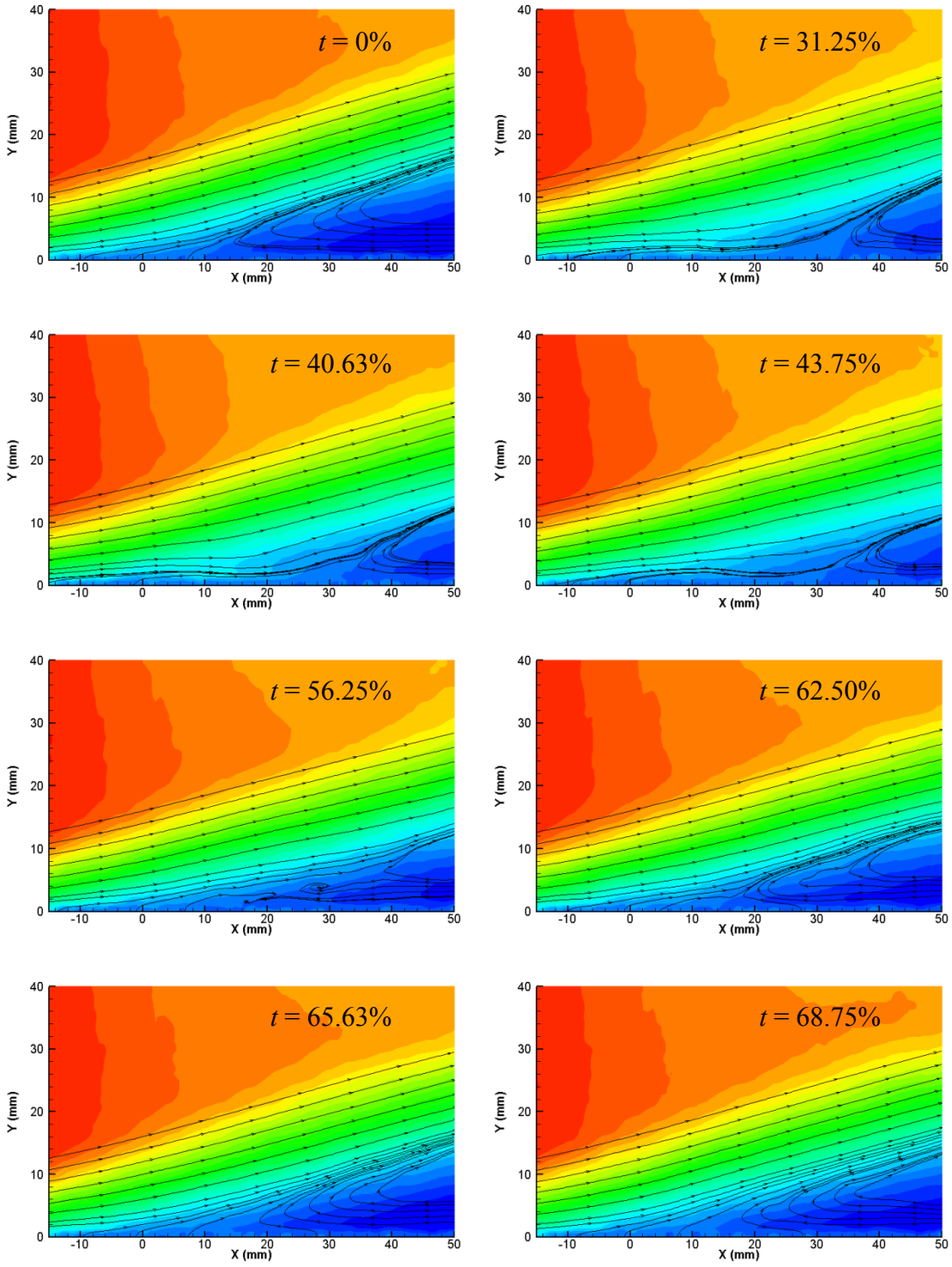

Figure 5.21: Instantaneous flow fields with pulsed actuation at 15.63 Hz, 47.1 kV_{pp}, 40%

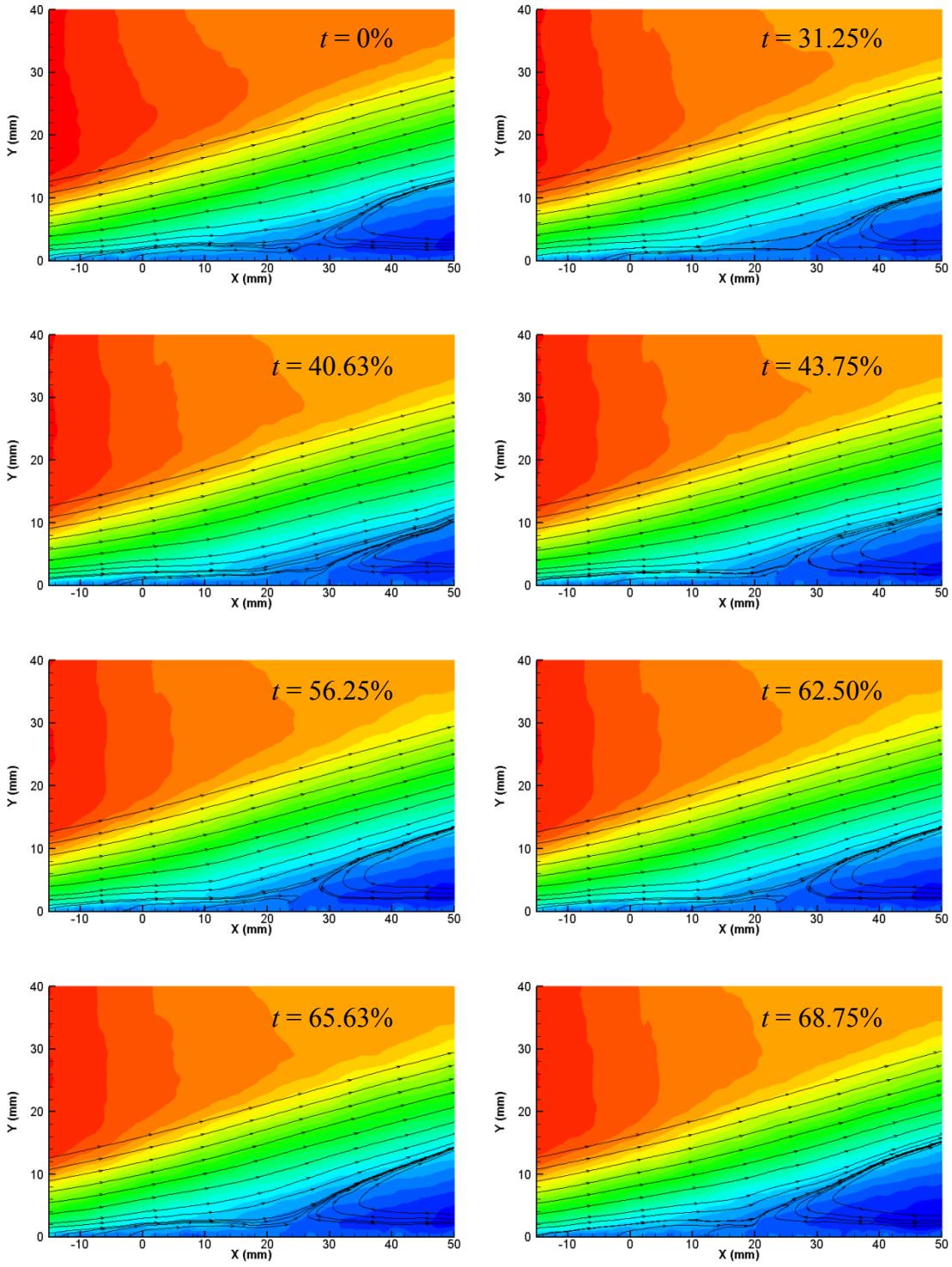

Figure 5.22: Instantaneous flow fields with pulsed actuation at 200 Hz, 47.1 kV_{pp}, 40%

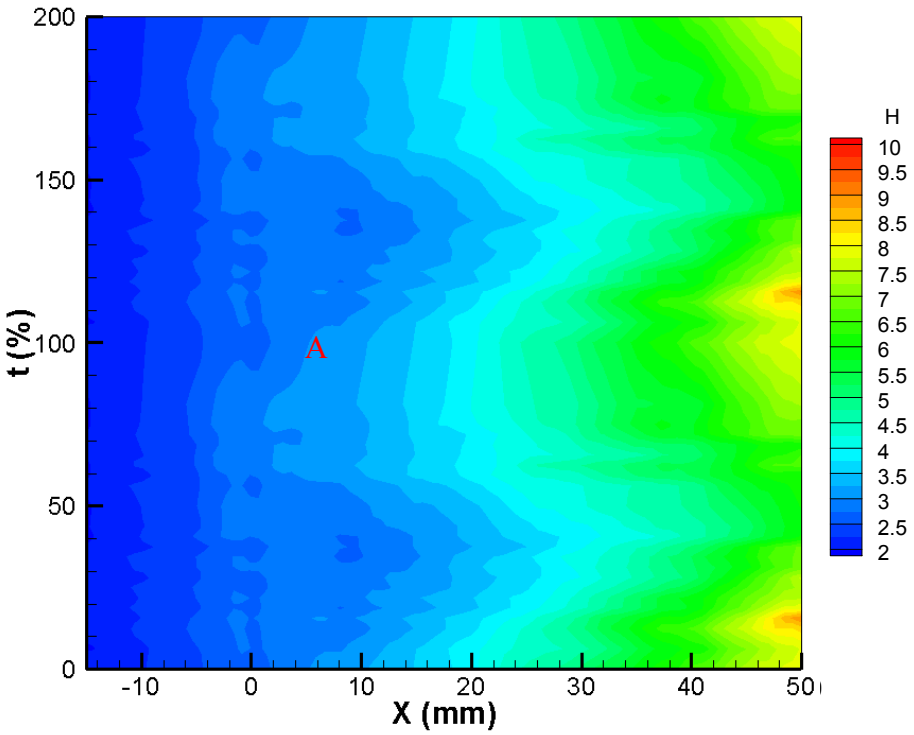

Figure 5.23: *x-t* diagram of phase-locked unsteady boundary layer shape factor *H* for the case with actuation at 40 Hz, 40%

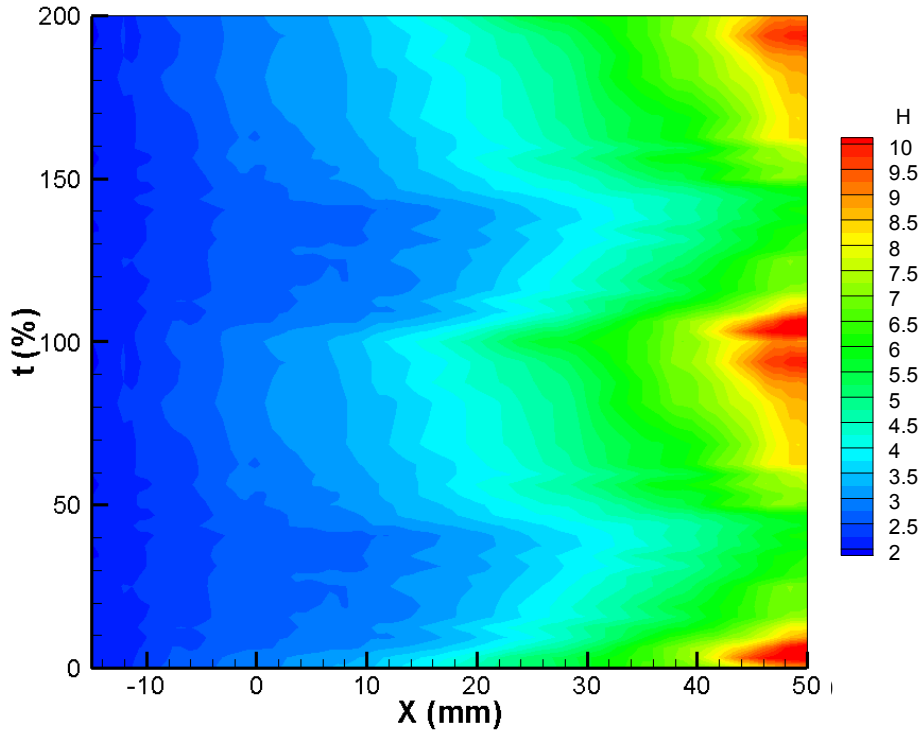

Figure 5.24: *x-t* diagram of phase-locked unsteady boundary layer shape factor *H* for the case with actuation at 15 Hz, 40%

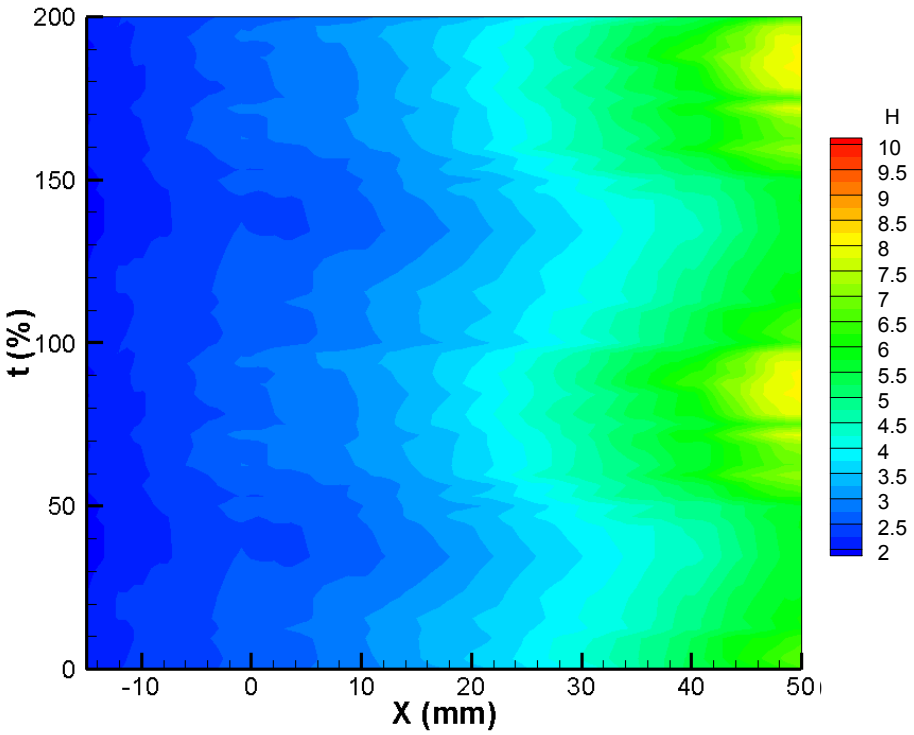

Figure 5.25: *x-t* diagram of phase-locked unsteady boundary layer shape factor *H* for the case with actuation at 200 Hz, 40%

5.3.3 Effect of Duty Cycle

The effect of duty cycle in pulsed actuation is investigated in this section. The surface pressure recoveries at different duty cycles are plotted in Figure 5.26 for three tests at 40 Hz with applied peak-peak voltage of 39.7, 47.1 and 52.7 kV, respectively. From this figure, the pressure recovery for each plot increases with duty cycle, with the 100% duty cycle (continuous actuation) having the highest. Note that the increased duty cycle also corresponds to increased power consumption, as shown in Figure 5.8. For the same duty cycle, the pressure recovery increases with applied peak-peak voltage, as in Figure 5.14.

To better demonstrate the effect of duty cycle, the time evolution of the phased-locked shape factor *H* is shown in Figures 5.27 and 5.28 for duty cycles of 20% and 60% at 52.7 kV_{pp}, respectively. Generally the development of the shape factor is similar to that in Figure 5.23, corresponding to the three phases: delayed separation when the actuation is on, the reverse

process after the actuation is turned off, and a stable level until the start of a new cycle. The applied duty cycle can be indicated by the most downstream location of contour initiating from the actuation location. As for the actuation at the duty cycle of 60%, the first phase is different from the previous cases in Figures 5.23-5.25, because a relatively stable level can be clearly observed. It appears similar to the flow structure expected from continuous actuation. This can be explained by the fact that the duty cycle is long enough for the flow to reach a quasi-equilibrium state. This observation for high duty cycle matches those (Figure 4.14) in CFD simulations. The delayed separation for a longer time than that with lower duty cycle (*e.g.*, 20%) contributes to higher control effectiveness. However, in some sense, this also contributes to reduced effectiveness of pulsed actuation at high duty cycle for the same power consumption, as seen in Figure 4.18, since the pulsed actuation works by enhancing the flow mixing between high-momentum outer and low-momentum inner flows.

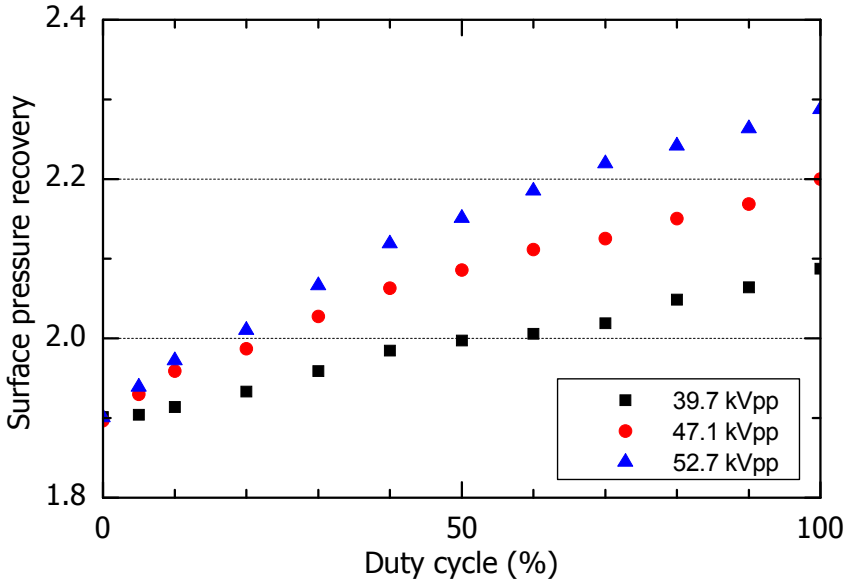

Figure 5.26: Pressure recovery versus different duty cycles for pulsed actuation at 40 Hz

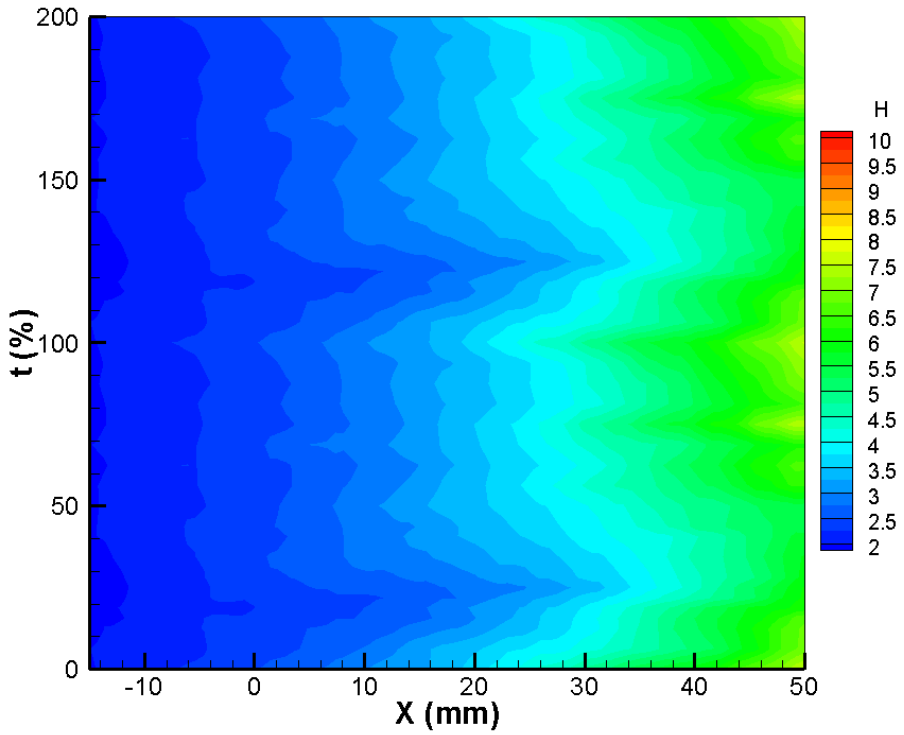

Figure 5.27: *x-t* diagram of phase-locked unsteady boundary layer shape factor *H* for the case with actuation at 20%, 52.7 kV_{pp}

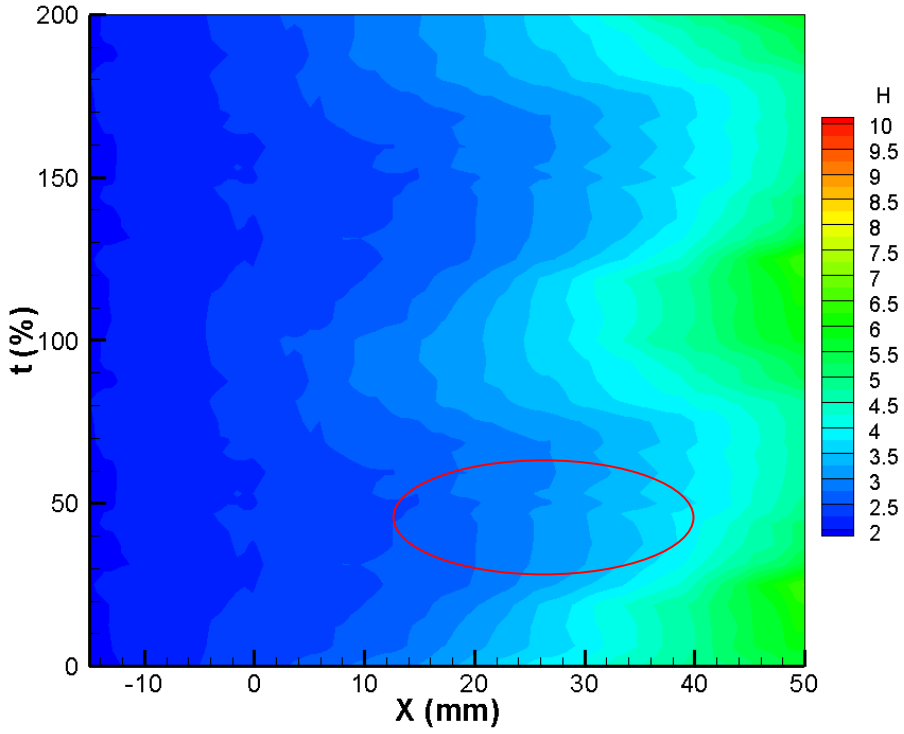

Figure 5.28: *x-t* diagram of phase-locked unsteady boundary layer shape factor *H* for the case with actuation at 60%, 52.7 kV_{pp}

5.4 POD Analysis

Proper orthogonal decomposition (POD) is a method used to extract a reduced number of typical modes in a signal associated with their time evolution (Hemon and Santi, 2003). POD has been used to extract the coherent structures in the separated shear layer around a wing by Hoarau *et al.* (2006), and in the turbulent separation bubble by Mathis *et al.* (2009). In the following study, POD is also proposed to extract the coherent structures in the flow with turbulent boundary layer separation (more features of the flow), and demonstrate the effect of plasma actuation.

The POD offers a representation of time-evolving vector fields by using energetic spatial and temporal modes called *topos* and *chronos*, respectively. Figure 5.29 shows 2-D *topos* of velocity (both axial and normal velocities) without actuation obtained from PIV measurement (first eight modes), while Figure 5.30 shows corresponding *chronos*. In Figure 5.29, the *topos* can be demonstrated by both contours of axial velocity and streamlines. In general, the *topos* demonstrates the increasing number of changes in sign with increasing mode number. Note that POD analysis in the current study excludes the mean flow (*e.g.*, the no-control case in Figure 5.11). These modes thus represent the fluctuation in the flow with different length/time scales, with the continually changing sign of corresponding *chronos*. The first mode is representative of the large scale fluctuations (large flow structures). It should be noted that the sign and amplitude of *topos*/*chronos* are not important but their product has a physical meaning.

From Figure 5.29, the *topos* 1 has a jet-like structure, which demonstrates the momentum transfer between the core flow and the separation bubble. Since the vector flow could be positive or negative, depending on the sign of the *chronos* 1, the momentum transfer can be in two directions. This applies to all modes. As for the *topos* 2, two vortices can be observed, with one located near the edge of the separated shear layer and the other in the separation bubble (compared with the time-averaged flow field in Figure 5.11). These two vortices highlight the momentum transfer in localized regions. The *topos* 3 corresponds to one vortex in the separated

shear layer. The *topos* 4 has four vortices, with two near the edge of the separated shear layer and two in the separation bubble. This mode can be regarded as the more refined version of the lower mode 2. The *topos* 5 is characterized by several vortices in the shear layer and the saddle point (x = 30 mm, y = 6 mm). In some sense, this mode is the refined version of mode 3. Furthermore, the *topos* 6 and 7 corresponds to the *topos* 4, while the *topos* 8 corresponds to the *topos* 3. The *topos* pattern of higher modes is very similar to ones of lower modes described above. Generally, the higher the mode number, the more complex the structure of its *topos*.

The *topos* of first six modes for cases with both continuous and pulsed actuation at 47.1 kV_{pp} are shown in Figures 5.31 and 5.32, respectively. The pulsed actuation has a duty cycle of 40% and pulsed actuation frequency of 40 Hz. From Figures 5.31 and 5.32, the *topos* 1-3 for both cases are characterized by similar structures, which are also comparable to those without actuation in Figure 5.29. As for the higher mode *topos* (above 3), different patterns are observed. This may be explained by the fact that the main structures in the flow are not significantly affected by the plasma actuation. The continuous actuation involves direct momentum input, the effect of which can be included in the mean flow. In contrast, pulsed actuation involves enhancing the momentum transfer in the flow through strengthening the original resonant structures, which are normally related to the large fluctuation (lower POD modes).

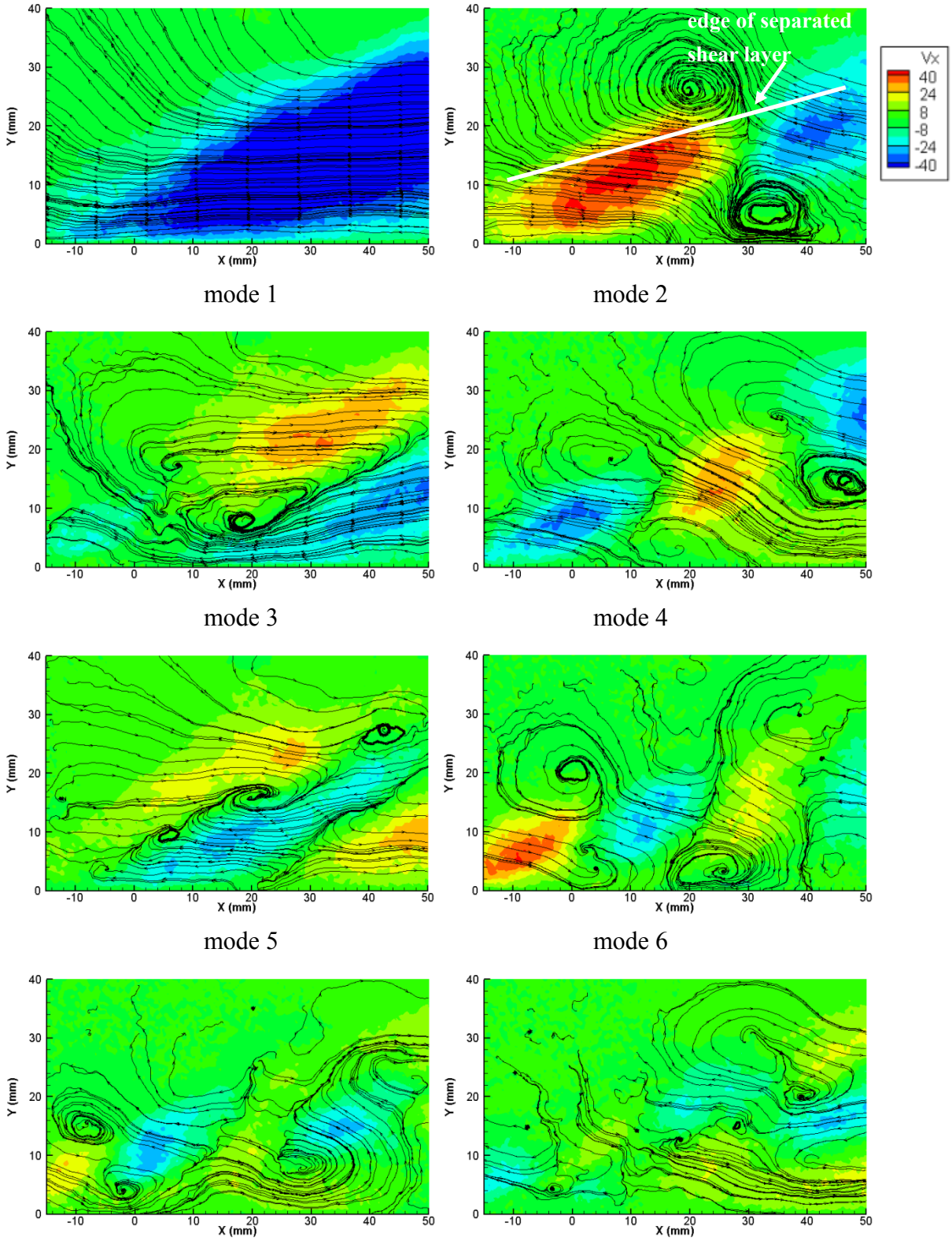

Figure 5.29: Topos of velocity for the case without actuation (contours of axial velocity and streamlines)

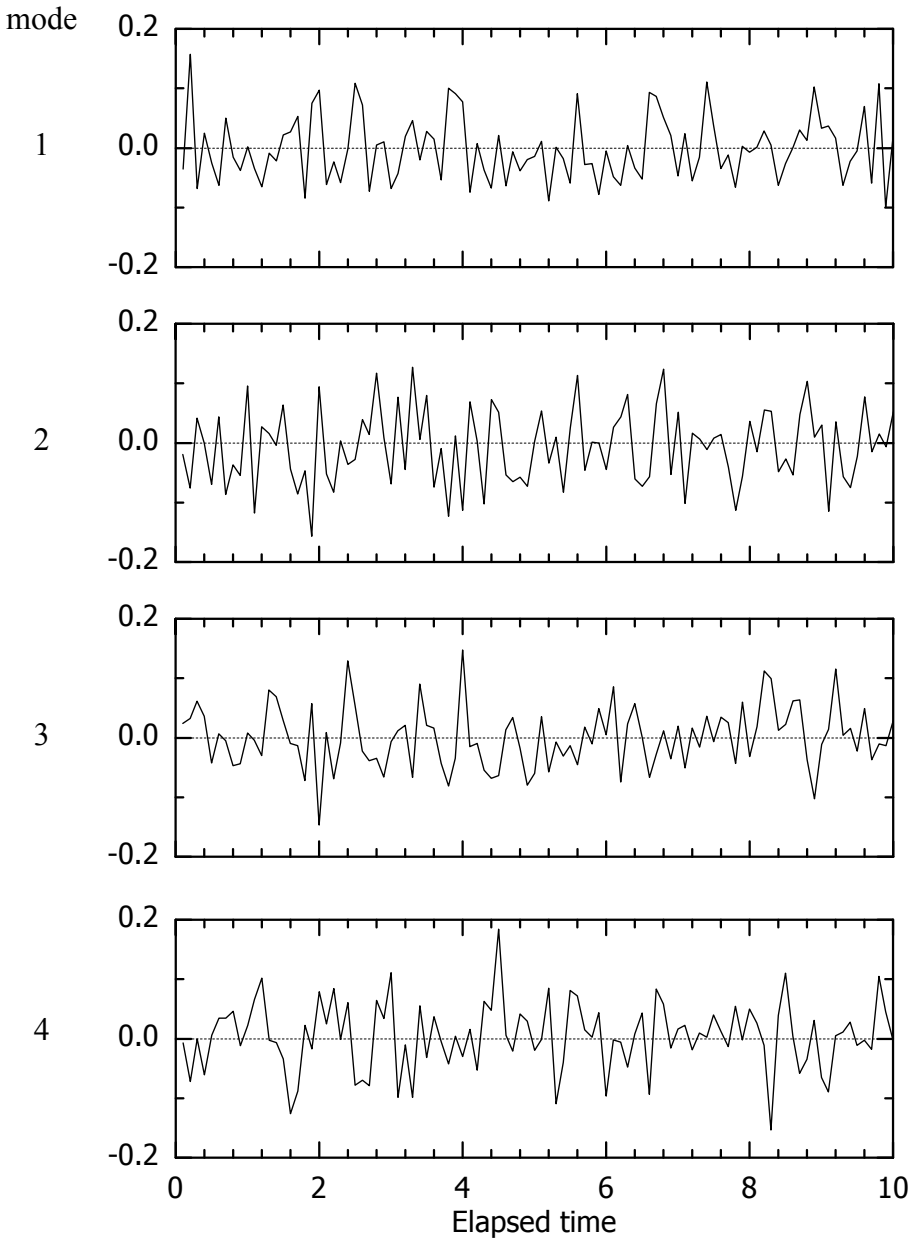

Figure 5.30: Chronos of velocity for the case without actuation

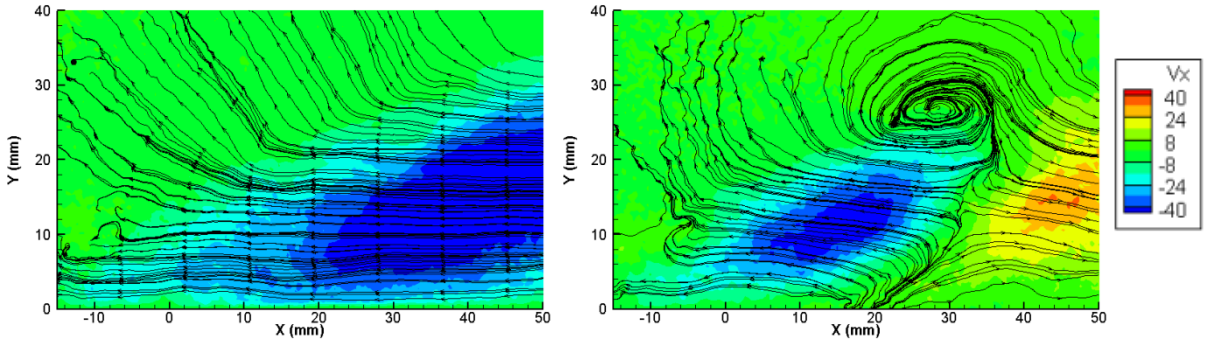

mode 1 mode 2

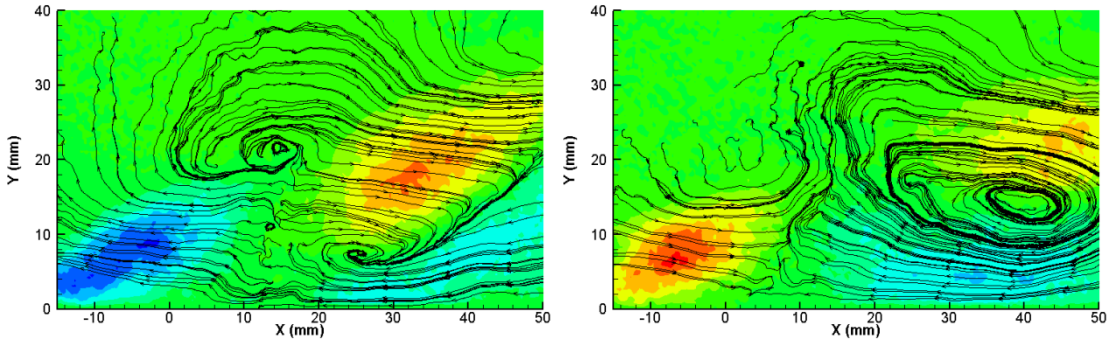

mode 3 mode 4

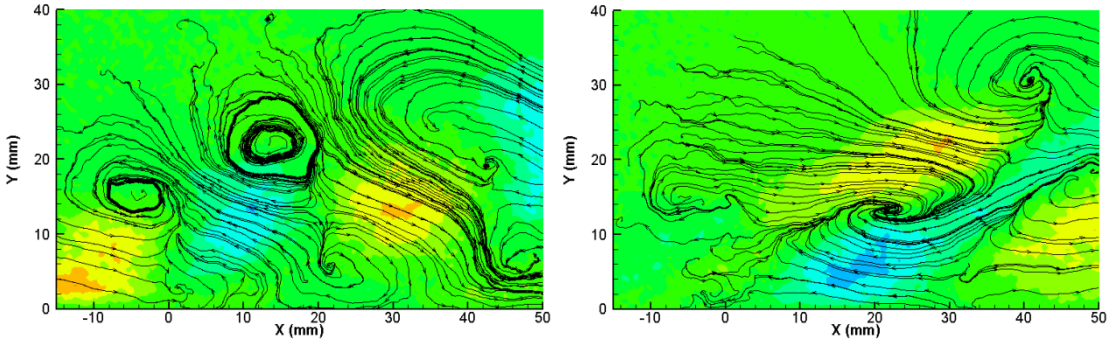

mode 5 mode 6

Figure 5.31: Topos of velocity for cases with continuous actuation at 47.1 kV_{pp}

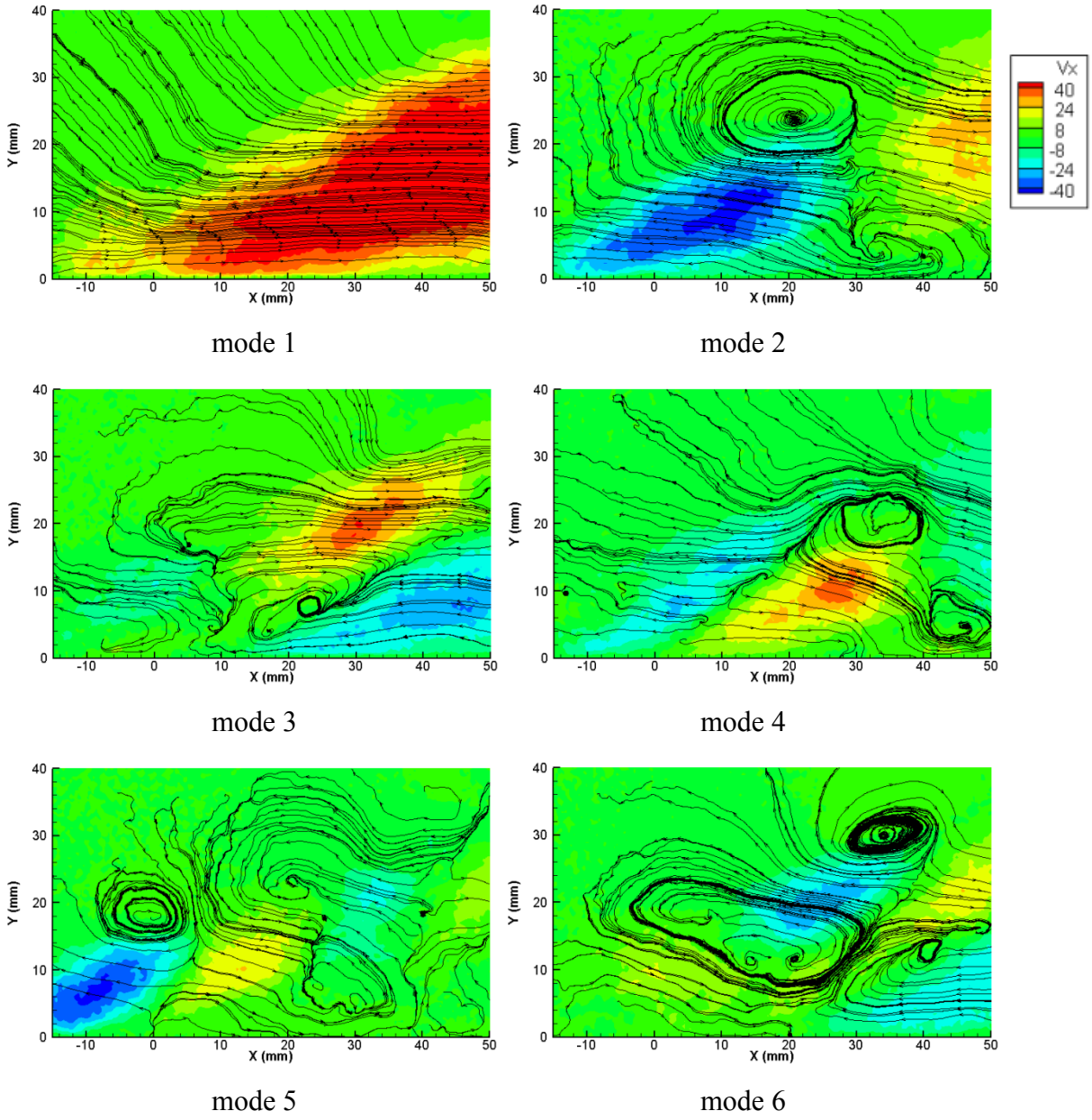

Figure 5.32: Topos of velocity for cases with pulsed actuation at 47.1 kV_{pp}, 40%, 40 Hz

Figure 5.33 shows the POD mode eigenvalues (energy distribution) for different cases. From this figure, it is observed that the POD converges rapidly, with the energy rapidly decreases with the mode number. The total energy of all modes is 100%. The case with continuous actuation has the lowest relative energy in the first mode, because the boundary layer separation is most reduced and the flow is more stable. For pulsed actuation, the case at the pulsed

frequency of 40 Hz (optimal frequency) has the highest energy in the first mode compared to 15 and 200 Hz, which corresponds to stronger fluctuation with large scale induced by pulsed actuation.

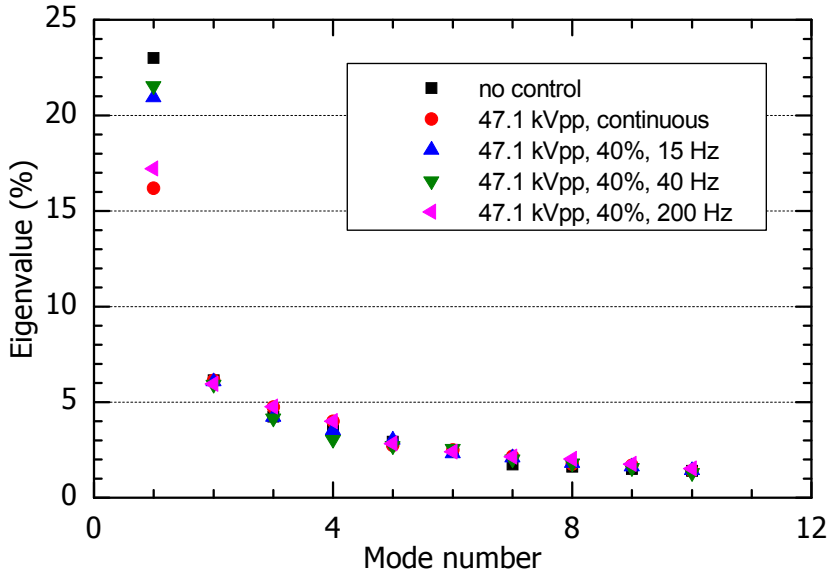

Figure 5.33: Energy distribution for different cases

5.5 Summary

Following the numerical study on separation control in 2-D diffusers in Chapter 4, the corresponding experimental study is carried on in this chapter, in order to look into the mechanism of plasma-based flow control, especially for the pulsed actuation. Both numerical and experimental studies on separation control in 2-D diffusers have demonstrated the effects of various parameters about plasma actuation and provide a guide for the application of plasma actuation in a realistic geometry, as presented in Chapter 6.

Chapter 6

Separation Control in S-shaped Ducts

In this chapter, the numerical simulation results without and with actuation in a 3-D S-shaped ITD are first compared with the experimental tests. Subsequently, the results of a numerical study using the validated CFD tool on the effects of plasma actuation parameters on boundary layer separation control and the loss reduction in the ITD are presented.

6.1 Boundary Layer Development in ITD Ducts

To demonstrate the effect of actuation in the ITD, flow characteristics without actuation are first investigated. The predicted pitchwise mass-averaged static pressure coefficients C_{ps} without actuation, and the corresponding measured pitchwise mass-averaged static pressure coefficients C_{ps} along the ITD end-walls are shown in Figure 6.1. The C_{ps} is defined as $(P_s - P_{sref}) / 0.5\rho V_{ref}^2$, where P_{sref} and V_{ref} are the static pressure and freestream velocity at the reference location upstream of swirl vanes (or the domain inlet for CFD simulations). The axial location is normalized by the duct axial length, and thus the axial positions 0 and 1 represent the first and last points of curvature change of the end-walls, respectively. The axial locations D1 (ITD inlet, normalized axial location of -0.09) to D5 (ITD outlet, normalized axial location of 1.18) serve as reference locations for subsequent contour plots. Please note that the freestream velocity at location D1 is about 30 m/s and the boundary layer can be regarded as turbulent as a result of the high turbulence level in the upstream flow.

As shown in Figure 6.1, along the casing, there is a favorable pressure gradient before the first bend, followed by a strong adverse pressure gradient between the first and second bends and then a weak favorable pressure gradient until the exit. The strong adverse pressure gradient over a large portion of the casing causes the boundary layer to separate, which will be shown in the flow visualization results. Along the hub, there is an adverse pressure gradient before the first

bend, and then the static pressure stays almost constant up to the second bend. There, a favorable pressure gradient is followed by a strong adverse pressure gradient from the second bend to the exit. The adverse pressure gradient in the two regions may cause boundary layer separation at the hub as well. Furthermore, due to the increasing effective flow area and the end-wall curvature, at the first bend, the static pressure at the casing is lower than that at the hub, while the opposite is true at the second bend. These radial pressure gradients tend to move fluid radially. In addition, the static pressure distribution from numerical simulations can capture the flow trend reasonably well. The deviation from the experimental data mainly comes from the casing downstream of the first bend, where the boundary layer separation arises (as observed by the slope change of C_{ps} versus axial location on casing in Figure 6.1). In other words, the numerical simulation predicts the separation on the casing further downstream than the experiment.

Flow visualization, contours of simulated shear stress and streamlines on the ITD casing without actuation are shown in Figure 6.2. The development of the measured mass-averaged total pressure coefficient C_{p0} $(=(P_0 - P_{0ref})/0.5\rho V_{ref}^2)$ along the duct without actuation is shown in Figure 6.3. In the definition of C_{p0}, P_{0ref} is the total pressure at the reference location upstream of swirl vanes (or the domain inlet for CFD simulations).

At the ITD inlet (location D1), the upstream wake is clearly shown by the regions of total pressure deficit. Since the upstream swirl vane has a constant exit angle distribution from casing to hub, the wake is almost normal to both the casing and hub at location D1. However, the wake is tilted along the ITD after location D1. As documented by Brookfield *et al.* (1996), the main sources of wake tilt are the initial blade twist angle, and the axial and tangential velocities. Due to the conservation of angular momentum, the tangential velocity decreases with the increased radius within the ITD. The local axial velocity is changed based on the increasing effective flow area and wall curvature. The axial velocity along the ITD hub decreases at the first bend, increases between the first and second bends, and then decreases again until the exit. The opposite occurs at the ITD casing region. Therefore, at the first bend, the casing region swirl

angle is reduced more quickly than the hub swirl, resulting in wake tilt in the opposite swirl direction. At the second bend, the hub swirl angle is decreased more rapidly than the casing swirl, which leads to a wake tilt in the swirl direction. Therefore, the wake is tilted clockwise at the first bend and counter-clockwise at the second bend.

In the hub region, due to the radial movement of the low momentum hub boundary layer and wake flow caused by the local radial pressure gradient (see Figure 6.1), a pair of hub counter-rotating vortices is formed. These hub counter-rotating vortices accumulate the hub region low momentum flow to form a high loss core at location D2. Due to the radial movement of the hub boundary layer and the favorable pressure gradient along the hub, the hub boundary layer remains relatively thin at locations D2, D3 and D4. The hub boundary layer separates around location D5 with highly 3-D features due to the streamwise adverse pressure gradient close to the exit.

In the casing region, the radial pressure at the first bend (see Figure 6.1) drives the wake low momentum radially into the casing boundary layer. This wake low momentum fluid accumulates into a low momentum core. Together with the casing streamwise adverse pressure gradient at the first bend, the casing boundary layer first separates in 3-D characteristics around location D2. Following this 3-D boundary layer separation, a whole annular boundary layer separation with 2-D characteristics is observed and persists until the second bend of the ITD. These casing boundary layer separation characteristics can be clearly detected in Figure 6.2. Note that the high total pressure loss is observed at locations D2 and D3 near the casing. In addition, due to the 3-D boundary layer and the radial pressure gradient at the second bend, a pair of casing counter-rotating vortices is generated, as shown at locations D4 and D5 in Figure 6.3.

The main observation above on flow visualization (see Figure 6.2(a)) can be also seen by the wall shear stress and streamlines from the numerical simulation (see Figure 6.2(b)). The boundary layer separation is associated with a low wall shear stress (near zero). However, the

onset location of casing boundary layer separation (around location D2) is predicted a little further downstream than that from experimental flow visualization (upstream of location D2). This is consistent with the static pressure coefficient distribution comparison in Figure 6.1.

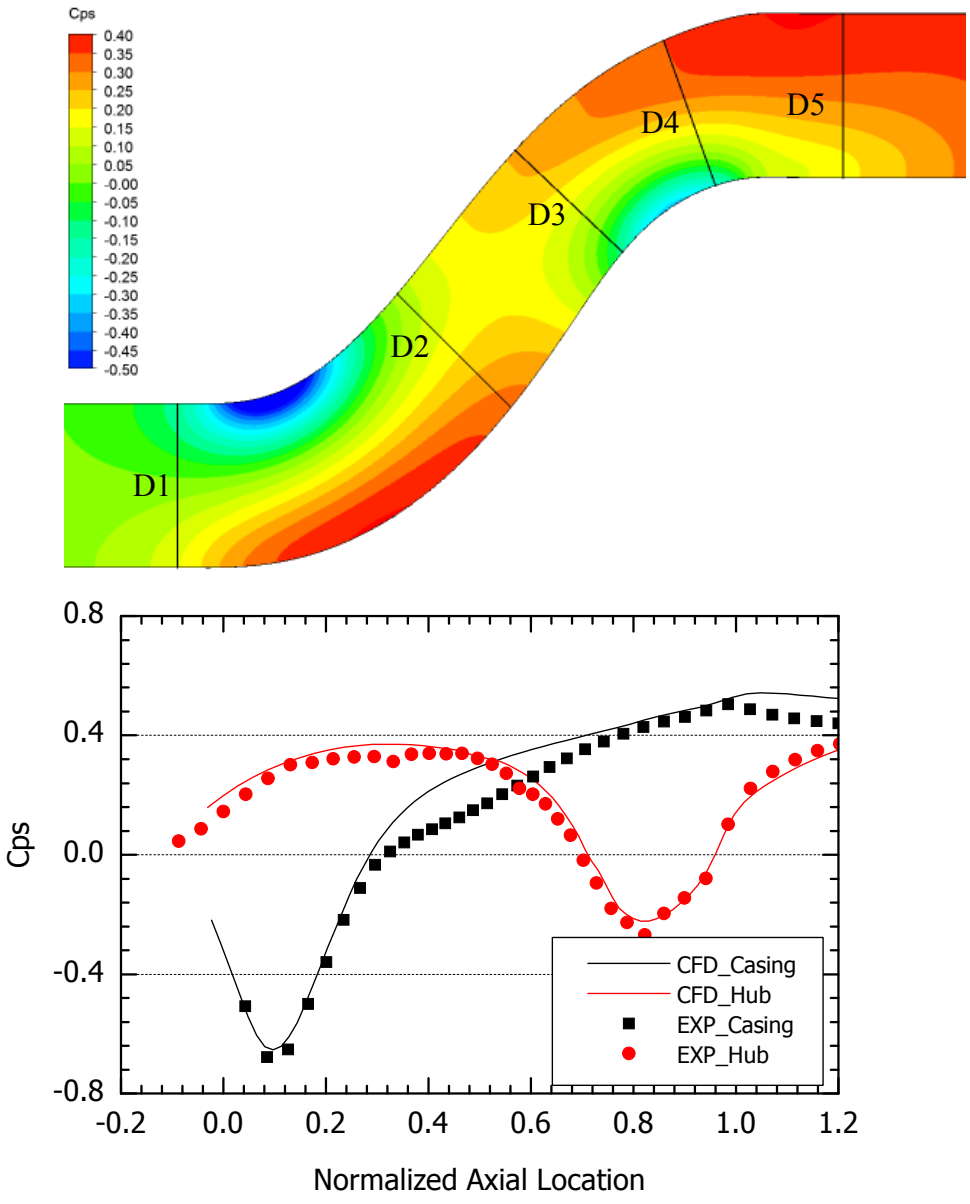

Figure 6.1: Pitchwise mass-averaged static pressure coefficients without actuation

To further validate the CFD results, the total pressure coefficients C_{p0} at the locations D1 to D5 without actuation from numerical simulations, as shown in Figure 6.4, are compared with the

above experimental data. At the locations D1 (ITD inlet) to D3, the numerical simulation captures the trend of C_{p0} very well. In contrast, at the locations D4 and D5 (ITD outlet), the numerical simulation captures the main structure of C_{p0} distribution. The main difference between prediction and experimental data results from the onset location and size of the casing boundary layer.

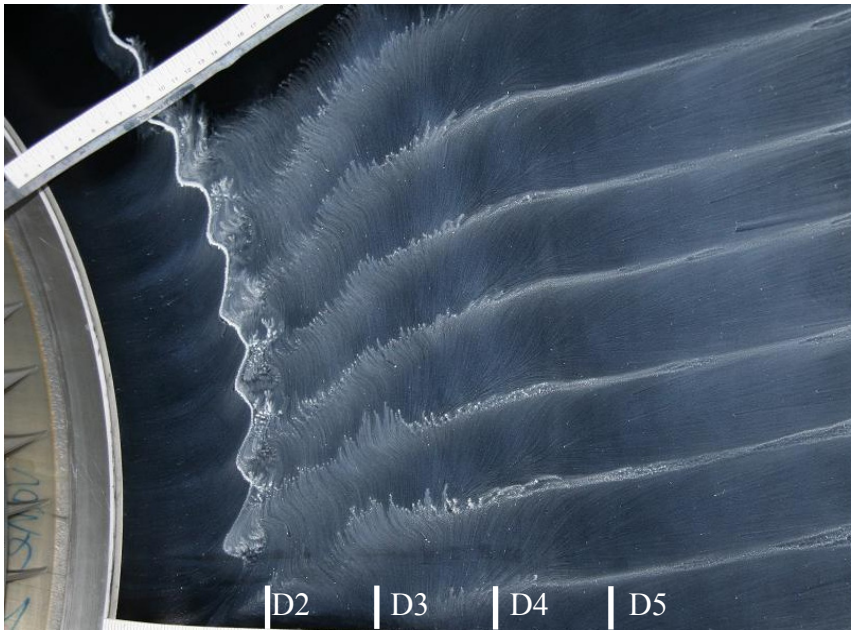

(a) flow visualization

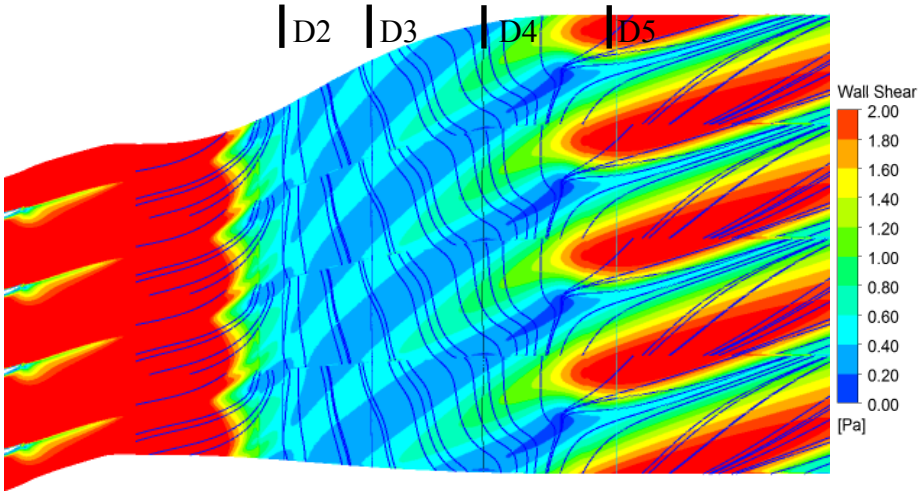

(b) simulated wall shear stress and streamlines

Figure 6.2: Flow visualization and simulated wall shear stress on ITD casing without actuation

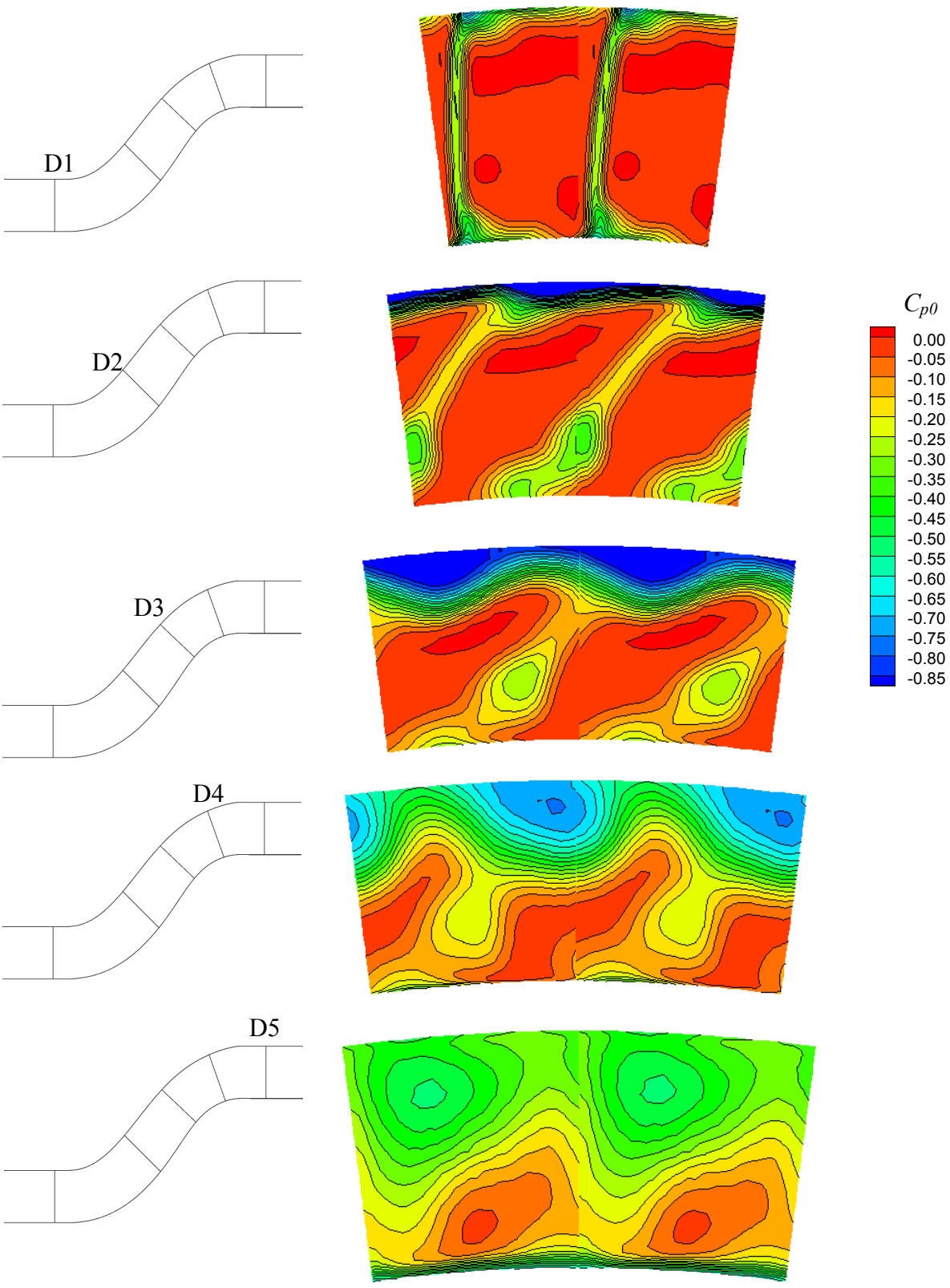

Figure 6.3: Development of measured total pressure coefficients along the duct without actuation

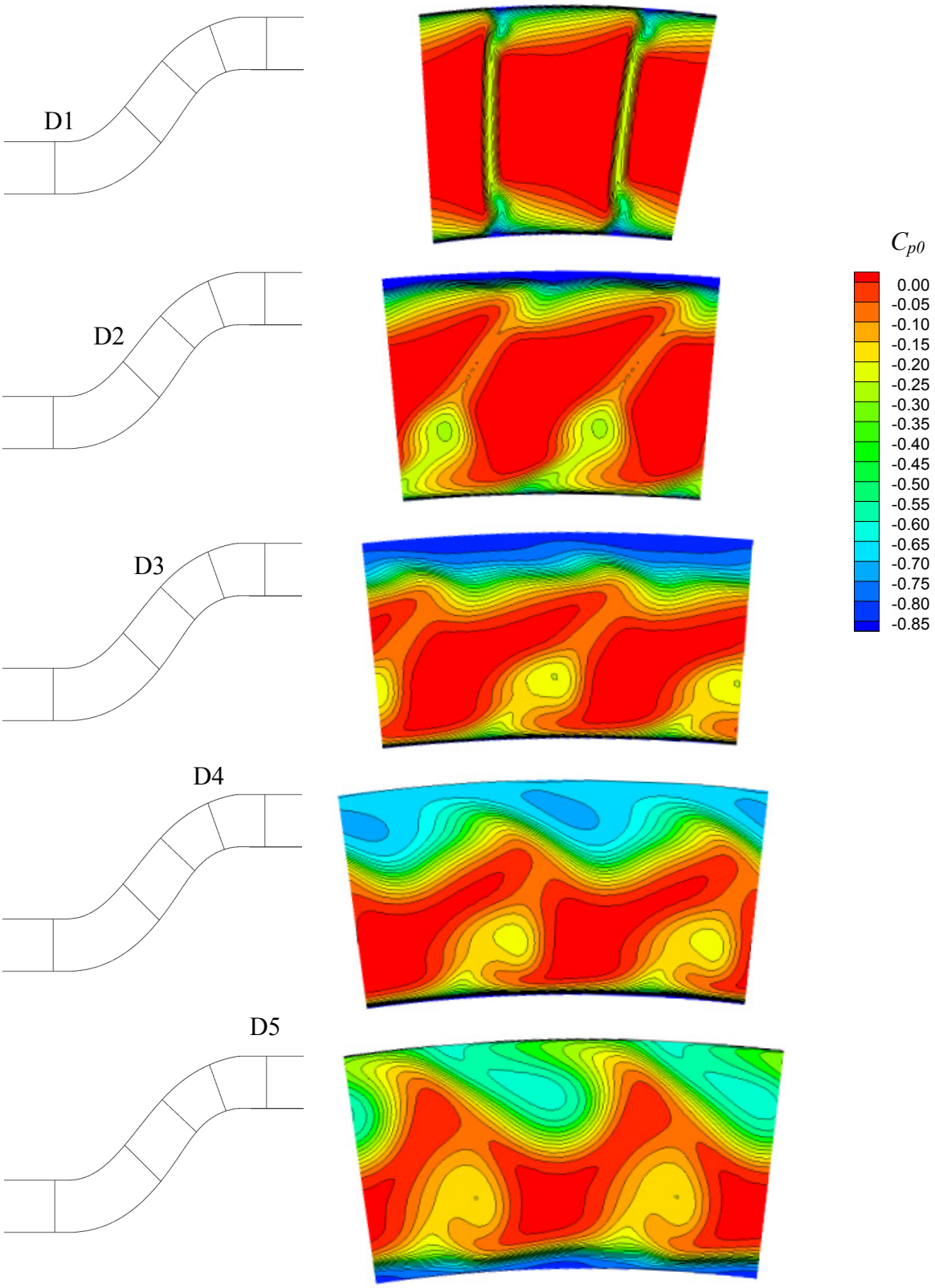

Figure 6.4: Development of simulated total pressure coefficients along the duct without actuation

6.2 Flow Control with Plasma Actuators in ITD Ducts

Total pressure loss in the above ITD occurs mainly near the casing, as shown in Figure 6.3. The plasma actuator is thus applied on the casing to control the boundary layer separation and reduce the total pressure loss there.

First, the numerical results with actuation are validated through comparison with the experimental results. Two plasma actuators are placed on the ITD casing, as shown in Figures 3.16 and 6.5. Each plasma actuator spans circumferentially on the casing and has a strength of about 60 mN/m, with the body force directed downstream. This chosen actuator strength is relatively low, because the actuator needs to be continuously run for at least 8 minutes in flow visualization measurement. To reduce the required time for flow visualization, the oil is put in dots instead of application on the whole surface. With actuation, the local reverse flow near the casing is modified to become streamwise, as shown by arrows in Figure 6.5(b). This can also be observed in the wall shear stress and streamlines from the numerical simulation (Figure 6.5(c)). Note that the boundary layer separation still exists upstream and downstream of the actuators. Because the actuator location is chosen too far downstream of the casing boundary layer separation due to the physical limit set by the location of the plastic window. However, the above discussion has demonstrated that CFD with integrated plasma actuator model can qualitatively simulate the effect of plasma actuation.

With this validation of the computational tool for a real application of plasma actuators, the effects of actuator location and actuator strength on ITD performance are further studied through numerical simulations. In this study, only one actuator in continuous mode is applied. The effect of plasma actuator location on ITD total pressure loss Y_p is shown in Figure 6.6, where Y_p is defined as

$$Y_p = C_{p0,C5} - C_{p0,C1} \tag{6.1}$$

where $C_{p0,C1}$ and $C_{p0,C5}$ are mass-averaged total pressure coefficient at location D1 and D5, respectively. The actuator strength is 300 mN/m. From Figure 6.6, the optimal actuator location

is observed at around normalized axial location 0.3, which is close to the boundary layer separation point from numerical simulation as shown in Figure 6.1. This observation is consistent with the discussion on optimal actuator location for boundary layer separation control in Section 4.2.

The effect of actuator strength on ITD total pressure loss Y_p is shown in Figure 6.7. The actuator is placed at the optimal location in Figure 6.6. Contours of simulated shear stress on the ITD casing with actuation are shown in Figure 6.8, while simulated total pressure coefficients at the ITD outlet (location D5) with actuation are shown in Figure 6.9. From Figure 6.7, the total pressure loss decreases with increasing actuator strength. With actuator strength of 90 mN/m, which can be experimentally achieved, the total pressure loss can be reduced by 1.4% of the reference dynamic pressure. The boundary layer separation on the casing is reduced with increasing actuator strength, as clearly shown in Figure 6.8. With actuator strength of 300 mN/m (Figure 6.8(c)), the boundary layer separation is almost fully suppressed as observed by the streamlines. From Figure 6.8, the actuator location can also be clearly identified, since the downstream shear stress is locally increased by plasma actuation. Note that the plasma actuation on the ITD casing has little effect on the separation on the hub as expected. This can be observed in the simulated total pressure coefficients at the ITD outlet with actuation in Figure 6.9. From this figure, the effect of plasma actuation is mainly on the casing boundary layer. The plasma actuation on the casing can re-energize the casing boundary layer and thus reduce the total pressure loss there. Even though the boundary layer separation on the casing is almost fully suppressed at actuator strength of 300 mN/m, the plasma actuation at 450 mN/m can further significantly reduce the total pressure loss (see Figure 6.9). This is because the casing boundary layer development is still the dominant loss source.

The required actuator strength to delay the separation point to a new location on the ITD casing can be also estimated by using the preliminary design rule established in Section 4.3. The input information for this estimation includes the pitchwise mass-averaged velocity profile

without actuation at the chosen actuator location and the static pressure distribution along the casing without actuation obtained from inviscid simulations. The required actuator strength is thus predicted by substituting the input information into Equations (4.7) and (4.9). In the following part, the case with continuous actuation at 180 mN/m (see Figure 6.8(b)) is taken as an example, because the boundary layer separation is not completely suppressed. To have the new separation point as that for the above case with 180 mN/m actuation, the required actuator strength is predicted as 230 mN/m (about 30% higher than the real strength of 180 mN/m). The conservative prediction above is qualitatively consistent with that applied in 2-D experiments shown in Section 5.3.1. In addition, the difference is partly due to the different actuator locations chosen, *i.e.*, associated with a shape factor H of 2.0 for the above case, while H of 2.5 for the preliminary design rule. Because the actuator location is chosen more upstream (smaller shape factor), the distance between the actuator location and the new separation point (also static pressure difference) is increased and thus the required actuator strength is predicted higher. Based on the above comparison, the preliminary design rule can be used to predict the required actuator strength with limited accuracy, and more work on it is still needed.

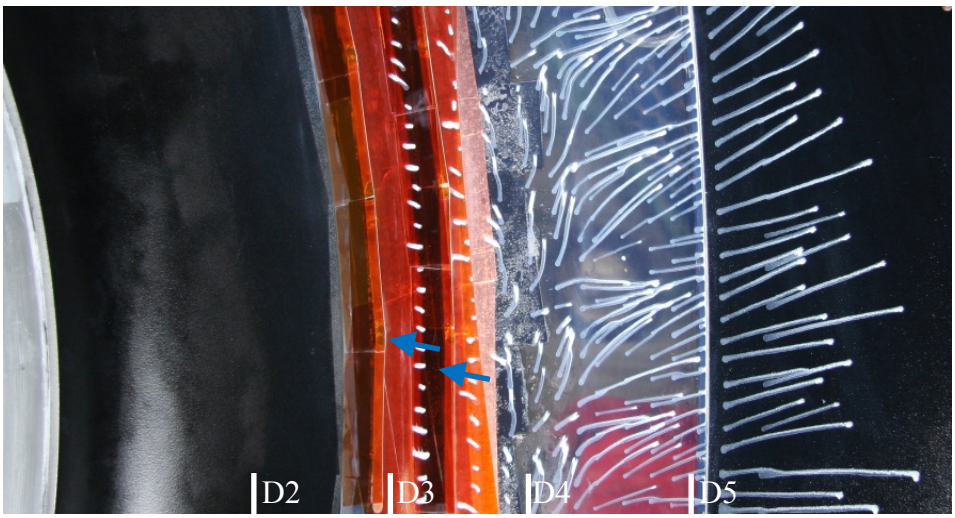

(a) oil dot flow visualization without actuation

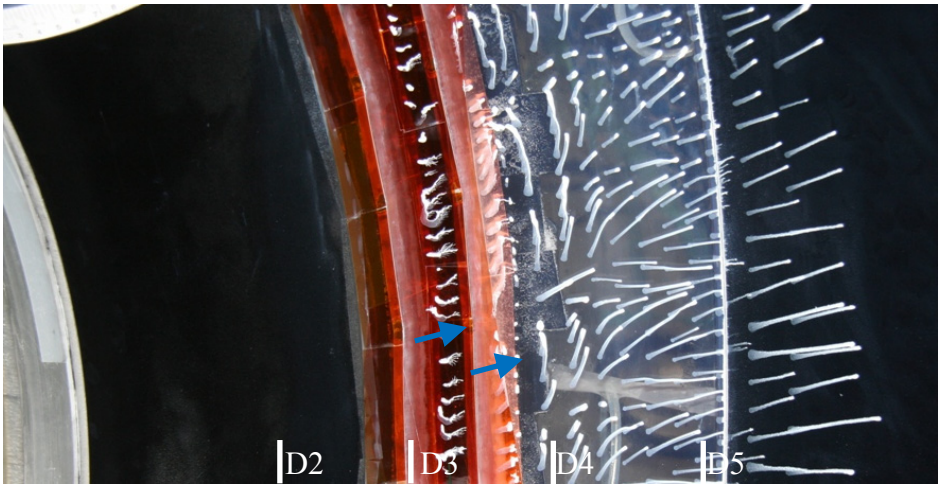

(b) oil dot flow visualization with actuation

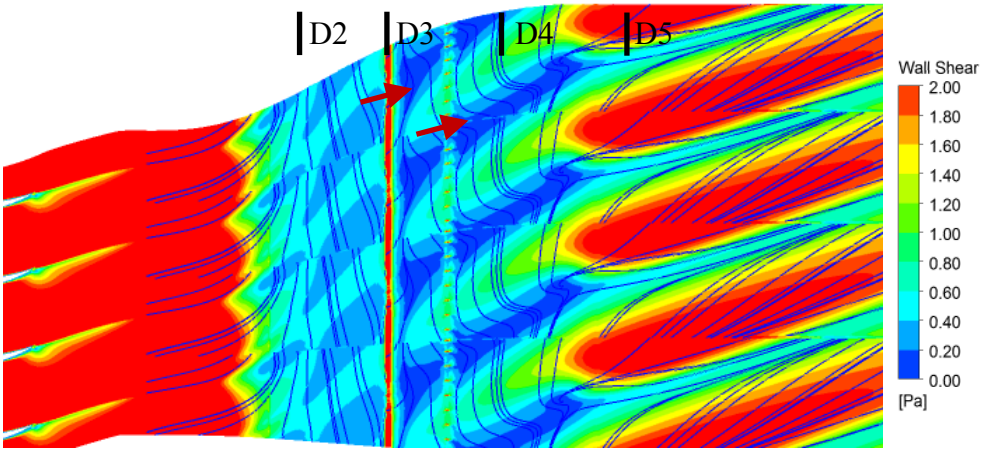

(c) simulated wall shear stress and streamlines with actuation

Figure 6.5: Flow visualization and simulated wall shear stress on ITD casing with actuation

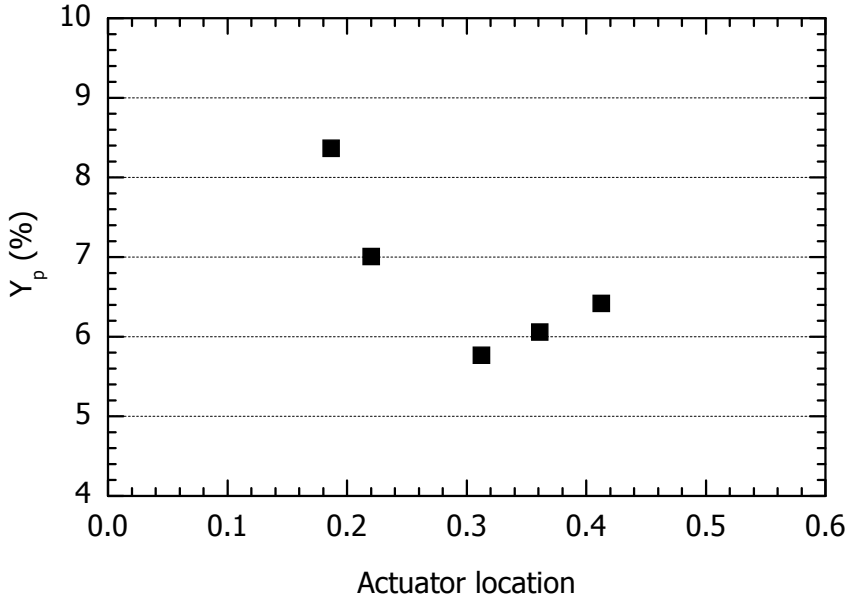

Figure 6.6: Effect of plasma actuator location (as normalized axial location) on ITD total pressure loss

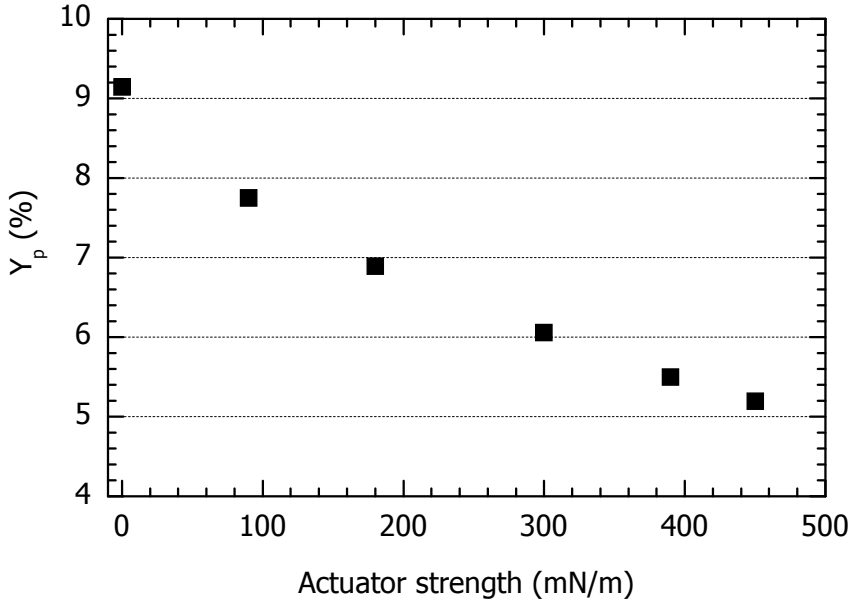

Figure 6.7: Effect of actuator strength on ITD total pressure loss for plasma actuator at optimal location in Figure 6.6

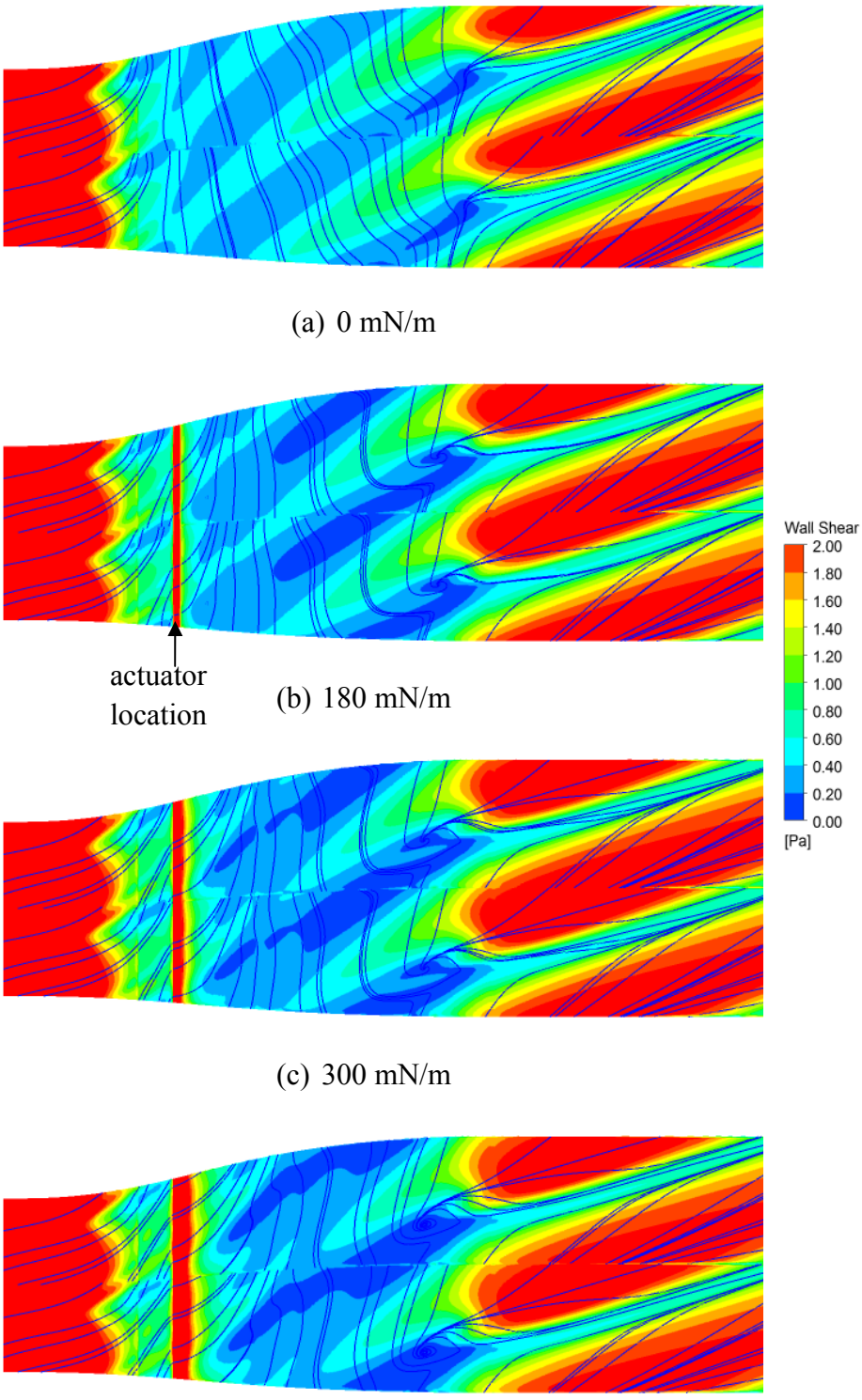

(a) 0 mN/m

(b) 180 mN/m

(c) 300 mN/m

(d) 450 mN/m

Figure 6.8: Contour of simulated wall shear stress on ITD casing with actuation

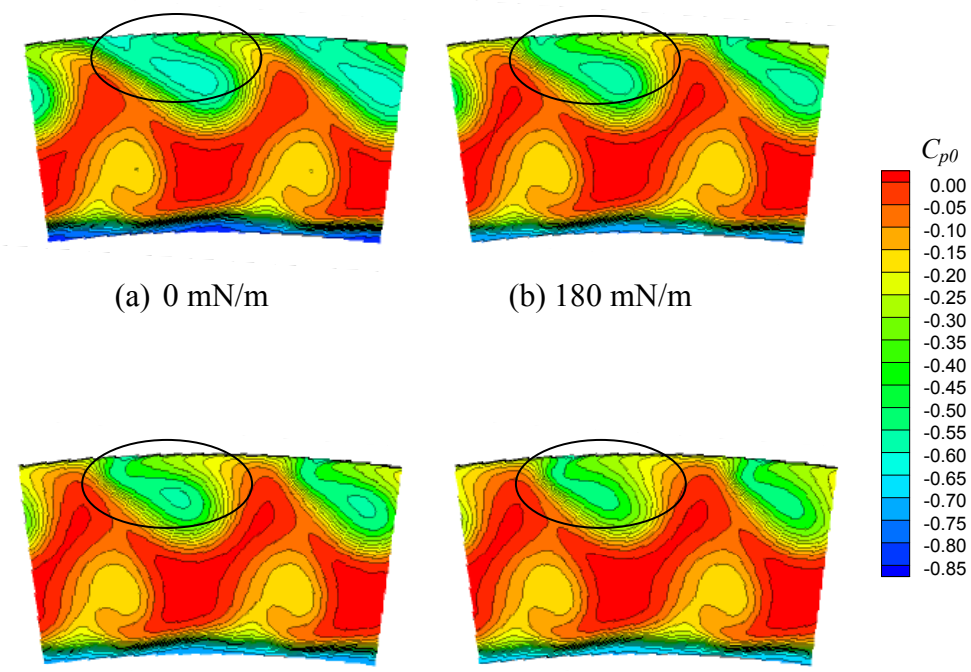

(a) 0 mN/m (b) 180 mN/m

(c) 300 mN/m (d) 450 mN/m

Figure 6.9: Simulated total pressure coefficients at ITD outlet with actuation

Chapter 7

Conclusions and Recommendations

The primary objective of the present work is to assess and demonstrate the concept of using DBD plasma actuators to suppress turbulent boundary layer separation, which is an important source of flow distortion and loss in aircraft engine ducts.

This research is carried out in three phases. The first is a numerical study to evaluate the concept in generic 2-D diffusers and to establish preliminary design rules in terms of actuator strength requirement. The second phase is an experimental demonstration of the concept in a 2-D diffuser. The final phase consists of a preliminary application of the concept and design rules to a realistic S-shaped inter turbine duct.

The main conclusions/findings are as follows:

1) The CFD software ANSYS CFX with integrated plasma actuator model can capture the main features of boundary layer separation, boundary layer transition and the effects of plasma actuation on the flow. Thus, it can serve as a numerical tool to study boundary layer flow control concepts with plasma actuators.
2) Plasma actuation can reduce turbulent boundary layer separation in both continuous and pulsed modes. The reduction increases with actuator strength. In pulsed mode, there exists a threshold in actuator strength below which the actuation is ineffective.
3) The optimal actuator location is generally close to the boundary layer separation point.
4) In the pulsed actuation mode, the optimal actuation frequency for suppression of turbulent boundary layer separation corresponds to a dimensionless frequency (based on freestream velocity and separation length) on the order of 1. This frequency is about equal to (within measurement resolution) the dominant frequency in the non-actuated flow. This implies that the most energetic turbulent structures in the boundary layer are amplified through resonance resulting in enhanced flow mixing between near-surface

low-momentum fluid and outer high-momentum fluid.

5) The effectiveness of turbulent boundary layer separation suppression increases with pulsed actuation duty cycle. However for optimum efficiency in terms of effectiveness versus power consumption, the duty cycle should be kept between 10% and 50%.
6) Pulsed actuation at the optimal actuation frequency is more effective than continuous actuation for the same effective actuation strength (power consumption).
7) Preliminary experiments and simulations of plasma actuation on an annular inter turbine transition duct indicate that plasma actuation concepts works in 3-D S-ducts with about the same optimal plasma actuator location as in 2-D diffusers and can be simulated with CFD.
8) Preliminary empirical design rules obtained from a numerical (CFD) parametric study of generic 2-D diffusers can give a rough conservative prediction of the plasma actuator strength required, even in 3-D ducts, for suppressing turbulent boundary layer separation in continuous actuation mode.
9) Proper orthogonal decomposition (POD) can be used to investigate more features of the flow, and the POD mode energy distribution can also quantify the effects of plasma actuation.

The contributions of this project are:

1) Numerical and experimental demonstration of control and suppression of turbulent boundary layer separation in 2-D diffusers and S-shaped engine ducts by plasma actuation.
2) Development of a computational tool that integrates plasma models into two commercial CFD codes (ANSYS CFX and FLUENT). This tool has already been used by other research students at École Polytechnique de Montréal to investigate novel concepts in plasma actuation for flight control and damping of flow-induced vibrations.
3) Improved experimental capability with construction of a new high-voltage plasma

generator and high actuator strength DBD plasma actuators obtained through experimental optimization, and development of preliminary design rules for the estimation of required plasma actuation strength for suppression of turbulent boundary layer separation.

Based on this research, the recommendations for future works include:

1) Improvement of design rules for continuous plasma actuation taking into account 2-D and 3-D effects on pressure distributions so as to provide more accurate predictions of required actuator strength.
2) Further development of design rules for turbulent boundary layer suppression to cover pulsed plasma actuation.

References

Anderson, B. H., Reddy, D. R., and Kapoor, K. (1994). Study on Computing Separating Flows within a Diffusing Inlet S-Duct. *Journal of Propulsion and Power, 10*(5), 661-667.

Arroyo, C., Axelsson, L. U., Håll, U., Johansson, G., Larsson, J., and Haselbach, F. (2006). Large-Scale Low-Speed Facility for Investigating Intermediate Turbine Duct Flows. AIAA Paper 2006-1312.

Aubry, N., Guyonnet, R., and Lima, R. (1991). Spatiotemporal Analysis of Complex Signals: Theory and Applications. *Journal of Statistical Physics, 64*(3-4), 683-739.

Axelsson, L. U., Arroyo, C., Cadrecha, D., and Johansson, G. (2007). Design, Performance Evaluation and Endwall Flow Structure Investigation of an S-Shaped Intermediate Turbine Duct. ASME Paper GT2007-27650.

Axelsson, L. U., and Johansson, G. (2008). Experimental Investigation of the Time-Averaged Flow in an Intermediate Turbine Duct. ASME Paper GT2008-50829.

Berrier, B. L., and Allan, B. G. (2004). Experimental and Computational Evaluation of Flush-Mounted, S-Duct Inlets. AIAA Paper 2004-0764.

Boeuf, J. P., Lagmich, Y., and Pitchford, L. C. (2009). Contribution of Positive and Negative Ions to the Electrohydrodynamic Force in a Dielectric Barrier Discharge Plasma Actuator Operating in Air. *Journal of Applied Physics, 106*, 023115.

Boeuf, J. P., and Pitchford, L. C. (2005). Electrohydrodynamic Force and Aerodynamic Flow Acceleration in Surface Dielectric Barrier Discharge. *Journal of Applied Physics, 97*(10), 103307.

Boxx, I. G., Woods, N. M., Newcamp, J. M., Franke, M. E., and Rivir, R. B. (2006). A PIV Study of a Plasma Discharge Flow-Control Actuator on a Flat Plate in an Aggressive Pressure

Induced Separation. ASME Paper GT2006-91044.

Brear, M. J., Warfield, Z., Mangus, J. F., Braddom, S., Paduano, J. D., and Philhower, J. S. (2004). Flow Separation within the Engine Inlet of an Uninhabited Combat Air Vehicle (UCAV). *Journal of Fluids Engineering, Transactions of the ASME, 126*(2), 266-272.

Castillo, L., Wang, X., and George, W. K. (2004). Separation Criterion for Turbulent Boundary Layers Via Similarity Analysis. *Journal of fluids Engineeing, 126*, 297-303.

Cherry, N. J., Hillier, R., and Latour, M. E. M. P. (1984). Unsteady Measurements in a Separated and Reattaching Flow. *Journal of Fluid Mechanics, 144,* 13-46.

Cierpka, C., Weier, T., and Gerbeth, G. (2007). Electromagnetic Control of Separated Flows Using Periodic Excitation with Different Wave Forms *Active Flow Control* (pp. 27-41). Berlin: Springer.

DalBello, T., Dippold, V., and Georgiadis, N. (2005). Computational Study of Separating Flow in a Planar Subsonic Diffuser.

Dominy, R. G., and Kirkham, D. A. (1995). The Influence of Swirl on the Performance of Inter-Turbine Diffusers. VDI Berichte 1186, 107-122.

Dominy, R. G., and Kirkham, D. A. (1996). The Influence of Blade Wakes on the Performance of Inter-Turbine Diffusers. *Journal of Turbomachinery, 118*, 347-352.

Dominy, R. G., Kirkham, D. A., and Smith, A. D. (1998). Flow Development through Inter-Turbine Diffusers. *Journal of Turbomachinery, 120*, 298-304.

Enloe, C. L., Font, G. I., McLaughlin, T. E., and Orlov, D. M. (2008). Surface Potential and Longitudinal Electric Field Measurements in the Aerodynamic Plasma Actuator. *AIAA Journal, 46*(11), 2730-2740.

Enloe, C. L., McLaughlin, T. E., VanDyken, R. D., Kachner, K. D., Jumper, E. J., and Corke, T. C. (2004). Mechanisms and Responses of a Single Dielectric Barrier Plasma Actuator:

Plasma Morphology. *AIAA Journal, 42*(3), 589-594.

Feng, Z., Lou, W., and Hourmouziadis, J. (1999). Numerical Study of Laminar-Turbulent Transition on a Plate in a Low-Speed Tunnel with Contoured Wall. *Journal of Thermal Science, 8*(2), 89-96.

Forte, M., Jolibois, J., Pons, J., Moreau, E., Touchard, G., and Cazalens, M. (2007). Optimization of a Dielectric Barrier Discharge Actuator by Stationary and Non-Stationary Measurements of the Induced Flow Velocity: Application to Airflow Control. *Experiments in Fluids, 43*(6), 917-928.

Göttlich, E., Marn, A., Pecnik, R., Malzacher, F. J., Schennach, O., and Pirker, H. P. (2007). The Influence of Blade Tip Gap Variation on the Flow through an Aggressive S-Shaped Intermediate Turbine Duct Downstream a Transonic Turbine Stage - Part Ⅱ: Time-Averaged Results and Surface Flow. ASME Paper GT2007-28069.

Gad-el-Hak, M. (2000). *Flow Control : Passive, Active, and Reactive Flow Management*. Cambridge, U.K. ; New York: Cambridge University Press.

Gaitonde, D. V., Visbal, M. R., and Roy, S. (2006). A Coupled Approach for Plasma-Based Flow Control Simulations of Wing Sections. AIAA Paper 2006-1205.

Guo, R. W., and Seddon, J. (1983). Swirl Characteristics of an S-Shaped Air Intake with Both Horizontal and Vertical Offsets. *Aeronautical Quarterly, 34*(pt 2), 130-146.

He, C., Corke, T. C., and Patel, M. P. (2007). Numerical and Experimental Analysis of Plasma Flow Control over a Hump Model. AIAA Paper 2007-935.

Hemon, P., and Santi, F. (2003). Applications of Biorthogonal Decompositions in Fluid-Structure Interactions. *Journal of Fluids and Structures, 17*(8), 1123-1143.

Herbst, A. H., and Henningson, D. S. (2006). The Influence of Periodic Excitation on a Turbulent Separation Bubble. *Flow, Turbulence and Combustion, 76*(1), 1-21.

Hoarau, Y., Braza, M., Ventikos, Y., and Faghani, D. (2006). First Stages of the Transition to Turbulence and Control in the Incompressible Detached Flow around a Naca0012 Wing. *International Journal of Heat and Fluid Flow, 27*(5), 878-886.

Hoskinson, A. R., and Hershkowitz, N. (2010). Differences between Dielectric Barrier Discharge Plasma Actuators with Cylindrical and Rectangular Exposed Electrodes. *Journal of Physics D: Applied Physics, 43*(6), 065205.

Hu, S., Zhang, Y., Zhang, X. F., and Vlasic, E. (2011). Influences of Inlet Swirl Distributions on an Inter-Turbine Duct: Part Ⅰ－ Casing Swirl Variation. ASME Paper GT2011-45554.

Huerre, P., and Monkewitz, P. A. (1990). Local and Global Instabilities in Spatially Developing Flows. *Ann. Rev. Fluid Mech., 22*, 473-537.

Hultgren, L. S., and Ashpis, D. E. (2003). Demonstration of Separation Delay with Glow-Discharge Plasma Actuators. AIAA Paper 2003-1025.

Jayaraman, B., and Shyy, W. (2008). Modeling of Dielectric Barrier Discharge-Induced Fluid Dynamics and Heat Transfer. *Progress in Aerospace Sciences, 44*(3), 139-191.

Jayaraman, B., Thakur, S., and Shyy, W. (2006). Modeling of Dielectric Barrier Discharge and Resulting Fluid Dynamics. AIAA Paper 2006-686.

Kiya, M., Shimizu, M., and Mochizuki, O. (1997). Sinusoidal Forcing of a Turbulent Separation Bubble. *Journal of Fluid Mechanics, 342,* 119-139.

Kriegseis, J., Dehler, T., Pawlik, M., and Tropea, C. (2009). Pattern-Identification Study of the Flow in Proximity of a Plasma Actuator. AIAA Paper 2009-1001.

Langtry, R. B. (2006). *A Correlation-Based Transition Model Using Local Variables for Unstructured Parallelized CFD Codes.* Ph.D., Universität Stuttgart.

Lemire, S., and Vo, H. D. (2008). *Reduction of Fan and Compressor Defect Using Plasma Actuation for Tonal Noise Reduction*. Paper presented at the ASME TURBO EXPO 2008

- Gas Turbine Technical Congress & Exposition: Power for Land, Sea and Air (GT2008).

Lemire, S., and Vo, H. D. (2011). Reduction of Fan and Compressor Wake Defect Using Plasma Actuation for Tonal Noise Reduction. *Journal of Turbomachinery, 133*(1), 11.

Little, J. C. (2010). *High-Lift Airfoil Separation Control with Dielectric Barrier Discharge Plasma Actuators*. Ph.D., The Ohio State University.

Macheret, S. (2008). Introduction: Weakly Ionized Plasmas for Propulsion Applications. *Journal of Propulsion and Power, 24*(5), 898-899.

Marn, A., Göttlich, E., Malzacher, F. J., and Pirker, H. P. (2009). The Effect of Rotor Tip Clearance Size onto the Separation Flow Though a Super-Aggressive S-Shaped Intermediate Turbine Duct Downstream of a Transonic Turbine Stage. ASME Paper GT2009-59934.

Marn, A., Göttlich, E., Pecnik, R., Malzacher, F. J., Schennach, O., and Pirker, H. P. (2007). The Influence of Blade Tip Gap Variation on the Flow through an Aggressive S-Shaped Intermediate Turbine Duct Downstream a Transonic Turbine Stage - Part I: Time-Averaged Results. ASME Paper GT2007-27405.

Mathis, R., Duke, D., Kitsios, V., and Soria, J. (2008). Use of Zero-Net-Mass-Flow for Separation Control in Diffusing S-Duct. *Experimental Thermal and Fluid Science, 33*(1), 169-172.

Mathis, R., Lebedev, A., Collin, E., Delville, J., and Bonnet, J. P. (2009). Experimental Study of Transient Forced Turbulent Separation and Reattachment on a Bevelled Trailing Edge. *Experiments in Fluids, 46*(1), 131-146.

Moreau, E., Sosa, R., and Artana, G. (2008). Electric Wind Produced by Surface Plasma Actuators: A New Dielectric Barrier Discharge Based on a Three-Electrode Geometry. *Journal of Physics D: Applied Physics, 41*(11), 115204.

Norris, G., and Dominy, R. G. (1997). Diffusion Rate Influences in Inter-Turbine Diffusers. *Journal of Power and Energy, 211*, Part A, 235-242.

Orlov, D. M., Apker, T., He, C., Othman, H., and Corke, T. C. (2007). Modeling and Experiment of Leading Edge Separation Control Using Sdbd Plasma Actuators. AIAA Paper 2007-0877.

Patel, M. P., Ng, T. T., Vasudevan, S., Corke, T. C., Post, M. L., McLaughlin, T. E., and Suchome, C. F. (2008). Scaling Effects of an Aerodynamic Plasma Actuator. *Journal of Aircraft, 45*(1), 223-236.

Pradeep, A. M., and Sullerey, R. K. (2006). Active Flow Control in Circular and Transitioning S-Duct Diffusers. *Journal of Fluids Engineering, Transactions of the ASME, 128*(6), 1192-1203.

Rizzetta, D. P., and Visbal, M. R. (2008). Plasma-Based Flow-Control Strategies for Transitional Highly Loaded Low-Pressure Turbines. *Journal of Fluids Engineering, Transactions of the ASME, 130*(4), 0411041-04110412.

Roth, J. R., and Dai, X. (2006). Optimization of the Aerodynamic Plasma Actuator as an Electrohydrodynamic (Ehd) Electrical Device. AIAA Paper 2006-1203.

Roy, S., and Gaitonde, D. V. (2006). Force Interaction of High Pressure Glow Discharge with Fluid Flow for Active Separation Control. *Physics of Plasmas, 13*(2), 023503.

Sanz, W., Kelterer, M., Pecnik, R., Marn, A., and Göttlich, E. (2009). Numerical Investigation of the Effect of Tip Leakage Flow on an Aggressive S-Shaped Intermediate Turbine Duct. ASME Paper GT2009-59535.

Schlichting, H. (1979). *Boundary Layer Theory* (7th ed.). New York: McGraw-Hill.

Seddon, J., and Goldsmith, E. L. (1999). *Intake Aerodynamics* (2nd ed.). Oxford: Blackwell Science ltd.

Shin, J., Narayanaswamy, V., Raja, L. L., and Clemens, N. T. (2007). Characterization of a Direct-Current Glow Discharge Plasma Actuator in Low-Pressure Supersonic Flow. *AIAA Journal, 45*(7), 1596-1605.

Shyy, W., Jayaraman, B., and Andersson, A. (2002). Modeling of Glow Discharge-Induced Fluid Dynamics. *Journal of Applied Physics, 92*(11), 6434-6443.

Singh, R. K., Singh, S., and Seshadri, V. (2008). Influence of the Inlet Shape on the Performance of Double Offset Transition S-Duct with Diffusion. *International Journal of Computational Methods, 5*(1), 1-19.

Slessor, M. D., Bond, C. L., and Dimotakis, P. E. (1998). Turbulent Shear-Layer Mixing at High Reynolds Numbers: Effects of Inflow Conditions. *Journal of Fluid Mechanics, 376*, 115-138.

Smith, B. L., and Glezer, A. (1998). The Formation and Evolution of Synthetic Jets. *Physics of Fluids, 10*(9), 2281-2297.

Sullerey, R. K., Mishra, S., and Pradeep, A. M. (2002). Application of Boundary Layer Fences and Vortex Generators in Improving Performance of S-Duct Diffusers. *Journal of Fluids Engineering, Transactions of the ASME, 124*(1), 136-142.

Sullivan, J. P., Murthy, S. N. B., Davis, R., and Hong, S. (1982). *S-Shaped Duct Flows*. Office of Naval Research Contract Number N-78-C-0701.

Suzen, Y. B., Huang, P. G., Jacob, J. D., and Ashpis, D. E. (2005). Numerical Simulation of Plasma Based Flow Control Applications. AIAA Paper 2005-4633.

Thomas, F. O., Corke, T. C., Iqbal, M., Kozlov, A., and Schatzman, D. (2009). Optimization of Dielectric Barrier Discharge Plasma Actuators for Active Aerodynamic Flow Control. *AIAA Journal, 47*(9), 2169-2178.

Visbal, M. R., and Gaitonde, D. V. (2006). Control of Vortical Flows Using Simulated Plasma

Actuators. AIAA Paper 2006-505.

Visbal, M. R., Gaitonde, D. V., and Gogineni, S. P. (1998). Direct Numerical Simulation of a Forced Transitional Plane Wall Jet. AIAA Paper 1998-2643.

Visbal, M. R., Gaitonde, D. V., and Roy, S. (2006). Control of Transitional and Turbulent Flows Using Plasma-Based Actuators. AIAA Paper 2006-3230.

Wellborn, S. R., Reichert, B. A., and Okiishi, T. H. (1994). Study of the Compressible Flow in a Diffusing S-Duct. *Journal of Propulsion and Power, 10*(5), 668-675.

Wu, Y. L., Ng, E. Y. K., and Wong, K. (2008). Numerical Study of the Swirl Flow in F-5e Intake with Subsonic Speeds. *Mathematical and Computer Modelling, 48*(3-4), 447-467.

Xu, X., Vo, H. D., Mureithi, N., and Zhang, X. F. (2010). Turbulent Boundary Layer Separation Control by Using DBD Plasma Actuators: Part Ⅰ－ Experimental Investigation. ASME Paper IMECE2010-37324.

Zhang, X. F., Hu, S., Benner, M., Gostelow, P., and Vlasic, E. (2010). Experimental and Numerical Study on an Inter-Turbine Duct. ASME Paper IMECE2010-37322.

Zhang, Y., Hu, S., Zhang, X. F., and Vlasic, E. (2011). Influences of Inlet Swirl Distributions on an Inter-Turbine Duct: Part Ⅱ－ Hub Swirl Variation. ASME Paper GT2011-45555.

Appendices

Appendix A: Preliminary Numerical Results

The preliminary numerical results on the suppression of laminar and laminar/turbulent separations by using plasma actuators are shown in the following part.

A.1 Laminar Boundary Layer Separation Suppression

The flow with only laminar separation is generated in the diffuser as shown in Figure 3.2 with moderate adverse pressure gradient. The throat plane is at x = 90 mm, and the exit plane is at x = 250 mm. To control this separated laminar boundary layer, various plasma actuation configurations are applied, as listed in Table 3. The cases with continuous actuation are run in steady state, while those with pulsed actuation in unsteady state. The actuator location is chosen at laminar separation point (LSP). As for the actuation direction, both co-flow and counter-flow are considered, as illustrated in Figure 3.4. The strength of plasma actuator (total body force) is 150 mN/m. It should be noted that this strength has been obtained in the Wind Tunnel Laboratory of Polytechnique and NRC GTL. In addition, a case with multiple actuators placed in series is also simulated.

Table 3: Simulation cases for laminar separation control

Actuation location	Actuation direction	Frequency & duty cycle	Strength (mN/m)	Note
laminar separation point (LSP)	co-flow	continuous	150	
	co-flow	continuous	150	3 actuators
	co-flow	100Hz, 50%	150	
	counter-flow	continuous	150	

Figure A.1 shows the contour of time-averaged turbulence kinetic energy (TKE) for the no-control case, while Figure A.2 zooms in on the pertinent region for the no-control case and those with different plasma actuation configurations. The TKE contours help to distinguish the laminar and turbulent boundary layers, and to assess the effects of plasma actuation on laminar boundary layer separation control. Please note that the vertical extent of the zoom-in region in Figure A.2 is expanded by a factor of two compared to the horizontal extent. Figure A.3 shows the time-averaged axial wall shear stress along the bottom plate for different cases. The zero

axial shear stress corresponds to the boundary layer separation or reattachment point.

For the no-control case, the boundary layer separates at x = 120 mm, and reattaches at x = 164 mm, as observed in Figure A.3. At the reattachment point, the boundary layer is already turbulent, as shown in Figure A.2(a). The actuation location is chosen at x = 116 mm, just upstream of the separation point. An actuator location near the separation point has been demonstrated by many authors (*e.g.*, Herbst and Henningson, 2006; Mathis *et al.*, 2008) to be effective in suppressing the boundary layer separation.

For the co-flow continuous actuation, the laminar separation can be delayed by one actuator and suppressed by three actuators, as shown in Figure A.3. The transition is delayed by using one actuator, as shown by the shift of the region of high TKE in Figure A.2(b). On the other hand, the transition is prevented by using three actuators, as shown by the disappearance of the region of high TKE in Figure A.2(c). The second and third actuator locations are chosen also near the delayed separation points, as seen from the jump of wall shear stress distribution along the plate in Figure A.3. It should be noted that, by the actuation of three actuators, the laminar separation is suppressed, the boundary layer is always kept laminar, and thus the wall shear stress (skin-friction drag) is relatively low compared to turbulent boundary layer.

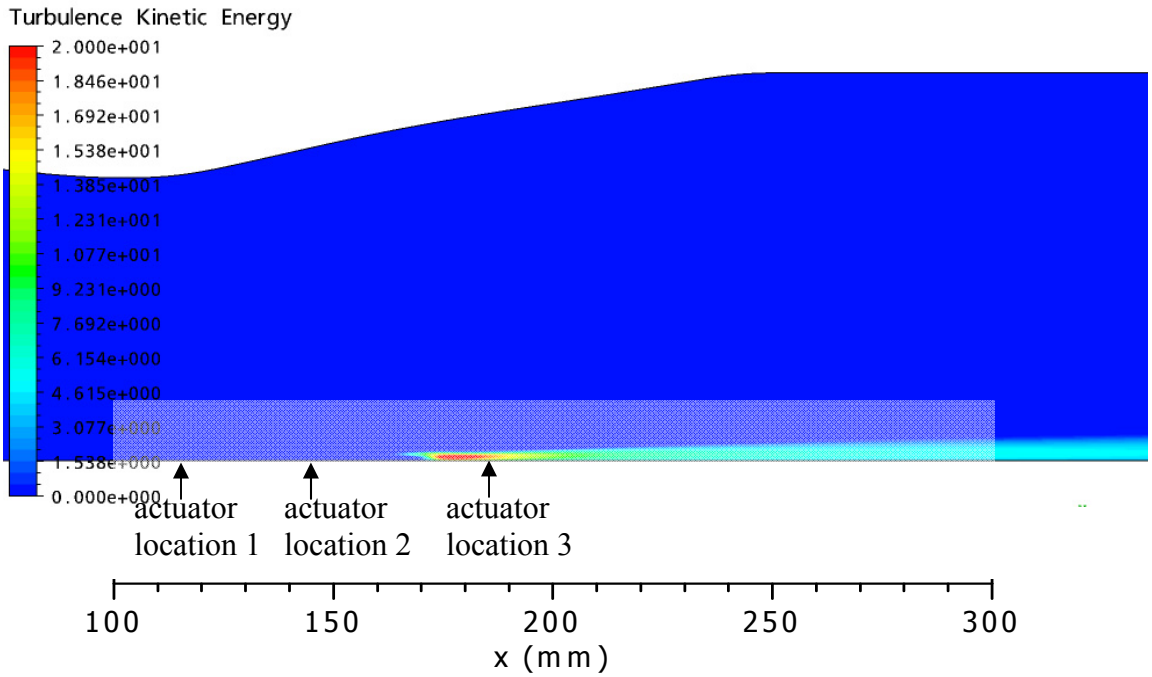

Figure A.1: Contour of TKE for laminar separation case without actuation

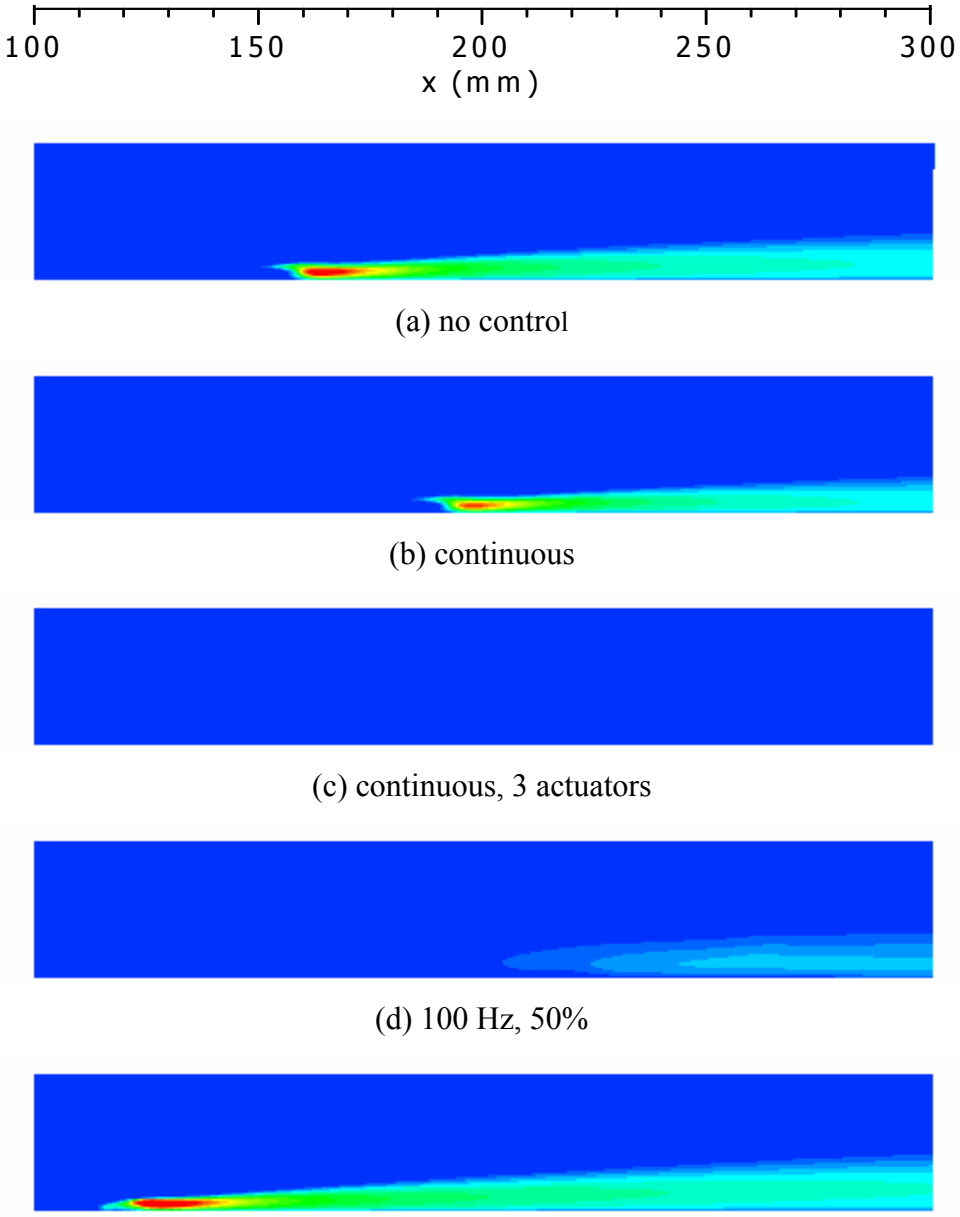

(a) no control

(b) continuous

(c) continuous, 3 actuators

(d) 100 Hz, 50%

(e) continuous, counter-flow

Figure A.2: Contours of time-averaged TKE for different cases in laminar separation control (vertical extent expanded by a factor of two)

For the co-flow pulsed actuation, the laminar separation is also delayed. Moreover, the transition length is extended such that the boundary layer is not fully turbulent at the diffuser exit (a fully-turbulent boundary layer should have a distribution of axial wall shear stress similar to that downstream of x = 210 mm for continuous actuation in Figure A.3).

For the counter-flow continuous actuation, the plasma actuation triggers the early transition,

by inducing strong local separation. From Figure A.3, both the length of the laminar separation bubble and length of separation-induced transition are decreased. The thereafter turbulent boundary layer (see Figure A.2(e)) can better endure the adverse pressure gradient and keep the flow attached, when compared to the original laminar boundary layer.

In summary, for a moderate adverse pressure gradient, the co-flow actuation, both continuous and pulsed, can delay or suppress the laminar separation, while at the same time the boundary layer can be kept laminar for a longer distance. In contrast, the counter-flow continuous actuation can suppress the laminar separation by inducing early transition over a shorter distance and make the boundary layer turbulent over a longer extent.

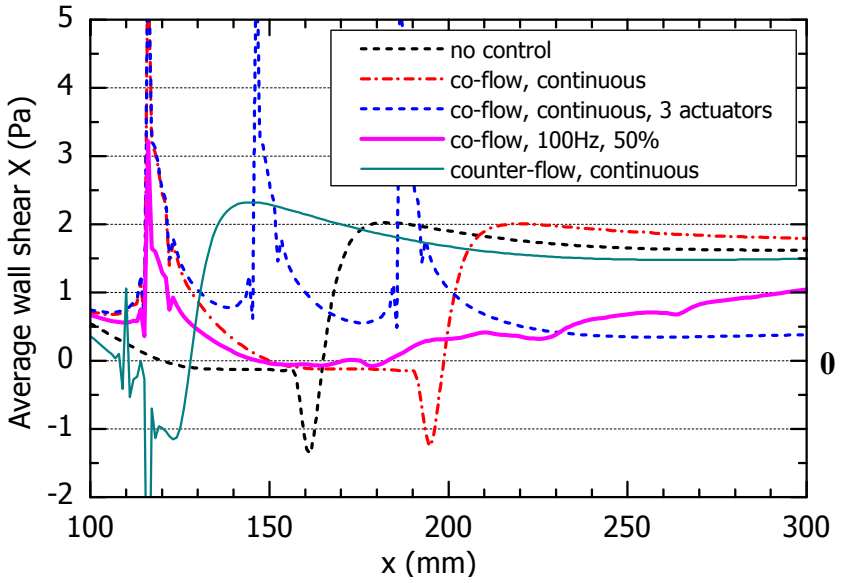

Figure A.3: Time-averaged axial wall shear for different cases in laminar separation control

A.2 Turbulent Boundary Layer Separation Suppression

The following work numerically studies the influence of different actuation parameters (*e.g.*, actuation location, direction and frequency) on suppression of tougher turbulent boundary layer separation. All the simulations are run in unsteady mode, because unsteady information need to be acquired for both flows without actuation and with pulsed actuation. Figure A.4 shows contours of the time-averaged axial velocity without actuation in the diffuser of Figure 3.3. The area-averaged throat velocity for the no-control case is U_{throat} = 34 m/s. Note that in the

parametric study, the origin of coordinates is referred to the leading edge of the bottom plate (see Figure 3.3). As such, the throat plane is at x = 110 mm, and the exit plane is at x = 280 mm. A boundary layer separation can be clearly observed in Figure A.4. This separation includes a laminar separation, separation-induced transition and a turbulent separation, as indicated by the time-averaged axial wall shear stress distribution in Figure A.5, where the zero axial shear stress corresponds to the separation or reattachment points. Figure A.5 also shows the absence of turbulent reattachment of the boundary layer due to the high adverse pressure gradient. The turbulent region is downstream of the location with minimum axial wall shear stress (Langtry, 2006). Two actuation locations are chosen as x = 120 mm (LSP, at the laminar separation point), and x = 160 mm (TRP, a location in the turbulent region). In addition, four monitor points are chosen in the flow field to capture the unsteadiness/instabilities which will be used for determining the pulsed actuation frequencies. These four monitor points correspond to the regions of the separated shear layer (point 1), core flow (point 2), turbulent separation (point 3) and edge of turbulent separation (point 4), respectively. The actuator locations and monitor points are indicated in Figure A.4. Table 4 summarizes all the simulated cases. The actuator strength is chosen as 300 mN/m as an obtainable force in the near future (a plasma force of 200 mN/m has been recently achieved by Thomas *et al.* (2009)). In addition, both co-flow and counter-flow actuations are investigated. The counter-flow actuation is chosen because counter-flow actuation even with low strength can induce perturbations in the flow and trigger laminar-turbulent transition to prevent the laminar separation (Visbal *et al.*, 2006) and may also be effective in resonating turbulent structures.

The time evolution of the velocity component normal to the wall at the four monitor points are captured for the no-control case. The normal velocity in the core flow region (point 2) is almost constant versus time, while the normal velocities at other three regions are unsteady. Figure A.6 shows time evolution of normal velocities at point 1 (separated shear layer) and point 3 (turbulent separation) for the no-control case. Spectral analysis is carried out on the signals at these two points, and the results are shown in Figure A.7. Although not shown, the power spectrum for point 4 (edge of turbulent separation) is similar to that for point 3. Three resonant frequencies, close to 100 Hz, 200 Hz and 400 Hz, are present in both regions (points 1 and 3). This indicates that large-scale vortices are shed from the separation bubble at those frequencies (Cherry *et al.*, 1984). The frequency of 2000 Hz corresponds to the Kelvin-Helmholtz instability

of the separated shear layer. The dimensionless frequencies $F^+ = fL_{se}/U_\infty$ corresponding to these frequencies are 0.91, 1.82, 3.65 and 18.25, respectively (based on a reattachment length, a distance between separation and reattachment points, L_{se} = 0.31 m and a freestream velocity at the separation point $U_\infty = 34$ m/s without actuation). The frequencies of 50 Hz (sub-harmonic frequency of 100 Hz), 100 Hz, 200 Hz, 400 Hz and 2000 Hz are chosen to assess the effect of the actuation frequency on boundary layer separation suppression. As for the parametric study of actuation location and direction with pulsed actuation, the frequency of 100 Hz (an optimal frequency) is adopted. The duty cycle is chosen as 30% (duty cycle for pulsed actuation is usually chosen to be smaller than 50% (Visbal and Gaitonde, 2006)).

Figure A.6 also shows time evolution of normal velocities for cases with continuous and pulsed actuation at the TRP (cases T1 and T3). The normal velocity for the continuous actuation is constant with time, while periodically fluctuating for pulsed actuation. This fluctuation period is equal to the inverse of actuation frequency of 100 Hz, and also corresponds to the period of fluctuation in the uncontrolled flow. The periodic fluctuation implies that either the flow with pulsed actuation is more organized or that the large-scale structures with the frequency of 100 Hz within the boundary layer are amplified.

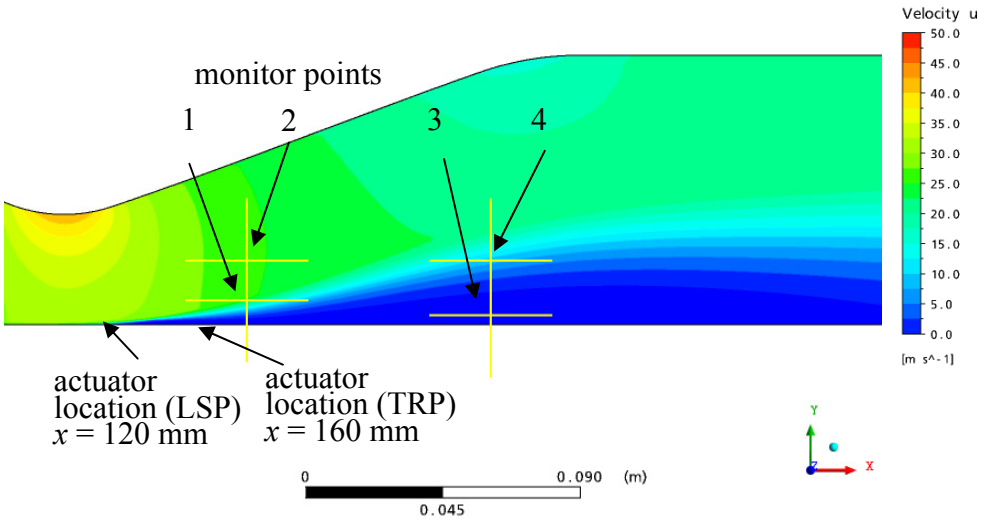

Figure A.4: Contour of time-averaged axial velocity without actuation with indicated monitor points

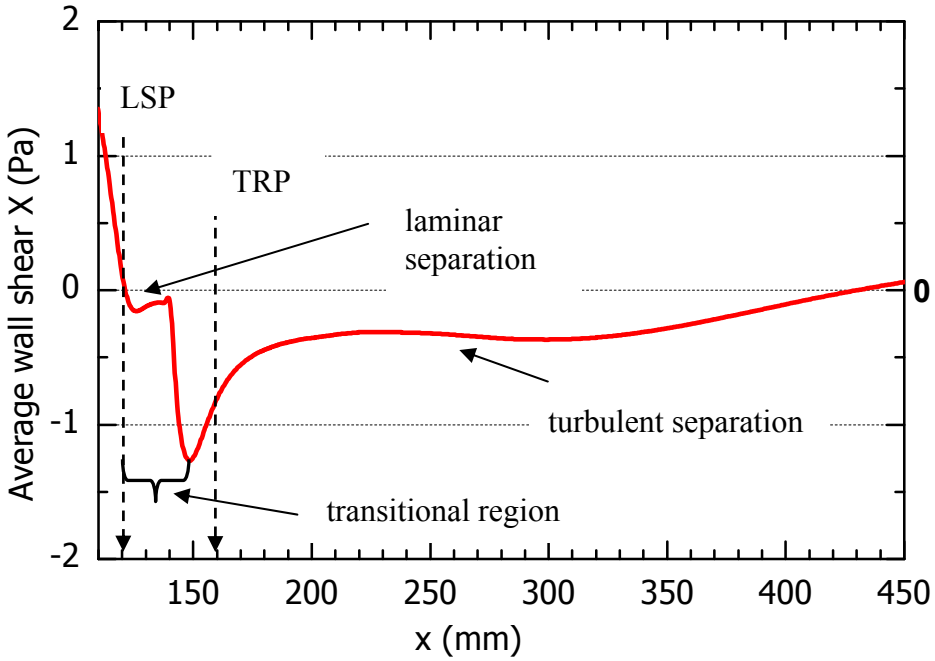

Figure A.5: Time-averaged axial wall shear stress along the plate in Figure A.4 without actuation

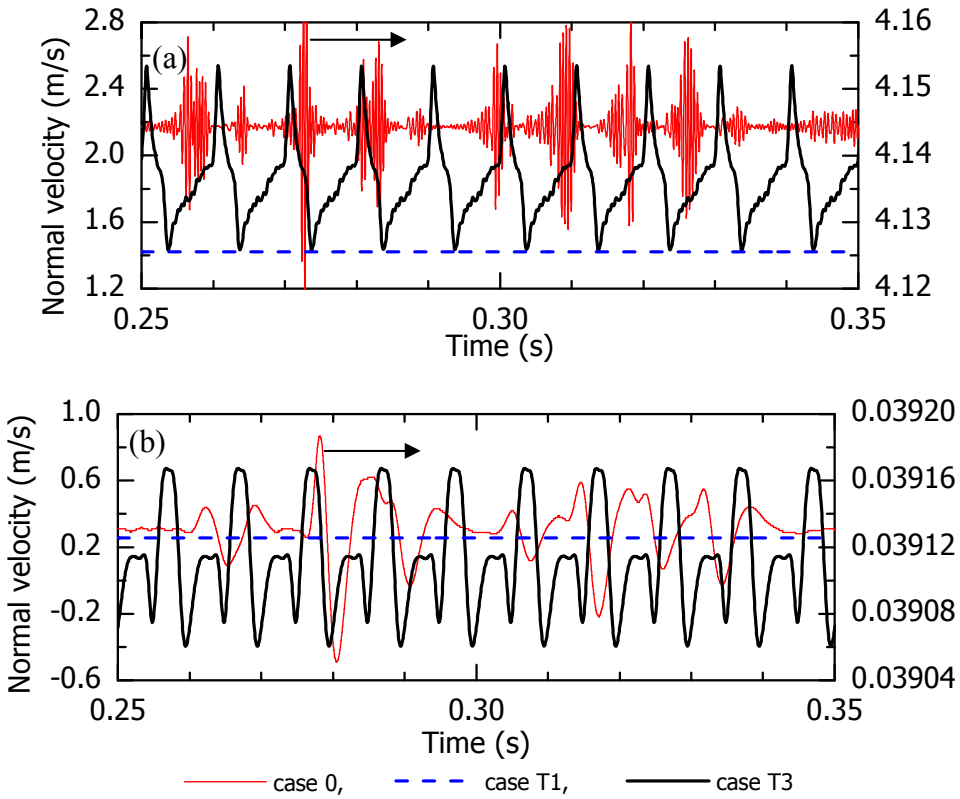

Figure A.6: Time evolution of normal velocities at monitor points: (a) point 1 (separated shear layer region), (b) point 3 (turbulent separation region)

Table 4: Pressure recovery for different cases with laminar/turbulent separation

Case number	Actuation location	Actuation direction	Frequency & duty cycle	Actuator strength (mN/m)	Pressure recovery η_p
0	no control				-0.568
L1	laminar separation point (LSP)	co-flow	continuous	300	0.426
L2		co-flow	100Hz, 30%	300	0.350
L3		co-flow	200Hz, 30%	300	0.364
L4		co-flow	400Hz, 30%	300	0.370
L5		co-flow	2000Hz, 30%	300	0.153
L6		counter-flow	100Hz, 30%	300	0.043
T1	location in turbulent region (TRP)	co-flow	continuous	300	0.383
T2		co-flow	50Hz, 30%	300	0.217
T3		co-flow	100Hz, 30%	300	0.223
T4		co-flow	200Hz, 30%	300	0.214
T5		co-flow	400Hz, 30%	300	0.181
T6		counter-flow	100Hz, 30%	300	-1.700

Figure A.8 shows the contours of time-averaged axial velocity with actuation, while Figure A.9 shows the contours of instantaneous axial velocity for several cases with pulsed actuation. The time-averaged axial wall shear stress along the bottom plate is shown in Figure A.10 for the actuation at the laminar separation point (LSP) and at the location in turbulent region (TRP), respectively. To compare the global effect of different actuation modes, the pressure recovery coefficient η_p is adopted, as defined in Equation (4.1). The pressure recovery for different cases is listed in Table 4.

The results in Table 4 indicate that for the same actuation location, *i.e.*, LSP or TRP, co-flow continuous actuation provides the highest pressure recovery, followed by co-flow pulsed actuation, with counter-flow pulsed actuation giving the lowest. In pulsed mode, the actuator strength of 300 mN/m (for pulsed mode, this is the strength when actuator is on) is the same, but the power consumption is only a fraction (equal to the duty cycle) of that of continuous actuation. If one compares the effect of plasma actuation location, *i.e.*, keeping other parameters the same, the actuation location at the LSP is found to surpass that at the TRP for both continuous and pulsed actuation. The pulsed actuation at the LSP at 400 Hz (case L4) has the pressure recovery (η_p = 0.370) close to that for the continuous actuation at the TRP (case T1, η_p = 0.383), while

with only 30% momentum input (power consumption).

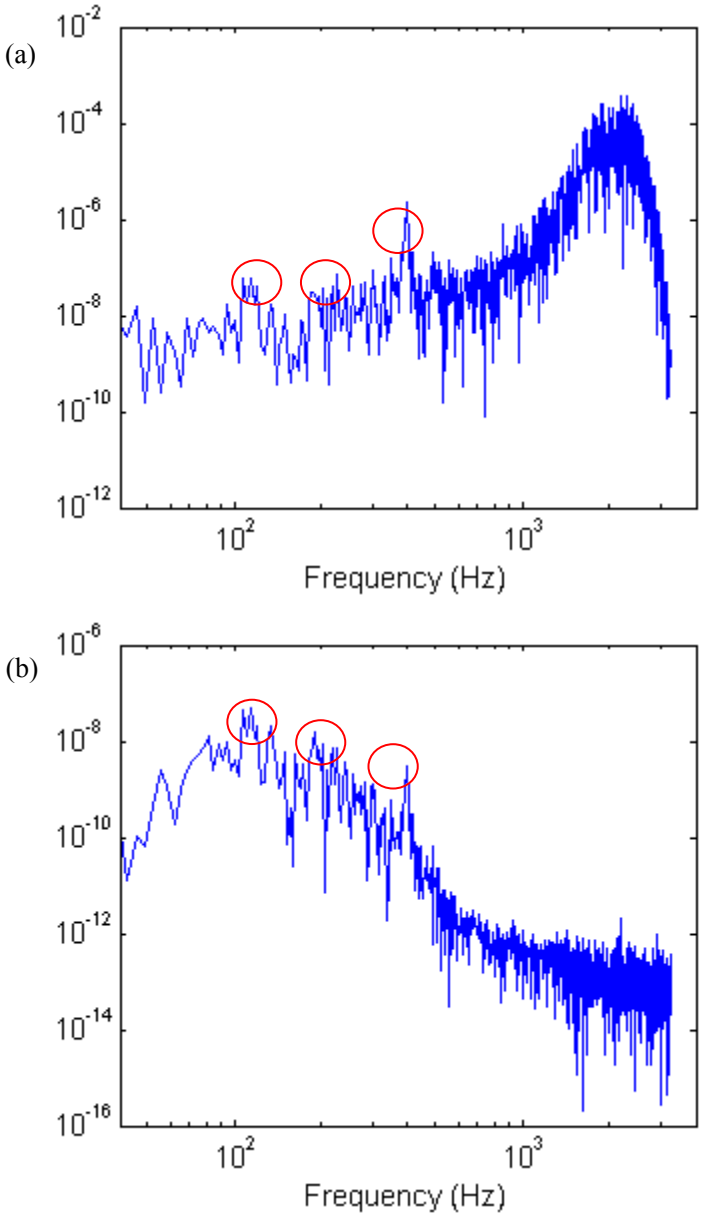

Figure A.7: Spectral analysis of normal velocities without actuation at two monitor points: (a) separated shear layer region (point 1), (b) turbulent separation region (point 3)

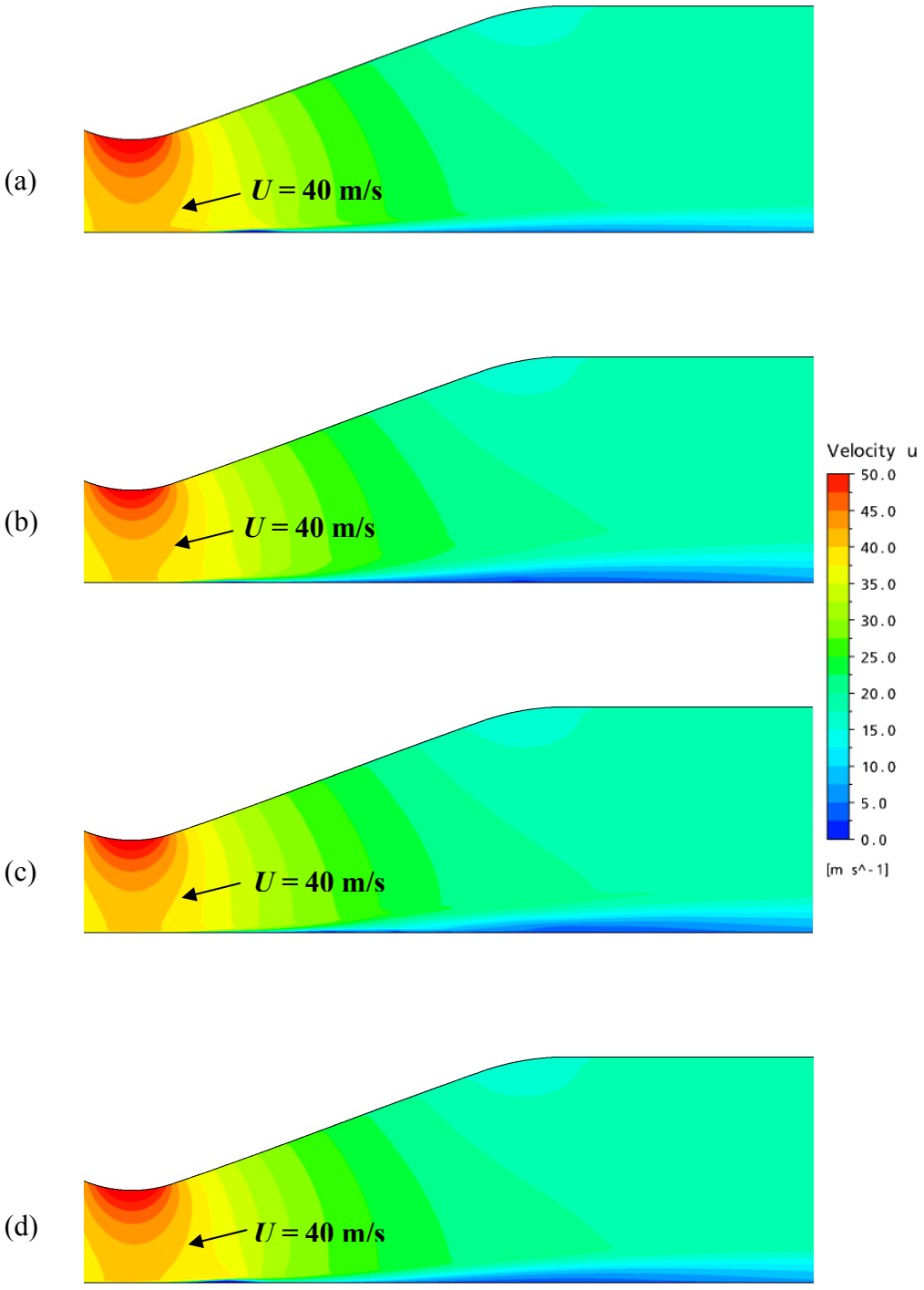

Figure A.8: Contours of time-averaged axial velocity with actuation: (a) LSP, co-flow, continuous (case L1), (b) LSP, co-flow, 100 Hz (case L2), (c) LSP, co-flow, 400 Hz (case L4), (d) TRP, co-flow, continuous (case T1)

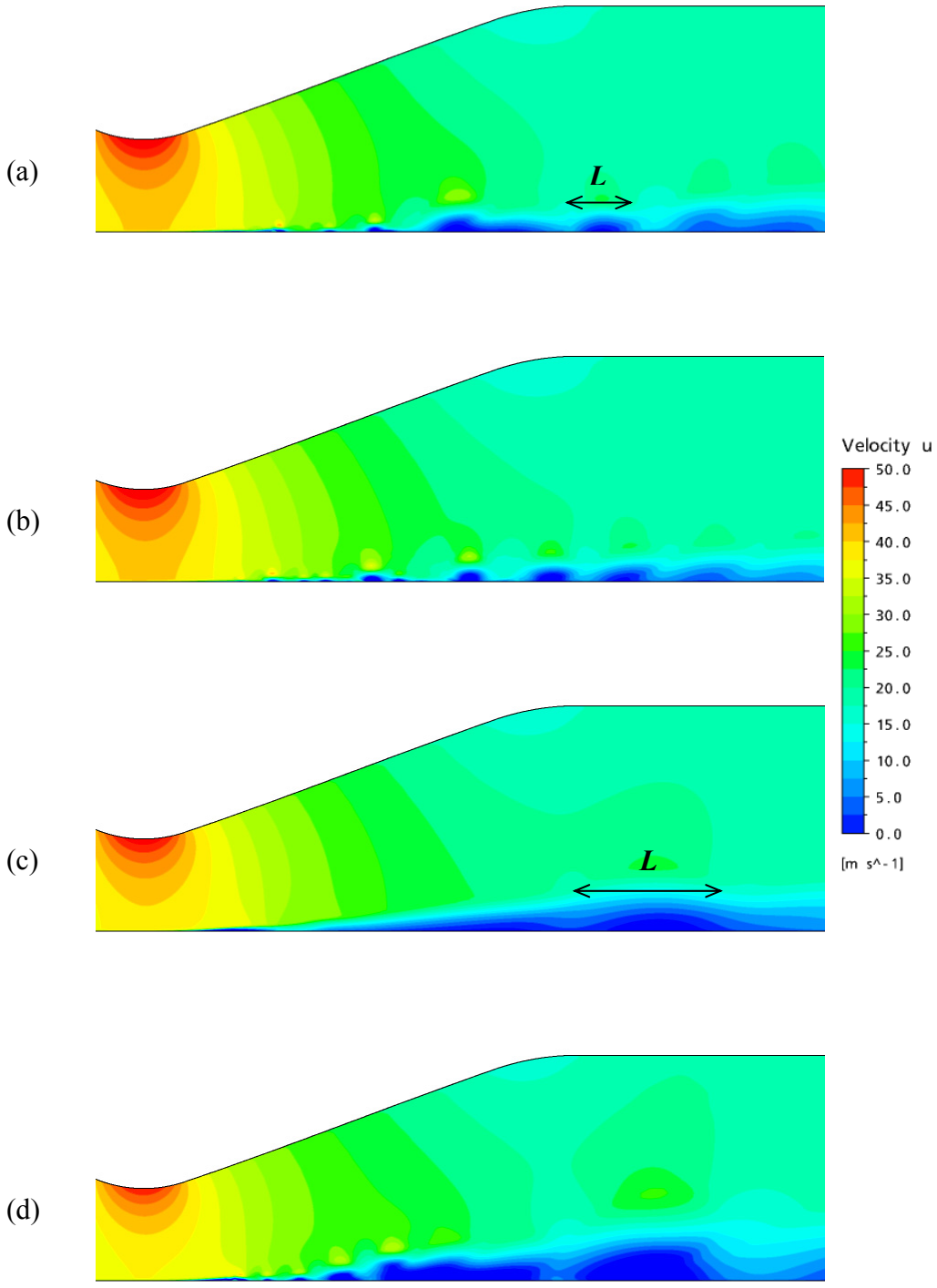

Figure A.9: Contours of instantaneous axial velocity with actuation: (a) LSP, co-flow, 100 Hz (case L2), (b) LSP, co-flow, 400 Hz (case L4), (c) TRP, co-flow, 100 Hz (case T3), (d) LSP, counter-flow, 100 Hz (case L6)

The effects of plasma actuation on the flow field is illustrated in Figures A.8 and A.10, which show the time-averaged axial velocity contours and wall shear stresses, respectively. In Figure A.8, the turbulent boundary layer separation is completely suppressed, as also shown in Figure A.10 for corresponding cases. The negative time-averaged axial wall shear stress between x = 135 and 165 mm in Figure A.10 is associated with laminar separation. The laminar boundary layer separation for all LSP actuation (except counter-flow pulsed actuation) is also delayed (Figure A.10(a)), while it is almost unchanged for TRP (Figure A.10(b)). The latter situation implies that the influence of plasma actuation is mainly on downstream flow. It should be noted that higher separation control effectiveness (reduced separation) leads to higher axial velocity at the diffuser throat (see discussion in Section 3.1.2), as observed from the 40 m/s axial velocity contour in Figure A.8.

As for the pulsed actuation, the instantaneous axial velocity contours, as shown in Figure A.9, give an indication of mixing (momentum transfer) between outer high-momentum and inner low-momentum flows. For the LSP actuation (Figures A.9(a) and (b)), the alternating fluid groups with positive and negative axial velocity along streamwise locations can be clearly observed, which indicates increased mixing. In contrast, for the TRP actuation (Figure A.9(c)), the flow mixing is less pronounced and only wave-like fluctuation in the flow is observed. It should be noted that the length scale of the fluctuations is approximately two times smaller for the LSP actuation (Figure A.9(a)) than for the TRP actuation (Figure A.9(c)) at the same actuation frequency of 100 Hz. The effect of actuation location on turbulent separation control can also be demonstrated in Figure A.11 through the time evolution of axial velocities with pulsed actuation at 100 Hz at two monitor points (Figure A.4). In Figure A.11, the evolution of axial velocity for the LSP actuation shows larger fluctuation. Two fluctuation peaks of axial velocity in each plasma actuation cycle can be clearly observed for the LSP case, which corresponds to the half length scale in Figure A.9(a). The LSP actuator location is better than the TRP one for the pulsed actuation, which is consistent with the general argument that the optimal actuation location for boundary layer separation control is near the separation point (Herbst and

Henningson, 2006; Romain Mathis *et al.*, 2008), if we consider the separation in the present work as including both laminar and turbulent parts.

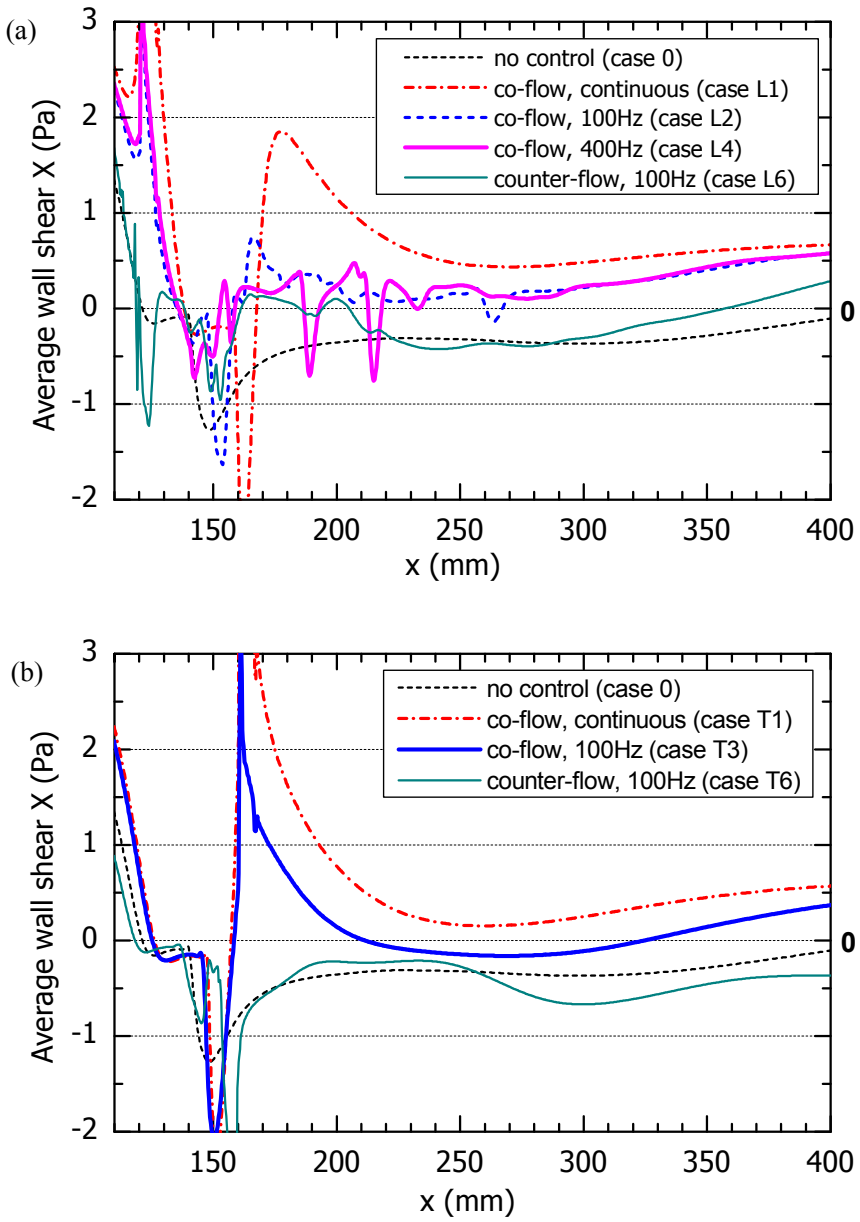

Figure A.10: Time-averaged axial wall shear stress for cases with actuation: (a) at the LSP, (b) at the TRP

As for the effect of actuation frequency in pulsed mode, the actuation frequency of 400 Hz is the best for the LSP location in terms of pressure recovery (Table 4), while the frequency of

100 Hz is the best for the TRP location. This is consistent with the power spectrum in Figure A.7, where 400 Hz is observed to be the dominant frequency (with the most turbulent energy) at monitor point 1 and 100 Hz is the dominant frequency at point 3. In other words, the most energetic large-scale structures in the flow are most amplified when the actuation frequency is the same as the natural dominant frequency in the uncontrolled flow, and thus the flow mixing of outer high-momentum flow and inner low-momentum flow is most enhanced. It should be noted that even though the frequency of 2000 Hz (corresponding to the Kelvin-Helmholtz instability) has more energy than 400 Hz at point 1 (Figure A.7(a)), the actuation frequency of 2000 Hz is not better than 400 Hz. This is because the mechanism which determines the most effective actuation frequency is the instability associated with the shedding of large-scale vortices from the separation bubble, which is not relevant to the Kelvin-Helmholtz instability. Figure A.12 shows the power spectra for different cases with pulsed actuation at 100 Hz and 400 Hz. Generally, various peak frequencies can be observed. For pulsed actuation at LSP with 400 Hz (case L4) and at TRP with 100 Hz and 400 Hz (cases T3 and T5), the dominant frequencies are locked on to the actuation frequencies. In other words, the turbulent structures in the flow with the same frequencies as the actuation frequencies are most amplified. In contrast, for pulsed actuation at LSP with 100 Hz (case L2), the dominant frequencies are 200 Hz and 400 Hz at two locations, which is different from the actuation frequency. This complexity of the dominant frequency can also been shown by instantaneous turbulent structures in Figure A.9(a), compared to the more organized structures in Figure A.9(b).

As for actuation direction, the counter-flow actuation is much less effective than co-flow actuation, even though it can also induce flow mixing (Figure A.9(d)). This situation is much different from that in the laminar boundary layer separation control, *e.g.*, on airfoils, where counter-flow actuation even with low strength can induce rapid laminar-turbulent transition and thus prevent the possible stall at high angles of attack (Visbal *et al.*, 2006). In contrast, the suppression of the turbulent boundary layer separation downstream of the laminar separation is the main goal in the present study, because total-pressure loss resulting from turbulent separation

is predominant. The counter-flow pulsed actuation is reducing streamwise momentum (similar to counter-flow continuous actuation) thus making the boundary layer more sensitive to the adverse pressure gradient. In other words, the counter-flow actuation weakens the positive effect from increased flow mixing by pulsed actuation.

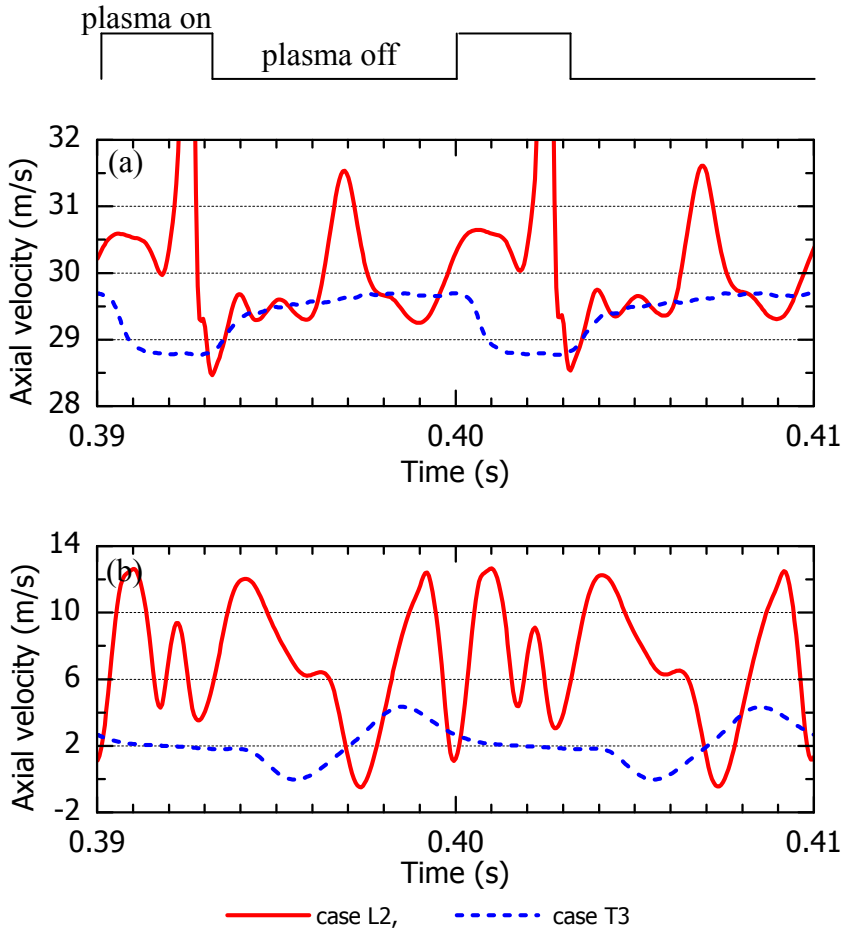

Figure A.11: Time evolution of axial velocities with actuation at two monitor points: (a) separated shear layer region (point 1), (b) turbulent separation region (point 3)

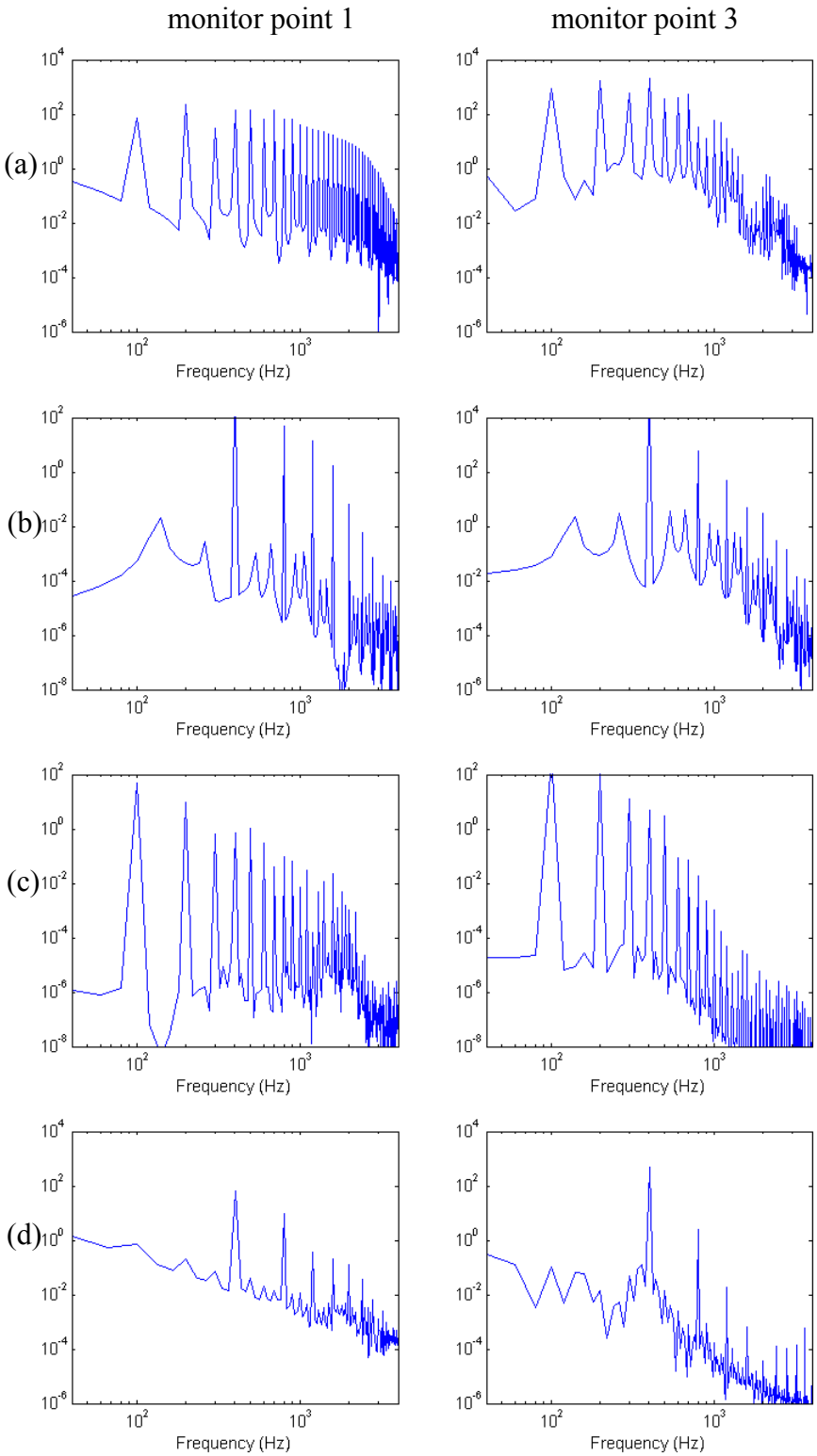

Figure A.12: Spectral analysis of axial velocities with actuation: (a) LSP, co-flow, 100 Hz, (case L2), (b) LSP, co-flow, 400 Hz (case L4), (c) TRP, co-flow, 100 Hz (case T3), (d) TRP, co-flow, 400 Hz (case T5)

Generally, co-flow actuation, both continuous and pulsed, can suppress the turbulent boundary layer separation, while counter-flow actuation is ineffective even though it can also induce flow mixing. As for the actuation location, the laminar separation point (LSP) is better than the location in the turbulent region (TRP). The optimal actuation frequency in pulsed actuation is $F^+ \sim O(1)$ (100 Hz or 400 Hz, depending on the actuator location in the present parametric study).

Appendix B: Preliminary Experiment Tests and Results

Proceedings of the ASME 2010 International Mechanical Engineering Congress & Exposition
IMECE2010
November 12-18, 2010, Vancouver, British Columbia, Canada

IMECE2010-37324

TURBULENT BOUNDARY LAYER SEPARATION CONTROL BY USING DBD PLASMA ACTUATORS: PART Ⅰ — EXPERIMENTAL INVESTIGATION

Xiaofei Xu
Ecole Polytechnique de Montreal
Montreal, QC, Canada

Huu Duc Vo
Ecole Polytechnique de Montreal
Montreal, QC, Canada

Njuki Mureithi
Ecole Polytechnique de Montreal
Montreal, QC, Canada

Xue Feng Zhang
National Research Council Canada
Ottawa, ON, Canada

ABSTRACT

Turbulent boundary layer separation is an important issue for a variety of applications, one of which is S-shaped aircraft engine intakes. The turbulent separation at the engine intake causes inlet flow distortion, which can deteriorate engine performance, cause fatigue and reduce engine component life. Various flow control techniques have been applied for turbulent boundary layer separation control, such as vortex generators, vortex generator jets and synthetic jets. The recent advent of dielectric barrier discharge (DBD) plasma actuators can potentially provide a robust method for the control of turbulent boundary layer separation. Compared to other flow control techniques, these new actuators are simple, robust and devoid of moving mechanical parts, which make them ideal for aerodynamic applications.

The present work studies the effects of DBD plasma actuators on the suppression of 2-D turbulent boundary layer separation induced by an imposed adverse pressure gradient. First, the flow field with and without actuation in a low-speed wind tunnel is investigated experimentally by Particle Image Velocimetry (PIV) measurements. The results show that plasma actuation can suppress turbulent boundary layer separation in both continuous and pulsed modes. In the pulsed mode, the actuation with an optimal actuation frequency, corresponding to a dimensionless frequency of order one, is found to most effectively suppress the turbulent separation. Moreover, the effects of plasma actuation on the flow is demonstrated and analyzed by using Proper Orthogonal Decomposition (POD). The effect of the actuation is found to be correlated to the second POD mode which corresponds to large flow fluctuations.

Keywords: turbulent boundary layer separation, plasma actuator, flow control, POD

1. INTRODUCTION

Inlet total-pressure distortion is common in engine intakes, especially in cross-wind conditions or for non-axial engine intakes. The reduced velocity in the distorted region of the engine face is detrimental to engine performance and causes undesirable fluctuating forces on the turbomachinery blades as they pass in and out of this region, which may lead to fatigue and shortened engine component life. Moreover, the inlet distortion reduces the stall margin of the fan and compressor and can result in engine surge, a flow instability characterized by flow oscillation across the engine, a catastrophic drop in thrust and damage to the engine.

Aircraft design considerations, such as in the case of turboprops and helicopters, can force the use of non-axial S-shaped engine inlets. The main cause of inlet distortion in this widely used intake geometry is the secondary flow and flow separation within the inlet duct itself, either from the curvature of inside wall bends or from high diffusion rates. The boundary layer separation in a realistic engine intake is usually turbulent, as a result of high Reynolds number and high adverse pressure gradient, resulting in boundary layer transition near the intake lip.

As shown in Fig. 1, for steady free-stream 2-D flows on streamlined surfaces, separation begins intermittently at a given location, i.e., the flow reversal occurs only over a fraction of the total time. The time fraction of forward flow decreases progressively downstream. For turbulent boundary layer separation with steady free-stream flow, Simpson [1] suggested

1 Copyright © 2010 by Her Majesty the Queen in Right of Canada

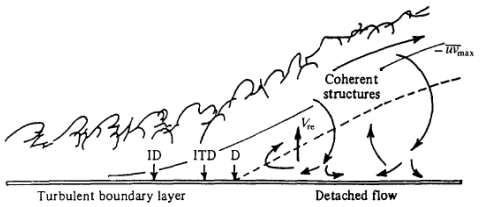

Figure 1: Turbulent boundary layer separation with turbulent structures supplying the small mean backflow (Simpson [2])

the following quantitative definitions on the flow detachment, with the definitions based on the forward-flow-fraction γ_{pu}. Incipient Detachment (ID) occurs with instantaneous backflow 1% of the time (γ_{pu} = 0.99); Intermittent Transitory Detachment (ITD) occurs with instantaneous backflow 20% of the time (γ_{pu} = 0.8); Transitory Detachment (TD) occurs with instantaneous backflow 50% of the time (γ_{pu} = 0.5); and Detachment (D) occurs with the time-averaged wall shear stress τ_w = 0. Simpson indicates that TD and D occur at the same axial location according to available data. In Fig. 1, the dashed line represents locations of zero mean axial velocity U; the solid line represents locations of maximum turbulent shear stress; and V_{re} represents the mean re-entrainment velocity along U = 0.

A large body of literature pertaining to boundary layer separation control and flow control in S-shaped inlet ducts exists. Sullerey et al. [3] studied the effect of various fences and vortex generator configurations in reducing distortion and improving total pressure recovery in 2-D diffusing S-ducts. Pradeep and Sullerey [4] later investigated the performance enhancement of 3-D diffusing S-ducts by secondary flow and separation control using vortex generator jets (VGJs). The VGJs (active flow control) were shown to be significantly more effective than tapered fin vortex generators (passive flow control). Moreover, an attempt was made to explain the physical mechanism of VGJs in secondary flow and separation control. The larger the size of the vortex, the more the mixing of the low-momentum boundary layer fluid with the high-momentum free-stream fluid and the more effective was the flow control. Separation control using zero-net-mass-flow (ZNMF) jets in diffusing S-ducts was studied by Mathis et al. [5]. The ZNMF jet actuators are unsteady flow control devices for which one of the important parameters is actuation frequency or Strouhal number (based on the rms velocity and the diameter of the ZNMF jet). With the ZNMF actuator located close to the time-averaged separation point operating at the most effective actuation frequency (corresponding to the most spatially unstable mode in the uncontrolled flow), only a very low energy input was necessary to suppress the separation in a duct with high degree of curvature.

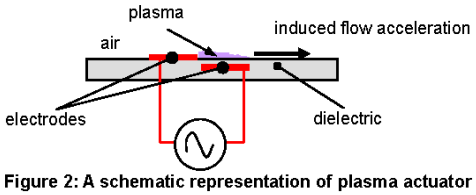

Figure 2: A schematic representation of plasma actuator

In spite of their effectiveness, there are some practical considerations that impede the use of the previously listed active flow control devices in real engine operating conditions. VGJs require an air supply system, likely taken from engine bleed, and associated pipes and valves, which imply penalty in engine performance and in weight. ZNMF jets require a system with oscillating mechanical parts that may limit the robustness of the actuator under operational conditions. Moreover, there is a risk of clogging of the orifices, especially if small actuators are used to minimize actuation power and response time. Compared to these relatively complex actuators, another active flow control technique, which is being more widely researched, is plasma-based actuation. Plasma-based actuation is generally based on the following mechanisms [6]: 1) thermal effect, i.e., rapid gas heating resulting from the Joule dissipation, such as direct-current (DC) filamentary discharges, 2) non-thermal effect, i.e., magneto-hydrodynamic (MHD) or electro-hydrodynamic (EHD) forcing by exerting forces to accelerate or decelerate the gas in the flow, such as DC glow discharges and single dielectric barrier discharge (DBD). The DBD plasma actuator is a fairly simple and robust device without moving parts that can effectively induce laminar-turbulent transition, and suppress and/or delay boundary layer separation. A typical DBD plasma actuator, as illustrated in Fig. 2, consists of two electrodes arranged asymmetrically, one exposed to the air and the other hidden beneath a layer of dielectric material. When the electrodes are subjected to a sufficiently high amplitude AC voltage (~1-10 kV_{pp}) at high frequency (~1-10 kHz), the air above the hidden electrode partially ionizes. In the presence of the electric field, this results in a flow acceleration (momentum addition to the flow) near the surface. More information on plasma actuators can be found in [7-9].

The DBD plasma actuator can be used in continuous mode or pulsed mode (steady or unsteady actuation). For the latter mode, the significant parameters, as shown in Fig. 3, include actuation frequency ($1/T_c$), duty cycle and strength. The continuous mode can be regarded as a duty cycle of 100%. In the pulsed mode, the pulsing frequency can be chosen to excite resonant turbulent flow structures in the boundary layer to improve momentum transfer from the outer high-velocity fluid and thus suppress separation with minimal power input.

Many researchers have studied the application of plasma actuators, e.g., lift increase on airfoils [10, 11], separation control on gas turbines [12] and vortex control on delta wings [13]. The research and results of plasma actuation, however,

 Copyright © 2010 by Her Majesty the Queen in Right of Canada

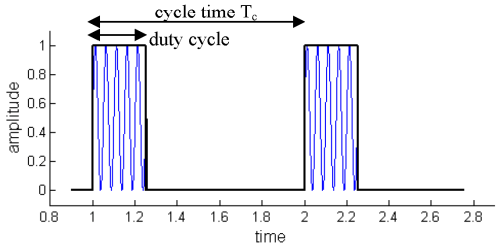

Figure 3: An illustration of pulsed actuation

mainly focus on the suppression of laminar separation [14, 15] and laminar-turbulent transition, which are very receptive to imposed small-amplitude disturbance [16]. Research on the control of the much tougher turbulent separation [17, 18] by plasma actuation is just beginning. In order to achieve sufficient control authority for turbulent boundary layers, the actuator amplitude must be above a certain threshold level.

The present work is part of a project to study the effects of DBD plasma actuators both experimentally and numerically on suppression of a 2-D turbulent boundary layer separation induced by an imposed adverse pressure gradient. In the present paper, the flow field with and without actuation in a low-speed wind tunnel is investigated by particle image velocimetry (PIV) measurements. The effects of plasma actuation on the flow is then demonstrated and analyzed by using Proper Orthogonal Decomposition (POD). Part II of this work aims to develop and validate a simulation tool that captures the effects of plasma actuators on the flow, and carry out a parametric study of the concept at flow regimes beyond the flow control capability of plasma actuators of conventional strength.

2. EXPERIMENTAL FACILITY AND DATA ANALYSIS

2.1 Experimental Setup

Plasma Actuator

The plasma actuator utilized in this experiment is illustrated in Fig. 4. The two electrodes made of tinned copper foil are separated by a Teflon sheet of 12.7 mm thickness and 150 mm width. The electrodes span only 130 mm, leaving 10 mm from either side-wall to avoid wall effects. The upper and lower electrodes have a width of 12.7 mm and 25.4 mm, respectively. The upper electrode is connected to a sinusoidal AC signal generated by a Minipuls6 generator from Electrofluidsystems, while the lower electrode is grounded and insulated from air by the Kapton film. The Minipuls6 generator is designed to generate high frequency and high voltages AC signal in a range from 5 to 30 kHz with amplitudes up to 68 kV_{pp} (peak-to-peak voltage). The device consists of one integrated low-voltage-control-circuit board and a high voltage transformer cascade. The power is supplied from a DC power supply (Voltcraft PS 3620). The whole plasma actuator is inserted into the grooved flat plate. The position of the actuator

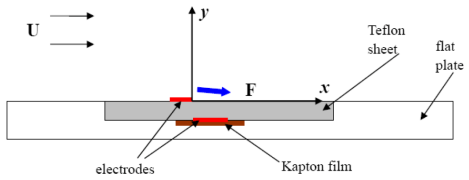

Figure 4: Configuration of plasma actuator implementation

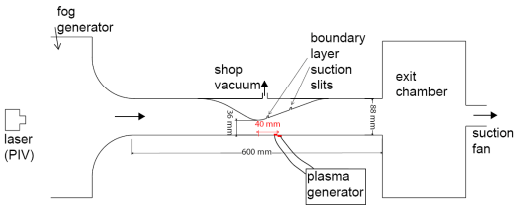

Figure 5: Configuration of experimental setup

(origin of the coordinates) is referred to the trailing edge of the upper (exposed) electrode. The effect of the plasma actuator can be represented by a body force (actuator strength).

In the present work, the plasma is generated at the voltage of 41.6 kV_{pp} and the frequency of 13.5 kHz, which corresponds to the predicted total body force (actuator strength) value around 40 mN/m. Both continuous and pulsed actuations are tested. For the pulsed mode, a 30% duty cycle (duty cycle for pulsed excitation is usually chosen smaller than 50% [13]) is chosen with different actuation frequencies of 5 Hz, 15 Hz and 25 Hz (discussed later).

Wind Tunnel and Test Section

A small-scale open-loop suction-type wind tunnel has been designed and constructed in the Wind Tunnel Laboratory of Ecole Polytechnique de Montreal. The wind tunnel, shown in Fig. 5, has a bell-mouth, a convergent-divergent test section and an exit chamber. The test section has a cross-section, at the diffuser exit, of 150 mm width and 88 mm height. The area ratio of throat to exit is 0.41. The main flow is generated by a suction fan connected to the exit chamber. The contoured upper wall imposes a desired pressure distribution on the bottom (lower) wall in the test section. To avoid the flow separation on the upper wall, suction slits are made on the diverging section of the upper wall, and are connected to a shop vacuum, to remove the upper wall boundary layer. Throat flow velocity (without actuation) for the experiment is 4.9 m/s. The plasma actuator is placed 40 mm downstream of the throat. A plexiglass window on the side-wall provides the optical access for PIV measurement.

2.2 Measurement Techniques

PIV Measurements

 Copyright © 2010 by Her Majesty the Queen in Right of Canada

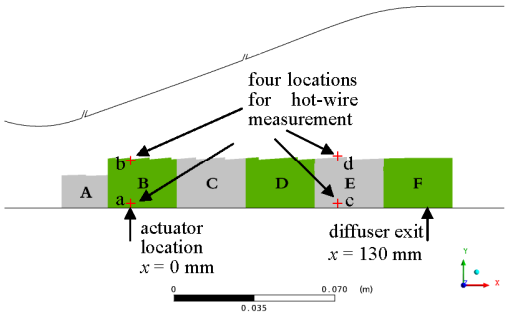

Figure 6: An illustration of windows for PIV measurement and four locations for hot-wire measurement

Particle Image Velocimetry (PIV) is used to investigate the flow characteristics in the diffuser. The Dantec Dynamics system consists of a Nd:YAG laser (New Wave, Solo PIV I-15, maximum repetition rate of 15 Hz) and a CCD camera (Flow Sense M2, 1600×1186 pixels). To seed the flow a particle generator (PIVTEC, Aerosol Generator PivPart30) is used. Upstream of the bellmouth, an inlet chamber is used to achieve a uniform concentration of seeding particles, which are suctioned into the test section for PIV measurement. The laser light sheet is directed into the test section (with the sheet plane at half the spanwise position) from the far upstream location. The images are captured by the camera at one side of the wind tunnel through the rectangular plexiglass windows. Fig. 6 shows the diffuser test section with the six PIV measurement windows highlighted. These windows cover the range from the diffuser throat to the exit plane. The windows B through F are 30 mm long by 21 mm high, while window A is 20 mm long by 14 mm high. The software Flow Manager is used for handling the measurements and for computing the velocity vector fields from the captured pictures. The velocity components are computed using a cross-correlation algorithm with adaptive multipass, interrogation windows of 32×32 pixels and an overlap of 50 %. The spatial resolution of the PIV measurement is 0.3 mm (16 pixels). The near-wall flow ($y < 0.6$ mm) cannot be captured because of wall reflection. In the present work, the sampling frequency is chosen as 14 Hz and thus each cycle of large fluctuations in the flow with pulsed actuation has 14 phase-fixed sampling points, assuming that the frequency of large fluctuations is locked on the actuation frequency (5 Hz, 15 Hz and 25 Hz). The duration dt between two successive image pairs ranges from 60 to 120 μs, depending on the imaging location with associated different velocity scales. 140 image pairs are acquired at each location.

Hot-Wire Measurements

A constant voltage hot-wire anemometer (CVA) is used to capture the resonant frequencies in the uncontrolled flow with turbulent boundary layer separation. The CVA is a type of hot-wire or hot-film anemometer specifically designed for high-bandwidth, high-sensitivity flow measurement. The hot-wire anemometer used in this work is a CVA-VC04 from Tao Systems, which has a frequency response bandwidth of around 400 kHz. The hot-wire probe is inserted into the test section from the upper wall, and is traversed in the vertical direction.

2.3 Proper Orthogonal Decomposition (POD) for Data Analysis

Proper orthogonal decomposition (POD) is a method to extract a reduced number of typical modes in a signal associated with their time evolution [19]. These signals can be pressure or velocity, obtained by experimental measurements or numerical simulations. The detailed equations and definitions can be found in the appendix. The POD offers representation of time-evolving vector field by using energetic spatial and temporal modes called *topos* and *chronos*, respectively. The energy contained in different modes decreases with increasing mode number (order), with the first mode normally corresponding to the mean field. Moreover, the entropy H, a normalized factor, can be used to compare the disorder levels of different signals. If all the energy is concentrated in the first mode, H is zero. In contrast, if the energy is uniformly distributed among all the modes, H attains its maximum value 1. Aubry et al. [20] suggested the entropy H as an effective way to detect the laminar-to-turbulent transition.

The POD has been used to extract the coherent structures in the separated shear layer around a wing by Hoarau et al. [21], and in the turbulent separation bubble by Mathis et al. [22]. In this paper, POD is also proposed to extract the coherent structures in the flow with turbulent boundary layer separation, and to quantify the effects of different plasma actuation regimes on boundary layer separation control.

3. RESULTS AND DISCUSSIONS

3.1 Mean Flow

Fig. 7 shows the velocity vectors and contours of the axial velocity from PIV measurements for the case without plasma actuation, while Fig. 8 shows the corresponding streamlines and contours of spanwise vorticity (normal to paper). It should be noted that both figures represent time-averaged flow fields. Without flow control, the laminar boundary layer on the flat plate separates just downstream of the throat, as seen in Fig. 7(a). The separated boundary layer then goes through laminar-turbulent transition and finally becomes fully turbulent. It should be noted that there is no turbulent reattachment downstream of the transition region (observed from the continuously negative axial velocity near the wall in Fig. 7), as a result of the high adverse pressure gradient. The separated flow develops along the six measurement windows. In windows D through F, only reverse flow can be observed. The vorticity for 2-D flow is $\omega = \partial v/\partial x - \partial u/\partial y$. If taking only axial velocity into account, positive vorticity corresponds to

 Copyright © 2010 by Her Majesty the Queen in Right of Canada

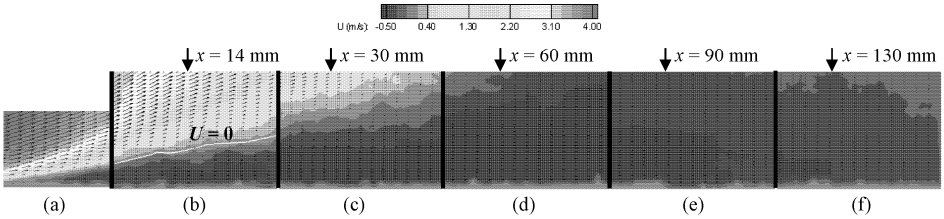

Figure 7: Velocity vectors and contours of axial velocity without actuation: (a)-(f) correspond to windows A-F in Fig. 6

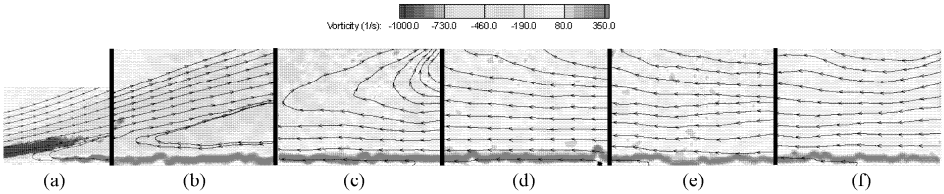

Figure 8: Streamlines and contours of vorticity without actuation: (a)-(f) correspond to windows A-F in Fig. 6

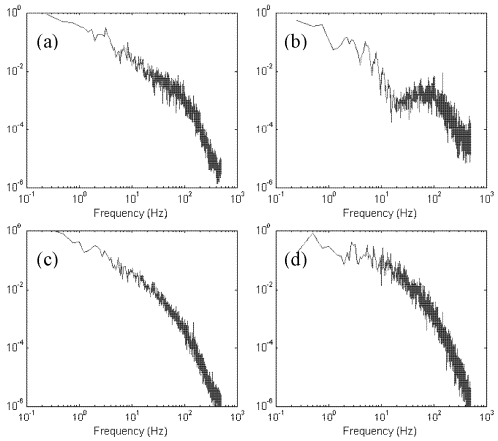

Figure 9: Power spectra of velocity fluctuation from hot-wire measurement without actuation at four diffuser locations in Fig. 6: (a), (c) and (d) inside the separated boundary layer; (b) at the boundary layer edge

$\partial u / \partial y < 0$ (increased amplitude of negative axial velocity with increased distance from the wall), while negative vorticity corresponds to $\partial u / \partial y > 0$ (increased amplitude of positive axial velocity with increased distance from the wall). In other words, the positive vorticity near the wall (in all windows of Fig. 8) corresponds to the reverse flow inside the separated boundary layer.

Fig. 9 shows power spectra of velocity fluctuations from hot-wire measurement without plasma actuation at four diffuser locations in Fig. 6, with two in the actuation plane (x = 0 mm) and two in the turbulent separation region (x = 90 mm). Please note that only the results in Fig. 9 are from hot-wire measurements, while other results presented later are from PIV measurement. Generally, there are various frequency peaks at each location. This indicates that large-scale vortices are shed from the separation bubble at those frequencies [23]. The corresponding lowest frequency is around 3 Hz, while the highest frequency is around 80 Hz (in Fig. 9(b)). Other frequencies include 5 Hz, 7.5 Hz and 15 Hz. The dimensionless frequencies $F^+ = fL_{se}/U_\infty$ corresponding to these frequencies are 0.18, 0.31, 0.46, 0.92 and 4.9, respectively (using the separation length L_{se} = 0.3 m and the area-averaged velocity at the diffuser throat plane U_∞ = 4.9 m/s). The frequency of 80 Hz (F^+ = 4.9) corresponds to the Kelvin-Helmholtz instability of the separated shear layer. The frequency of 3 Hz (F^+ = 0.18) appears to be related to an integral feature of a fully turbulent separation [23]. The optimal frequency for boundary layer separation control is $F^+ \sim O(1)$, based on the work by Herbst and Henningson [24] and Cierpka et al. [25]. In the present experiment, 15 Hz (F^+ = 0.92) is assumed to be the most effective frequency for separation control. This frequency and two other frequencies, namely 5 Hz (F^+ = 0.31) and 25 Hz (F^+ = 1.53), are chosen to demonstrate the effect of the actuation frequency.

Figs. 10 and 12 show the time-averaged velocity vectors and contours of axial velocity for cases with continuous actuation and pulsed actuation at 15 Hz, which corresponds to the most effective actuation in pulsed mode and will be discussed later. The streamlines and contours of the spanwise vorticity for the two cases above are shown in Figs. 11 and 13, respectively. Note that these figures represent time-averaged

 Copyright © 2010 by Her Majesty the Queen in Right of Canada

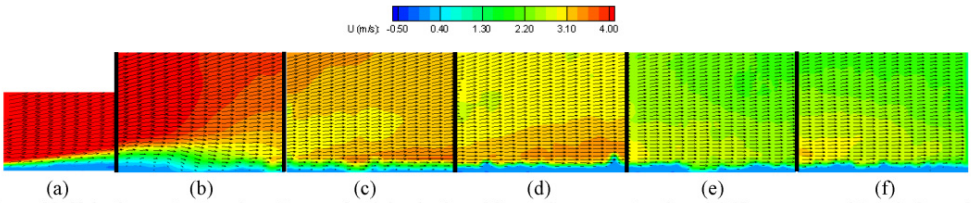

Figure 10: Velocity vectors and contours of axial velocity with continuous actuation: (a)-(f) correspond to windows A-F in Fig. 6

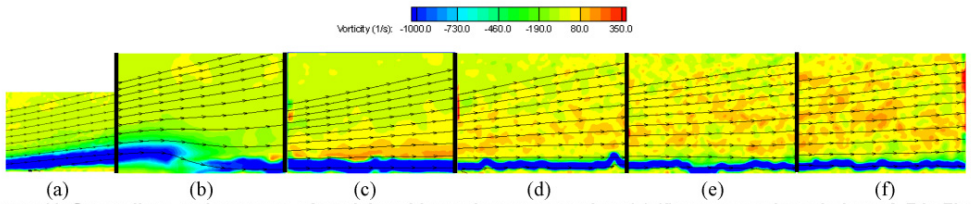

Figure 11: Streamlines and contours of vorticity with continuous actuation: (a)-(f) correspond to windows A-F in Fig. 6

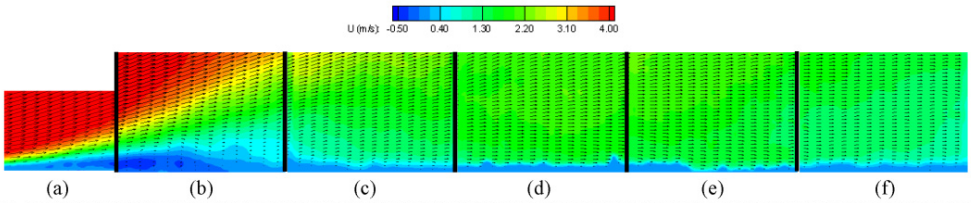

Figure 12: Velocity vectors and contours of axial velocity with pulsed actuation: (a)-(f) correspond to windows A-F in Fig. 6

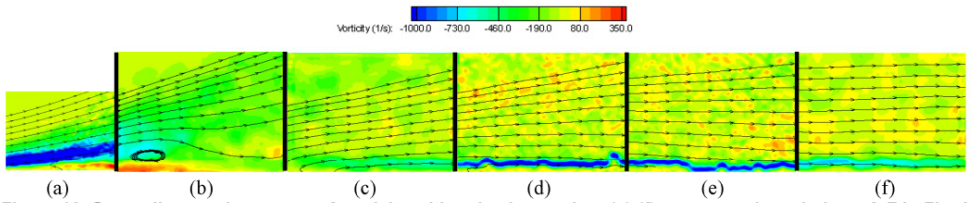

Figure 13: Streamlines and contours of vorticity with pulsed actuation: (a)-(f) correspond to windows A-F in Fig. 6

flow fields.

Fig. 14 shows the measured axial velocity profiles from the PIV measurements for different cases, at five locations, namely 14 mm, 30 mm, 60 mm, 90 mm and 130 mm (diffuser exit) downstream of the actuator.

With plasma actuation, both continuous and pulsed, the turbulent separation is completely suppressed, as shown in Figs. 10, 12 and 14. The negative vorticity (in windows C through F of Figs. 11 and 13) corresponds to the streamwise flow affected by plasma actuation. However, as observed in windows A and B of Figs. 10 and 12, a small laminar separation bubble still exists. The separated shear layer can be clearly observed in windows A and B of Figs. 11 and 13. However, the separated shear layer is thinner than in the uncontrolled flow (see Fig. 7). The separated shear layer then reattaches near the actuation location in window B.

In a turbulent boundary layer with separation, large-scale structures supply the turbulence energy to the near-wall separated flow. This energy, however, is not sufficient to prevent boundary layer separation. Continuous actuation involves direct input of momentum or energy into the flow to prevent boundary layer separation. In contrast, pulsed actuation works by enhancing the mixing of high-momentum outer flow and low-momentum near-wall flow, or, by amplifying these

 Copyright © 2010 by Her Majesty the Queen in Right of Canada

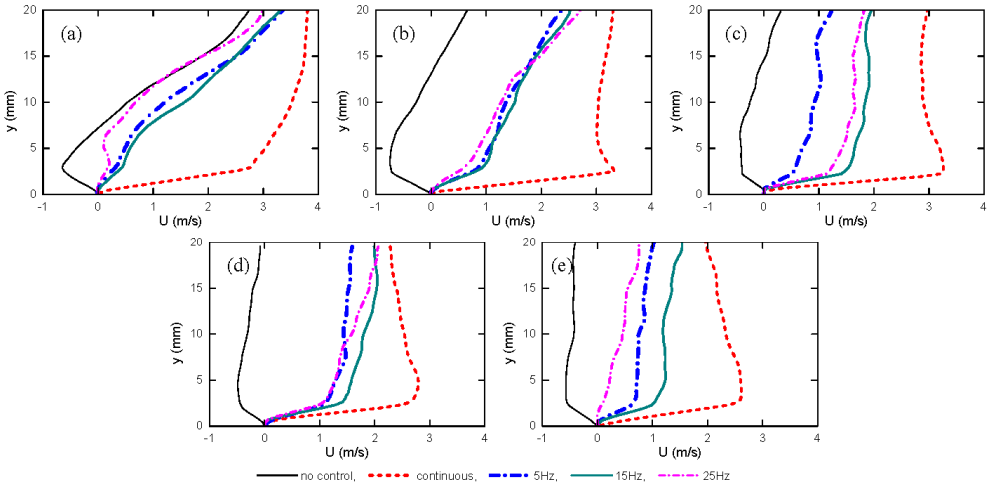

Figure 14: Axial velocity profiles at five locations downstream of actuation location: (a) 14 mm, (b) 30 mm, (c) 60 mm, (d) 90 mm, (e) 130 mm (diffuser exit)

large-scale structures within the boundary layer [26].

For the pulsed mode, the actuation frequency of 15 Hz is found to most effectively suppress the turbulent separation, as seen from the larger axial velocity at the chosen locations in Fig. 14. It should be noted that higher separation control effectiveness (reduced separation) corresponds to higher axial velocity at the diffuser throat. This is because the reduced separation can allow larger pressure recovery and lower static pressure at the test section inlet, and by extension higher mass flow rate for the same inlet total pressure and exit static pressure. The "bursting" frequency f of the most energetic eddies near the wall is correlated by $U / f\delta = 10$, where U is the mean velocity outside the boundary layer and δ is the boundary layer thickness [27]. In the present work, 15 Hz corresponds to this bursting frequency with $U = 3$ m/s and $\delta = 0.02$ m at $x = 0$ mm for the no-control case.

Concerning the variation of axial velocity versus axial distance in Fig. 14, the value with 15 Hz is always larger than that with 5 Hz and 25 Hz. In addition, the axial velocity with 5 Hz, compared to 25 Hz, is smaller in the near-actuation region (see Fig. 14(c)) while larger in the near-diffuser-exit region (see Fig. 14(e)). It should be noted that the present comparison is only for the axial range of $x > 30$ mm, excluding the actuator-related effects, based on two considerations: 1) a recirculation zone exists in the vicinity of the upper electrode (-12.7 mm $< x <$ 0 mm)[28], and 2) the process of momentum addition from plasma actuator ranges a distance over the lower electrode (maximum distance is same as the lower electrode width of 25.4 mm). As discussed above, the mechanism of separation control by pulsed actuation involves the mixing enhancement of high-momentum outer flow with the low-momentum near-wall flow. The mixing enhancement can be achieved through a series of vortices generated by pulsed plasma actuation. Increased actuation frequency results in a mean flow with a more focused wall jet and higher velocity overshoots closer to the surface [13]. The pulsed actuation with 25 Hz thus has more effect on near-wall flow than 5 Hz. On the other hand, the pulsed actuation with 5 Hz has more effect on the boundary layer edge and generates larger vortices with associated stronger flow mixing. Therefore, the effect of pulsed actuation with 25 Hz is more immediate while less downstream. However, pulsed actuation with 5 Hz has a larger time/length scale and its effect on the flow can extend further downstream.

The continuous actuation is more effective on the suppression of this turbulent separation. The free-stream velocity in all windows of Figs. 10 and 12 is larger for the continuous actuation than the pulsed actuation with 15 Hz, indicating higher mass flow. The axial velocity at the diffuser exit for continuous actuation is twice as high as that of the pulsed actuation with 15 Hz (see Fig. 14(e)). However, it must be noted that pulsed actuation has a 30% duty cycle and thus consumes only 30% of the power of continuous actuation.

3.2 Flow Fluctuation

In contrast to the time-averaged flow fields with boundary layer separation, instantaneous flow fields are significantly different (e.g., time-varying velocity, combination of various turbulent structures, variation of instantaneous separation

 Copyright © 2010 by Her Majesty the Queen in Right of Canada

point), especially for the cases without and with pulsed actuation.

To describe the different states of turbulent flow detachment near the wall, a set of definitions based on the forward-flow-fraction γ_{pu} includes ID, ITD, TD and D (see Fig. 1). The points TD and D generally are at the same axial location. The TD point can be evaluated as a position where γ_{pu} near the wall reaches the value 0.5, while the D point corresponds to a position with zero mean axial velocity (zero mean axial shear stress) near the wall. Fig. 15 shows the fraction of positive axial velocity in window B for different cases without actuation, with continuous actuation and with pulsed actuation at 15 Hz, respectively. Since the boundary layer separates just downstream of the throat and no attachment is observed in Fig. 7(a), direct comparison of TD and D is not available. However, the curve with zero mean axial velocity in Fig. 7(b) and the curve with $\gamma_{pu} = 0.5$ in Fig. 15(a) match well. With the separation suppressed by both continuous and pulsed actuations, the region with low γ_{pu} is also suppressed. The curve with $\gamma_{pu} = 0.5$ in Figs. 15(b) and (c) also match well with the curve with zero mean axial velocity in Figs. 10(b) and 12(b), respectively.

In a turbulent boundary layer with separation, large-scale structures supply the turbulence energy to the near-wall separated flow. Thus turbulent kinetic energy (TKE) in the flow is an important parameter for both no-control and actuation cases as an indicator of control effectiveness. Since the instantaneous values of the TKE can vary substantially, the mean TKE values are preferred as more representative of the overall flow. The mean TKE in 2-D flows is given by

$$ke = \frac{1}{2}\frac{\overline{uu} + \overline{vv}}{U_{throat}^2} \qquad (1)$$

where u and v denote the primary (axial) and secondary (normal) components of the fluctuating velocity, respectively.

Fig. 16 shows the TKE in window B for different cases. For the no-control case, the maximum TKE is located above the curve of zero mean axial velocity (Fig. 7(b)). In other words, the maximum fluctuations are in the middle of the separated boundary layer, which is different from the zero-pressure-gradient case (the maximum is near the wall)[2]. With continuous actuation, the TKE is substantially reduced in most of the region, implying that the controlled flow is much steadier. However, with pulsed actuation, the maximum TKE is increased while the region of high TKE is decreased. This is because the separation is suppressed by the mixing enhancement of high-momentum outer flow and low-momentum inner flow. It should be noted that the maximum TKE for the case with pulsed actuation is also located in the middle of the boundary layer.

The contribution of the TKE in axial and normal directions can be decomposed by computing the normal turbulent Reynolds stresses $\overline{uu}/U_{throat}^2$, $\overline{vv}/U_{throat}^2$ and the shear

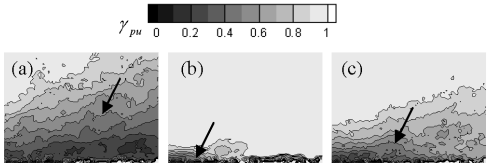

Figure 15: Fraction of positive axial velocity in window B (arrows indicate γ_{pu} = 0.5) with (a) no actuation, (b) continuous actuation, (c) pulsed actuation at 15 Hz

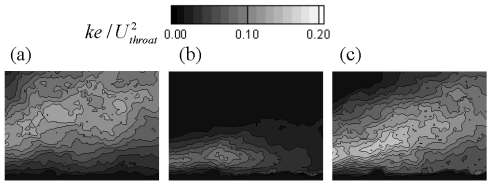

Figure 16: Turbulent kinetic energy in window B with (a) no actuation, (b) continuous actuation, (c) pulsed actuation at 15 Hz

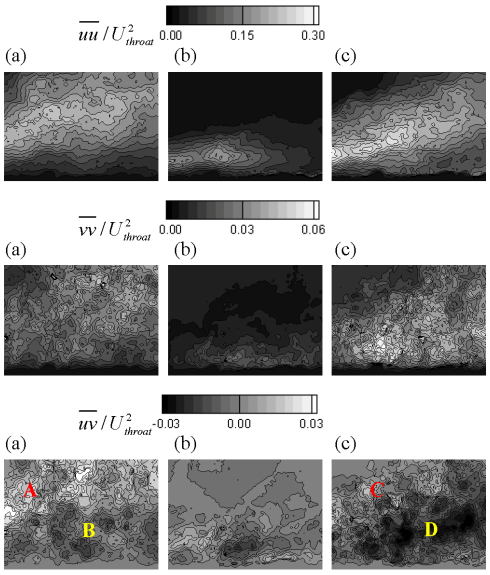

Figure 17: Turbulent Reynolds stresses in window B with (a) no actuation, (b) continuous actuation, (c) pulsed actuation at 15 Hz

 Copyright © 2010 by Her Majesty the Queen in Right of Canada

turbulent Reynolds stress $\overline{uv}/U_{throat}^2$. The turbulent Reynolds stresses indicate the contribution of turbulent motion (fluctuation) to the mean momentum transfer, of which the shear Reynolds stress $\overline{uv}/U_{throat}^2$ plays a dominant role [29]. Fig. 17 shows the turbulent Reynolds stresses in window B for different cases. It can be observed that the $\overline{uu}/U_{throat}^2$ component is the main source of the TKE for all cases. As for $\overline{uv}/U_{throat}^2$, the maximum positive values for cases without and with pulsed actuation (A and C in Fig. 17) are located near the boundary layer edge, while the maximum negative values (B and D in Fig. 17) are located in the middle of the boundary layer. The distribution of negative $\overline{uv}/U_{throat}^2$ is consistent with that for turbulent boundary layer separation on flat surfaces [2], which indicates the momentum transfer by turbulent fluctuation from the high-momentum outer flow to low-momentum near-wall flow. In contrast, the positive $\overline{uv}/U_{throat}^2$ near the boundary layer edge indicates the entrainment process from the boundary layer to the outer-flow, induced by the high diffusion rate especially just downstream of the diffuser throat. In addition, the maximum negative $\overline{uv}/U_{throat}^2$ is larger for pulsed actuation than for no-control case (D versus B in Fig. 17), corresponding to the increased momentum transfer by flow fluctuation resulting from pulsed actuation.

3.3 POD Analysis

Topos and Chronos

Fig. 18 shows 1-D topos (1-D decomposition on vertical lines) of the axial velocity in the plane at x = 14 mm with continuous actuation, while Fig. 19 shows corresponding chronos. The topos demonstrates the increasing number of changes in sign with increasing mode number. Generally, the first mode of the POD is representative of the mean, as observed from the almost constant non-zero chronos for the first mode in Fig. 19 and compared with mean axial velocity in Fig. 14. Other modes represent the fluctuation in the flow with different length/time scales, with the continually altered sign of corresponding chronos. The second mode is thus representative of the fluctuation with large scale (large flow structures).

It should be noted that the sign of topos/chronos is not important but their product has a physical meaning. For example, the negative value of mode 1 in Fig. 18 associated with the negative value of mode 1 in Fig. 19 represents the positive axial velocity, resulting from the separation suppression by the plasma actuation.

Figs. 20 and 21 show the development of the second mode of the 1-D topos versus axial distance for cases with no actuation and continuous actuation, respectively. Note that the topos magnitudes in these two figures are not necessarily the same. The location in the normal direction with peak value of the topos is lower for the case with continuous actuation than that for the no-control case. This is because plasma actuation suppresses the turbulent boundary layer separation and at the same time reduces the fluctuation within the boundary layer. The fluctuation length scale in the normal direction (wall-

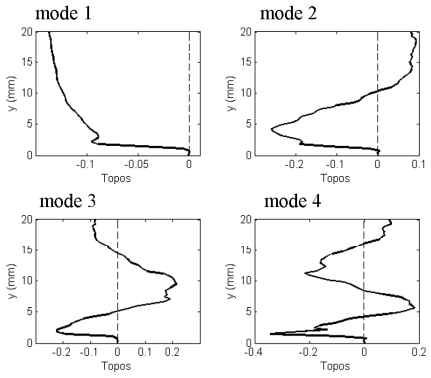

Figure 18: Topos of axial velocity at the location of x = 14 mm with continuous actuation

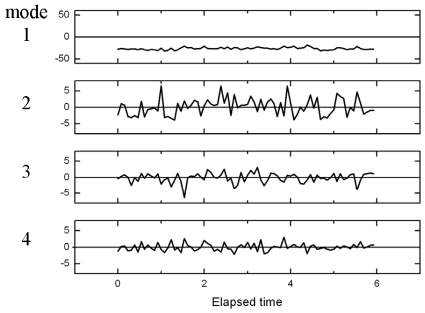

Figure 19: Chronos of axial velocity at the location of x = 14 mm with continuous actuation

distance of the zero-crossing of the second modes) increases versus axial distance, as observed from Fig. 20(a-c), Fig. 21(a-c) and Fig. 21(d-g), respectively. This is a reflection of the downstream development of the normal spreading of the shear layer [30]. For the case with continuous actuation, the flow control reshapes the boundary layer, with the associated new development of fluctuations (length scale in the normal direction) in Fig. 21(d-g). This trend of the length scale is consistent with that of the boundary layer thickness in the mean flow (see Fig. 10), which can endure more adverse pressure gradient without separation.

Energy Distribution

Fig. 22 shows the eigenvalues (energy distribution) for different cases at the location x = 30 mm. From this figure, it is observed that the POD converges rapidly, with the energy rapidly decreases with the mode number. The case with continuous actuation converges fastest because the main energy

 Copyright © 2010 by Her Majesty the Queen in Right of Canada

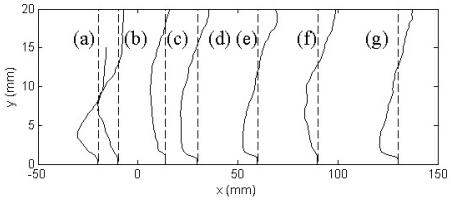

Figure 20: Development of second mode of topos without actuation

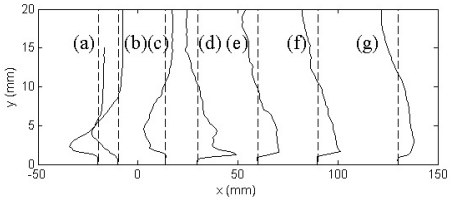

Figure 21: Development of second mode of topos with continuous actuation

is included in the mean, while the no-control case converges slowest because quite a lot of energy is included in the fluctuation associated with the separated flow. This is consistent with Simpson's argument [2] that the velocity fluctuations in the reverse flow region are greater than or at least comparable to the mean reverse velocities.

Entropy Development

The cumulated entropy (see Eqn. (6)) increases with mode number, because the addition of higher mode increases the disorder of the whole system. For the cases in this paper, the cumulated entropy almost reaches the maximum at the mode number of 20. The maximum cumulated entropy is thus a global entropy (abbreviated as entropy in the following presentation). Fig. 23 shows the development of entropy versus axial distance for different cases. With no actuation, the entropy reaches a maximum in the middle part ($x \approx 30$ mm). This is because the energy upstream of this location is mainly included in the positive mean flow while downstream it is in the reverse mean flow. With both continuous and pulsed actuation, the entropy is reduced at each location, implying that the flow is more stable and more energy is included in the mean flow. Moreover, it is observed that a local minimum entropy exists for all cases between actuation location and diffuser exit. In terms of the local minimum entropy, the continuous actuation has the most upstream location, followed by pulsed actuation at 15 Hz and 25 Hz, and 5 Hz with the most downstream location. This can be explained by the fact that the further upstream the location with local minimum entropy, the earlier the effect of actuation on the flow is activated. This trend is consistent with

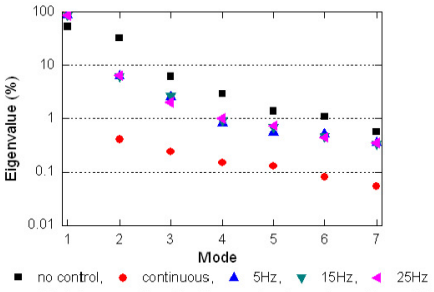

Figure 22: Energy distribution at the location of x = 30 mm

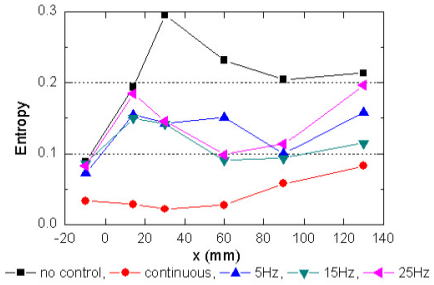

Figure 23: Development of entropy

the development of mean velocity in Fig. 14. In addition, near the diffuser exit, the entropy increases again for all cases, since the plasma actuation is far from this location, and its effect is significantly reduced.

Since the entropy is a normalized quantity, it can be used to compare the disorder levels of different signals. In other words, it can be used in this paper to quantify the effects of different plasma actuation regimes on boundary layer separation control. The smaller the entropy, the more effective the control. As shown in Fig. 23, the continuous actuation is most effective, followed by the pulsed actuation at 15 Hz.

Spectra

The spectra of axial velocity fluctuation based on PIV measurement can also show some features of the flow with pulsed actuation, even though the sampling frequency f_s is not high enough. Fig. 24 show the spectra of axial velocity fluctuation in the plane of x = 30 mm, without actuation and with pulsed actuation, respectively. The spectrum for the case without actuation is more complex than that with pulsed actuation, indicating that the flow with pulsed actuation is more organized. The near-wall flow for each case has smaller fluctuation, as observed from the lower spectrum power near the wall. In addition, the spectra for each case reveal the similar distributions for different frequencies along the normal location

 Copyright © 2010 by Her Majesty the Queen in Right of Canada

in the same plane, and thus these spectra at the same axial location can be averaged to obtain a smooth one.

Fig. 25 shows the average spectra of axial velocity fluctuation for different cases in the plane of x = 30 mm and 90 mm. Because of the low sampling frequency f_s and thus aliasing effect, the observed frequencies f_{ob} with peak values are not the realistic ones f_{real} within the flow. The corresponding relation is [31]

$$f_{real} = f_{ob} + 2Nf_N \quad or \quad = -f_{ob} + (2N+1)f_N \qquad (N = 0,1,2\cdots) \qquad (2)$$

where $f_N = f_s/2$ is the Nyquist frequency (7 Hz for most cases, except 6.5 Hz for the no-control case). For example, f_{ob} = 1 Hz could correspond to f_{real} = 15 Hz with N = 1, f_N = 7 Hz. For the no-control case in Fig. 25, various peaks can be observed, which is qualitatively similar to the spectra from hotwire measurement (Fig. 9). This also indicates that large-scale vortices are shedding from the separation bubble over those frequencies [23]. For the cases with pulsed actuation, the shedding of large-scale vortices in the flow at x = 30 mm is locked on the actuation frequencies of 5 Hz, 15 Hz and 25 Hz (as observed from the sharp peaks at f_{ob} = 5 Hz, 1 Hz and 3 Hz), respectively. This is consistent with the finding of Hwang et al. [32]. For the 5 Hz case, another observed frequency 4 Hz may correspond to a superharmonic frequency of 10 Hz. However, the situation at x = 90 mm is different, with more peaks observed. This is because this location is far from the actuation source and the effect of actuation is less significant.

4. CONCLUSION

The present paper studies the effects of DBD plasma actuators experimentally on suppression of a 2-D turbulent boundary layer separation in a diffuser with high adverse pressure gradient. Both continuous and pulsed actuations are applied and shown to effectively suppress the turbulent boundary layer separation. For the pulsed actuation, the actuation frequency of 15 Hz, corresponding to the dimensionless frequency of $F^+ \sim O(1)$, is found to the most effectively suppress the turbulent separation. The variations of turbulent kinetic energy and Reynolds shear stress demonstrate the increased momentum transfer by fluctuations in the flow with pulsed actuation. To better analyze the results from PIV measurements, the POD method was applied to extract the spatial modes and their temporal counterparts. The effect of continuous actuation can be demonstrated by the variation of the second spatial mode (corresponding to large fluctuation in the flow). Moreover, the entropy, indicating the energy distribution of various modes, is proposed to quantify the effects of different plasma actuation regimes on boundary layer separation control. In addition, from spectral analysis the flow with pulsed actuation is observed to be locked on the actuation frequencies near the actuation location, while the result is not obvious far from the actuation location.

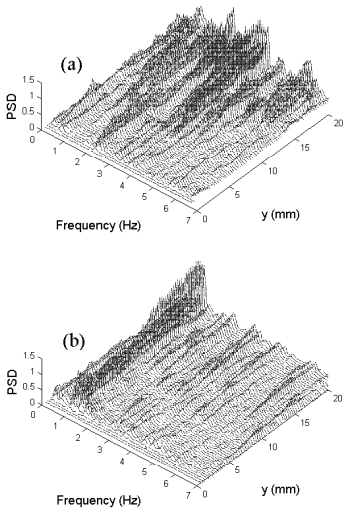

Figure 24: Spectra of axial velocity fluctuation at the location of x = 30 mm with (a) no actuation, (b) pulsed actuation

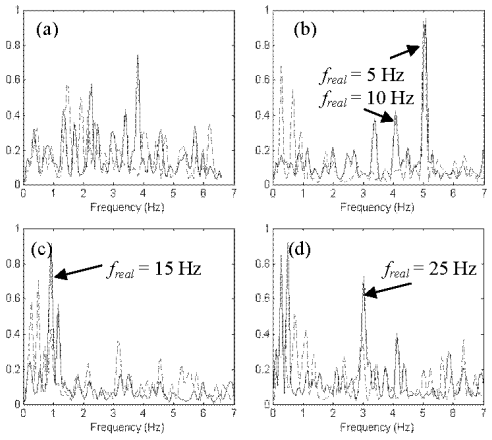

Figure 25: Averaged spectra of axial velocity fluctuation at the locations of x = 30 mm (solid blue line) and 90 mm (dashed red line) for the cases with (a) no actuation, (b) pulsed actuation at 5 Hz, (c) pulsed actuation at 15 Hz, (d) pulsed actuation at 25 Hz

 Copyright © 2010 by Her Majesty the Queen in Right of Canada

ACKNOWLEDGMENTS

The authors are pleased to acknowledge the support from the National Research Council Canada (NRC) and the assistance of Mr. P. Versailles, Mr. S. Ueno and Mr. K. Huynh at École Polytechnique de Montréal with the experimental setup.

REFERENCES

[1] Simpson, R. L., 1981, "A Review of Some Phenomena in Turbulent Flow Separation," Journal of Fluids Engineering, **103**(4), pp. 520-533.

[2] Simpson, R. L., 1996, "Aspects of Turbulent Boundary-Layer Separation," Progress in Aerospace Sciences, **32**(5), pp. 457-521.

[3] Sullerey, R. K., Mishra, S., and Pradeep, A. M., 2002, "Application of Boundary Layer Fences and Vortex Generators in Improving Performance of S-Duct Diffusers," Journal of Fluids Engineering, Transactions of the ASME, **124**(1), pp. 136-142.

[4] Pradeep, A. M., and Sullerey, R. K., 2006, "Active Flow Control in Circular and Transitioning S-Duct Diffusers," Journal of Fluids Engineering, Transactions of the ASME, **128**(6), pp. 1192-1203.

[5] Mathis, R., Duke, D., Kitsios, V., and Soria, J., 2008, "Use of Zero-Net-Mass-Flow for Separation Control in Diffusing S-Duct," Experimental Thermal and Fluid Science, **33**(1), pp. 169-172.

[6] Shin, J., Narayanaswamy, V., Raja, L. L., and Clemens, N. T., 2007, "Characterization of a Direct-Current Glow Discharge Plasma Actuator in Low-Pressure Supersonic Flow," AIAA Journal, **45**(7), pp. 1596-1605.

[7] Enloe, C. L., Mclaughlin, T. E., Vandyken, R. D., Kachner, K. D., Jumper, E. J., and Corke, T. C., 2004, "Mechanisms and Responses of a Single Dielectric Barrier Plasma Actuator: Plasma Morphology," AIAA Journal, **42**(3), pp. 589-594.

[8] Forte, M., Jolibois, J., Pons, J., Moreau, E., Touchard, G., and Cazalens, M., 2007, "Optimization of a Dielectric Barrier Discharge Actuator by Stationary and Non-Stationary Measurements of the Induced Flow Velocity: Application to Airflow Control," Experiments in Fluids, **43**(6), pp. 917-928.

[9] Roth, J. R., and Dai, X., 2006, "Optimization of the Aerodynamic Plasma Actuator as an Electrohydrodynamic (EHD) Electrical Device," AIAA Paper 2006-1203.

[10] Patel, M. P., Ng, T. T., Vasudevan, S., Corke, T. C., Post, M. L., Mclaughlin, T. E., and Suchome, C. F., 2008, "Scaling Effects of an Aerodynamic Plasma Actuator," Journal of Aircraft, **45**(1), pp. 223-236.

[11] Orlov, D. M., Apker, T., He, C., Othman, H., and Corke, T. C., 2007, "Modeling and Experiment of Leading Edge Separation Control Using SDBD Plasma Actuators," AIAA Paper 2007-0877.

[12] Rizzetta, D. P., and Visbal, M. R., 2008, "Plasma-Based Flow-Control Strategies for Transitional Highly Loaded Low-Pressure Turbines," Journal of Fluids Engineering, Transactions of the ASME, **130**(4), pp. 0411041-04110412.

[13] Visbal, M. R., and Gaitonde, D. V., 2006, "Control of Vortical Flows Using Simulated Plasma Actuators," AIAA Paper 2006-505.

[14] Hultgren, L. S., and Ashpis, D. E., 2003, "Demonstration of Separation Delay with Glow-Discharge Plasma Actuators," AIAA Paper 2003-1025.

[15] Boxx, I. G., Woods, N. M., Newcamp, J. M., Franke, M. E., and Rivir, R. B., 2006, "A PIV Study of a Plasma Discharge Flow-Control Actuator on a Flat Plate in an Aggressive Pressure Induced Separation," ASME Paper GT2006-91044.

[16] Schlichting, H., 1979, Boundary-Layer Theory, McGraw-Hill, New York, Origin of Turbulence.

[17] Visbal, M. R., Gaitonde, D. V., and Roy, S., 2006, "Control of Transitional and Turbulent Flows Using Plasma-Based Actuators," AIAA Paper 2006-3230.

[18] He, C., Corke, T. C., and Patel, M. P., 2007, "Numerical and Experimental Analysis of Plasma Flow Control over a Hump Model," AIAA Paper 2007-935.

[19] Hemon, P., and Santi, F., 2003, "Applications of Biorthogonal Decompositions in Fluid-Structure Interactions," Journal of Fluids and Structures, **17**(8), pp. 1123-1143.

[20] Aubry, N., Guyonnet, R., and Lima, R., 1991, "Spatiotemporal Analysis of Complex Signals: Theory and Applications," Journal of Statistical Physics, **64**(3-4), pp. 683-739.

[21] Hoarau, Y., Braza, M., Ventikos, Y., and Faghani, D., 2006, "First Stages of the Transition to Turbulence and Control in the Incompressible Detached Flow around a Naca0012 Wing," International Journal of Heat and Fluid Flow, **27**(5), pp. 878-886.

[22] Mathis, R., Lebedev, A., Collin, E., Delville, J., and Bonnet, J. P., 2009, "Experimental Study of Transient Forced Turbulent Separation and Reattachment on a Bevelled Trailing Edge," Experiments in Fluids, **46**(1), pp. 131-146.

[23] Cherry, N. J., Hillier, R., and Latour, M. E. M. P., 1984, "Unsteady Measurements in a Separated and Reattaching Flow," Journal of Fluid Mechanics, **144**, pp. 13-46.

[24] Herbst, A. H., and Henningson, D. S., 2006, "The Influence of Periodic Excitation on a Turbulent Separation Bubble," Flow, Turbulence and Combustion, **76**(1), pp. 1-21.

[25] Cierpka, C., Weier, T., and Gerbeth, G., 2007, Active Flow Control, Springer, Berlin, Electromagnetic Control of Separated Flows Using Periodic Excitation with Different Wave Forms.

 Copyright © 2010 by Her Majesty the Queen in Right of Canada

[26] Gad-El-Hak, M., 2000, *Flow Control : Passive, Active, and Reactive Flow Management*, Cambridge University Press, Cambridge, U.K. ; New York.
[27] Simpson, R. L., Strickland, J. H., and Barr, P. W., 1977, "Features of a Separating Turbulent Boundary Layer in the Vicinity of Separation," Journal of Fluid Mechanics, **79**, pp. 553-594.
[28] Kriegseis, J., Dehler, T., Pawlik, M., and Tropea, C., 2009, "Pattern-Identification Study of the Flow in Proximity of a Plasma Actuator," AIAA Paper 2009-1001.
[29] Tennekes, H., and Lumley, J. L., 1972, *A First Course in Turbulence*, The MIT Press, Cambridge and London.
[30] Manhart, M., and Wengle, H., 1993, "A Spatiotemporal Decomposition of a Fully Inhomogeneous Turbulent Flow Field," Theoretical and Computational Fluid Dynamics, **5**(4), pp. 223-242.
[31] Aliasing, April 29 2010, http://en.wikipedia.org/wiki/Aliasing#cite_ref-mitchell_0-0
[32] Hwang, K. S., Sung, H. J., and Hyun, J. M., 2001, "An Experimental Study of Large-Scale Vortices over a Blunt-Faced Flat Plate in Pulsating Flow," Experiments in Fluids, **30**(2), pp. 202-213.

APPENDIX
Proper Orthogonal Decomposition (POD)

In the POD, a turbulent space-time velocity field $\tilde{u}_i(\vec{x},t)$ (i = 1, 2, 3) can be split as [19]

$$\tilde{u}_i(\vec{x},t)=\sum_{k=1}^{\infty}\psi_k(t)\varphi_{ik}(\vec{x}) \tag{3}$$

where $\varphi_{ik}(\vec{x})$ is the spatial mode (called *topos*) of order k and $\psi_k(t)$ is the corresponding temporal mode (called *chronos*). Each combination of $\psi_k\varphi_{ik}$ represents a basic state embedded in the random turbulent flow field.

To solve Eqn. (3), the singular value decomposition of matrix A is applied

$$A=U\sum V^T=QV^T \tag{4}$$

where U and V are orthogonal and $\sum$ is a diagonal matrix whose coefficients α_k are the singular values of A. Thus Eqn. (3) is solved, with Q and V corresponding to ψ and φ, respectively.

The eigenvalues λ_k ($\lambda_k=\alpha_k^2$) is representative of the energy associated with the mode k. Thus the global energy of the signal is equal to the sum of the eigenvalues

$$\sum_{k=1}^{\infty}\lambda_k=\sum_{k=1}^{\infty}\alpha_k^2 \tag{5}$$

The global entropy of the signal characterizing its degree of disorder is defined as [20]

$$H=-\lim_{M\to\infty}\frac{1}{\log M}\sum_{k=1}^{M}\lambda_{rk}\log\lambda_{rk} \tag{6}$$

with

$$\lambda_{rk}=\lambda_k/\sum_{k=1}^{\infty}\lambda_k \tag{7}$$

where M is the total mode number (M = 73 in the present paper).

 Copyright © 2010 by Her Majesty the Queen in Right of Canada

Appendix C: Plasma Generation System

The new plasma generation system (Thomas *et al.*, 2009), as shown in Figure C.1, is composed of signal generator, power amplifiers, resistor module and transformers. The detailed information of each component and assembly will be discussed in the following part.

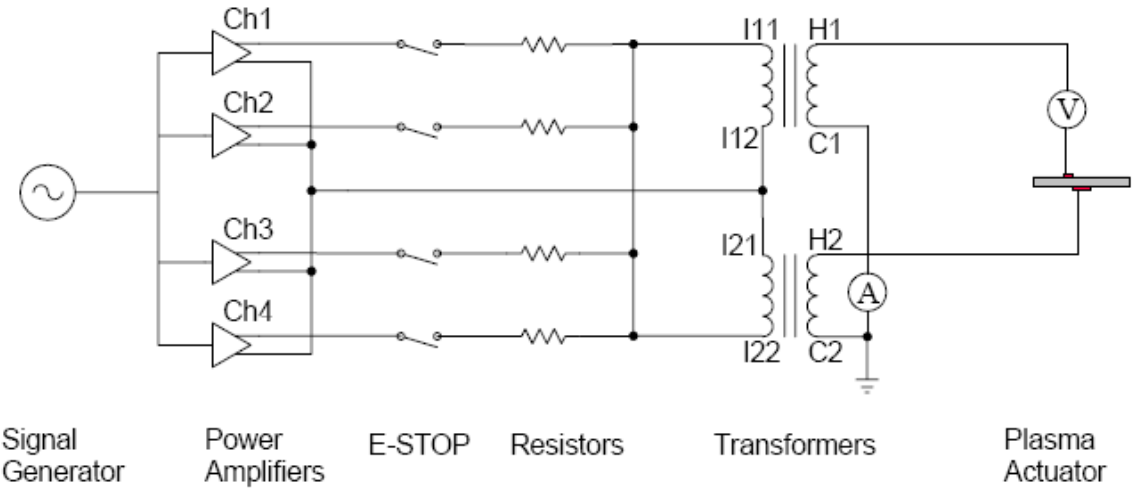

Figure C.1: A schematic representation of plasma generation system

Signal Generator

The AC signal (up to 10 V_p) can be generated by standard signal generators or NI DAQ cards (*e.g.*, PCI-6110). The waveform types include sine, square, triangle and sawtooth. When pulsed actuation (modulation) is required, especially for flow control, it is better to use NI DAQ cards to generate signal, because the complex functions can be easily fulfilled in LabView code. The corresponding LabView interface is shown in Figure C.3. The highlighted part A is used for the setting of the plasma AC cycle, while part B is for modulation setting. The part C is for setting the trigger signal which can be used to trigger data acquisition or phase-locked PIV measurement.

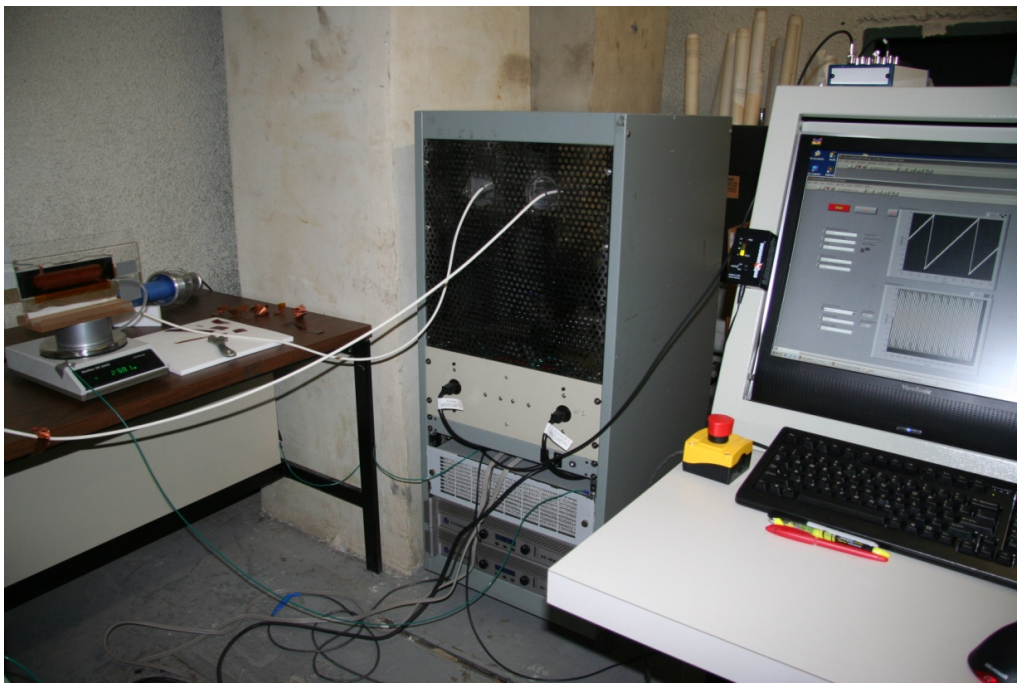

Figure C.2: Plasma generation system

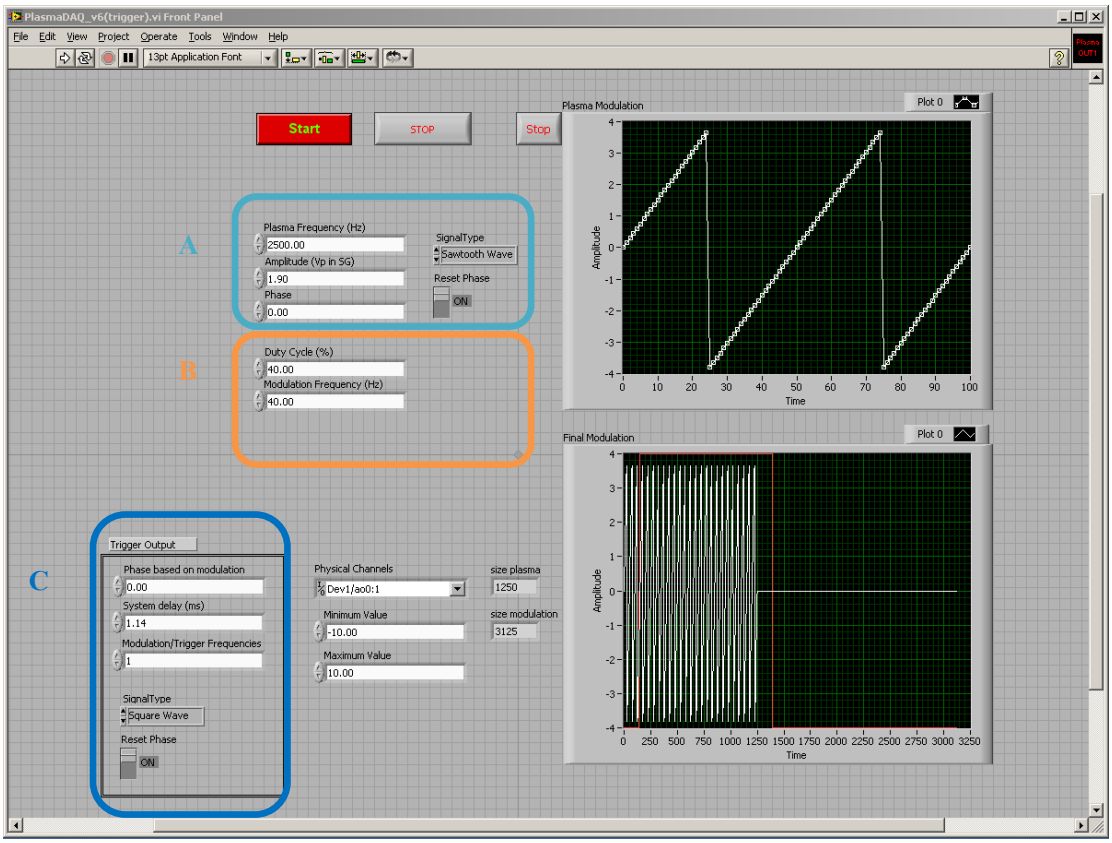

Figure C.3: LabView interface for signal generation

Power Amplifiers

Two Crown XTi-4000 Power Amplifiers, consisting of totally four channels, are used to supply high power. The input cables include CC1 and CC2 (see Table 5 for detailed descriptions), where CC1 is for receiving signal from signal generator, while CC2 for signal transfer between LINK/OUT connectors of power amplifiers. The output cables are CC4, which is also connected to Ballast Resistor Module. The working function of power amplifier is set as DSP OFF (no signal processing is applied). The amplifying ratio is usually chosen the same for all channels through rotary level control.

The two power amplifiers should be powered by two independent AC line sources (110 V, 15 A), respectively. In addition to the power switches of power amplifiers, the on/off of four channels is especially controlled by an emergency stop (E-STOP), which can directly cut off the AC power supply from the line sources (wall jackets).

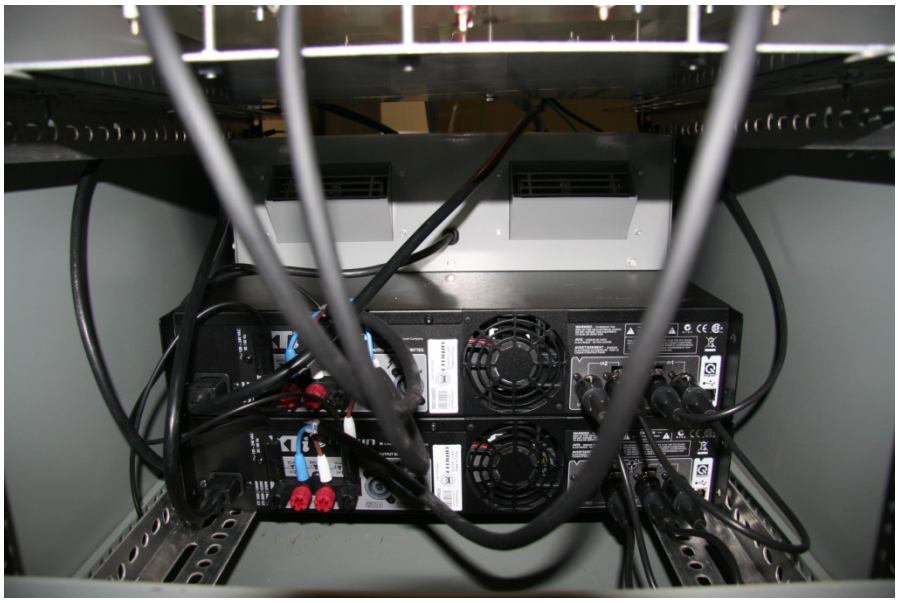

Figure C.4: Power amplifier connection

Resistor Module

The Resistor Module, mounted on a PC board, consists of four ballast resistors (2 ohms, 300

W), corresponding to four channels of power amplifiers. This selection is based on 1) the minimum load impedance of each channel is 2 ohms, 2) the current through the resistors and thus the heating loss are very high. To avoid the over-heating of the board, the resistors should be lifted at least 0.5 inches. The inputs of four resistors are connected to each channel, while the four outputs are connected together, which is then connected to two transformers.

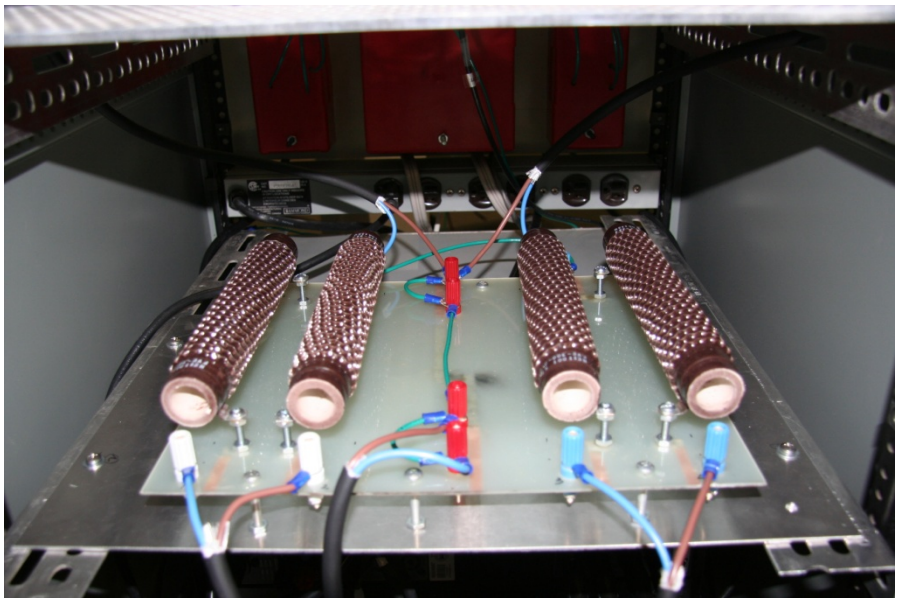

Figure C.5: Resistor module

Transformers

To obtain AC high voltage (~10 kV), two CMI-5525 transformers made by Corona Magnetics are used, as shown in Figure C.6. Each transformer has a turns ratio (secondary to primary) of 360:1, working frequency of 0.9-5 kHz, maximum output of 25 kV_{rms}. These two transformers are mounted on a porous aluminum plate.

To obtain totally ratio of 720:1, these two transformers are connected parallel (see Figure C.1) as 1) I11 and I22 to the output of resistor module, 2) I12 and I21 to the common of amplifiers, 3) C1 and C2 to ground, 4) H1 to one electrode of plasma actuator and H2 to the other electrode. Please note that the cable CC5 (refer to Table 5) is used for primary side wiring, while the high voltage cable CC6 for the secondary side wiring to the plasma actuator.

In the case of lower required voltage difference between actuator electrodes or that one electrode need to be grounded, only one transformer is used. The connection is such as 1) I11/I21 to the output of resistor module, 2) I12/I22 to the common of amplifiers, 3) grounded C1/C2 to one electrode of plasma actuator, 4) H1/H2 to the other electrode. Note that two transformers with the exactly same connections should not be used, since the CLIP state of amplifiers (instantaneous power consumption too high) would be easy to occur. This is because the instantaneous power is twice and much larger than realistic (time-averaged) power consumption.

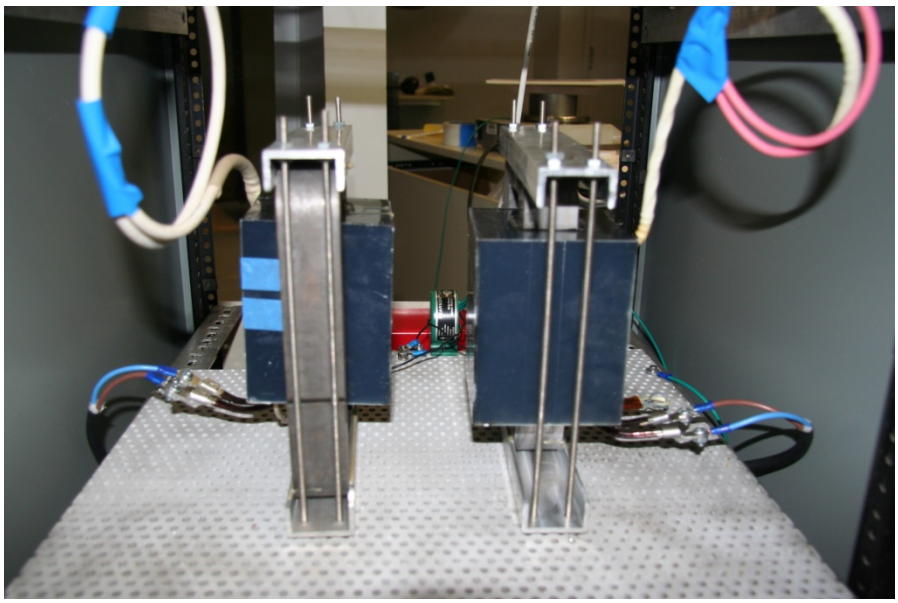

Figure C.6: Transformers

Assembly

The main components of plasma generation system introduced above, *i.e.*, two power amplifiers, ballast resistor module and two transformers, are mounted in a standard 19-inch equipment rack as shown in Figure C.7. The side walls of the rack are made of solid metal plate while the front and rear walls are made of porous metal plate, which is better for airflow and cooling. The bottom-to-top order of these components is power amplifiers, ballast resistor module and two transformers. To enhance cooling, especially for the ballast resistors and transformers, a fan is equipped below the resistor module, with the up-rear blowing direction. Generally, the cool air comes in from the front and the hot air goes out from the rear.

For safety, all component cases or metal plates for mounting must be grounded. This can be easily done, by connecting them to the grounded rack. Moreover, to avoid high voltage discharge, the high voltage leads of transformers should be kept a distance from any metal surface. In addition, the rack made of metal plate can effectively reduce electromagnetic interference with other electronic units, *e.g.*, computer, data acquisition system.

Figure C.7: Main components of plasma generation system

Measurement Techniques

To evaluate the performance of the plasma actuator and the new system, various measurement techniques are adopted.

The instantaneous high voltage at the electrodes of the plasma actuator is obtained by using a PVM-3 high voltage probe (40 kVDC, max frequency of 40 MHz, divider ratio of 10000:1, uncertainty lower than 3% for 200 Hz-5 MHz), made by North Star High Voltage. This probe is

located near one electrode of the plasma actuator to exclude the voltage drop along the high-voltage wire. The voltage difference between the plasma actuator electrodes (for the configuration in Figure C.1) is obtained by doubling the measured value from the probe, based on a preliminary study.

The instantaneous current through the plasma actuator is obtained by using a Pearson 4100 current monitor (output ratio of 1 V/A, frequency of 140 Hz-35 MHz, uncertainty lower than 1%). This current monitor is located near the common lead of the transformer secondary side, instead of the high voltage lead, to avoid the high voltage discharge to the monitor case.

The instantaneous signals from high voltage probe and current monitor are simultaneously acquired by a NI DAQ card associated with a LabView program in Figure C.8. The dissipated power can thus be obtained by point-by-point integration of the instantaneous product of voltage and current over many AC cycles (N=20 is found enough for convergence).

The force (thrust) produced by a plasma actuator is measured by a high precision electronic balance (Mettler Toledo PE3600 DeltaRange) with a resolution of 0.01 g (0.098 mN). The plasma actuator is supported vertically in a block of dielectric material, which is directly placed on the balance, as shown in Figure C.9. The plasma actuator is oriented in such a way that the plasma-induced flow is directed upward and the reactive thrust acting downward is measured directly by the balance. The highly flexible wire is used for the leads that power the plasma actuator, to reduce the influence of wire tension on thrust measurement. To obtain the quasi-steady thrust, a waiting time of more than 5 seconds is required, even though the electrical properties are reached periodically stable after only two AC cycles (~ 1 ms).

It should be noted that the plasma generation system/plasma actuators need warm up before application, by running the plasma actuator at medium/high voltage for several times. The stability can be evaluated by measuring the induced thrust.

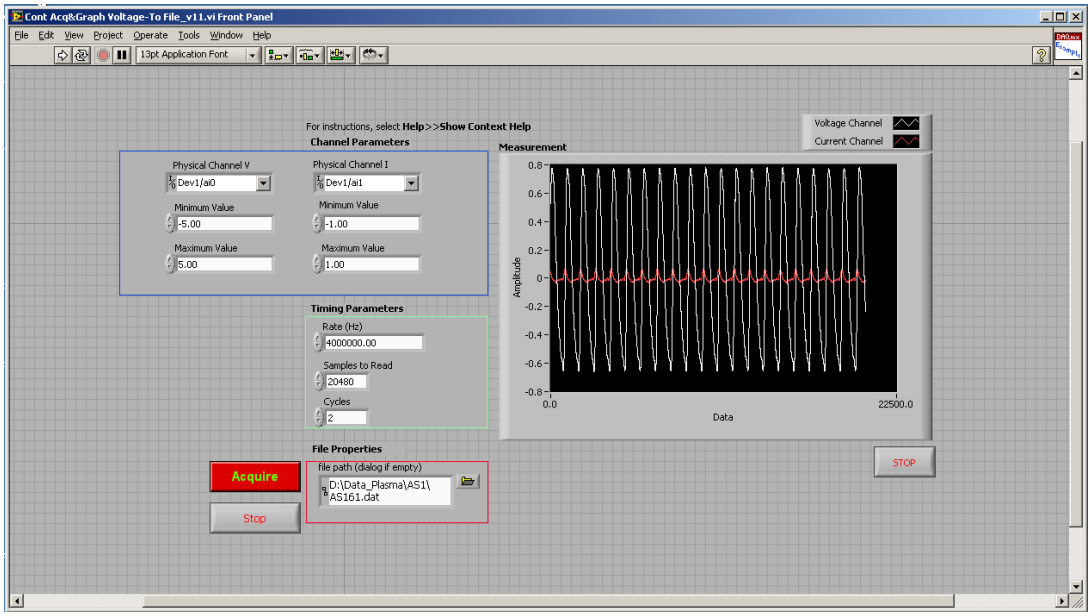

Figure C.8: LabView interface for data acquisition

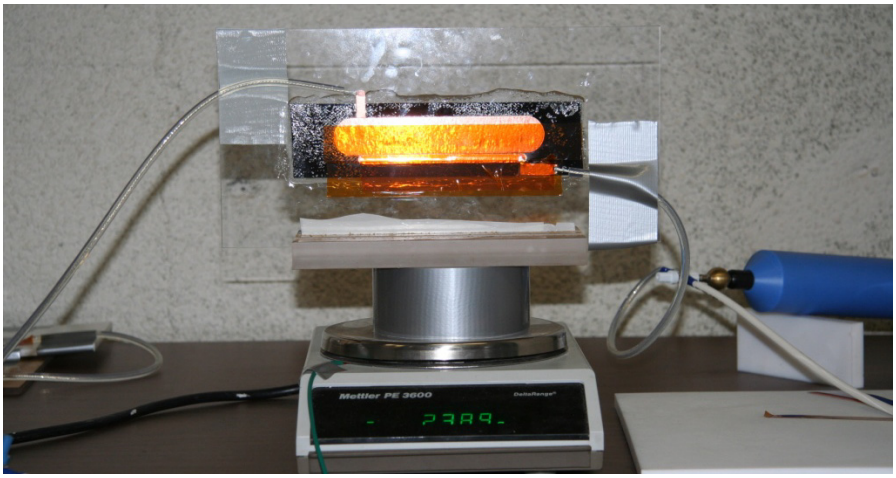

Figure C.9: Force/thrust measurement

Table 5: Cables and Connectors

Index Number	Wire	Connector 1	Connector 2
CC1	RG-58/U coaxial cable (impedance of 50 ohms, conductor size of 20 AWG)	BNC male	3-pin XLR male[1]
CC2	RG-58/U	3-pin XLR male	3-pin XLR female
CC3	RG-58/U	BNC male	BNC male
CC4	14 AWG, 300 V	Banana male	Banana male
CC5	14 AWG, 300 V	Spade terminal	Spade terminal
CC6	18 AWG, 42 kVDC	Spade terminal	Spade terminal

1. The pins 1 and 3 are both connected to the shield of coaxial cable

Table 6: Transformer Leads

Index Number			Definitions
	Transformer 1	Transformer 2	
Primary Side	I11	I21	H1 and H2 have the same phase, when the same AC signal is input into I11 and I21
	I12	I22	Similar to the above
Secondary Side	H1	H2	High voltage leads
	C1	C2	Common leads/grounded

Appendix D: Parametric Study on DBD Plasma Actuators

Using the newly-built plasma actuator system, this section studies the effects of different operation parameters and configurations of DBD plasma actuators in order to optimize them for flow control. The investigated operation parameters of plasma actuators include dielectric material, applied waveform and frequency, and different shapes of exposed electrode, while the investigated configurations include bi-electrode and tri-electrode configurations. The detailed information about the parametric study is listed in Table 7.

Table 7: Parametric study test matrix

Optimization Goal	Dielectric Material	Waveform and Frequency	Exposed Electrodes			Tri-electrode (AC+DC)
			Wire-type (Diameter)	Straight Foil-type (Insulted Width)	Serrated Foil-type (Triangular)	
Increase maximum force	Teflon (6.35 mm)	sine, sawtooth, square waves	0.013, 0.02, 0.07, 0.25 mm	electrode width: 6.35, 12.7, 25.4 mm	width: 3.18, 6.35, 12.7 mm	AC: 10~20 kV_{rms}
Improve efficiency	Plexiglas (6.35 mm)	2, 3, 4 kHz		insulted width: 0~100%	width-height ratio: 1:1, 1:4, 4:1	DC: 20~40 kV

For dielectric material, Teflon and Plexiglas are chosen. Because Teflon has a lower dielectric constant compared to other dielectric materials, and it can significantly increase the maximum achievable voltage before the saturation, while Plexiglas is hard, easy to machine, and cheap.

For the shapes of exposed electrode, the straight foil-type, serrated foil-type and wire type are chosen as shown in Figure D.2.

As for the straight foil-type exposed electrode, the effect of the insulation width on the electrode is studied as shown in Figure D.3. As we already know, using the insulation on the upstream edge of the exposed electrode can increase the net plasma force in one direction.

A normal DBD plasma actuator is composed of two electrodes excited by an AC high voltage, while the tri-electrode configuration (shown in Figure D.4) has a third electrode at a positive DC high voltage. In the tri-electrode configuration, the AC voltage is to weakly ionize the air, while the DC component is to extend the discharge region and accelerate the ion drift velocity (Moreau *et al.*, 2008).

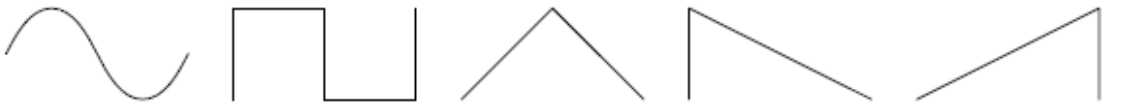

Figure D.1: Different waveform shapes

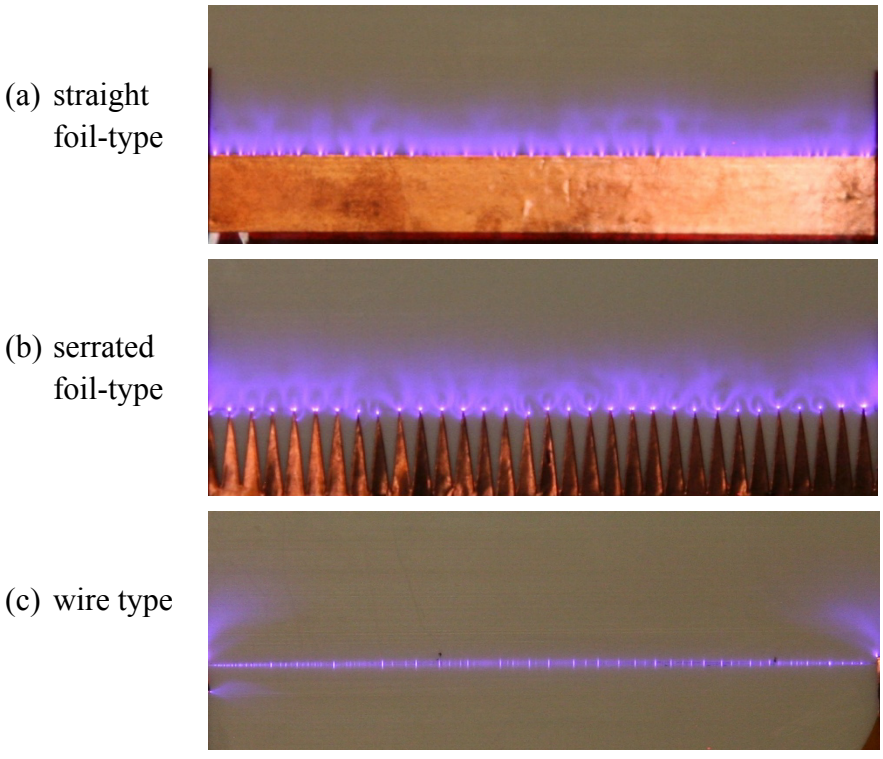

Figure D.2: Exposed electrodes with different shapes

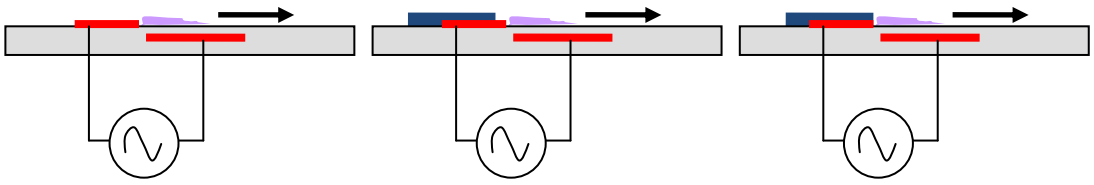

(a) uncovered (b) partially covered (c) fully-covered

Figure D.3: Foil-type exposed electrode with different insulation

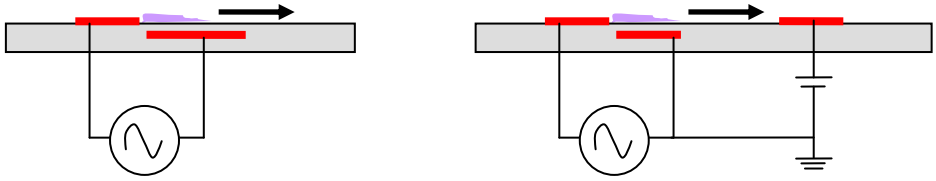

(a) bi-electrode (b) tri-electrode

Figure D.4: Bi-electrode versus tri-electrode configurations

D.1 Effect of Dielectric Material

As discussed in Section 5.1.1, the dielectric material plays an important role in plasma-induced force generation. However, only two kinds of dielectric material are tested here, *i.e.*, Teflon and Plexiglas with 6.35 mm thick. The hidden electrode has a width of 25.4 mm, while the fully covered exposed one (refer to Figure D.3) has a width of 6.35 mm. The corresponding results are shown in Figure D.5, in terms of the measured actuator thrust versus applied RMS voltage. It should be noted that in this test only one transformer is used, while two transformers are used for the remaining parametric studies (see Figure C.1). Two transformer configuration is useful to obtain higher applied voltage on plasma actuators. In contrast, one transformer configuration is useful for the flow control, because one electrode need be grounded. Two kinds of connections thus exist, namely HV exposed and HV covered. The HV exposed connection means the exposed electrode is connected to high voltage while the hidden electrode is grounded. The plasma actuator is operated at 2.5 kHz with negative sawtooth voltage input (Figure D.1) for all cases.

From Figure D.5, the measured thrust increases with applied AC voltage. The maximum

thrust is about 230 mN/m with the applied voltage of 21 kV_{rms}. As for the effect of dielectric material, Teflon has a higher maximum obtainable thrust than Plexiglas (*e.g.*, 230 versus 180 mN/m). At any specific applied voltage, Plexiglas has a higher measured thrust. These observations are consistent with the general argument that using a dielectric material of lower dielectric constant can significantly increase the maximum obtainable thrust while one obtains lower thrust at the same applied voltage (Thomas *et al.*, 2009). For many applications of plasma actuators, the dielectric with higher dielectric constant may be a good choice. Because to obtain the same thrust, a lower applied voltage is needed, which reduce the risk to affect and even damage other associated equipments. It should be noted that the Plexiglas actuator with HV covered connection can be continuously operated at 11.9 kV_{rms} (a thrust of 69 mN/m) for at least 10 minutes.

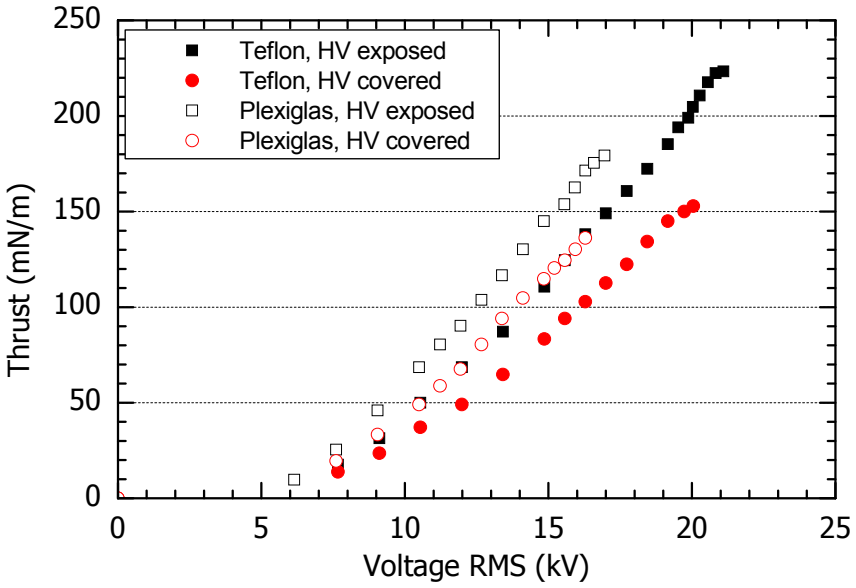

Figure D.5: Effect of dielectric material

As for the effect of different connections, the plasma actuator with HV exposed connection can obtain both higher thrust at the same applied voltage and higher maximum achievable thrust. The high voltage applied at the exposed electrode should favor the ionization process of air near the electrode, which then contribute to more ion movement and higher flow acceleration, even

though the voltage difference between the two electrodes is the same.

Figure D.6 shows the time-averaged flow field induced by plasma actuator from PIV measurement for two cases with different applied voltages, which correspond to plasma actuator of "Teflon, HV exposed" in Figure D.5. The location x = 0 mm corresponds to actuator location, the trailing edge of exposed electrode in Figure 1.5. From Figure D.6, one could observe how the actuator pulls the upstream ambient air toward the wall and blows the air downstream parallel to the wall forming a wall jet. This induced wall jet is very thin, with the height of less than 10 mm. The peak velocity is very close to the wall (around 1 mm above the wall). This can also be clearly observed in Figure D.7, which plots the time-averaged profile derived from the PIV measurements and from Pitot tube at locations of x = 15 and 40 mm downstream of the actuator location, respectively. The axial location x = 15 mm corresponds to the maximum induced peak velocity, with the details discussed later. The peak velocity increases with applied voltage. Please note that the axial velocity above y = 8 mm at x = 15 mm (Figure D.7(a)) is negative, while the corresponding velocity is almost zero at x = 40 mm (Figure D.7(b)). This is because the suction process from ambient air is very fast especially near the plasma actuator that local mass exchange leads to the negative velocity.

Figure D.7 also shows that the results from PIV measurement and Pitot tube match well, in terms of profile shape, peak velocity location. From PIV measurements, the maximum velocity and its location can be easily found. As for the measurement by the use of Pitot tube, this can also be done through plots of velocity at several axial locations. With different applied voltage, the maximum velocity for the tested actuators is always located approximately at x = 15 mm and y = 1 mm. Since the maximum velocity is downstream of actuator location (x = 0 mm), one could argue that the process of momentum addition from plasma actuator covers a distance over the hidden electrode (maximum distance is same as the width of hidden electrode of 25.4 mm). The maximum velocity versus applied voltage from both PIV and Pitot tube measurements at this location is shown in Figure D.8. The results from both measurements match well. The maximum

velocity is obtained as 6.8 m/s at 18.3 kV_{rms}, which corresponds to a measured thrust of 176 mN/m.

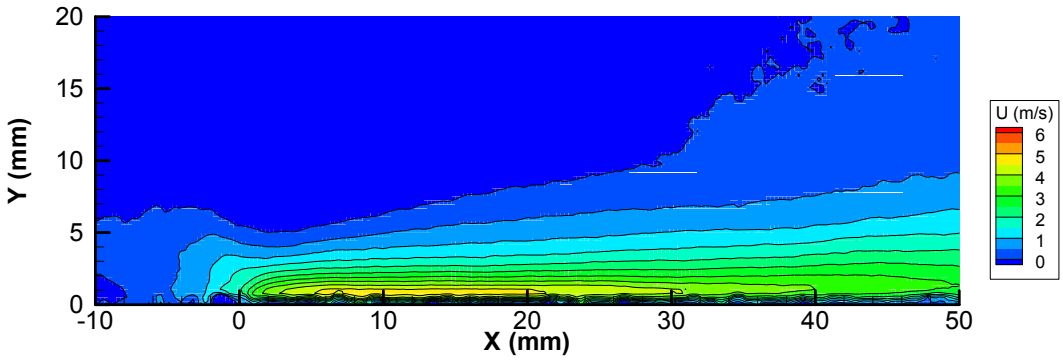

(a) 46.2 kV_{pp} (12 kV_{rms})

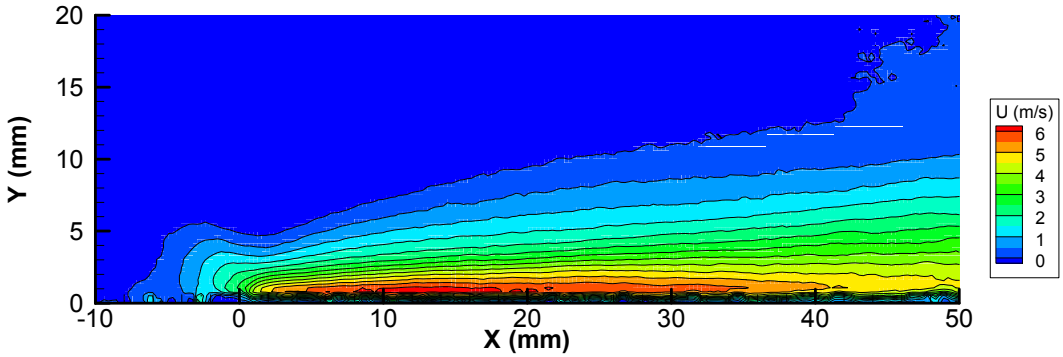

(b) 61.2 kV_{pp} (16.3 kV_{rms})

Figure D.6: Contour of axial velocity with Teflon sheet and HV exposed electrode for different voltages

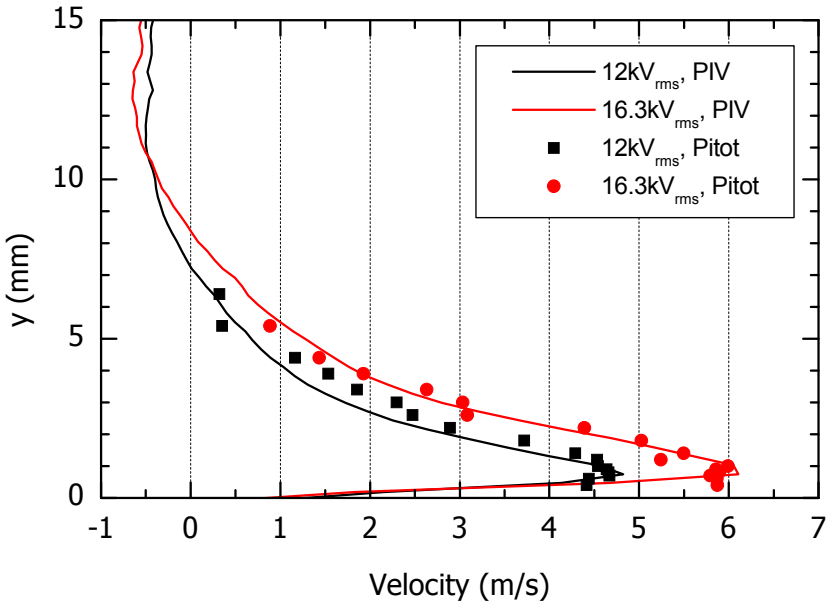

(a) x = 15 mm

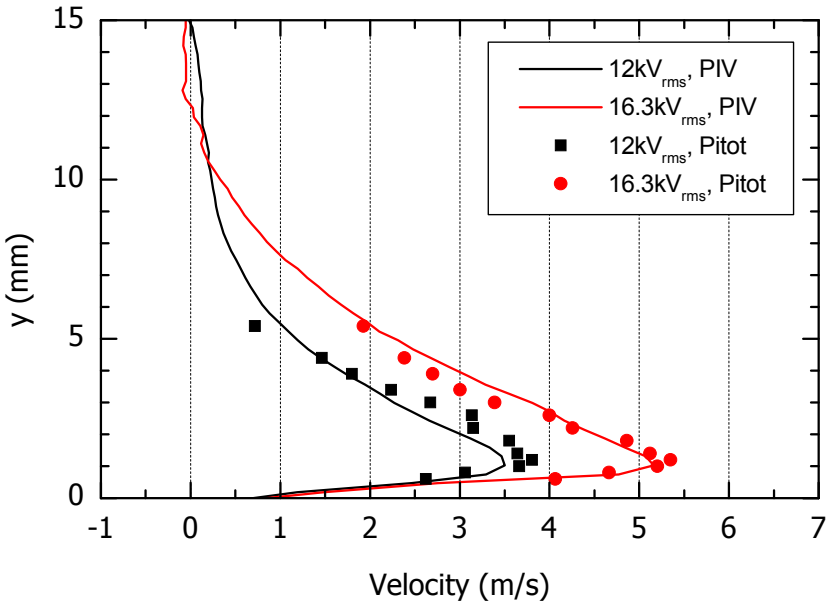

(b) x = 40 mm

Figure D.7: Profile of axial velocity with Teflon sheet and HV exposed electrode for different location

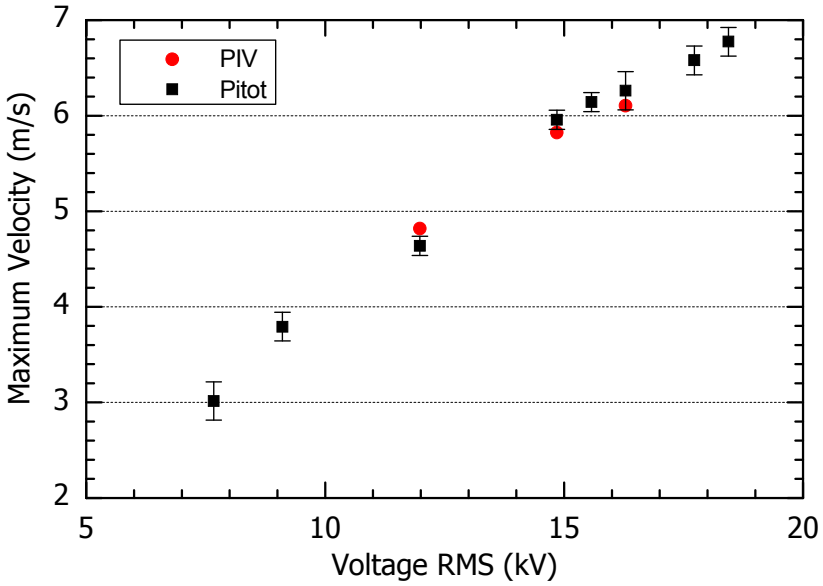

Figure D.8: Maximum induced axial velocity with Teflon sheet and HV exposed electrode for different voltages (x = 15 mm, y = 1 mm)

D.2 Effect of Waveform and AC Frequency

In this section, the effects of input waveform and AC frequencies on maximum obtainable thrust and force efficiency are studied. In these tests the plasma actuator has a Teflon sheet with 6.35 mm thick. The hidden electrode has a width of 25.4 mm, while the fully covered exposed one (refer to Figure D.3) has a width of 6.35 mm.

Figure D.9 plots the measured thrust versus the consumed power for various waveforms, while Figure D.10 plots the electrical measurement for negative sawtooth, positive sawtooth, sinusoidal and square waveforms, respectively. In Figure D.10, the left side corresponds to normal plasma operated at medium applied AC voltage, while the right side corresponds to those near the filamentary mode at high applied voltage. Note that all cases are operated at 2.5 kHz. Even though the input signal to the generator has a perfect shape (see Figure D.1), the actual voltage waveform applied at the electrodes is modified (see Figure D.10).

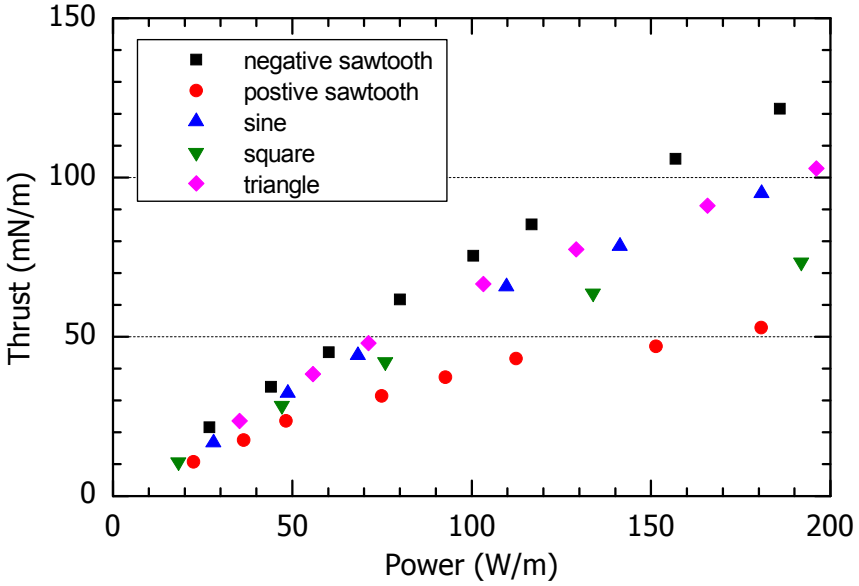

Figure D.9: Thrust versus power for various waveforms

As shown in Figure D.9, negative sawtooth waveform has a highest force efficiency while positive sawtooth has a lowest one. The sinusoidal and triangle waveforms have the similar force efficiency, since both waveforms are symmetrical. From Figure D.10, backward discharge (positive-going or increasing voltage starting from zero) always corresponds to high current pulse, while forward discharge (negative-going or decreasing voltage starting from zero) corresponds to low current pulse at medium applied voltage and high current pulse at high applied voltage. Generally, this is consistent with the observation of Boeuf *et al.* (2009). As for the effect of waveform type, negative sawtooth is most efficient since most part in one cycle is forward discharge. The forward discharge performs most of the momentum transfer to the air (Boeuf *et al.*, 2009; Enloe *et al.*, 2008). The square waveform with one steep positive-going and one steep negative-going part can be understood as the combination of negative and positive sawtooth.

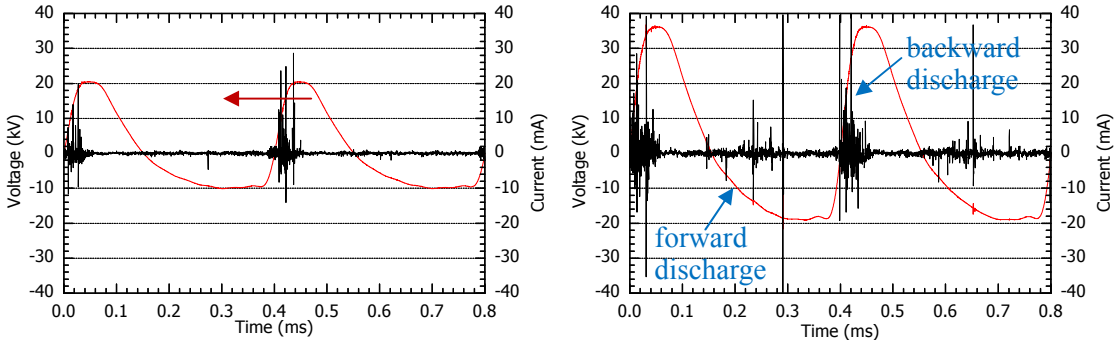

(a) negative sawtooth, 10.78 kV_{rms} versus 19.68 kV_{rms}

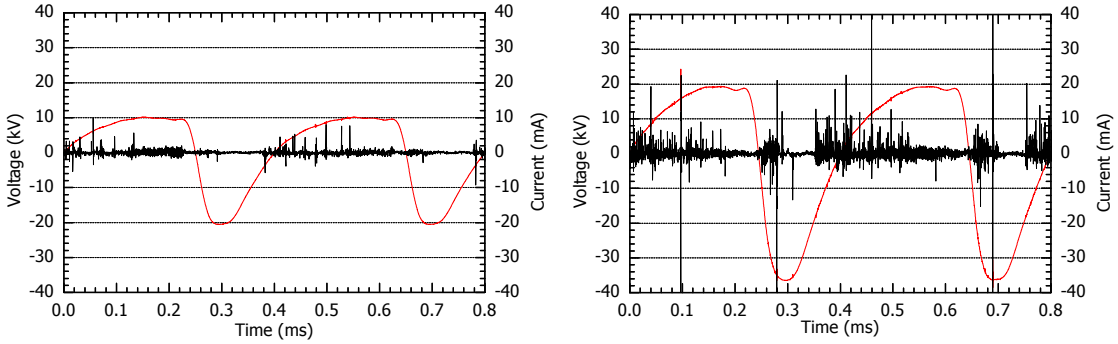

(b) positive sawtooth, 10.81 kV_{rms} versus 19.77 kV_{rms}

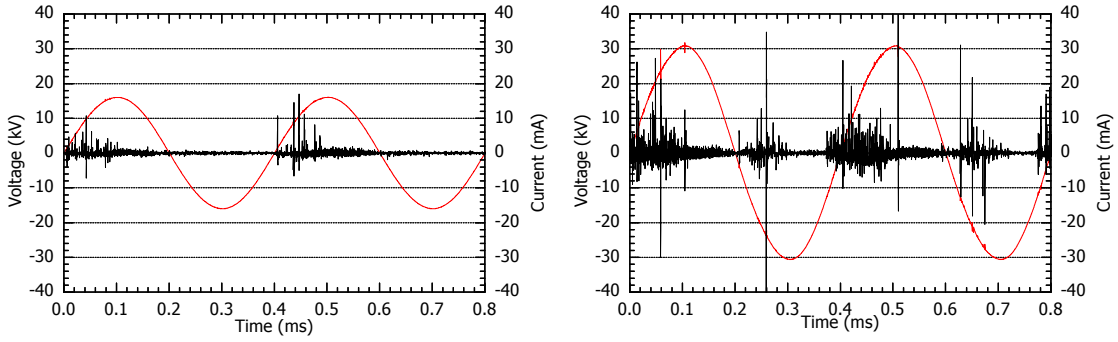

(c) sinusoidal, 11.33 kV_{rms} versus 21.68 kV_{rms}

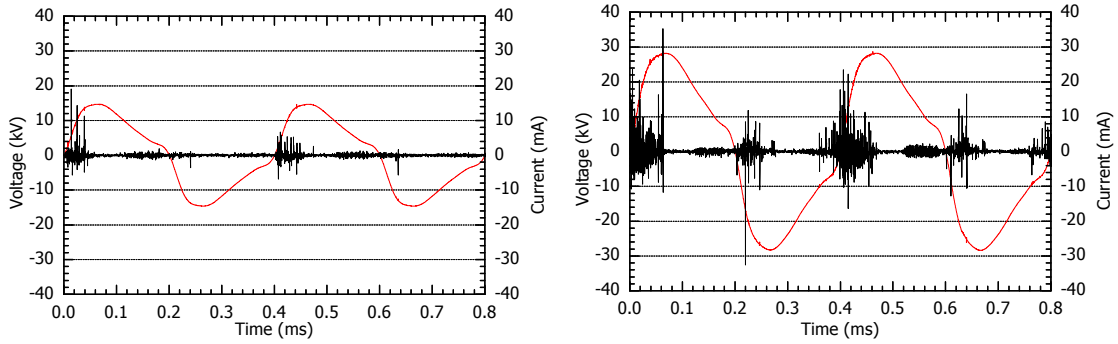

(d) square, 9.81 kV_{rms} versus 19.39 kV_{rms}

Figure D.10: Electrical measurement for various waveforms at 2.5 kHz

The measured thrust versus the consumed power for various AC frequencies is shown in Figure D.11, while the corresponding measured thrust versus peak-to-peak voltage is shown Figure D.12.

For the sinusoidal waveform, higher AC frequency corresponds to higher thrust at the same applied voltage below the onset of filamentary mode but with lower force efficiency (thrust versus power). However, the increased saturation thrust is associated with the actuator operated at lower AC frequencies. This trend is similar to that in the work by Thomas *et al.* (2009) for sinusoidal waveform. Below the onset of filamentary mode, higher frequency at a specific peak-to-peak voltage corresponds to higher voltage increase rate and thus higher voltage gradient, which results in higher electro-hydrodynamic (EHD) force (thrust). When the voltage is high enough, filamentary mode is reached for the higher frequency while not for the lower frequency. Eventually higher voltage can be reached without filamentary mode for the lower frequency, which is associated with the higher saturation thrust.

For the negative sawtooth, the trend of force efficiency is similar to that of sinusoidal waveform, while the AC frequency has little effect on the measured thrust at the same peak-to-peak voltage. As for the square waveform, the AC frequency has little effect on the force efficiency below the onset of filamentary mode while the measured thrust for the higher frequency is higher at the same peak-to-peak voltage. However, the higher frequency has the larger saturation thrust, *e.g.*, 90 mN/m for 4 kHz versus 60 mN/m for 2 kHz, which is different from that for the sinusoidal waveform. As shown in Figure D.13, the positive-going and negative-going parts are similar for the 2 kHz and 4 kHz (compare the indicated parts). However, during the same period, the number of these two parts is twice for the 4 kHz, resulting in almost twice the thrust below the saturation (see Figure D.11). In addition, the voltage shape for the 4 kHz is similar to the sinusoidal waveform, resulting in similar force efficiency and relation of thrust to peak-to-peak voltage (see Figures D.11 and D.12). For the frequency more than 4 kHz, the performance of plasma actuator at square waveform is close to the corresponding sinusoidal

waveform.

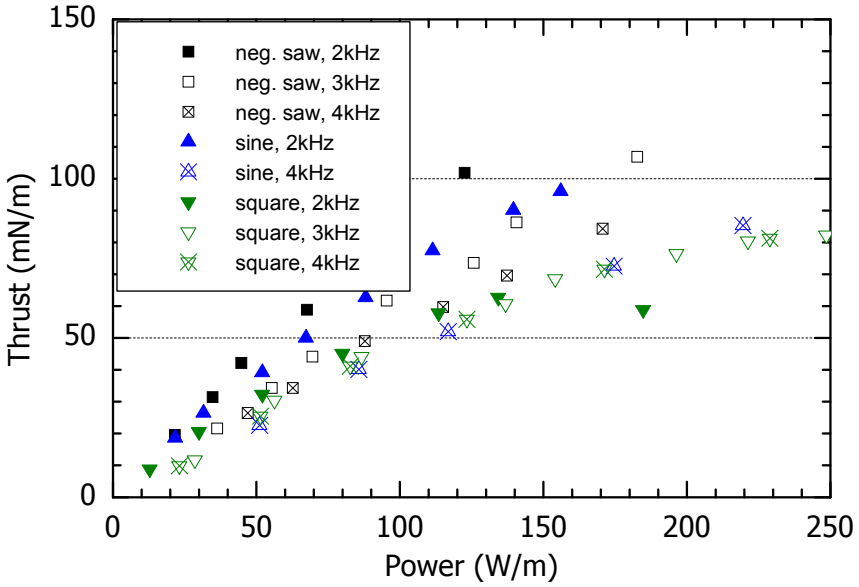

Figure D.11: Thrust versus power for various AC frequencies

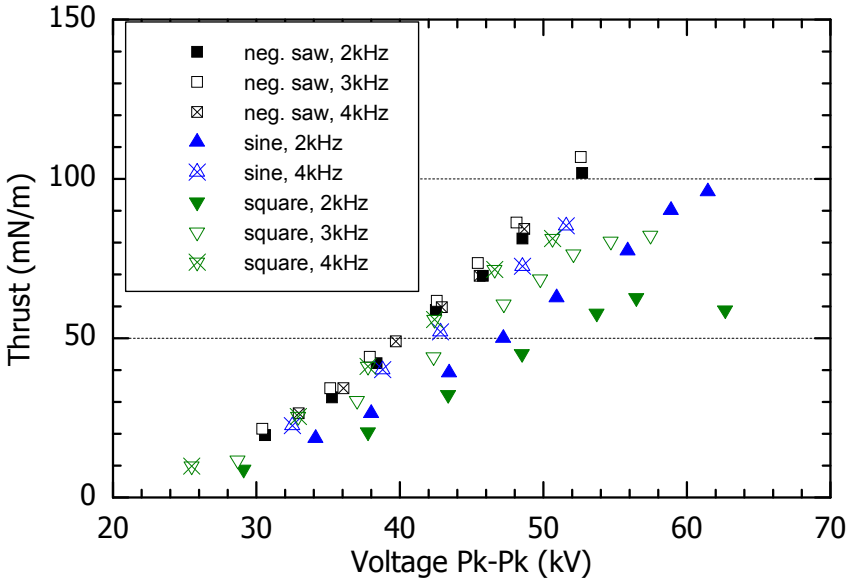

Figure D.12: Thrust versus peak-to-peak voltage for various AC frequencies

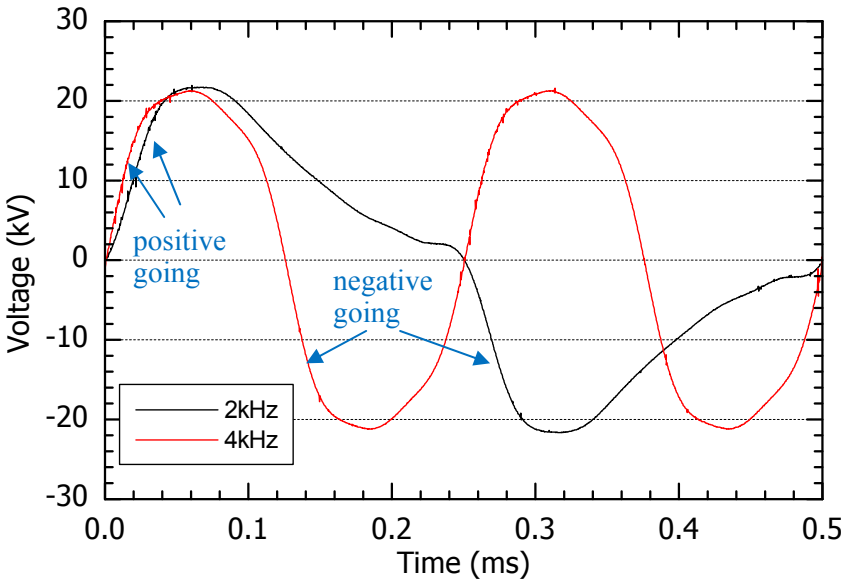

Figure D.13: Voltage measurement for various frequencies with square waveform

D.3 Effect of Insulation Width

In this section, the effects of exposed electrode width and covered width (see Figure D.3) are studied. The plasma actuator has a Teflon sheet with 6.35 mm thick. The hidden electrode has a width of 25.4 mm, while the exposed electrode has widths *w* of 6.35, 12.7 and 25.4 mm. For the covered width on exposed electrode, four cases with increased insulation width are chosen, which correspond to covered 0 mm (uncovered), covered 1 mm, exposed 1 mm and exposed 0 mm (fully covered). The input waveform is negative sawtooth at 2 kHz.

Figures D.14 and D.15 show the measured thrust versus the peak-to-peak voltage and versus consumed power, respectively. Please note that the results for 6.35 mm and 25.4 mm wide exposed electrode are sufficient to demonstrate the effect of insulation width. For uncovered cases, both the measured thrust and force efficiency decrease with exposed electrode width, which is consistent with the observation by Hoskinson and Hershkowitz (2010).

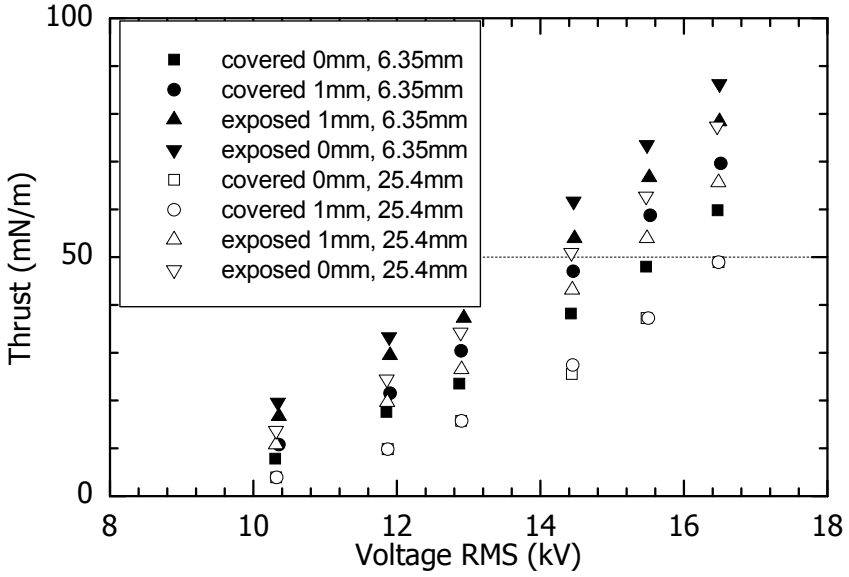

Figure D.14: Thrust versus RMS voltage for the effect of insulated exposed electrode

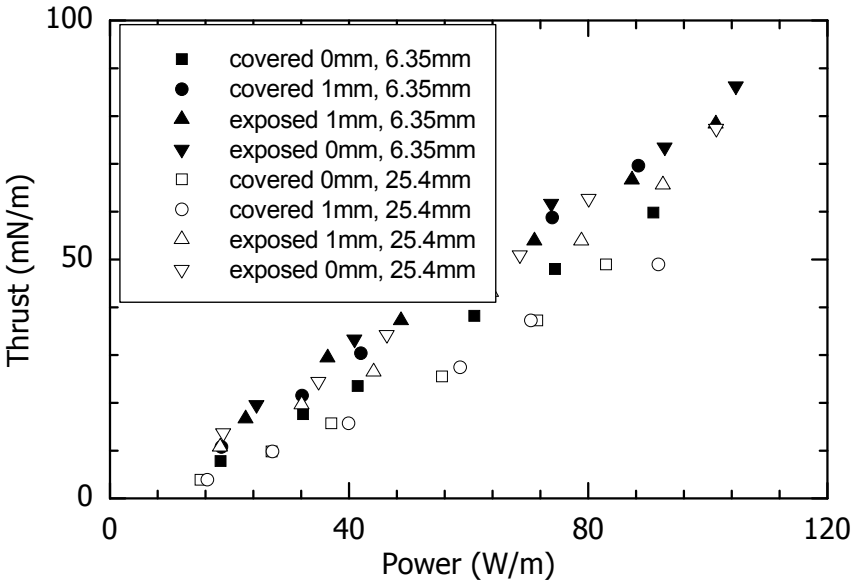

Figure D.15: Thrust versus power for the effect of insulated exposed electrode

In general, for the specific exposed electrode width, measured thrust at the same voltage increases with insulation width. The increase between the uncovered and 1 mm covered mainly results from the removal of the plasma and associated induced $-x$ force at the upstream edge of

the exposed electrode. However for the width of 12.7 and 25.4 mm, the thrust difference between uncovered and 1 mm covered is insignificant. This is because the plasma at upstream edge and induced force in $-x$ direction is small for the wider electrode.

The thrust increase between 1 mm covered and 1 mm exposed is mainly caused by the suppression of the circulation (associated with the reverse flow) over the exposed electrode. This difference for the electrode width of 6.35 mm is smaller than that for 12.7 and 25.4 mm, which is consistent with the PIV measurements in Kriegseei *et al.* (2009), showing the increasing flow circulation above the exposed electrode with the increased electrode width.

The thrust increase between 1 mm exposed and fully covered is comparable to that between 1 mm covered and 1 mm exposed, showing that the thrust is very sensitive to the exposed width in the small range (less than 1 mm). Note that the circulation on the exposed electrode may not be the main change as the exposed width is further reduced, since the reverse flow is already largely suppressed for the exposed width of 1 mm (Kriegseis *et al.*, 2009). This similar phenomena (thrust increase below the exposed width of 1 mm) is also observed by Hoskinson and Hershkowitz (2010), although they only change the exposed electrode width.

Based on the above observation, the plasma actuator with narrow fully-covered exposed electrode has a higher force efficiency and higher thrust at the same applied voltage. For the later application, the fully-covered exposed electrode with a width of 6.35 mm is chosen

D.4 Effect of Serrated Foil-type Electrode

The results presented previously are based on the exposed electrode with straight edge (Figure D.16(a) and (b)). In this section, the downstream edge of the exposed electrode is made serrated (composed of a series of triangular parts) and its effect on the actuator performance is studied. As discussed by Thomas *et al.* (2009), a serrated electrode corresponds to locally increased electric field at the triangle tips, since the edge of the electrode represents an iso-potential line. The locally increased electric field can favor the plasma generation and the

induced thrust. As shown in Figure D.16(c) and (d), the plasma is generated at low voltage near the triangle tips (observed from the brighter points), while the plasma is more uniform at high voltage. Please note that plasma is also observed upstream the tips.

As shown in Figure D.16, the serrated electrode in these experiments is characterized by the height h and the width a of the triangular serration. Three combinations of h and a with the electrode width of 25.4 mm are tested, in which h = 12.7 mm and a = 3.2 mm is shown the best in terms of force efficiency. The optimal serrated electrode (higher ratio of h/a) generally has higher local electric field and the higher density of the serration. In fact all three geometries improve the actuator performance.

Figures D.17 and D.18 show the measured thrust of the actuator with optimal serrated exposed electrode versus the consumed power and versus peak-to-peak voltage, respectively. The actuator is operated at 4 kHz for both negative sawtooth and square waveforms. The results are compared with the straight foil-type electrodes. Please note that the triangle tip and the leading edge of hidden electrode are located with the gap of 0 mm.

For the negative sawtooth waveform, the difference of measured thrust at the same power and applied voltage between serrated and straight exposed electrodes decreases with increased applied voltage. In contrast, these differences for the square waveform are almost kept constant as the voltage increases. Moreover, the performance improvement by using the serrated electrode is more obvious for the square waveform, even though the negative sawtooth waveform always has the better performance at the same condition. In addition, the maximum obtainable thrust for the square waveform is also increased (102 versus 82 mN/m). This is different from that in Thomas *et al.* (2009), which argue that the saturation thrust with serrated electrode at negative sawtooth waveform is similar to that with the straight electrode. One possible reason is that the non-uniform fine spots at the straight electrode (it depends on the electrode quality) favor the filamentary discharge at higher voltage (the streamer can be observed at these locations when filamentary mode is reached), compared to the uniform tips at the serrated electrode. Anyway

these fine spots at the straight electrode are also beneficial for the initialization of the plasma at low applied voltages (see Figure D.16). However, since they are non-uniform, the effect is not as good as for the serrated electrode.

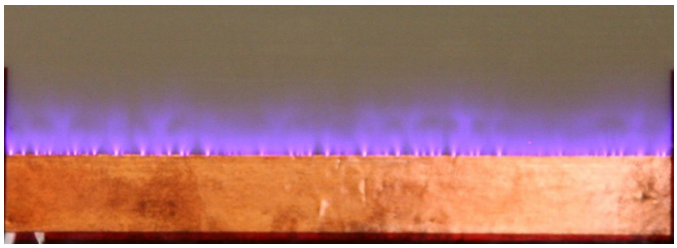

(a) 10.17 kV_{rms}, straight electrode

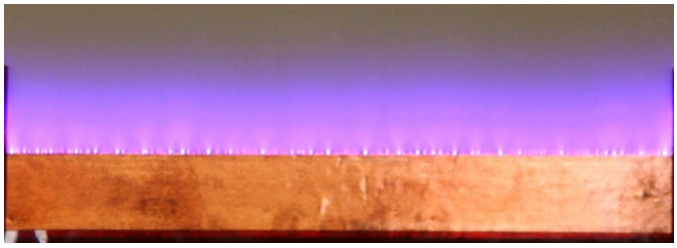

(b) 15.04 kV_{rms}, straight electrode

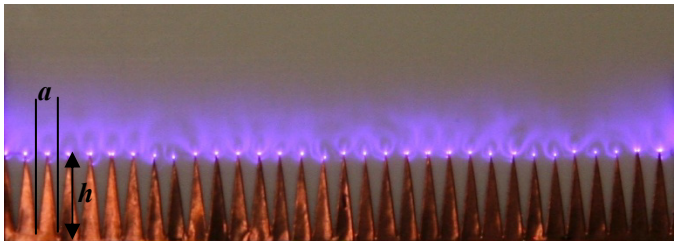

(c) 10.15 kV_{rms}, serrated electrode

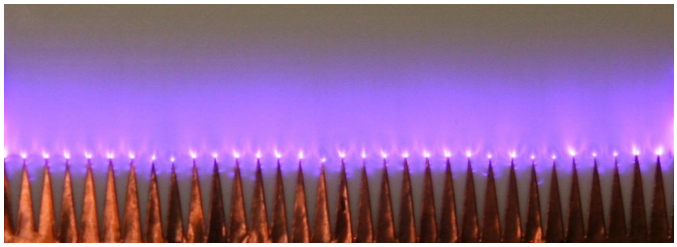

(d) 15.01 kV_{rms}, serrated electrode

Figure D.16: Plasma for the serrated and straight exposed electrodes (negative sawtooth)

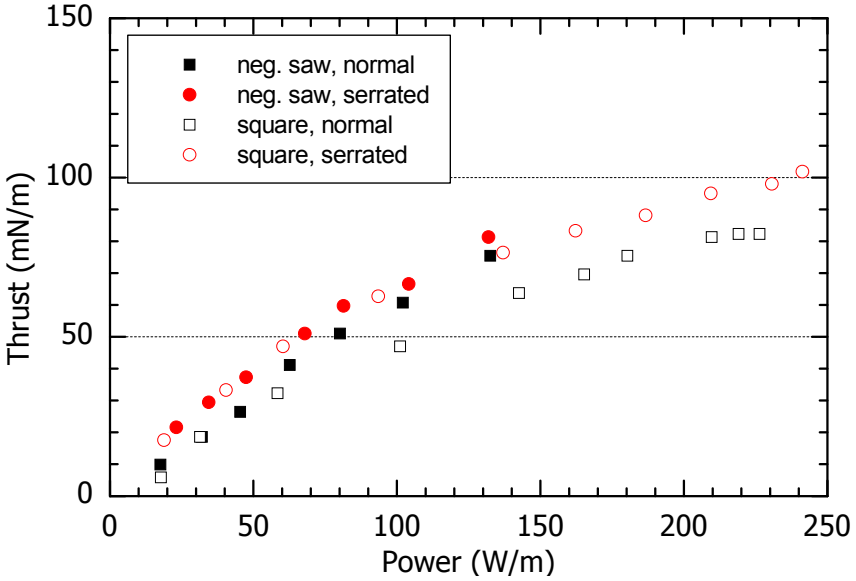

Figure D.17: Thrust versus power for the effect of exposed electrode shape

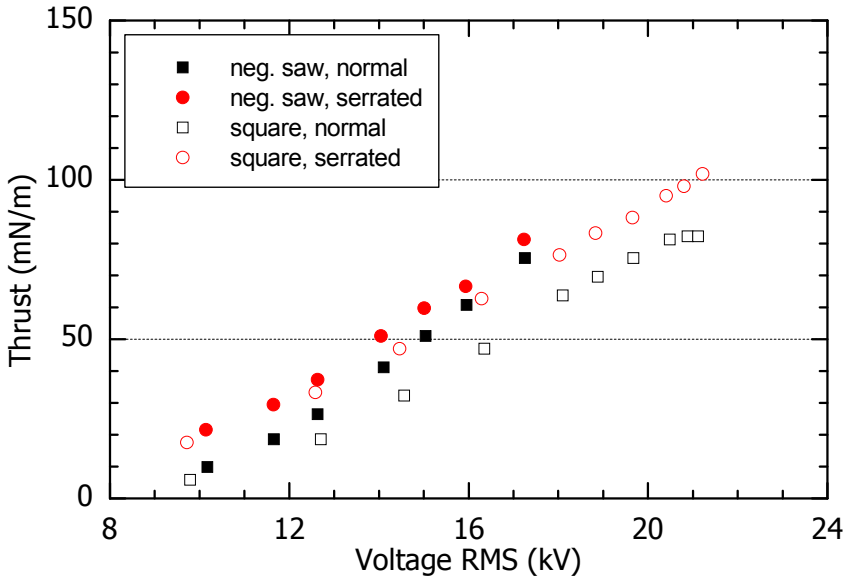

Figure D.18: Thrust versus RMS voltage for the effect of exposed electrode shape

D.5 Effect of Wire-type Electrode

Section D.3 has shown that the actuator performance decreases with the width of the exposed electrode. In this section, the exposed electrodes are replaced by a fine wire with a

diameter of 0.025 mm, 0.076 mm and 0.254 mm, respectively. The actuators are operated at 2 kHz for both negative and positive sawtooth waveforms.

Figures D.19 and D.20 show the measured thrust versus RMS voltage and versus the consumed power, respectively. Figure D.21 plots the electrical measurements for several cases (the left side corresponds to the smaller electrode diameter of 0.025 mm while the right side the larger diameter of 0.254 mm). From Figures D.19 and D.20, the actuator performance for both waveforms decreases with increasing wire diameter. This trend is similar to foil-type electrode in Figures D.14 and D.15. For the cases with thin wire-type electrode at low applied voltage, as shown in Figure D.21(a) and (c), the current spikes (corresponding to filaments) during the positive-going part are significantly reduced and even suppressed. This is referred as filament-free plasma (Hoskinson and Hershkowitz, 2010), which either occurred between each filamentary microdischarge or instead of filamentary microdischarges when the applied voltage is reduced. When the plasma actuator is operated in filament-free mode, the backward discharge is observed similar to the forward discharge. In other words, when the filament-free mode appears, the brightness is lower, the required power consumption begins to decrease and the induced force begins to increase sharply (Hoskinson and Hershkowitz, 2010). For the cases with thin wire-type electrode at higher voltage or with wider wire-type electrode, the current evolution is qualitatively the same as that of foil-type electrode in Figure D.10.

As discussed in the previous section, the actuator performance with foil-type exposed electrodes is much better for the negative sawtooth waveform than the positive one. This can also be observed for the wire-type electrode with the diameter larger than 0.076 mm (see Figures D.19 and D.20). However, for the finer wire (*e.g.*, 0.025 mm), this phenomena is not obvious, especially for the plot of thrust versus RMS voltage in Figure D.19. This may also result from the filament-free mode for thin electrode, *i.e.*, the plasma evolution for both waveforms is mainly composed of forward discharge at low voltage while composed of backward discharge at high voltage.

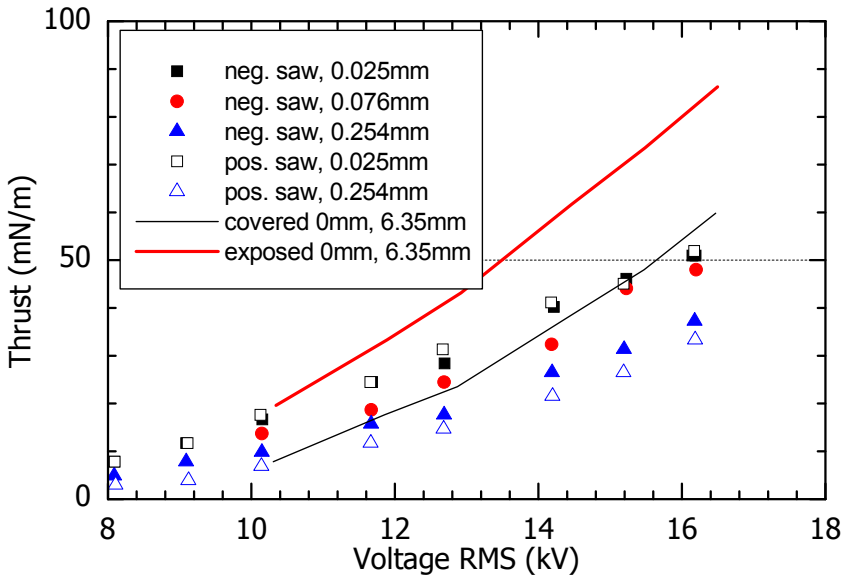

Figure D.19: Thrust versus RMS voltage for wire-type exposed electrode

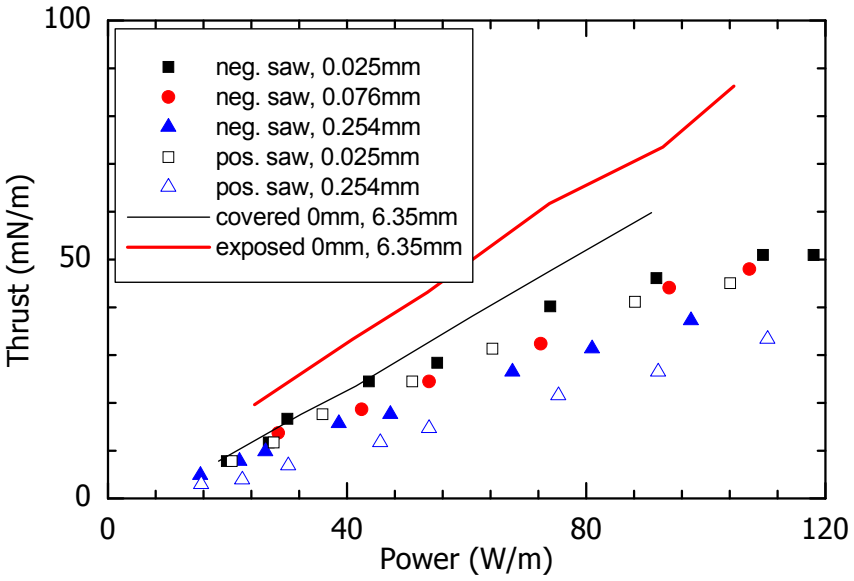

Figure D.20: Thrust versus power for wire-type exposed electrode

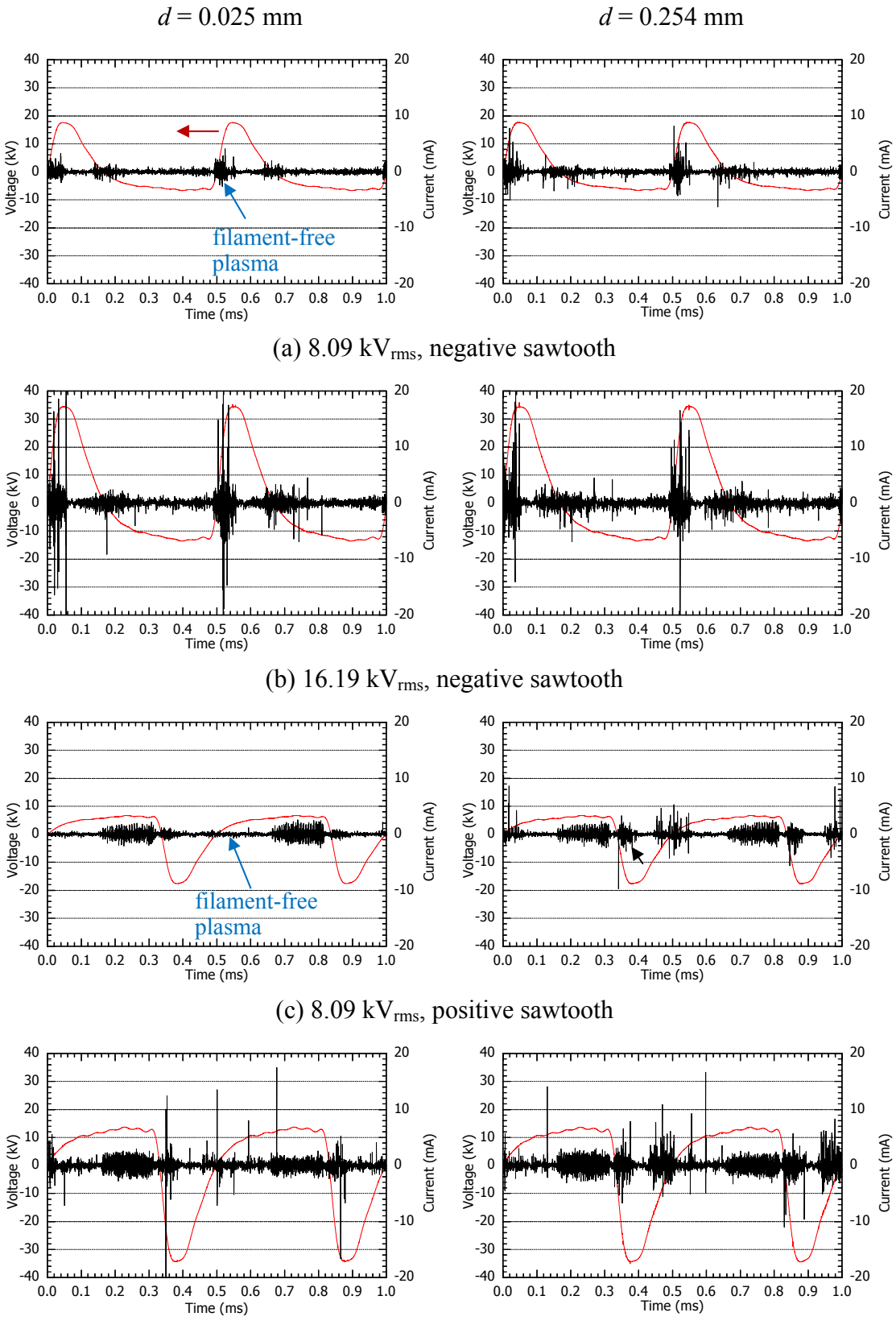

(a) 8.09 kV_{rms}, negative sawtooth

(b) 16.19 kV_{rms}, negative sawtooth

(c) 8.09 kV_{rms}, positive sawtooth

(d) 16.19 kV_{rms}, positive sawtooth

Figure D.21: Electrical measurement for the actuators with wire-type electrode at 2 kHz

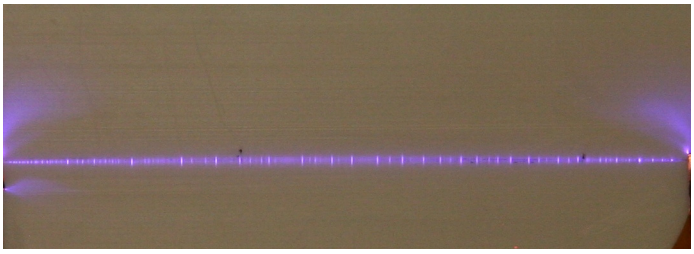

(a) 8.09 kV_{rms}

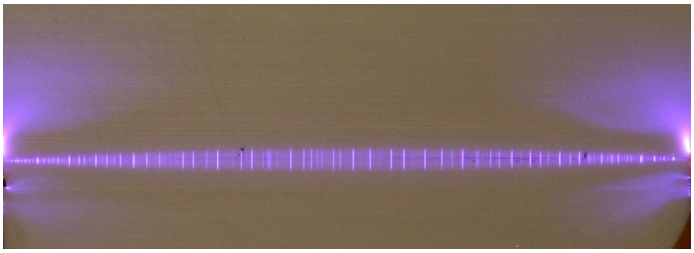

(b) 12.69 kV_{rms}

Figure D.22: Plasma for wire-type exposed electrode with a diameter of 0.025 mm

As for the comparison of wire-type and foil-type exposed electrode without insulation, the former is better at low applied voltage while worse at high applied voltage in terms of the measured thrust versus applied voltage. This is caused by the filament-free discharge at low voltage and the more filamentary discharge at higher voltage for the wire-type electrode. Moreover, the fine wire at high voltage is unstable, like spring, as shown in Figure D.22. In other words, the plasma actuator with thin wire-type electrode can not be operated at high voltage. This limits the potential of fine wire to achieve the higher maximum obtainable force. The actuator performance at low voltage is similar to that in Hoskinson and Hershkowitz (2010), where the plasma actuator operated at higher voltage was not tested. In addition, the fully covered foil-type electrode always has higher measured thrust than wire-type electrode. As for the force efficiency (Figure D.20), the wire-type electrode is always lower than the foil-type electrode, regardless if it is covered or not.

D.6 Effect of Tri-electrode Configuration

The previous parametric study is based on a normal DBD plasma actuator composed of two electrodes excited by an AC high voltage. The tri-electrode configuration (shown in Figure D.4)

is recently proposed (Moreau *et al.*, 2008) in order to obtain higher plasma force. In the tri-electrode configuration, the AC voltage serves to weakly ionize the air, while the DC component aims to extend the discharge region and accelerate the ion drift velocity. If the third electrode is at a negative DC high voltage, one can produce a luminescent plasma sheet (namely sliding discharge). If it is at a positive DC high voltage, one can obtain a discharge that visually looks like DBD plasma. For our application of flow control, the latter one is chosen. In our test, the third electrode with a width of 6.35 mm ,connected with a positive DC source, is put 60 mm downstream of the DBD plasma actuator (trailing edge of the exposed electrode). The DBD plasma actuator has a Teflon sheet of 6.35 mm thick. As for the AC voltage, both negative sawtooth and square waveforms are adopted.

When the negative sawtooth is applied to the plasma actuator, the measured thrust increases with applied AC voltage, and also increases with applied DC voltage, as shown in Figure D.23. The maximum thrust increase of 50 mN/m can be achieved when the DC voltage is 40 kV and the AC voltage is 24 kV_{rms}. However, since the plasma actuator with negative sawtooth does not reach filamentary mode, the limit of tri-electrode configuration can not be observed. In the following test, the square waveform is thus chosen in order to investigate the limit.

The measured thrust versus RMS voltage and versus the consumed power (the sum of AC and DC power) for square waveform are shown in Figures D.24 and D.25, respectively. At any specific RMS voltage lower than saturation voltage, the plasma actuator at a DC voltage of 25 or 30 kV has the highest measured thrust. When the AC voltage is more than 18.5 kV_{rms}, the filamentary mode is reached and the thrust begin to decrease. Reaching the filamentary mode should explain the fact that the plasma actuator at DC voltage of 35 kV has a worse performance.

As for the force efficiency (thrust versus power in Figure D.25), it decreases with DC voltage if the filamentary mode is not reached. In other words, there is an up-limit of force efficiency at DC voltage of 0 kV. Near the saturation state of plasma actuator, the best performance corresponds to a DC voltage of 25 kV. This is because the DC voltage can postpone

the filamentary mode and thus produce higher force. If one focus on each part of power consumption, *i.e.*, DC and AC power, the AC power is shown to increase with AC voltage and independent of DC voltage (see Figure D.26). It can thus be interpreted that the third electrode with a DC voltage has very small effect on the AC part. This observation is consistent with that by Moreau *et al.* (2008). In contrast, the DC power consumption is mainly related to the DC voltage and weakly depends on the AC voltage except at high DC voltage of 30 and 35 kV (see Figure D.27). At the high voltage of 30 and 35 kV, the plasma actuator is not stable, since it is close to the air breakdown between the two exposed electrodes.

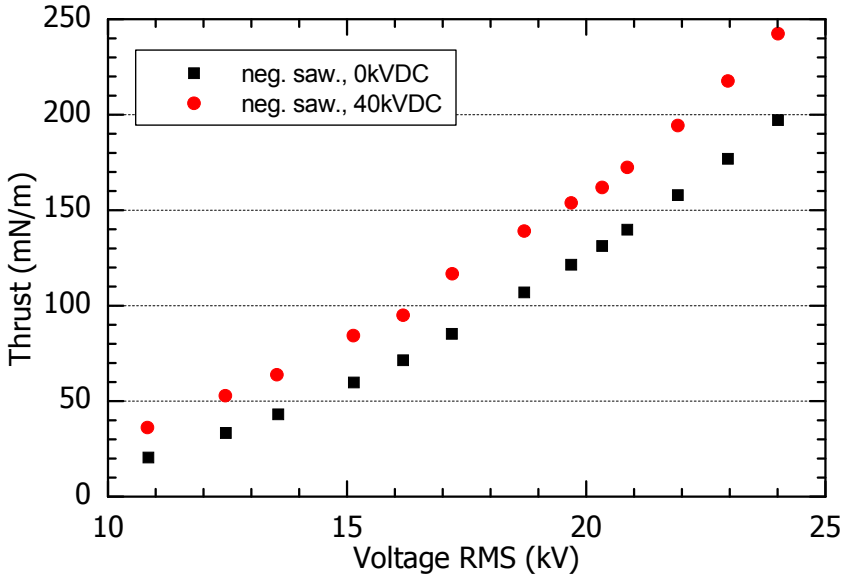

Figure D.23: Thrust versus RMS voltage (negative sawtooth) for tri-electrode configuration

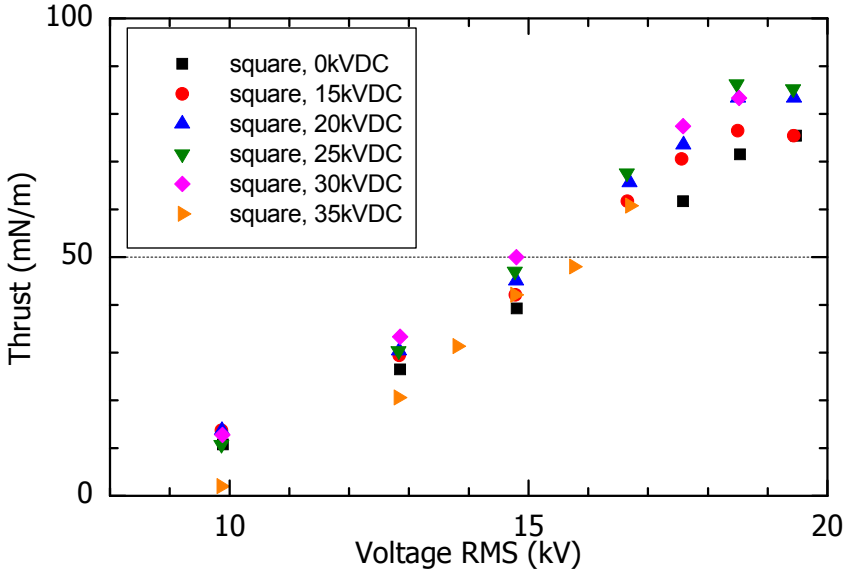

Figure D.24: Thrust versus RMS voltage for tri-electrode configuration

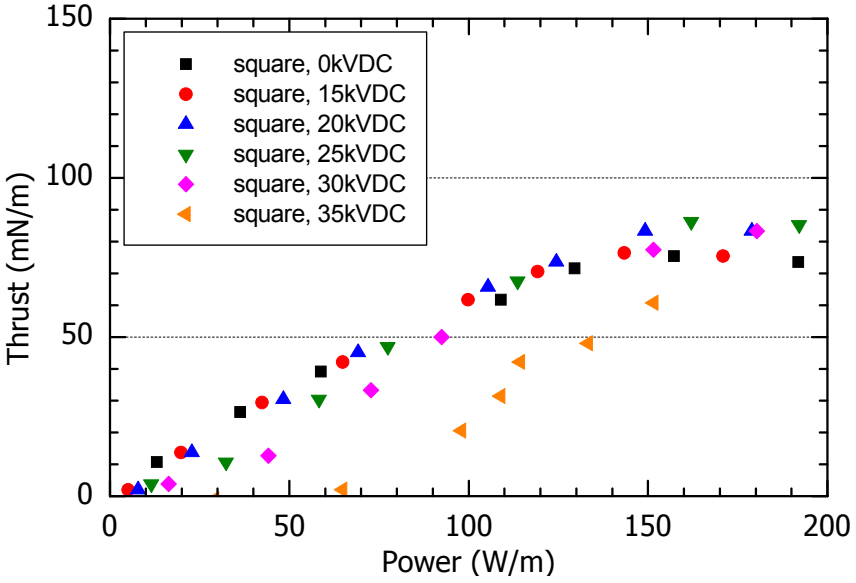

Figure D.25: Thrust versus power for tri-electrode configuration

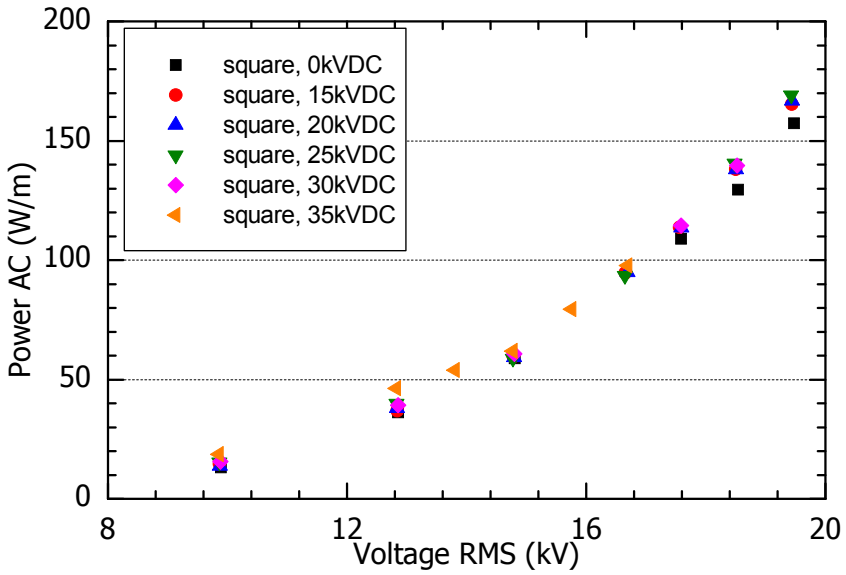

Figure D.26: AC power versus RMS voltage for tri-electrode configuration

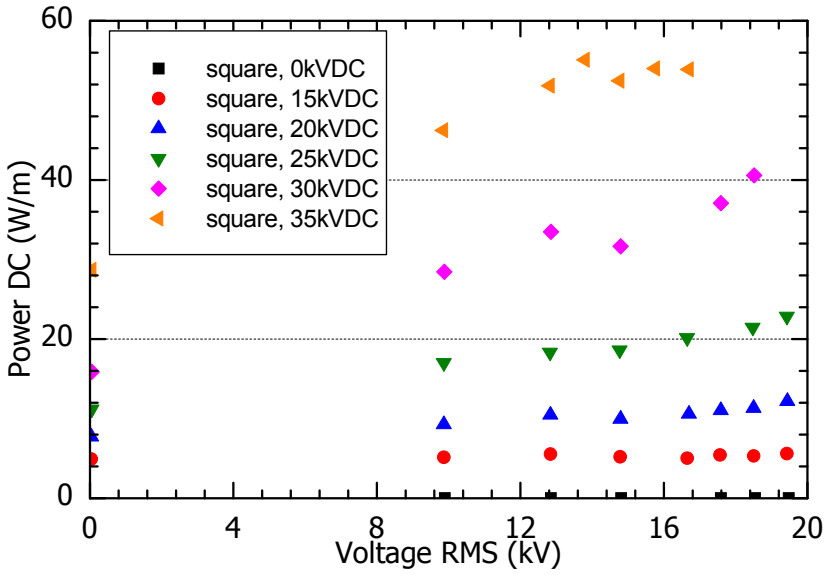

Figure D.27: DC power versus RMS voltage for tri-electrode configuration

Appendix E: Proper Orthogonal Decomposition (POD)

In the POD, a turbulent space-time velocity field $\tilde{u}_i(\vec{x},t)$ (i = 1, 2, 3) can be split as (Hemon and Santi, 2003)

$$\tilde{u}_i(\vec{x},t) = \sum_{k=1}^{\infty} \psi_k(t)\varphi_{ik}(\vec{x}) \tag{E.1}$$

where $\varphi_{ik}(\vec{x})$ is the spatial mode (called *topos*) of order k and $\psi_k(t)$ is the corresponding temporal mode (called *chronos*). Each combination of $\psi_k\varphi_{ik}$ represents a basic state embedded in the random turbulent flow field.

To solve Equation (E.1), the singular value decomposition of matrix A is applied

$$A = U\sum V^T = QV^T \tag{E.2}$$

where U and V are orthogonal and $\sum$ is a diagonal matrix whose coefficients α_k are the singular values of A. Thus Equation (E.1) is solved, with Q and V corresponding to ψ and φ, respectively.

The eigenvalues λ_k ($\lambda_k = \alpha_k^2$) is representative of the energy associated with the mode k. Thus the global energy of the signal is equal to the sum of the eigenvalues

$$\sum_{k=1}^{\infty} \lambda_k = \sum_{k=1}^{\infty} \alpha_k^2 \tag{E.3}$$

The global entropy of the signal characterizing its degree of disorder is defined as (Aubry *et al.*, 1991)

$$H = -\lim_{M\to\infty} \frac{1}{\log M} \sum_{k=1}^{M} \lambda_{rk} \log \lambda_{rk} \tag{E.4}$$

with

$$\lambda_{rk} = \lambda_k / \sum_{k=1}^{\infty} \lambda_k \tag{E.5}$$

where M is the total mode number (M = 320 in the present study).